Laser Powder Bed Fusion and Post-Treatments of (α+β) and Metastable β Titanium Alloys with Adapted Biocompatibility and Improved Mechanical Performance

zur Erlangung des akademischen Grades
DOKTOR DER INGENIEURWISSENSCHAFTEN (Dr.-Ing.)
der Fakultät für Maschinenbau
der Universität Paderborn

genehmigte
DISSERTATION

von
M.Sc. Maxwell Hein
aus Bad Wildungen

Tag des Kolloquiums:	10.08.2023
Referent:	Prof. Dr.-Ing. habil. Mirko Schaper
Korreferent:	Prof. Dr. med. vet. Manfred Kietzmann

Danksagung

Die Fertigstellung meiner Dissertation am Lehrstuhl für Werkstoffkunde (LWK) in der Fakultät Maschinenbau der Universität Paderborn wäre ohne die Unterstützung und Hilfe vieler Menschen nicht möglich gewesen. Sie ist das Resultat einer kollektiven Anstrengung und einer Vielzahl von wertvollen Beiträgen. An dieser Stelle möchte ich meinen aufrichtigen Dank ausdrücken und mich für die Unterstützung und das Vertrauen, das mir entgegengebracht wurde, bedanken.

Prof. Dr.-Ing. habil. Mirko Schaper danke ich herzlich für die Betreuung meiner Arbeit, sowie das Vertrauen und konstruktive Feedback. Deine fachliche Unterstützung und dein Rat haben meine Forschung und mich persönlich maßgeblich geprägt.

Mein herzlicher Dank gilt auch meinem Zweitgutachter, Prof. Dr. med. vet. Kietzmann, für die Übernahme des Korreferats, sowie die wertvollen Diskussionen und kritischen Anmerkungen bei den Projekttreffen.

Für den Vorsitz des Prüfungsausschusses möchte ich Prof. Dr.-Ing. Schöppner meinen Dank aussprechen.

Besonderer Dank gebührt Dr.-Ing. Kay-Peter Hoyer. Deine engagierte Unterstützung, dein fachlicher Input und dein Rat in kritischen Phasen meiner Forschung und Tätigkeit haben mir wertvolle Perspektiven eröffnet und meine Arbeit bereichert.

Ich bedanke mich bei meinen Projektpartnern der Stiftung Tierärztliche Hochschule Hannover sowie der Technischen Universität Dortmund für die gute Zusammenarbeit. Der Deutschen Forschungsgemeinschaft danke ich für die finanzielle Förderung, die Teile dieser Arbeit ermöglicht hat.

Für die konstruktive, freundschaftliche und persönliche Zusammenarbeit bedanke ich mich bei meinen jetzigen Kollegen der Hesse GmbH, den ehemaligen Kollegen vom LWK sowie den studentischen Hilfskräften, Studien- und Abschlussarbeitern.

Meiner Familie und insbesondere meinen Eltern, Lydia und Peter, sowie meinen Freunden danke ich von Herzen. Euer bedingungsloser Rückhalt und eure stetige Ermutigung haben mich in den herausfordernden Zeiten motiviert und gestärkt.

Mit tiefer Dankbarkeit möchte ich meiner Frau Christina für ihre unermüdliche Unterstützung, ihr entgegengebrachtes Verständnis und ihre Geduld während meiner gesamten Promotion und vor allem in den letzten intensiven Phasen danken. Deine Bereitschaft, mich zu ermutigen, mir beizustehen und mich zu motivieren, ist für mich von unschätzbarem Wert. Ich bin unendlich dankbar, dich und Emil an meiner Seite zu haben und freue mich, die kommenden kleinen und großen Abenteuer gemeinsam mit euch zu erleben!

Paderborn, im November 2023

Maxwell Hein

Abstract

Titanium and titanium alloys offer various possible applications, particularly in medical technology. The additive processing of these alloys by laser powder bed fusion enables the individualization and manufacture of load-bearing, patient-specific implants. The laser powder bed fusion process leads to characteristic material behavior and microstructures. Hence, the (α+β) titanium alloy Ti-6Al-7Nb, already established in conventional biomedical engineering, and the promising metastable β titanium alloy Ti-24Nb-4Zr-8Sn are processed additively. They show significant differences in the resulting microstructure and mechanical properties due to process restrictions and their different chemical compositions. The mechanical performance of Ti-6Al-7Nb is characterized in terms of quasi-static, low-cycle, and high-cycle fatigue behavior. The material performance, particularly the quasi-static and fatigue strengths, can be tailored and partially improved through various heat treatments with subsequent coating by physical vapor deposition with TiN, TiCN, and a-C:Ag. Heat treatment of additively processed Ti-24Nb-4Zr-8Sn leads to a wide range of material properties depending on the process route. It shows considerable potential for use as an implant due to the low elastic modulus.

Kurzfassung

Titan und Titanlegierungen bieten vielfältige Einsatzmöglichkeiten insbesondere im Bereich der Medizintechnik. Die additive Verarbeitung dieser Legierungen mittels des pulverbettbasierten selektiven Laserstrahlschmelzens ermöglicht die Individualisierung und Herstellung von lasttragenden, patientenspezifischen Implantaten. Das pulverbettbasierte selektive Laserstrahlschmelzen führt, bedingt durch die besonderen prozessinhärenten Bedingungen, zu einem charakteristischen Werkstoffverhalten und Mikrostrukturen. Die (α+β) Titanlegierung Ti-6Al-7Nb, bereits in der konventionellen Biomedizintechnik etabliert, und die vielversprechende metastabile β Titanlegierung Ti-24Nb-4Zr-8Sn werden additiv verarbeitet und zeigen prozessbedingt und aufgrund ihrer chemischen Zusammensetzungen gravierende Unterschiede in Bezug auf die sich einstellende Mikrostruktur und daraus folgend auch auf die mechanischen Eigenschaften. Die mechanische Performance von Ti-6Al-7Nb wird hinsichtlich des auf das quasi-statischen, Kurz- und Langzeitermüdungsverhalten charakterisiert. Mittels verschiedener Wärmebehandlungen lassen sich die mechanischen Eigenschaften einstellen und zum Teil mit anschließender Beschichtung durch physikalische Gasphasenabscheidung mit TiN, TiCN und a-C:Ag insbesondere in Bezug auf die quasi-statischen Festigkeiten und Dauerfestigkeiten verbessern. Die Wärmebehandlung von additiv verarbeitetem Ti-24Nb-4Zr-8Sn führt je nach Prozessroute zu vielfältigen Materialeigenschaften. Zudem weist die Legierung durch den geringen E-Modul erhebliches Potential für die Verwendung als Implantat auf.

List of Publications

Parts of this thesis are already published in the following pre-publications:

Peer-reviewed Publications

Tillmann, W.; Lopes Dias, N.F.; Franke, C.; Kokalj, D.; Stangier, D.; Filor, V.; Mateus-Vargas, R.H.; Oltmanns, H.; Kietzmann, M.; Meissner, J.; Hein, M.; Pramanik, S.; Hoyer, K.-P.; Schaper, M.; Nienhaus, A.; Thomann, C.A.; Debus, J.: Tribo-mechanical properties and biocompatibility of Ag-containing amorphous carbon films deposited onto Ti6Al4V. In: *Surface and Coatings Technology*, 421 (2021).
DOI: 10.1016/j.surfcoat.2021.127384

Hein, M.; Hoyer, K.-P.; Schaper, M.: Additively processed TiAl6Nb7 alloy for biomedical applications. In: *Materialwissenschaft und Werkstofftechnik*, 52 (2021).
DOI: 10.1002/mawe.202000288

Hein, M.; Kokalj, D.; Lopes Dias, N.F.; Stangier, D.; Oltmanns, H.; Pramanik, S.; Kietzmann, M.; Hoyer, K.-P.; Meissner, J.; Tillmann, W.; Schaper, M.: Low Cycle Fatigue Performance of Additively Processed and Heat-Treated Ti-6Al-7Nb Alloy for Biomedical Applications. In: *Metals*, 12 (2022), 122.
DOI: 10.3390/met12010122

Tillmann, W.; Lopes Dias, N.F.; Kokalj, D.; Stangier, D.; Hein, M.; Hoyer, K.-P.; Schaper, M.; Gödecke, D.; Oltmanns, H.; Meissner, J.: Tribo-functional PVD thin films deposited onto additively manufactured Ti6Al7Nb for biomedical applications. In: *Materials Letters*, 321 (2022).
DOI: 10.1016/j.matlet.2022.132384

Hein, M.; Lopes Dias, N.F.; Pramanik, S.; Stangier, D.; Hoyer, K.-P.; Tillmann, W.; Schaper, M.: Heat Treatments of Metastable β Titanium Alloy Ti-24Nb-4Zr-8Sn Processed by Laser Powder Bed Fusion. In: *Materials*, 15 (2022), 3774.
DOI: 10.3390/ma15113774

Hein, M.: Influence of Physical Vapor Deposition on High-cycle Fatigue Performance of Additively Manufactured Ti-6Al-7Nb Alloy. In: *Crystals*, 12 (2022), 1190.
DOI: 10.3390/cryst12091190

Hein, M.; Lopes Dias, N.F.; Kokalj, D.; Stangier, D.; Hoyer, K.-P.; Tillmann, W.; Schaper, M.: On the Influence of Physical Vapor Deposited Thin Coatings on the Low-cycle Fatigue Behavior of Additively Processed Ti-6Al-7Nb Alloy. In: *International Journal of Fatigue*, 166 (2022).
DOI: 10.1016/j.ijfatigue.2022.107235

Presentations

Hein, M.; Hoyer, K.-P.; Schaper, M.:Additiv verarbeitete TiAl6Nb7-Legierung zur Anwendung als permanentes Implantat. DGM – Werkstoffwoche. 18.09.2019. Dresden, Germany.

Hein, M.; Hoyer, K.-P.; Schaper, M.:Additively Processed TiAl6Nb7 Alloy for Biomedical Applications. DGM – LightMat. 06.11.2019. Manchester, UK.

Hein, M.; Hoyer, K.-P.; Schaper, M.:Additiv verarbeitete β-Titanlegierung für die Medizintechnik. DGM – Fachtagung Werkstoffe und Additive Fertigung. 20.05.2020. Potsdam, Germany/online.

Hein, M.; Stangier, D.; Kokalj, D.; Lopes Dias, N.F.; Filor, V.; Mateus-Vargas, R.H.; Meissner, J.; Hoyer, K.-P.; Kietzmann, M.; Tillmann, W.; Schaper, M.:PVD beschichtete, additiv gefertigte TiAl6Nb7-Legierung für biomedizinische Anwendungen. DVM – Workshop – Zuverlässigkeit von Implantaten und Biostrukturen. 26.11.2020. Berlin, Germany/online.

Hein, M.; Lopes Dias, N.F.; Stangier, D.; Kokalj, D.; Filor, V.; Mateus-Vargas, R.H.; Oltmanns, H.; Meissner, J.; Hoyer, K.-P.; Kietzmann, M.; Tillmann, W.; Schaper, M.:PVD Coated, Additively Processed TiAl6Nb7 Alloy for Biomedical Applications. DGM – 6th Euro BioMat. 05.05.2021. Online.

Hein, M.; Stangier, D.; Kokalj, D.; Lopes Dias, N.F.; Oltmanns, H.; Hoyer, K.-P.; Meissner, J.; Tillmann, W.; Schaper, M.:Fatigue Behavior of Additively Processed, PVD Coated Ti-6Al-7Nb Alloy for Biomedical Applications. TMS 2022 Annual Meeting & Exhibition. 07.03.2022. Anaheim, California, USA/online.

Contents

1 Introduction

The world is getting older! According to the medium scenario of the United Nations (UN) global population prospects, the global population will be at 10.4 billion by the end of the century. People continue to live longer – the global life expectancy at birth reached 72.8 years in 2019, an increase of almost nine years since 1990, and is expected to rise to 77.2 years in 2050. [1]
The size and share of the older population are increasing, also known as demographic change, which describes the changes in population size and structure caused by changes in birth rates, death rates, and migration [2, 3]. The causes for the demographic change are diverse: longer life expectancy, fewer births, an aging population, smaller households, migration, a changing population size, improvements in hygiene, health education, and healthcare, and so forth [1, 4, 5]. The projected demographic change of the world population is visualized in Figure 1.1.

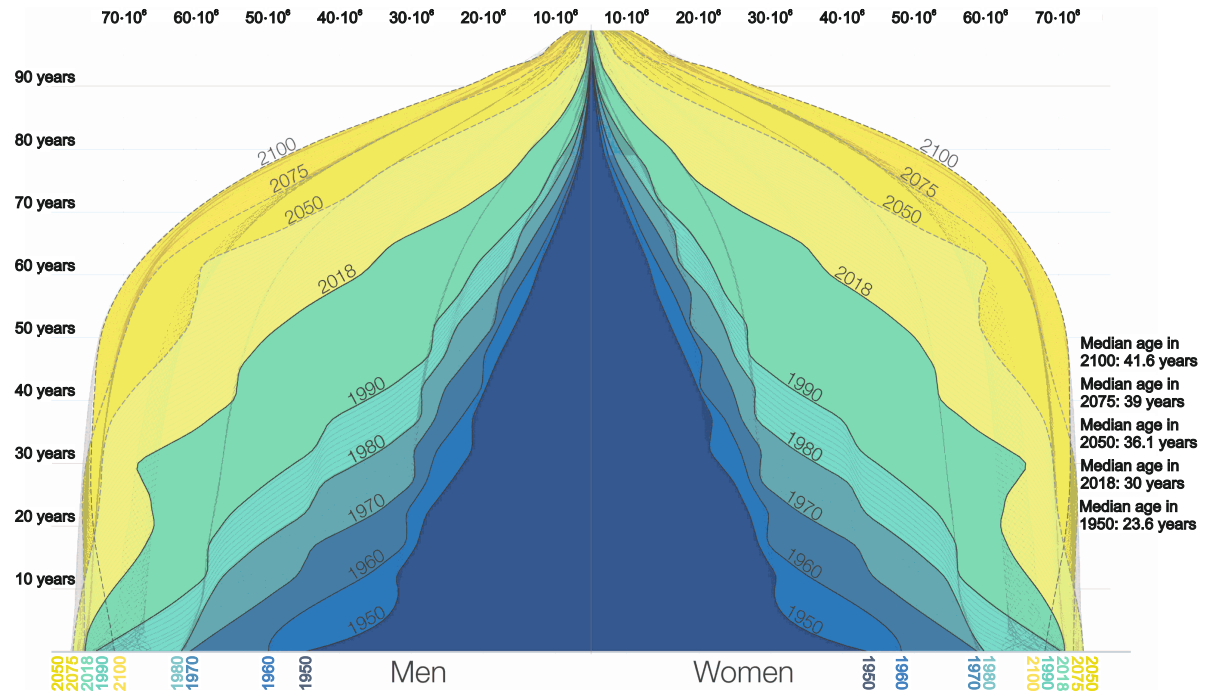

Figure 1.1: Age distribution of the world population by sex from 1950 to 2018 and the *UN Population Division´s* projection until 2100, according to [6].

As people get older, their diseases usually increase as well. In addition to diseases such as impending dementia and depression, cardiovascular diseases and cancer occur more frequently with age. Unavoidably, musculoskeletal diseases and injuries also appear, including osteoarthritis, rheumatic joint and muscle diseases, or osteoporosis. In particular, musculoskeletal diseases can be treated by improved medical care, for example, joint arthroplasty. The aging population, accompanied by improved medical care, in-

evitably leads to an increasing number of total joint replacements (TJR) and, therefore, to increasing implant failure due to various complications [7, 8]. Up to now, replacing damaged joints with artificial joints has been one of the most commonly performed surgical operations [9]. The estimated need for joint replacement in the UK and the US shows increasing numbers for primary total hip replacements (THR), total knee replacements (TKR), and revision THR and TKR. The number of primary operations is growing, especially among those aged 60 years and older [10, 11]. Caused by the demographic change alone, the projected need for THR in the UK for three decades shows estimated numbers increasing by 40 % [12]. These trends and projections are also observable for dental implants in the US [13]. Likewise, hip arthroplasty continues to increase significantly in countries participating in the Organisation for Economic Co-Operation and Development (OECD countries). The utilization of THR in these countries will increase from 1.8 million per year in 2015 to 2.8 million in the year 2050, while the mean utilization rate (incidence) of hip implants will increase from 184 to 275 per 100,000 total population at the same time [14].
The challenge is as follows: life expectancy, body weight, activity level, and disease incidence have increased during the past decades. Therefore, the patients having a TJR are more challenging recipients for a successful TJR [11]. One of the consequences is a significant increase in revision surgeries – the cumulative revision frequency 20 years after THR, including all diagnoses and reasons, is >20 %. Out of all primary revisions, more than every fifth implant must be revised later, mainly within a few years. The interval between multiple revisions shortens with each revision [14–16]. In addition, the need and demands for implants for bone fractures, metastases, infections, osteoporosis, osteoarthritis, and other diseases of the bone tissue and musculoskeletal apparatus have increased significantly [9, 17]. Furthermore, patient-related factors (e.g., body mass index, activity, genetics, age, gender), surgical factors (e.g., experience, fixation, stability), and implant-associated factors (e.g., design, fabrication, and material properties) are crucial for durable and successful implantation and function of an endoprosthesis [18–20]. Biomaterials used as implants interact with surrounding body tissues and fluids and are exposed to many influences [21, 22]. Conventional biomedical devices are mainly made of stainless steel, titanium, and cobalt-chromium alloys, as these materials offer good corrosion resistance and high biocompatibility. In general, the wear resistance of these alloys is comparably low. During implantation, the average life expectancy of implants with moving parts, such as a hip implant, is about ten years, mainly due to abrasive particles from mechanical wear [23]. In projecting TJR's future performance, considering several potentially opposing factors is reasonable and necessary. There have been significant improvements in implant design and construction, materials used, surgical techniques, and training in the past. Therefore, it is reasonable to assume that these improvements will lead to better clinical outcomes and enhanced longevity of TJR. However, there are also potentially opposing changes in the population needing TJR. Obese and overactive patients are challenged with the durability of joint arthroplasty. The typical 65-year-old patient receiving a TJR is physiologically not as old as when the joint replacement was first introduced, and his or her expectation of longevity of joint function increases with life expectancy. The combination of these factors raises significant new limits on achieving lifelong joint replacement with a single operation. [11]

2 State of Science and Technology

2.1 Preliminaries on Titanium Alloys

Metal materials, such as copper, iron, and aluminum, have been widely produced and used throughout the history of humankind. With the increased demands on material properties, these materials could not meet the requirements anymore. Therefore, developing new metal materials and alloys with excellent performance is required [24]. Titanium is the ninth most common element and the fourth metal in the Earth´s crust, behind iron, aluminum, and magnesium. The primary use of titanium is as oxide in various industries of everyday life. Nevertheless, due to the complex and costly reduction of titanium oxide to pure titanium, titanium is rarely used [25]. However, a variety of titanium alloys have been developed, which generally can be grouped into three major categories: α, β, and (α+β) titanium alloys, based on their microstructure. The microstructure dictates the material properties and depends on the chemical composition and thermo-mechanical processing routes [26].
With a density of 4.51 g/cm^3 for pure titanium, titanium can be classified as a light metal. Typically, titanium is used in various technical applications, such as corrosion (e.g., tanks, heat exchangers, reactor vessels) or load-bearing applications, such as structural components [27]. High strength purposes can be found in the aerospace industry due to the high weight and space limitations, increased operating temperatures, and corrosive environments [28]. Titanium is also used in the automotive sector. Its use cases are mainly racing and special-purpose cars, such as Formula 1, where titanium is used for engine parts or structural components [29, 30]. Additionally, titanium is often used for biomedical applications due to its superb biocompatibility, corrosion behavior, and outstanding mechanical properties, such as reduced elastic modulus, high strength-to-weight ratio, tailorable properties, and so on. Especially for load-bearing implants, like TJR (hip and knee), titanium is widely used [31–34].

2.1.1 Titanium Alloys Classification

Titanium exhibits allotropic behavior and can crystallize in various crystal structures depending on the temperature applied. Each of these crystal structures or modifications is stable within a specific temperature range. The temperature where this transformation occurs is called transus temperature, in particular $\beta_{transus}$ temperature. [26]
The α titanium is the allotropic, low-temperature modification of titanium with a hexagonal closed-packed (hcp) structure. Above the so-called $\beta_{transus}$ temperature, which is $(882 \pm 2)\,^{\circ}\mathrm{C}$ for pure titanium, the stable allotropic, high-temperature modification is β titanium, with a body-centered cubic (bcc) crystal structure [35]. The $\beta_{transus}$ temperature depends on the chemical composition and purity of the titanium [36]. A metastable,

non-equilibrium β phase can evolve in (α+β) alloys containing a sufficiently high concentration of β-stabilizers when rapidly cooled through the (α+β) phase field, see Figure 2.1. The α′ phase is a supersaturated, hexagonal, non-equilibrium phase, which occurs in some alloys by a diffusionless transformation of the β phase. The α″ phase is also a supersaturated but orthorhombic, non-equilibrium phase, which occurs in some alloys due to a diffusionless transformation of the β phase. [35, 37]
The reason for the versatility properties of titanium lies primarily in the different crystal structures with various properties and their proportion in the solid. Depending on their effect on stabilizing the α or β phases, the alloying elements can be classified as neutral, α- or β-stabilizers [35, 36, 38]. According to their position in the titanium lattice crystal, the elements are interstitial (oxygen, nitrogen, carbon, hydrogen) or substitutional (e.g., aluminum, copper, iron, niobium, tin, vanadium, zirconium) [38, 39]. Neutral alloying elements, such as tin or zirconium, have a negligible effect on the $\beta_{transus}$ temperature. β-stabilizers lower this temperature, whereas α-stabilizers increase it (e.g., aluminum, oxygen, nitrogen, carbon). Additionally, β-stabilizers can be further divided into β-isomorphous (e.g., molybdenum, vanadium, tantalum, niobium), stabilizing the β phase along all compositions, and β-eutectoid (e.g., iron, manganese, chromium, nickel, cobalt, copper, silicon, hydrogen), leading to a eutectoid transformation of the β phase, see Figure 2.1. As aluminum (Al) and molybdenum (Mo) are the essential α- and β-stabilizers, the α- and β-stabilizing capacity of alloying elements is expressed by the calculated Al-equivalent Al_{Eq} [40–42] and Mo-equivalent Mo_{Eq} [42–45], respectively. Metastable β alloys typically have a Mo_{Eq} >10 %, and stable alloys have a Mo_{Eq} >30 %. The risk estimation of alloy embrittlement due to the formation is given by the Al_{Eq} (>9 %) [46].

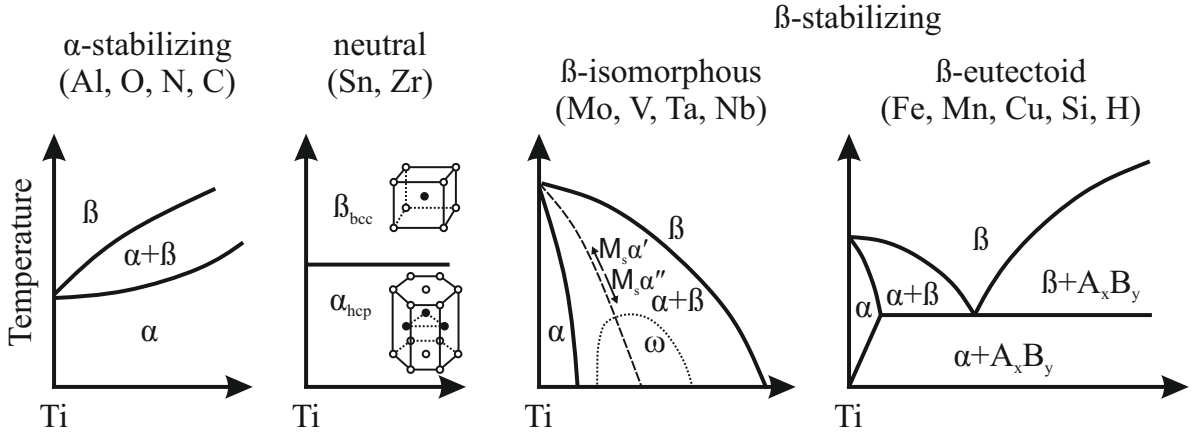

Figure 2.1: Schematic pseudo-binary phase diagrams illustrating the influence of alloying elements on the phase formation for neutral elements, α-stabilizer, and β-stabilizer (isomorphous and eutectoid); the neutral diagram depicts titanium hcp α and bcc β unit cells; the β-isomorphous diagram shows equilibrium hcp α-phase field, and bcc β-phase field, metastable ω-phase field, metastable hcp α′-martensite start temperature $M_S\alpha'$, and orthorhombic α″-martensite start temperature $M_S\alpha''$, according to [35, 46–48].

Below the $\beta_{transus}$ temperature, the time- and temperature-dependent diffusion processes run considerably slower. Therefore, a very fine lamellar microstructure can evolve by high cooling rates or a very coarse lamellar microstructure by low cooling rates. The continuous $\beta \rightarrow \alpha$ transformation can be isomorphic or eutectoid in alloys. The densely packed

bcc slip planes of the β phase $\{110\}_\beta$ merge into the hcp basal planes $\{0001\}_\alpha$ of the α phase. The formation of α lamellae is parallel to the $\{110\}_\beta$ plane. This bcc-hcp transformation is typical and was first observed by Burgers on zirconium crystals [49]. The orientation relation $\{0001\}_\alpha \parallel \{110\}_\beta$ and $<1120>_\alpha \parallel <111>_\beta$ for the sliding planes and sliding directions merging into each other are therefore called the "Burgers-relationship". For titanium, this fundamental relationship was confirmed at an early stage [50, 51]. In addition, the transformation can also occur under other complex orientation relations that have not yet been fully explored. These are referred to as „non-Burgers" α. Some authors consider that in some alloys, the „Burgers α" acts as a precursor to the „non-Burgers" α and that the latter is the thermodynamically more stable variant [52, 53].
With sufficient cooling rates, single lamellae grow at the grain boundary and from the growth front of individual lamellae packages. Diffusionless martensitic transformation of the bcc β phase into the hcp α phase requires fast cooling rates from above the M_S temperature. It results in metastable, very fine plate-like or acicular martensite formation. In contrast to ferrous materials, no significant decrease in the material's ductility occurs; only a slight increase in strength is achieved. Two different forms of titanium martensite can be formed: the hexagonal α′ and the orthorhombic α″ modification; the latter is usually formed during cooling from relatively low temperatures (<900 °C) and exhibits good ductility [35, 54, 55]. Another athermal phase, the ω-phase, can lead to embrittlement [46].
According to the previous description, pure titanium and its alloys can be classified into three groups: α, (α+β), and β. Besides this classification, a more detailed subdivision of the alloys is typical: commercially pure titanium (CP-Ti) alloy, α alloy, near-α alloy, (α+β) alloy, near- or metastable-β alloy, β alloy, and Ti-Aluminides. Only 20 to 30 of more than 100 available titanium alloys have reached commercial position. [26]
CP-Ti contains mainly the α phase and some impurities. According to the *American Society of Testing and Materials*, CP-Ti is available in four purity grades (CP-Ti Grade I to IV) [56]. The grades are distinguished based on their oxygen, nitrogen, hydrogen, iron, and carbon content [57]. These impurities dictate the material properties, mainly oxygen and iron [58]. 20 % - 30 % of the worldwide titanium consumption is covered by CP-Ti [25].
A solid solution of the α phase forms the so-called α alloys. Due to the single α phase, the microstructure of these alloys cannot be adjusted by heat treatments [36]. Generally, α alloys exhibit good high-temperature properties and are used in chemical and process engineering industries because of their superior corrosion behavior and high ductility [35]. 26 % of all titanium consumption in the US titanium market is α alloys [38].
The near-α alloys contain mainly α phase with a small share of β phase (<10 %) due to a small amount of β-stabilizers (1 % - 2 %) [59]. The β phase enhances strength and processability. These alloys are a good compromise of higher strength (α+β alloys) and creep resistance (α alloys). The commercially most applied high-temperature alloys belong to this class and are usable up to temperatures of 550 °C [35, 36].
The (α+β) alloys are the most widely used titanium alloy (>50 %) worldwide and in the United States (>70 %), respectively [35, 38]. These alloys contain about 4 % - 16 % of β-stabilizing elements and typically 10 % - 14 % of β phase at room temperature [59]. The most widely used (α+β) alloy is Ti-6Al-4V, covering over 56 % of the US and more than 50 % of the global titanium consumption [25, 36, 38].
Near-β alloys, also called metastable-β alloys, contain a large amount of about 10 % -

15 % β-stabilizers and only a small amount of α-stabilizers [36]. The formation of α-martensite is suppressed at room temperature, but the (α+β)-phase region is passed, see Figure 2.1 [46].
About 4 % of the titanium consumption in the US is β alloys [38]. The β-stabilizers favor the maintenance of the β phase in a metastable state at room temperature. The main characteristic of these metastable β alloys is that they can be aged, resulting in the precipitation of a very fine α phase distributed in the β matrix. These alloys can be tailored for high strength and toughness, much higher than (α+β) alloys [35, 38]. With a higher amount of β stabilizers, the stable β alloys contain only a single β phase, without any α phase formation, and can be processed at lower temperatures or can even be cold deformable [38, 46]. The corrosion behavior is better or equal compared to (α+β) alloys, and the tolerance for hydrogen pickup is higher, making these alloys usable in corrosive or hydrogen-rich environments [38].
Titanium aluminides (Ti-Al), particularly γ-TiAl- and α_2-Ti_3Al-based alloys, are experiencing increasing interest in the aerospace and automotive industries due to their superior physical and mechanical properties [26, 60].

2.1.2 Biocompatibility of Titanium Alloys

Medical devices used in the human body should be biocompatible and not harm the human body. Biocompatibility generally describes the compatibility between a technical and a biological system and can be divided into structural and surface compatibility [61]. In 2008, a definition for biocompatibility was proposed as follows: "Biocompatibility refers to the ability of a biomaterial to perform its desired function with respect to a medical therapy, without eliciting any undesirable local or systemic effects in the recipient or beneficiary of that therapy, but generating the most appropriate beneficial cellular or tissue response in that specific situation, and optimizing the clinically relevant performance of that therapy" [62]. In 2018 biomaterial experts defined as follows: "Biocompatibility is defined as the ability of a material to perform its desired functions with respect to a medical therapy, to induce an appropriate host response in a specific application and to interact with living systems without having any risk of injury, toxicity, or rejection by the immune system and undesirable or inappropriate local or systemic effects" [63, 64]. The degrees of biocompatibility for bone implants can be distinguished and defined as follows [65]:

- **Incompatible:** release of substances in toxic concentrations or antigens that can cause immune reactions and lead to allergies, foreign body reactions, inflammatory reactions, necrosis, or possible rejection reactions;
- **Biocompatible:** release of substances in non-toxic concentrations that can lead to encapsulation in connective tissue or weak foreign body reactions;
- **Bioinert:** no release of toxic substances;
- **Bioactive:** positive interaction with tissue differentiation and, as a consequence, binding or adhesion of bone along the interface between the implant and recipient tissue;
- **Inductive:** induction of heterotopic bone formation; and
- **Conductive:** material serves as a scaffold for bone deposition, but only in an osteogenic environment.

Non-viable materials used in medical devices are called biomaterials. These biomaterials are intended to interact with biological systems, such as the human body [61]. Biomaterials, synthetic or natural, can be used in human health applications, performing functions or replacing body parts or tissues. Additionally, these materials are used to augment, repair or replace tissue, organ, or function of the human body lost through trauma, disease, or injury [66]. Biomaterials, particularly materials for permanent implants, are developed to have superior corrosion and wear resistance in corrosive body environments, excellent biocompatibility, and decent material properties in load-sustaining and fatigue [67, 68]. Wear that results in wear debris can lead to inflammatory responses in the body, leading to osteolysis (active resorption of bone matrix by osteoclasts) [69, 70]. This leads to implant loosening due to the body´s attempt to process the wear debris [71, 72].

2.1.2.1 Classification of Biomaterials

Biomaterials are an indispensable element in improving human health and quality of life. The most commonly used biomaterials for implants can be classified as polymers, ceramics, and metals [73]. All three types must meet various demands. According to Hasirci and Hasirci, the most important ones are that they should [74]:

- be biocompatible (non-toxic, non-carcinogenic, non-allergenic, etc.);
- have physical properties (density, form, topography, etc.) similar to those of the tissue;
- have sufficient mechanical properties (compression, tensile, fatigue, wear, etc.);
- have appropriate service lives (corrosion resistance, degradation behavior, etc.);
- have chemical properties comparable to that of the tissues (hydrophilic or -phobic, functional groups, etc.);
- be processable and sterilizable;
- have appropriate bioactivity (inert, bioactive agents, etc.); and
- be economical and available.

The used materials are chosen based on their mechanical properties depending on the operational site. Metallic materials are suitable for load-bearing applications (every type of load), while ceramics are used when compressive stresses appear.
Polymeric biomaterials are macromolecules and represent a versatile and essential class of biomaterials and are widely used due to their low toxicity, biocompatible nature, sterilizability, ease of fabrication, durability, flexibility, and wide range of mechanical, chemical, electrical, and thermal behavior [75, 76]. The use of polymeric biomaterials depends primarily on the requirements, function, and environment of the intended application. Polymers are used, for example, in dental applications (e.g., implants, fillers), therapeutic treatments (e.g., cardiovascular and general surgery, drugs and drugs delivery, implants), contact lenses, diagnostics (e.g., gene arrays, biosensors), medical supplies (e.g., packaging, blood bags, surgical tools), and emerging regenerative medicine (e.g., tissue-engineering of skin and cartilage) [73].
Ceramic biomaterials, also called bioceramics, can be synthetic or natural in origin [77]. Ceramics are inorganic solid materials consisting of metals and metalloids, mainly connected by ionic bonds, e.g., oxides, nitrides, sulfides, and carbides, and can be crystalline or amorphous. They are characterized by excellent biocompatibility, superior corrosion

and wear resistance, high strength, hardness, and stiffness [75]. Bioceramics can be divided into bioinert (e.g., alumina (Al_2O_3) and zirconia (Zr_2O_3)) and bioactive biomaterials (e.g., calcium phosphates and glasses), whereas the latter can be resorbable or non-resorbable. Most clinical applications are related to repairing the skeletal system, including bones, joints, and teeth, and augmenting hard and soft tissue [78].
Metallic biomaterials are the most used biomedical materials essential in the medical field. Most metallic biomaterials are crystalline, having a regular atomic arrangement. Metals usually have high strength, fracture toughness, and better elasticity and stiffness than ceramics and polymers. Their mechanical performance is specified due to dislocations and crystallization. Metallic biomaterials are widely used for load-bearing implant applications such as orthopedic, dental, and maxillofacial surgery. Additionally, metals are also used for stents in cardiovascular surgery. The most common biomedical metals and alloys are stainless steels, titanium, titanium-based, cobalt-based, magnesium-based, and tantalum-based alloys. [75]

2.1.2.2 Biomedical Titanium Alloys

Titanium raised attention not only in aerospace and automotive but also in the biomedical industry, mainly due to its good biocompatibility, corrosion resistance, and decent mechanical properties [79–81]. In recent decades, titanium and its alloys have been used as biomaterials, for example, in dentistry as machined dental implants, crowns, and bridges [82], wrought forms [83, 84], and as casted titanium [85, 86].
CP-Ti is widely used in the chemical industry and process engineering, mainly due to its good corrosion resistance [87]. Mainly oxygen and nitrogen, as interstitial alloying elements, have a significantly embrittling effect and decrease the ductility. These impurities or intentional addition of these elements affect the mechanical properties. These are adjustable in a specific range, such as tensile strength ranging from 240 MPa - 550 MPa, yield strength from 170 MPa - 480 MPa, and breaking elongation from 15 % - 24 % [27, 87]. Especially in a biological environment, CP-Ti has better corrosion resistance and better biocompatibility than, for example, stainless steel [88–91]. Nevertheless, due to the relatively low tensile strength (<550 MPa) combined with poor wear resistance, the use of CP-Ti is limited for load-bearing implants (e.g., THR, TKR) and comprises mainly maxillofacial and dental applications [33, 67].
The **($\alpha + \beta$) alloys** are the most widely used titanium alloys not only in the medical industry. By adjusting, adapting, and varying the dual-phase microstructure, (α+β) alloys, such as Ti-6Al-4V, Ti-5Al-2.5Fe, and Ti-6Al-7Nb, offer the possibility of achieving balanced properties and are thus used frequently. Initially, Ti-6Al-4V was developed and designed for aerospace applications [92]. It is the most commonly used and investigated titanium alloy, mainly due to its well-balanced and diverse properties and, therefore, applicable in various fields. Biomedical investigations have shown that vanadium has hazardous potential and may lead to diseases due to its cytotoxicity [93]. Within further development, the critical element vanadium was substituted with non-toxic iron and niobium, leading to the design of Ti-6Al-7Nb and Ti-5Al-2.5Fe. In particular, Ti-6Al-7Nb is used for biomedical applications. This alloy was developed by SULZER Medical Technology in 1978 and has been used for clinical applications since 1985 [94, 95]. Generally, (α+β) alloys have excellent biocompatibility and corrosion resistance compared to other biomaterials used for load-bearing implants. Nevertheless, they often contain aluminum

as an α-stabilizer. Aluminum is referred to be cytotoxic and may lead to osteomalacia, neuropathy, and Alzheimer's disease [96]. Another weak point of these alloys concerning the medical application is that the elastic modulus differs from the modulus of the human bones [97]. The mismatch in elastic modulus may lead to stress shielding, resulting in implant failure [98, 99].
The third group of titanium alloys highlighted refers to the **β alloys**, e.g., the metastable β-alloy Ti-24Nb-4Zr-8Sn. To meet the mismatch of elastic modulus, which is related to stress shielding, and due to the cytotoxic contexts of the alloying elements, new biomedical β titanium alloys were developed. The goal is to meet the requirements of implant biomaterials, such as non-cytotoxicity, good mechanical properties (e.g., elastic modulus and strength), an improved interface between implant and bone. Accordingly, different β titanium alloys with low elastic modulus and sufficient strength properties were developed, e.g., Ti-12Mo-6Zr-2Fe [100], Ti-15Zr-4Nb-2Ta-0.2Pd [101], Ti-6.8Mo-4.5Fe-1.5Al (Timetal LCB) [46], Ti-24Nb-4Zr-8Sn [102]. Within these developments, Ti-24Nb-4Zr-8Sn achieved the lowest elastic modulus. The phase composition of mainly bcc β phase results in low elastic modulus (42 GPa - 50 GPa) and high strength (up to 850 MPa), whereas the chemical composition results in good biocompatibility. Ti-24Nb-4Zr-8Sn has superb mechanical properties, such as high strength, damping, and super-elasticity, and shows a stress-induced martensitic transformation [102].

2.1.3 Mechanical Performance of Biocompatible Titanium Alloys

As previously described, the mechanical properties of titanium alloys are dictated by the unique properties of the α and β phases, depending on the alloying elements, their volume fraction, and spatial arrangement. The general density of titanium is reduced by light alloying elements, such as α-stabilizing aluminum, and increased by heavier β-stabilizing elements. The spatial arrangement of the phases and microstructural formation predestine the mechanical properties [35]. A fine microstructure increases strength and ductility, delays fatigue crack nucleation, and is a prerequisite for superplastic deformation. In contrast, a coarse microstructure is more resistant to creep and fatigue cracking. Equiaxial microstructures often exhibit high ductility and fatigue strength and are ideal for superplastic deformation. By contrast, lamellar microstructures have high fracture toughness and better resistance to creep and fatigue crack growth. Bimodal microstructures combine the advantages of lamellar and equiaxed structures, resulting in a balanced property profile. [26, 35]
The properties of titanium and its alloys can be improved by alloying, processing, and composites. Alloying enables to increase the strength (e.g., precipitation hardening, solid-solution strengthening, age hardening), generates ordered structures (e.g., intermetallic compounds), determines the physical properties (e.g., elastic modulus, density), and affects the chemical behavior (e.g., corrosion). The properties can be adjusted by different microstructures generated by various thermo-mechanical treatments (e.g., rapid solidification, mechanical alloying, hot-isostatic pressing). [35]
Prosthesis and biomaterials are subjected to different *in vivo* loads and stresses, which are individual, like the patient. The load sets vary according to the patient's anatomy, diseases, prosthesis design, bone quality, and implantation techniques [103–105]. Therefore, implant failures still occur due to overloading and cracking, static and dynamic. The acting forces can be several times higher, depending on the movement, movement

speed, and the patient's body weight [106]. Static material requirements, particularly for Ti-6Al-7Nb, are concluded within the ASTM F1295-16 and ISO 5832-11 standards. The ISO 7206 standard defines the laboratory tests and test setup to determine the endurance properties of hip implants [107–109].
The mechanical loading on biomaterials can vary in a specific range. It is estimated that the hip implants used in an average nonactive patient can experience 1×10^6 to 2.5×10^6 cycles of stress in a year [110]. For a mid-twenty-year-old patient with a life expectancy of 70 to 80 years, this equals approximately 10^8 cycles of loading in a lifetime. It is obvious that the loads and cycles are a function of the weight and activity level of the patient and that the need for longtime cyclic capability in fatigue is crucial [23]. Baleani et al. summarize the load history for implanted hip prostheses within one year for active patients. The annual activity occurrence is separated into specific activities, such as walking, jogging, ascending and descending stairs, and stumbling. In addition, the cycles per year [111, 112] and the maximum hip joint load corresponding to each activity are given [113–115]. Depending on the movement, the maximum load in the hip can reach 720 % of the patient's body weight during stumbling. [116]
As described above, the materials used for implants are subjected to cyclic mechanical loading. Therefore, the fatigue properties and the underlying mechanisms are essential and explained in the following. The purpose is to briefly review the critical aspects of the fatigue behavior of titanium alloys. Fatigue failure may be divided into three phases: crack initiation, (micro) crack propagation, and (macro) crack growth. Typically, the resistance of titanium against crack propagation and growth is relatively low, which is why the crack initiation phase determines the lifetime of these alloys. In general, the fatigue properties in terms of fatigue strength of β titanium alloys tend to be slightly better than for α- or (α+β)-alloys. Due to the hcp crystal structure and, in particular, the asymmetry between longitudinal and basal planes, the properties are anisotropic. Here, the β alloys with their bcc crystal structure are advantaged, but the α precipitates must be considered. The fatigue behavior of titanium alloys is affected by various aspects; nevertheless, adaptions affecting/reducing the crack initiation tendency often have contrary effects on crack propagation and growth. Therefore, it is not trivial to optimize all three phases at once. The possible effects of adjusting the fatigue properties are [46]:

- **Effect of the tensile strength:** As generally known, the fatigue strength increases with increasing yield/ultimate tensile strength (YS/UTS), as shown for CP-Ti and near-α alloys with the addition of oxygen [117]. Compared to α alloys, β titanium alloys have favorable properties due to the higher tensile strengths achieved by precipitation hardening. Nevertheless, the increase in fatigue strength is limited due to the ratio of hardened β matrix to soft primary α phase and precipitation-free zones near the grain boundaries of the β grains [118]. Okazaki and Gotoh compared the ratio of UTS to the fatigue strength for various titanium alloys and showed a tendency for increasing fatigue strength with increasing UTS, but additionally depending on the microstructure and previous processing methods [119].

- **Effect of the grain size:** The influence of grain size on fatigue properties is contradictory concerning crack initiation and propagation. For CP-Ti, micro crack propagation along the planar slip bands is inhibited by the coarse grains, while coarse grains also reduce the macro crack growth resistance and the lifetime [117].

Everaerts et al. show that increasing α grain size generally decreases fatigue life in Ti-6Al-4V wires, as the grain size controls the slip-based or cleavage-based fracture mechanisms [120]. As described by Wu et al., the fatigue strength of Ti-6Al-4V declines with increasing α grain size in equiaxed or α lamellar microstructures [121]. Wagner et al. summarize different grain sizes and their effect on fatigue properties [122].

- **Effect of the microstructure:** In general, the fatigue strength decreases in the order of bimodal, lamellar, and equiaxed microstructure [121]. Dependent on the processing route or the heat treatment (α+β) alloys are adjustable in terms of equiaxed or lamellar microstructure. Bimodal (α+β) microstructures show good fatigue properties due to the crack inhibiting β lamellae [123]. Elongated primary α precipitates act as crack growth paths, increasing the crack growth rate [124]. Crack initiation often starts at intersecting planar slip bands or slip bands intersecting with grain boundaries [125, 126]. Within β alloys, crack growth occurs at secondary α_S-β-interfaces [124]. Changing the α_S precipitates is limited, so alternatively controlled precipitation of the ω phase increases crack resistance. However, the ω phase is considered to embrittle the β matrix [127, 128]. For single β phase alloys, crack initiation is preferred at large-angle grain boundaries or grain boundaries triple points [129, 130].
- **Effect of the texture:** The β alloys are generally isotropic due to their bcc crystal structure. Nevertheless, α and (α+β) alloys can be anisotropic due to the anisotropic hcp crystal structure [122]. The texture of α, whether the processing or mechanical deformation determines it, significantly affects the fatigue behavior. The basal plane acts as the preferred crack initiation plane. Depending on the orientation of the loading direction, the texture affects the fatigue behavior. The texture sensitivity increases with an increasing amount of primary α and grain size. [131–133]
- **Effect of the loading situation:** Titanium alloys, especially near-α and (α+β), obtain a high sensitivity on the mean stress during fatigue tests, also known as the anomalous mean stress effect, which is dependent on the crystallographic texture and loading direction and is controlled by crack initiation [122]. This sensitivity can be affected by the ω particles mentioned above, as cutting the particles leads to increased crack closure [134].
- **Effect of the surface:** Although the compression and introduction of near-surface residual stresses are limited, surface treatments can improve fatigue behavior. Generally, the surface roughness, the residual stresses, and the degree of cold work or dislocation density are modified by surface treatments [122]. The surface roughness determines the control mechanisms of fatigue strength, crack initiation controlled (smooth surfaces), or crack propagation controlled (rough surfaces) [135]. A hardened surface layer on smooth surfaces may lead to retardation of crack initiation due to increased strength. In contrast, no crack initiation phase is present for rough surfaces due to the low residual ductility caused by the hardened surface layer [136]. The potential of enhancing the fatigue behavior of (α+β) alloys is better compared to β alloys due to the higher potential for strength increase of the surface [137, 138]. Residual stresses (compressive) in the surface are favorable due to significantly retarding micro crack propagation when cracks are present in the specimen [122]. In

addition, mechanical surface treatments are not necessarily stable, and their improving effect can be removed, for example, by heat treatments. Nevertheless, surface treatments can be used to tailor the fatigue properties of titanium components [122].

2.2 Processing of Titanium Alloys via Laser Powder Bed Fusion

Additive Manufacturing (AM) is an emerging manufacturing technology. Material and energy are delivered to one point to produce a solid, where the three-dimensional part is then built layer-wise [79]. Whereas the initial usage of AM methods was generating prototypes, the technology developments have improved the quality of the produced parts and components to enable the use of the produced parts [139]. AM has a several advantages: producing components almost without geometrical restrictions, avoiding the need for tools and manufacturing them, and sustainable fabrication with a minimum of wasted material. Concerning the lightweight design and the increasing demand for individualized products, AM technologies have gained importance. AM can be divided into three groups based on the raw material used:

- solid-based systems (e.g., fused deposition modeling (FDM)),
- liquid-based systems (e.g., stereolithography (SLA)), and
- powder-based systems (e.g., selective laser sintering (SLS), laser powder bed fusion (LPBF)).

Within AM, the LPBF process enables the flexible processing of various metallic powder materials. It has established itself as one of the most important technologies in the field. The processing of metallic materials enables applications for load-bearing components and structural parts [140, 141]. Due to the high degree of design freedom, LPBF can produce complex lightweight structures optimized for external conditions, such as external stresses and thermal conditions. Typical application areas include lightweight structures and components for the aerospace and biomedical sectors, such as dental crowns made of cobalt-chromium alloys or patient-specific implants made of titanium alloys [142–144]. In medical technology, particularly LPBF offers a cost-effective adaptation of both the external shape and the stiffness of implants to the conditions required in individual cases and patients, resulting in economic and medical benefits [145–148].
A commercially available LPBF system (type LT12 SLM, DMG Mori Ag, Germany) is depicted as an example in Figure 2.2a. The left part of the machine contains the control electronics, the computer, the laser and the optical bench. The right side includes the powder module (so-called rePLUG) with a powder supply and process gas filtration system. The center contains the actual process chamber. Figure 2.2b shows the essential components of the latter and the LPBF process schematically. The powder supply stocks the powder required for the building process. A powder feeder conveys additional powder from the powder module into the powder supply unit during the process. The recoater provides and uniformly distributes a defined amount of powder, depending on the layer thickness, on the build platform. The powder overflow absorbs the excess powder of each coating sequence, and previously formed welding spatter and process residues. The laser beam provides the energy required for melting the powder material. The elevator with the building platform fixes the molten and resolidified powder areas in the XY-plane

(horizontal) and incrementally lowers the powder bed in the z-direction (vertical). In addition, if necessary, the build platform is heated to improve bonding and reduce any residual stresses that may occur. Two shield gas flows, one for the optical unit and one for the volume, provide an almost inert atmosphere to avoid chemical reactions with oxygen and nitrogen from the ambient air.

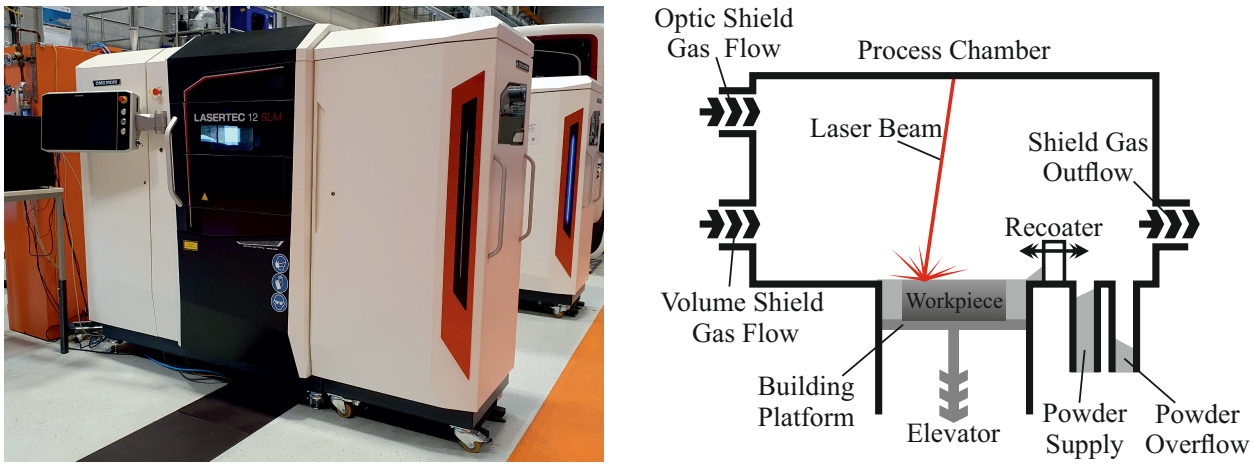

(a) **(b)**

Figure 2.2: (a) DMG Mori LT12 SLM and (b) schematic illustration of the main components of an LPBF process chamber, according to [149].

The initial basis for processing with LPBF is a 3D CAD data set of the component to be manufactured. This is converted into the standard triangle language (STL) format. The component is then sliced into horizontal layers, with the layer thickness set corresponding to that in the subsequent process. The layer-related geometry information, possibly with support structure information, is transferred to the LPBF machine. Here, the process parameters used for melting are set and adjusted. The actual manufacturing process consists of three iterative process steps. First, a powder layer is distributed on the build platform using the recoater. Due to the limited packing density of the powder material, the powder layer thickness is far greater than the later, almost fully dense manufacturing layer thickness. Second, after powder application, local melting of the powder takes place according to the geometry information and set process parameters. In the third step, after the solidification of the material, the build platform is lowered by the predefined layer thickness, and a new powder layer is applied. These steps are repeated until the last layer has been applied and exposed. After a cooling phase, the loose, unmolten powder is removed, the build platform is taken from the process chamber, and the finished part is separated from the platform. The excess powder is sieved to remove the weld spatter and process residues, dried, and can then be returned to the powder supply unit.
The following essential LPBF process parameters decisive for the part quality:

- laser power P_L,
- scanning speed v_s,
- hatch distance h_s,
- layer thickness h_z,
- building platform temperature T_B, and
- scan strategy.

The first four can be used to calculate the energy density E_V according to the following equation:

$$E_V = \frac{P_L}{v_s \cdot h_s \cdot h_z}.$$

The temperature of the build platform represents an important parameter and reaches approximately 300 °C in standard LPBF machines. The main reason for its use is a reduction in process-induced residual stresses. Nevertheless, the adjustable temperature is relatively low compared to the melt pool temperature (2000 °C to 3000 °C), which means that the residual stress problem remains decisive for the resulting component quality and properties [150–152].
The scan strategy refers to the direction and sequence of individual scan vectors during exposure. Depending on the component and geometry, it is common to use different strategies, for example, uni- and bidirectional exposures, strip, checkerboard, or meander-like scan patterns. This leads to reduced residual stresses or macroscopic distortion, and detachment of the component from the platform can be avoided. In addition to strategies within a layer, cross-layer strategies such as rotation of scan vectors are typical. Furthermore, using different exposure parameters for the volume/hatch and the contour is common. Typically, the scan speed of the contour parameters is slower in order to set a smoother, stable melt pool. [86, 153, 154]

2.2.1 Microstructural Evolution during LPBF

The processing of powder materials by LPBF involves cyclic melting, solidification, and remelting of the exposed material. Therefore, considering the processes occurring during the solidification of metals is of particular importance to obtain a fundamental understanding of the microstructure resulting from the LPBF process. Therefore, the relevant phenomena during solidification are summarized below.

2.2.1.1 Solidification Behavior and Texture Formation

The microstructure of metallic materials formed during solidification from the melt is largely determined by the chemical composition and the cooling conditions during the transition from the molten to the solid phase. The LPBF process produces a three-dimensional part. Therefore, the thermo-kinetics vary in different directions within one layer and across the layers of the component. Each region in the complex LPBF process experiences a distinct and unique thermal history. This history includes multiple melting, solidifying, annealing, and tempering heat treatments, resulting in a unique microstructure all over the part. During solidification in the LPBF process, dendritic crystal growth is often observed due to constitutional supercooling [141, 155, 156]. Due to the small beam diameter (35 µm - 600 µm), the laser interacts with a tiny region of the powder bed, and, therefore, the melt pool size is extremely small with diameters of 0.1 mm - 0.2 mm [157, 158]. The small spot, in turn, leads to very high power density ($>10^4$ W s^{-2}), where the introduced energy and heat rapidly dissipate into the surrounding substrate, resulting in very high cooling rates of up to 10^4 K s^{-1} - 10^7 K s^{-1} [159, 160]. Therefore, relatively small average grain sizes are present after additive manufac-

turing [155, 161].
Since the powder surrounding the melt pool acts mainly as a thermal insulator [162], the heat in LPBF dissipates primarily into the underlying substrate, i.e., the build platform or the previous molten and solidified material layers. Directional solidification occurs comparable to welding or casting [141, 163]. In combination with epitaxial growth, the formation of pronounced texture is observed during the layer-by-layer buildup. While the laser beam interacts with the material, a melt pool forms. After the energy source leaves the area, the epitaxial growth of the partially molten grains from the substrate or previous layer starts during solidification. The temperature gradient G, solidification rate R, undercooling ΔT, and solute diffusion coefficient D_L determine the geometry of the liquid-solid interface in terms of planar, cellular, columnar dendritic, and equiaxed dendritic fronts. At the bottom of the melt pool, where the solidification rate is $R \approx 0$, the ratio of G/R is infinite, resulting in a planar grain structure. Cellular solidification occurs near the planar region when the ratio G/R decreases until $G/R < \Delta T/D_L$. Further decrease of the ratio G/R leads to columnar dendritic formation. Equiaxial solidification typically occurs near the surface of the melt pool, where the temperature gradient is comparatively low. In addition to the grain morphology, grain growth directions align with the temperature gradient direction as solidification progresses. Grain growth is favored along specific crystallographic orientations. Thus, grains with the same or similar orientation to the temperature gradient grow faster. In contrast, grains with other orientations gradually stop growing due to the competitive growth of the different grains. This competitive growth leads to unidirectional columnar grains or microstructure, typically observed in LPBF-manufactured components. [164, 165]

2.2.1.2 Process-related Effects and Grain Growth Characteristics

The process parameters, such as laser power, scanning speed, hatch distance, and layer thickness, significantly affect the temperature gradient, cooling conditions, and heat flow direction, affecting the grain morphology, size, and orientation. Different studies showed that grain size increases with increasing laser power (higher energy-induced grain coarsening) and decreases with increasing laser scanning speed (shorter exposure and faster solidification) [166, 167]. Additionally, the cell spacing (distance between adjacent grains) decreases with increasing scanning speed, while the misorientation angle gets uniform [168, 169]. With decreasing hatch distance, new melt tracks remelt the center of previous melt tracks (typically small equiaxed grains due to constitutional undercooling), leading to epitaxial grain growth [170]. Furthermore, the scanning strategies can significantly influence grain growth and heat flow direction [150, 155, 171].
Besides process-related methods affecting grain growth, different methods can be applied to manipulate or adjust the microstructural evolution. The addition of additives into the powder bed or the powder itself, such as second-phase nanoparticles, can lead to nucleation sites in front of the liquid-solid interface and reduce the critical undercooling needed for producing ideal equiaxed structures [164, 172, 173]. Various methods to adjust the grain structure of LPBF-fabricated parts are currently being investigated, such as electromagnetic or ultrasonic vibration [174, 175].

2.2.1.3 Microstructural Evolution during Additive Manufacturing of Titanium Alloys

Within the LPBF of titanium alloys, phase transformation and evolution play a significant role in the performance of additively manufactured components. The rapid heating and cooling cycles during manufacturing are responsible for the microstructure and properties.
The LPBF of titanium and its alloys results in different phases, including α, β, α', α'', and ω [176]. Powders, such as commercial Ti-6Al-4V powder, consist of α and β phases, transforming to α' martensite during manufacturing [177]. As described, the process parameters and the chemical composition can determine the formation of the various phases in titanium alloys [178–180]. Simultaneous to phase formation, precipitation can occur during LPBF, affecting the mechanical performance of the titanium alloys. Again, these precipitations can be controlled, more or less, by the process parameters and especially the chemical composition of the alloys. Depending on the initial titanium alloy, various precipitates and amounts of precipitations can form depending on the process parameters, see Figure 2.3. [181–184]
Furthermore, in-situ heat treatments can adjust the microstructural evolution and grain growth. Therefore, different strategies are used to manipulate the constituent phases, tailoring the mechanical properties, for example, by in-situ decomposing α' to α and β phase. [179, 185, 186]

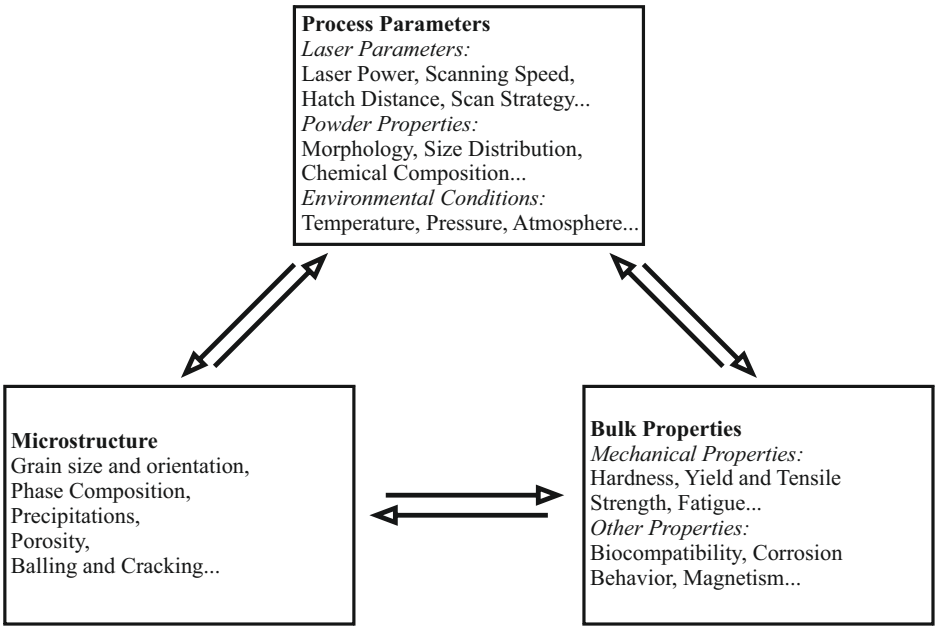

Figure 2.3: Correlation among the LPBF process parameters, microstructure, and as-built part properties, according to [164].

2.2.2 Mechanical Properties of Additively Manufactured Titanium Alloys

As the demand for LPBF processed materials increases, it is essential to understand the process-microstructure relationship to improve process control and the performance

of LPBF fabricated parts. The relationship between various process parameters, microstructural aspects, and the resulting bulk properties is shown in Figure 2.3 [164]. The mechanical properties of the materials depend mainly on their microstructure, which is strongly influenced by the AM processing conditions, characterized by repeated heating and cooling cycles, due to the layer-by-layer manufacturing [140, 187]. After scanning by laser, the molten pool solidifies rapidly, producing a fine-grained microstructure; during exposure of subsequent layers, the solidified volume is repeatedly exposed to heat. This complex thermal history can lead to metastable microstructures and compositional phases that can vary in the component volume [140]. The resulting microstructures depend on the chemical composition and the class of titanium alloys. Therefore, the following explanation is divided into the main titanium alloys; α, (α+β), and β.

The **α titanium alloys**, like CP-Ti, undergo an allotropic phase transformation from high-temperature hcp β to low-temperature bcc α at around 890 °C. This transformation affects texture, microstructure, slip and twin systems, and, therefore, the mechanical properties [188, 189]. Depending on the process parameters, the microstructure of as-built CP-Ti consists of coarse plate-like hcp α grains. With increasing laser power and scanning speed CP-Ti consists of fine, acicular α' martensite due to very high cooling/heating rates [190]. As the microstructure changes, the mechanical properties change as well. With increasing scanning speed and laser power, the hardness and tensile strength increase due to residual stress increase, change of α phase to α' martensite, grain morphology, and grain refinement [190–192]. Due to their hcp structure, α and α' are anisotropic. While CP-Ti has four independent slip systems (compared to five in general polycrystalline materials), twin systems are required to maintain the compatibility of deformation [193, 194]. Therefore, the interaction and competition between dislocation slip and deformation twinning influence the mechanical properties, while grain refinement affects this competition. The grain refinement leads to the reduced twinning propensity in coarse-grained hcp materials, and dislocations can be activated, improving the ductility of hcp titanium alloys [195]. A further reason for increasing the strength is the formation of a martensitic structure. The α' martensite consists of more closely spaced interfaces, separating adjacent plates and laths, and a higher dislocation density compared to α structure. Hence, the martensitic structure with twinned plates leads to a more effective barrier against dislocation movement during deformation, resulting in the strengthening of titanium [196].

For **($\alpha + \beta$) titanium alloys** elongated columnar, prior β grains form during solidification along the building direction of the parts [197–200]. Due to the high cooling rates and rapid solidification process, the higher thermal gradient results in a higher undercooling. Subsequently, the β grains transform mainly to the ultrafine, acicular martensitic α' phase. [140, 201, 202]. As described for α alloys, the microstructure of (α+β) titanium is sensitive to the processing parameters, where the microstructure varies with increasing scanning speed from equiaxed to mixed equiaxed-columnar grains and columnar grains. The acicular structure was refined and transformed from an (α+β) to α' phase [203]. The described aspects result in a finer microstructure, which leads to higher static strength according to the Hall-Petch relation [140, 190]. Increasing the laser power increases the hardness while increasing the scanning speed reduces the hardness. Increasing scanning speed increases elongation at break while increasing the laser power decreases the elongation. These aspects are attributed to the combined effect of grain refinement of α' and the formation of nano-β particles [203]. In addition, the marten-

sitic α' phase exhibits higher yield, tensile strength, and lower breaking elongation [140, 204–206].

Metastable β and β titanium alloys are promising materials for biomedical applications due to their very low Young's modulus, superb biocompatibility, and high strength [207]. The sensitivity of the mechanical properties concerning the process parameters is also given for these alloys. The hardness of alloys, such as Ti-24Nb-4Zr-8Sn, decreases with increasing speed [208]. Typically, mainly β phase in the form of elongated grains, oriented along the building direction, is present. However, small amounts of phases such as α or α'' are possible, depending on the manufacturing conditions [209, 210]. Equiaxed β grains without any α are possible as well [211]. The α phase precipitates act as a dislocation barrier and may improve yield strength by blocking dislocations [212–214]. Whereas the ω phase, formed by in-situ heat treatment during the process, reduces the elastic modulus and embrittlement [215], precipitation of the α'' in the β matrix lowers the elastic modulus and yield strength [212]. Additionally, the process conditions and alloying elements significantly affect the phase transformation in β alloys [216, 217].

Generally, the additively manufactured as-built specimens tend to have higher hardness and strength values but lower breaking elongations than conventionally manufactured titanium alloys. As described, the rapid cooling and solidification lead to metastable microstructures and phases. Thermal post-treatments can easily modify these to obtain better mechanical properties. Indeed, the choice of post-treatment variant can significantly influence the properties, such as grain size and orientation, precipitation, phase evolution densification phenomena, and stress relief. Table 2.1 summarizes different titanium alloys' mechanical properties compared to LPBF and conventional fabricated processing methods.

Table 2.1: Comparison of mechanical properties (hardness and tensile properties) of different titanium alloys processed by laser powder bed fusion (LPBF) and conventional methods; Vickers hardness, elastic modulus E, yield strength YS, ultimate tensile strength UTS, and breaking elongation ϵ.

Alloy	Processing method	Hardness in HV	E in GPa	YS in MPa	UTS in MPa	ϵ in %	Ref.
CP-Ti	LPBF	261±13	106±3	555	757	19.5	[190]
	LPBF	–	–	500	650	17	[218]
	Sheet forming	–	–	170–655	240–550	15–24	[219]
	Full annealed	–	–	432	561	14.7	[220]
	Casting	169–171	108±4	523±11	673±11	24±1	[221, 222]
Ti-6Al-4V	LPBF	409	102–109	962–1137	1166–1267	1.7–7.6	[201, 206]
	Sheet forming (ELI)	–	–	830 (934)	897 (863)	8 (6)	[219]
	Casting	346	110	847–999	876–1173	5–14	[67, 97, 206, 222]
	Wrought	315	–	832–930	933–995	12.5–14	[206, 223]
	Forging	–	–	836	908	14.5	[224]
Ti-6Al-7Nb	LPBF	337±23	105–116	868–940	967–1109	9.9–14.4	[225, 226]
	LPBF	348–376	108–109	1081–1147	1227–1308	5±2	[227]
	–	–	114	880–950	900–1050	8.1–15	[97]
	Wrought	–	–	800–1000	900–1100	10–15	[228]
	Casting	257±29	–	817	933	7.1	[97, 221]
	ISO 5832-11	–	–	800	900	10	[108]
Ti-24Nb-4Zr-8Sn	LPBF	219±8	49±1	490±16	700±6	22±1	[229]
	LPBF	220–230	53±1	563±38	665±18	13.8±4.1	[208]
	Hot rolling	–	46	700	830	15.0	[230]
	Hot forging	230–370	55	570	750	13.0	[231]
	Warm rolling	265	56	–	1150	8	[232]

2.3 Fundamentals of Physical Vapour Deposition

Thin films are present in our daily life. Almost every device or part includes coated parts, such as electronics, cars, watches, tools, and glasses [233–235]. The deposition of thin films is usually a vapor-based process. According to DIN 8580, physical vapor deposition (PVD) is one of the coating manufacturing processes with an initial gaseous state of the coating materials [236]. PVD is a manufacturing process for metallic and ceramic coatings. Under physical impact in a vacuum, the material is transferred from a source, also called the target or cathode, to the vapor phase. The material is evaporated by various mechanisms (heating, high-energy ionized gas bombardment (sputtering), or electron gun) in a vacuum or low-pressure gaseous or plasma environment [23].

2.3.1 Basics of Magnetron Sputtering and Deposition

The cathode sputtering process begins at low pressures with the ignition of the plasma in a process gas atmosphere (e.g., argon, krypton, and nitrogen). During this process, electrons move from the cathode in the direction of the anode/substrate, whereby the process gases are positively charged by impact ionization and an electron release. The positively charged ions, e.g., argon ions, are then accelerated to the negatively charged cathode. As a result of the collision with the target atoms, these are atomized (detached) and can move freely in the plasma as neutral target atoms. If these hit the surface of the substrate, they can be adsorbed and finally form a layer through further accumulation after nucleation and island growth. [23, 237–240]
A further development of cathode sputtering is magnetron sputtering, in which magnets are mounted behind the target material. These form a magnetic field that is superimposed with the existing electric field and preferentially “traps“ electrons near the target. The higher density of electrons leads to more frequent collisions with atoms of the process gas, which enhances the ionization process and creates a denser plasma near the target [241, 242]. Consequently, the electric current is one to two orders of magnitude higher, and the electric voltage is correspondingly lower [237–240, 242]. The higher ionization increases sputtering efficiency and rate and allows significantly lower process pressures [237–240, 243, 244]. A low process pressure reduces the particles' scattering on their way to the substrate, resulting in a higher kinetic energy transfer of the particles upon impact on the growing layer, leading to denser layers with lower porosity [240, 245]. The BIAS voltage can also influence denser layers. During coating, it is usually between -60 V and -120 V and causes target ions and process gas ions to accelerate onto the substrate surface. Upon collision with the coating, the kinetic energy can be transferred to coating atoms, causing the more mobile coating atoms to reduce porous structures and heal lattice defects [237, 240].
The film growth process typically includes several steps: nucleation, island growth, impingement and coalescence of islands, formation of polycrystalline islands and channels, development of a continuous structure, and film growth. The coating processes of ceramic materials usually exhibit a columnar microstructure containing elongated grains [23].
Elements, molecules, and compound materials can be used to deposit films. Compounds are deposited by the reaction of depositing material with the ambient gas atmosphere (e.g., titanium nitride (TiN)) or with co-depositing material (e.g., titanium car-

bide (TiC)) [246–248]. Different materials are used as PVD films depending on the applications, the desired properties, and behavior. TiN, titanium aluminum nitride (TiAlN), chromium aluminum nitride (CrAlN), and diamond-like carbon (DLC) are commercially used and technically matured PVD films. These coatings are applied to increase wear and corrosion resistance, as a diffusion barrier, as a solar energy absorber or IR reflector, etc. [23]. Additionally, PVD films are applied to improve the biocompatibility of materials for medical applications, such as TiN, TiCN, and DLC films.

2.3.2 Effects of PVD Coatings on the Material Behavior

Usually, surface modifications, such as PVD, improve the surface properties of wear, corrosion, and oxidation for different substrate and coating materials [249–251]. PVD thin films are applied to increase tool properties, e.g. hardness and toughness [252–254]. Furthermore, research showed that PVD films improve tribological properties and biocompatibility [255–257]. In addition, PVD coatings can increase tensile strength and improve fatigue properties. The hard thin surface layer restricts the plastic deformation of the substrate with superior mechanical strength, high residual stresses, and good adhesion between thin film and substrate. Characteristics, such as tensile strength and fatigue resistance, are changed depending on the physical and mechanical properties of the substrate and coating material, thickness, hardness, chemical composition, the applied stresses, and strains, etc. [258–262]
The residual stresses of PVD coatings are mechanical stresses that occur inside a material without needing external forces. They are particularly interested in coatings since they correlate with the maximum successful coating thickness without flaking. Additionally, they significantly influence the material's mechanical properties [237, 238]. For PVD coatings, lattice distortions result in residual stresses. They can be caused by layer growth, mismatch of thermal expansion to the substrate, and lattice defects such as dislocations, point defects, and grain boundaries [263, 264].
The use of magnetron sputtering reaches across several industries depending on the function of the coating. Hard, wear-resistant, low friction, oxidation, and corrosion-resistant coatings are used, for example, in aerospace, energy, automotive, and tooling industries [265]. Furthermore, magnetron sputtering is applied to produce coatings with specific optical and electrical properties for the semiconductor industry, optical coatings in the glass industry, and decorative coatings in the jewelry industry [266].
PVD coatings are often used for dry machining to achieve low wear, low friction, and anti-sticking between the contact surfaces of tools and workpieces. Additionally, PVD films are applied in the bipolar plates of proton-exchange membrane fuel cells, mainly carbon and nitride-based films, due to their high electrical conductivity, as well as mechanical and chemical stability. [23]
In the past, materials for biomedical applications were selected based on their material or bulk properties. Today, however, it is evident that the surface properties of a medical device are crucial for its biomedical application. Therefore, various surface modifications are suitable for improving biocompatibility and antibacterial activity. [267, 268]
Among others, TiN, TiCN, and DLC coatings are the most widely used [269–273]. Therefore, these three coatings are reported in detail, in particular regarding their biocompatible features:

- **TiN** is a hard ceramic film with various mechanical properties regarding its stoichiometry, as the microstructure is highly important for the properties. The hardness is typically high, between 2000 HV to 2500 HV, whereas defects in the films, such as voids, may lower the hardness [23]. TiN shows biocompatible features in biomedical environments, such as non-cytotoxicity, dermal irritations, or toxic responses [274–276]. TiN films have already been used for prostheses (orthopedic and dental), and cardiac devices, concluding that it is tolerated by the human body [277, 278]. Nevertheless, the corrosion resistance strongly depends on the film porosity [279]. Compared to other materials, such as cobalt-chromium or stainless steel, TiN-coated materials exhibit high wear resistance in some biomedical environments [280, 281].
- **TiCN** coatings are usually employed due to their tribological behavior, excellent wear resistance, high hardness, and good thermal and electric conductivity. They are often used as protective layers in semiconductors and tools steels. The superior corrosion resistance, non-cytotoxicity, and mechanical properties make it a promising coating material for biomedical applications. [250, 273, 282–285]
- **DLC** is a metastable constitution of amorphous carbon. Although DLC films are isotropic disordered thin films without grain boundaries, they exhibit extreme properties similar to diamonds, such as hardness, elastic modulus, and chemical inertness, due to sp^3 bonds. Various types of DLC are used, such as hydrogen-free DLC, also called amorphous carbon (a-C), hydrogenated DLC (a-C:H), or dotted with silicon or metals, such as a-C:Si or a-C:Ag [23]. DLC films also show good biocompatibility, as toxicological or cytotoxic effects on cell growth were not observable [286–289]. Metal-doped DLC coatings show different results depending on the metal used. DLC dotted with Ti promotes cell growth, while DLC dotted with elements such as copper, silver, or vanadium, inhibits cell growth and good antibacterial behavior [268, 288, 290–292]. For load-bearing applications, the reported results on wear properties are contradictory regarding wear properties in biological fluids [256, 287].
- **Other coatings** deposited by PVD have been reported. It was concluded that TiAlN, TiN/TiAlN, tantalum nitride, and zirconium nitride, applied by different coating procedures, showed improved biocompatibility. [293–295]

3 Motivation and Research Hypothesis

The preceding elaboration regarding the processing and application of titanium alloys allows for summarizing a definition of an ideal biomaterial. The biomaterial should have a biocompatible chemical composition to avoid adverse tissue reactions, and it should not cause adverse reactions in the body and should also be neither toxic nor carcinogenic. The material should have a specific resistance to degradation, so for use as a permanent implant, the highest possible corrosion resistance. Both physical and mechanical properties should be adequate to augment or replace body parts or tissues, especially to withstand the cyclic loading of the joints. To minimize bone resorption due to stress shielding, an elastic modulus as low as possible, comparable to that of bone, is desirable. A high wear resistance avoids or reduces the formation of wear particles, which can cause adverse effects such as tissue reactions. Finally, an ideal biomaterial should be able to be formed or machined into various shapes while being relatively inexpensive and, above all, readily available.
The results and projection needs of TJR show considerable challenges to tackle in the future. The aging population and high growth rates of primary TJR replacements in the younger population will, in particular, lead to rising numbers of revision surgeries above average. The rise of joint arthroplasties will likely lead to shortcomings in health systems (e.g., increasing waiting times, cost pressure, and limited medical access). For this reason, timely policy interventions are necessary, such as [14]:

- increasing the quality of joint arthroplasty procedures to extend the life span of implants and reduce the complication rates, and
- reducing the number of unnecessary surgeries for patients who can be treated equally well with conservative, non-surgical procedures.

Concluding the previous elaboration, considerable challenges for the future of implants and implant materials need to be mastered. Based on this, there is potential for improvement, particularly in the materials used. These materials must be optimized for longevity and their permanent use as implants, ideally tailored to the requirements and needs of the patients. According to that, the following list specifies the main- and sub-hypotheses:

H1 LPBF-manufactured Ti-6Al-7Nb, combined with heat treatments and PVD thin coatings, offers improved biocompatibility and mechanical performance.

H1a Additively manufactured Ti-6Al-7Nb provides superior properties compared to conventionally manufactured material.

H1b The microstructure of Ti-6Al-7Nb is customizable by heat treatments and affects the quasi-static mechanical properties depending on the heat treatment.

H1c Depending on the loading situation in low-cycle fatigue (LCF) tests, the microstructure influences the LCF properties.

H1d PVD thin coatings, particularly TiN, TiCN, and a-C:Ag, affect the material behavior and enhance the quasi-static mechanical properties.

H1e The coating systems, TiN, TiCN, and a-C:Ag, and stress-relief heat treatment improve the LCF and high-cycle fatigue (HCF) material behavior.

H2 Alternative titanium alloys, such as the metastable β Ti-24Nb-4Z-r8Sn alloy, offer advantages in terms of biocompatibility and material behavior compared to commercially used Ti-6Al-7Nb alloy.

As can be concluded from the previous, the subsequent HT and PVD deposition can tailor the material properties and improve the material performance and therefore is crucial for the successful application of LPBF titanium alloys for biomedical devices. Consequently, this work aims to understand the mechanisms and effects of microstructural changes and PVD thin coatings. Firstly, the Ti-6Al-7Nb and Ti-24Nb-4Z-r8Sn powders are processed via LPBF to achieve parts with high relative densities. The various conditions of the different alloys before and after HT are microstructurally investigated and related to the mechanical properties, including hardness, tensile properties, LCF, and HCF properties. Additionally, the effect of PVD thin coatings on the mechanical performance, particularly regarding fatigue behavior, is examined.

4 Publications

Paper A

M. Hein, K.-P. Hoyer, and M. Schaper

Additively processed TiAl6Nb7 alloy for biomedical applications

Materialwissenschaft und Werkstofftechnik, 52, 703–716, 2021 [225].

Materialwiss. Werkstofftech. **2021**, *52*, 703–716 doi.org/10.1002/mawe.202000288

Additively processed TiAl6Nb7 alloy for biomedical applications

Additiv verarbeitete TiAl6Nb7-Legierung für die medizintechnische Anwendung

M. Hein[1, 2], K.-P. Hoyer[1, 2], M. Schaper[1, 2]

Laser beam melting (LBM) is an advanced manufacturing technology providing special features and the possibility to produce complex and individual parts directly from a CAD model. TiAl6V4 is the most common used titanium alloy particularly in biomedical applications. TiAl6Nb7 shows promising improvements especially regarding biocompatible properties due to the substitution of the hazardous vanadium. This work focuses on the examination of laser beam melted TiAl6Nb7. For microstructural investigation scanning electron microscopy including energy-dispersive x-ray spectroscopy as well as electron backscatter diffraction are utilized. The laser beam melted related acicular microstructure as well as the corresponding mechanical properties, which are determined by hardness measurements and tensile tests, are investigated. The laser beam melted alloy meets, except of breaking elongation A, the mechanical demands like ultimate tensile strength R_m, yield strength $R_{p0.2}$, Vickers hardness HV of international standard ISO 5832-11. Next steps contain comparison between TiAl6Nb7 and TiAl6V4 in different conditions. Further investigations aim at improving mechanical properties of TiAl6Nb7 by heat treatments and assessment of their influence on the microstructure as well as examination regarding the corrosive behavior in human body-like conditions.

Keywords: Laser beam melting **/** titanium alloy **/** TiAl6Nb7 **/** biomedical engineering **/** implants

Das Laserstrahlschmelzen (LBM) ist eine fortschrittliche Fertigungstechnologie, die besondere Merkmale und die Möglichkeit bietet, komplexe und individuelle Teile direkt aus einem CAD-Modell herzustellen. TiAl6V4 ist die am häufigsten verwendete Titanlegierung, insbesondere in biomedizinischen Anwendungen. TiAl6Nb7 zeigt vielversprechende Verbesserungen insbesondere hinsichtlich der biokompatiblen Eigenschaften durch die Substitution des schädlichen Vanadiums. Diese Arbeit konzentriert sich auf die Untersuchung von selektiv laserstrahlgeschmolzenem TiAl6Nb7. Für mikrostrukturelle Untersuchungen werden die Rasterelektronenmikroskopie einschließlich energiedispersiver Röntgenspektroskopie sowie die Elektronenrückstreuung eingesetzt. Die aus dem selektiven Laserstrahlschmelzen resultierende nadelförmige Mikrostruktur sowie die entsprechenden mechanischen Eigenschaften, die durch Härtemessungen und Zugversuche be-

[1] Paderborn University, Faculty for Mechanical Engineering, Lehrstuhl für Werkstoffkunde (Chair of Materials Science), Warburger Straße 100, 33098 PADERBORN, GERMANY
[2] Direct Manufacturing Research Center, Mersinweg 3, 33100 PADERBORN, GERMANY

Corresponding author: M. Hein, Paderborn University, Faculty for Mechanical Engineering, Lehrstuhl für Werkstoffkunde (Chair of Materials Science), Warburger Straße 100, 33098 PADERBORN, GERMANY,
E-Mail: hein@lwk.uni-paderborn.de

stimmt werden, werden untersucht. Die mittels selektivem laserstrahlschmelzen verarbeitete Legierung erfüllt, mit Ausnahme der Bruchdehnung *A*, die mechanischen Anforderungen wie Zugfestigkeit R_m, Streckgrenze $R_{p0,2}$ und Vickershärte HV der internationalen Norm ISO 5832-11. Die nächsten Schritte beinhalten einen Vergleich zwischen TiAl6Nb7 und TiAl6V4 in verschiedenen Zuständen. Weitere Untersuchungen zielen auf die Verbesserung der mechanischen Eigenschaften von TiAl6Nb7 durch Wärmebehandlungen und die Beurteilung ihres Einflusses auf die Mikrostruktur sowie auf die Untersuchung des korrosiven Verhaltens unter körperähnlichen Bedingungen.

Schlüsselwörter: Selektives Laserstrahlschmelzen / Titanlegierungen / TiAl6Nb7 / Biomedizintechnik / Implantate

1 Introduction

Additive manufacturing has received increasing attention from academia as well as industry in the recent years due to the progress in computation and systems technology. The process has developed to an advanced technology with high potential for both, industrial applications and university research [1]. Additive manufacturing is defined by DIN EN ISO/ASTM 52900 as a manufacturing process where parts and objects are joined of materials from 3D model data, layer by layer [2, 3]. Compared to conventional, e. g. subtractive manufacturing technologies, additive manufacturing enables the fabrication of very complex parts directly based on a 3D Computer Aided Design model.

Laser powder bed fusion of metal parts or laser beam melting is, regarding additive manufacturing of metals, one of the most established technique, as a consequence of the possibility to fabricate fully dense metal parts with complex geometric features and mechanical properties comparable to conventionally manufactured components [1, 4, 5]. Laser beam melting provides a wide range of advantages, such as reduced production time, an increased manufacturer flexibility and material utilization. For small and medium batch sizes in biomedical and aerospace industry laser beam melting is already established. For now, challenges of the laser beam melting technology still exist, e. g. microstructural challenges, like anisotropy or undesired phase compositions, and processing challenges, like remaining defects or low build-up rates [6]. Laser beam melting enables the manufacturer to be free in design as well as to have the so called complexity-for-free, and to produce patient-specific, individual implants customized to each patient [7]. In laser beam melting processes the fast heating rates, respectively cooling rates, result in a characteristic microstructure compared to conventional manufactured materials [8–10]. These microstructural features in additively manufactured materials, like anisotropy or grain refinement, are strongly connected to the prior process conditions and restrictions. By local melting of the powder through the laser beam, the top and some of the beneath, already solidified layers are metallurgical bonded. Usually the used laser scan velocity is around $500\,\mathrm{mm\,s^{-1}}$–$2000\,\mathrm{mm\,s^{-1}}$. In the resulting melt pool, the cooling rate is around $10^3\,\mathrm{K\,s^{-1}}$–$10^6\,\mathrm{K\,s^{-1}}$ [11]. The interaction period between the laser and the powder is approximately $4{\cdot}10^{-3}$ s–$4{\cdot}10^{-4}$ s, resulting in a much faster cooling compared for example to die casting [12]. Therefore, each layer experiences cyclic heating and cooling, lead to a quenched and tempered microstructure.

Biomedical materials have gained increasing attention in the recent decades. According to the specific application, biomaterials can be used in different parts of the human body. Often the biomedical materials are used for replacing lost or diseased biological structures, to increase the life quality of a patient [13–15]. Implants must have adequate properties, including mechanical properties like high wear resistance, corrosion resistance, excellent biocompatibility, osseointegration, and non-cytotoxicity to avoid revision surgeries [16]. Immediately after an implant is placed, reactions between the surface of the implant and the host tissue take place. Here, the biocompatibility of the material leads to success or failure of the implantation [17]. To increase the biocompatibility, toxic elements are

Materialwiss. Werkstofftech. **2021**, *52*, 703–716

avoided. Elements like titanium, niobium, molybdenum, tantalum, zirconium, gold, tungsten, and tin are biocompatible, whereas aluminum, vanadium, chromium, nickel are probably hazardous elements for the human body [18, 19]. Next to the mandatory biocompatible features of the alloys, the usage for specific applications is determined by the mechanical properties. For the use as load bearing implants the elastic modulus, tensile strength, elongation, and fatigue strength are important factors [20]. Titanium and its alloys possess in addition to other biomaterials, like stainless steels and cobalt chrome alloys, promising characteristics for biomedical applications based on their specific mechanical properties, biocompatibility features and high corrosion resistance [21–25]. The high mechanical biocompatibilities, e. g. Young's modulus, tensile strength, ductility, fatigue life, wear properties, etc., have to be adjusted to the structural properties of the human organism for the application as implants for replacing hard tissues [23]. Adjusting the structure, for example building porous structures, as well as microstructural adjustments of allotropic titanium alloys, could lead to adequate properties [24]. There are two allotropic forms of titanium. The α phase is the low temperature, hexagonal close-packed crystal structure. Above 882 °C titanium has a body-centered cubic structure, called β. The transformation temperature, known as β-transus temperature, of pure titanium either increases or decreases regarding to the alloying elements, either α stabilizers (e. g. aluminum, oxygen, nitrogen) or β stabilizers (e. g. vanadium, molybdenum, niobium, iron, chromium). The largest application among biomedical titanium have (α + β) and metastable β alloys [26–31]. TiAl6V4 and TiAl6Nb7 are the most commonly established (α + β) titanium alloys used for biomedical applications. Typically they are used in the annealed condition [14, 26, 27, 30]. Both alloy belong to the group of (α + β) titanium alloys, whereas the microstructure depends on the cooling rates, respectively the quenching parameters, from the β phase field at higher temperatures and the following heat treatment [32, 33]. The heat flow during the laser beam melting process is, caused by laser beam, predominantly downwards, through the previously solidified alloy and substrate material, due to which the material is heated with each laser beam scan to above or below the β transus temperature. The microstructure is strongly connected to the build strategy and the number of layers of the parts [34]. Laser beam melted TiAl6V4 consists of a fine acicular α' martensite microstructure within prior β-grains. The columnar β-grains transformed from the body-centered cubic lattice to the hexagonal close-packed α' microstructure. TiAl6V4 is the most common used titanium alloy in biomedical applications. Further investigations on new (α + β)-type titanium alloys, more specifically TiAl6Nb7, are being conducted. TiAl6Nb7 possess similar or favorable mechanical properties based on a quite similar microstructure, as well as advantageous corrosion resistance, and biocompatibility due to the substitution of the hazardous vanadium by niobium [35–37]. In this study, the titanium alloy TiAl6Nb7 is investigated. Laser beam melted material is examined regarding the microstructural and mechanical features with the overall objective to substitute the vanadium containing TiAl6V4 with TiAl6Nb7.

2 Material and methods

The laser beam melted specimens for microstructural and mechanical characterization were fabricated using a LT30 SLM machine (DMG MORI AG, Germany) equipped with a continuous wavelength fiber laser with a beam spot size of 70 µm, and a maximum power of 600 W. For data preparation the software Magics 21 (Materialise GmbH Leuven, Belgium) and RDesigner (DMG MORI AG, Germany) were used. To obtain the maximum possible material density with laser beam melting, the specific parameters are employed, *Table 1*. All specimens were fabricated with a constant scanning strategy, 5 mm stripes and a layer-wise rotation of the scanning vectors of 67°. The process takes place in an inert argon atmosphere to prevent oxidation of titanium with an oxygen content between 0.08 %–0.13 %.

Table 1. Laser beam melting parameter used for processing the test specimens.

Alloy	Laser power W	Laser scanning speed mm s^{-1}	Hatch distance mm	Layer thickness µm
TiAl6Nb7	250	880	0.11	50

Table 2. Chemical compositions of the powder material and the as-built TiAl6Nb7 alloy in wt%; as-built characterized by means of inductively coupled plasma optical emission spectrometry (OES) [38].

Alloy	Condition	Al	Nb	Fe	O	Ti	Method
TiAl6Nb7	ISO 5832-11	5.5–6.5	6.5–7.5	<0.25	<0.2	Bal.	
TiAl6Nb7	Powder	6.03	6.75	0.09	0.10	Bal.	external
TiAl6Nb7	as-built	5.50	6.81	0.12	0.18	Bal.	OES

TiAl6Nb7 powder is supplied by TLS Technik GmbH & Co. Spezialpulver KG (Germany). Powder particles were examined concerning particle size distribution, particle morphology and chemical composition. The particle size distribution is inspected with a Mastersizer 2000 (Malvern Instruments Ltd, United Kingdom) using laser diffraction to measure the size of the particles. The determination range of the particle size is between 0.02 µm to 2000 µm. Furthermore, the chemical compositions of the laser beam melted materials was measured by means of inductively coupled plasma optical emission spectrometry by Q4 TASMAN (Bruker AXS GmbH, Germany). In addition, revierlabor GmbH (Germany) investigated the powder material of TiAl6Nb7 by means of x-ray fluorescence analysis, combustion analysis with IR-detection and standard carrier gas hot extraction technique. The chemical compositions are in accordance to ISO 5832-11, *Table 2* [38].

Relative density was analyzed with a digital confocal microscope Keyence VHX5000 (KEYENCE GmbH, Germany) on the basis of metallographic cross-sections. Grayscale differentiation was used to identify and to count pores by means of the device-specific analysis software. The surface roughness was measured with an optical 3D macroscope VR-3100 (KEYENCE GmbH, Germany). The arithmetical mean roughness R_a and root square mean roughness R_q were determined on the surfaces of the as-built and electrical discharge machined (EDM) specimens. Five specimens per condition were measured with five line measurements (length ≈ 6.8 mm) per side. The powder morphology as well as macroscopic observations and classification of the fractured surfaces were investigated with secondary electron imaging on a scanning electron microscope (SEM) Zeiss Ultra Plus (Carl Zeiss AG, Germany). Microstructural investigations of the x-z-plane, parallel to the build direction of the laser beam melted alloy, is examined by means of scanning electron microscopy equipped with an electron backscatter diffraction unit to detect phases and textures as well as an energy-dispersive x-ray spectroscopy unit for chemical characterization. The specimens were grinded with sandpaper (grain size 2500) and subsequently vibration polished for 12 h on a VibroMet (Buehler, ITW Test & Measurement GmbH, Germany). The Vickers hardness was measured on surfaces perpendicular to the build direction on the laser beam melted specimens. Indentation hardness was measured with a fully automated hardness tester KB 30 FA (KB Prüftechnik GmbH, Germany) according to Vickers HV5. Five specimens of each alloy were tested with nine hardness indentations per sample. The tensile tests were conducted at room temperature. For the unidirectional, quasi-static tensile loading examinations mini tensile specimens were built, while other specimens were wire-cut with an electrical discharge machined from laser beam melted cuboids, *Figure 1*a, b. For both conditions the samples were loaded in build direction parallel to the z-axes of the specimens. Otherwise the orientation of solidification direction of the molten

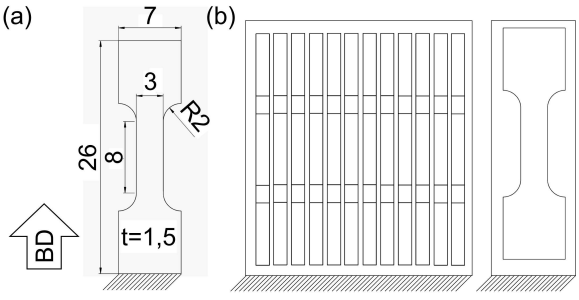

Figure 1. Geometry of the tensile specimens; (a) as-built, laser beam melted specimens; (b) wire-cut electrical discharge machined specimens of laser beam melted cuboids; BD indicating the build direction.

Materialwiss. Werkstofftech. **2021**, *52*, 703–716

material would be different for both types. Tensile tests were performed by means of a servo-hydraulic test-rig MTS 858 Table Top System equipped with a 20 kN load cell and an extensometer 632.29F-20 (both MTS Systems Corporation, USA) with a gage length of 3 mm. The test procedure was according to DIN EN ISO 6892-71 displacement controlled with a crosshead speed of 1.5 mm min^{-1} at ambient temperature. Five samples for each condition were tested to determine the mechanical properties, yield strength $R_{p0.2}$, ultimate tensile strength R_m, Young's modulus E and elongation at break A.

3 Results and discussion

3.1 Characterization of chemical compositions and powder

The chemical compositions of the TiAl6Nb7 powder, as well as the laser beam melted material are in agreement with ISO 5832–711. The TiAl6Nb7 powder batch has a nominal particle size distribution comprises 26.9 µm (D_{10}) and 52.1 µm (D_{90}) with a Gaussian distribution centered at 37.6 µm (D_{50}), *Figure 2*b. Powder particle morphology consists of mainly spherical particles with only a few agglomerations on bigger particles, Figure 2a.

3.2 Microstructure of TiAl6Nb7

The as-built microstructure is characterized by columnar primary β grains, oriented along the heat flow direction and nearly perpendicular to the laser beam scan vectors [14, 26, 27, 30, 32–34], *Figure 3*. Long plates of α' martensite were created inside the columnar prior β grains. Primary β grain boundaries are indicated by the white lines. The number of layers as well as the length of the scan vectors and therefore the time between the single laser passes, have a large effect on the size of the columnar, primary β grains [34, 39]. With increasing number of layers, and decreasing length of scan vectors, respectively time between scanning the same spot, the β grains get longer. Reheating of the already solidified layers above β transus temperature, while scanning and melting the top powder layer, leads to epitaxial growth of columnar grains. The laser scan results in a local melting of the surface and the remelting of the previous layers above β transus temperature [34]. If used in the as-built conditions the unidirectional β grain growth has to be considered due to the possible influence of the anisotropy on the mechanical properties. The anisotropy, as well as the coarser, primary β grains affect the mechanical properties of the specimens [40]. The emerging α grain orientation is random for the twelve α variants possibly resulting from the Burger's relationship If there is no preferred variant selection, the influence of the coarse, primary β grains on the mechanical properties is probably negligible [41]. The preferred crystallographic growth orientation is approximately 45° inclined to the build direction (z-axis), Figure 3 [33].

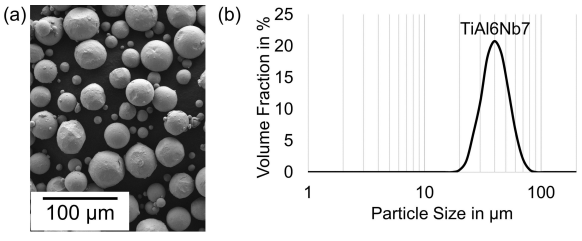

Figure 2. (a) Powder morphology (scanning electron microscope secondary electrons image) and (b) particle size distribution of TiAl6Nb7.

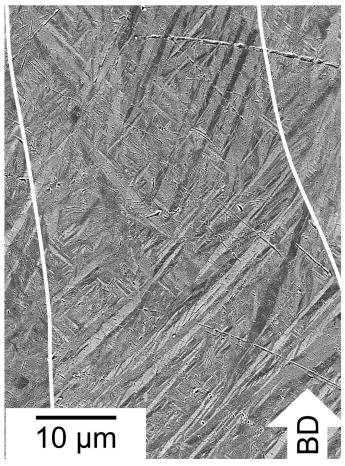

Figure 3. Cross-section of scanning electron microscope secondary electrons image of laser beam melted TiAl6Nb7 parallel to the build direction; primary β-grain boundaries (white lines) and primarily α' martensite lamellas.

The electron backscatter diffraction analysis of the additively manufactured TiAl6Nb7 shows a very fine, acicular, lamella like structure, *Figure 4*a, b. Regarding the inverse pole figure the fine-lamellar α' grain structure is strongly oriented inside the prior β grains. The α' grains have a width

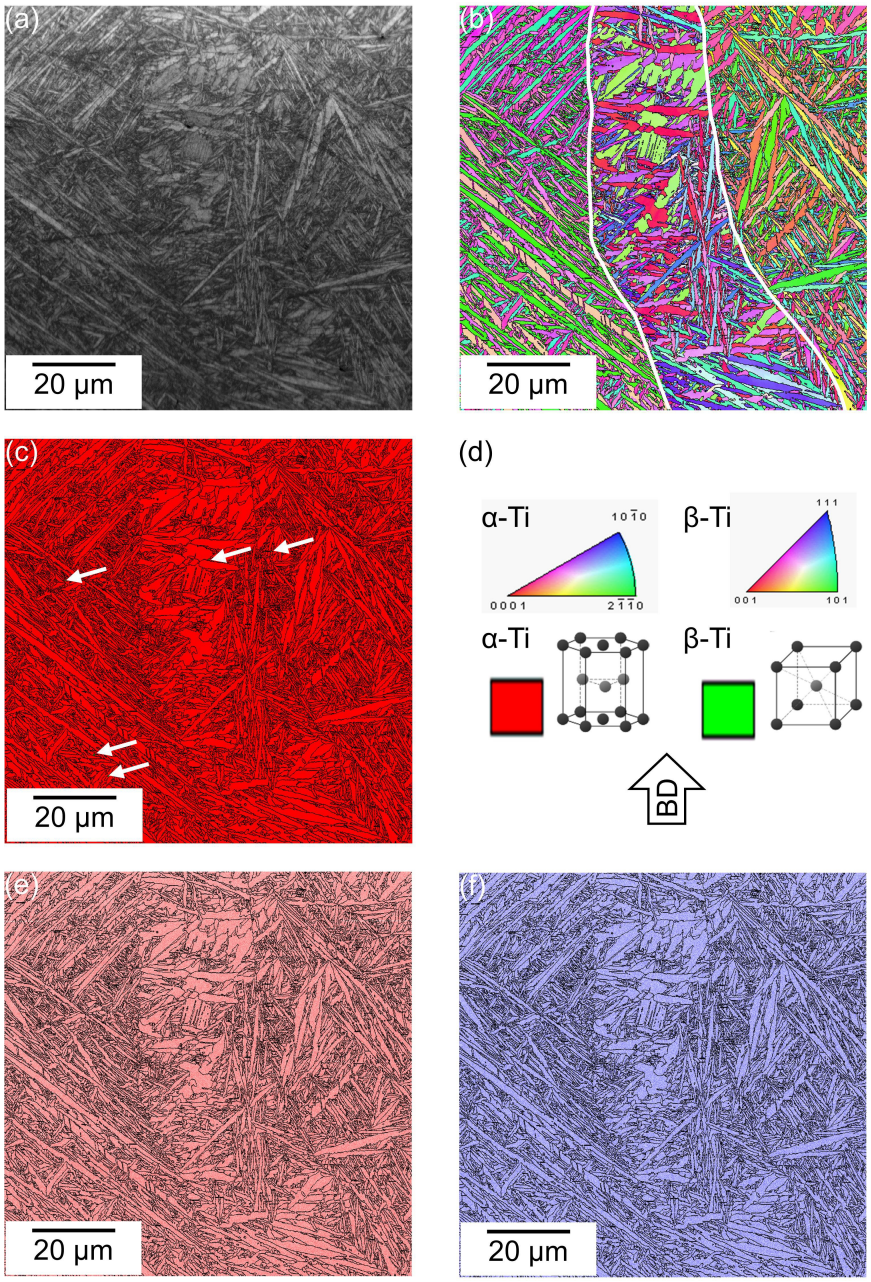

Figure 4. Electron backscatter diffraction mapping of additively manufactured TiAl6Nb7. (a) image quality signal, (b) inverse pole figure, white lines indicate prior β grain boundaries (c) phase map with α-Ti (red) and β-Ti (green, at tips of white arrows), (d) color legend for inverse pole figure, phase map coloring and build direction, (e) homogenous distribution of alloying element aluminum, and (f) of niobium.

from 1 µm–2 µm and a length ranging from a few µm to 60 µm. The size of these fine needles is decreasing with increasing cooling rate during solidification [11, 42, 43]. The white lines indicate the primary β grain boundaries, Figure 4b. During solidification of the molten titanium the prior β grains begin to evolve. During solidification, the body-centered cubic β phase preferentially grows in the $<100>$ direction, and therefore the elongated, columnar primary β grains evolve [44–46]. The $<100>$ direction of these grains is accordingly parallel to the build direction. The rotation of these grains is random, resulting in a fibre-like texture [46]. Due to the fast cooling and passing the β transus temperature, these β grains transform to α' phase according to the Burgers relation in 12 possible orientations (transformation variants) [41, 47–49]. The electron backscatter diffraction analyses determine the hexagonal close-packed grid structure (α and α') and the body-centered cubic structures (β). The difference between the martensitic α' and α phase is only a minimal structure distortion, which is not detectable by means of electron backscatter diffraction [50]. Due to the high cooling rate in laser beam melting processes the probability of the α' formation is very high [43, 51, 52]. In the phase map the α phase is colored red, respectively α', whereas the β phase is green, Figure 4c. In the laser beam melted specimens only small amounts of β phase can be detected (white arrows). β phase should additional surround the acicular α' lamellas in form of a thin film [46, 50, 53]. The distribution of the alloying elements aluminum and niobium, Figure 4e, f. Both alloying elements are evenly distributed in the investigated areas. No depletion or enrichment of any element is observable. The rapid cooling during laser beam melting, therefore, leads to a martensitic transformation and a limitation of diffusional transformation [54]. Due to the fast cooling the alloying elements are not able to diffuse in the metal evolving in a homogeneous concentration distribution [41].

3.3 Surface roughness

The arithmetical mean roughness R_a as well as the root mean square roughness R_q of the different specimens are summarized in *Table 3*. For one specimen of each condition the line measurements and the surfaces are shown in *Figure 5*. The roughness of the as built condition is higher compared to

Table 3. Results of mechanical tests on the as-built and electrical discharge machined (EDM) TiAl6Nb7.

Condition	R_a µm	R_q µm	$R_{p0.2}$ MPa	R_m MPa	E GPa	A %	*HV5*
as-built	5.1 ± 0.4	6.6 ± 0.6	868 ± 48	967 ± 34	105 ± 17	9.9 ± 2.4	337 ± 23
EDM	3.0 ± 3.9	4.1 ± 1.3	1118 ± 37	1223 ± 5	109 ± 4	7.6 ± 1.3	401 ± 8

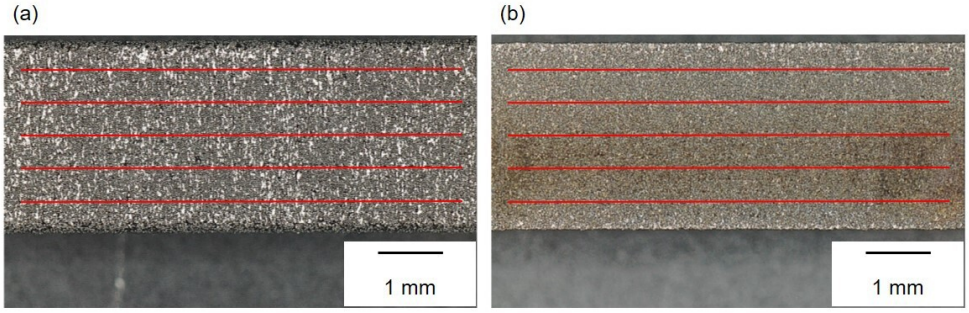

Figure 5. (a) Surface of an as-built specimen with red lines indicating the five measured lines for surface roughness measurements; (b) surface of an electrical discharge machined specimen with red lines indicating the five measured lines for surface roughness measurements.

the electrical discharge machined specimens. The roughness for the as built condition has values for R_a of 5.1 µm ± 0.4 µm and R_q of 6.6 µm ± 0.6 µm. Due to unmelted powder particles and the surface of the layerwise fabrication the roughness is higher than for the electrical discharge machined specimens with R_a of 3.0 µm ± 0.9 µm and R_q of 4.1 µm ± 1.3 µm, which have a smoother surface due to the machining process [55].

3.4 Hardness of TiAl6Nb7

The measured hardness of additively manufactured TiAl6Nb7 in as-built conditions is 337 HV5 ± 23 HV5 and in electrical discharge machined conditions 401 HV5 ± 8 HV5 [34]. For casted TiAl6Nb7 the hardness is 257 HV0.05 ± 29 HV0.05 [22]. Regarding the material data sheet of SLM Solutions Group AG (376 HV10 ± 6 HV10) the hardness of the as-built specimens is slightly lower [56]. The hardness of TiAl6Nb7 is connected with the grain size of the primary β grains, whereas larger prior β grains transform into longer and thicker α' martensite laths [34]. Due to smaller, finer, acicular α' laths and therefore hardening by grain refinement according to the Hall-Petch relation, the hardness for the laser beam melted specimens is higher than for conventionally manufactured specimens and the hardness of lamellar structures is higher than for equiaxed microstructures [57–61], Table 3. The hardness of the additively manufactured specimens is enhanced due to an improved densification, higher residual stresses, the martensitic transformation to α' instead of α and grain refinement as a strengthening mechanism [62]. The electrical discharge machined specimens show almost 20 % higher hardness values, than the as-built specimens. Due to the electrical discharge machining process the hardness may be increased. Metallurgical transformation like phase changes and grain refinement, surface hardening due to hydrogen or oxygen embrittlement or diffusion of alloying elements as well as residual stress states could favour the enhancement in hardness [55, 63–69].

3.5 Tensile properties of TiAl6Nb7

The mean values and standard deviations of the Young's modulus E, tensile yield strength $R_{p0.2}$, ultimate tensile strength R_m, and plastic elongation A of the two states are summarized and compared to the international standard for implants for surgery (ISO 5832-11), claiming minimum values for tensile strength and breaking elongation, Table 3 [38]. Exemplary presentations of two stress-strain curves for each conditions are shown in *Figure 6*a.

For the as-built TiAl6Nb7 the ultimate tensile strength R_m is 967 MPa ± 34 MPa and the yield strength $R_{p0,2}$ is 868 MPa ± 48 MPa and for the electrical discharge machined TiAl6Nb7 1223 MPa ± 5 MPa and 1118 MPa ± 37 MPa, re-

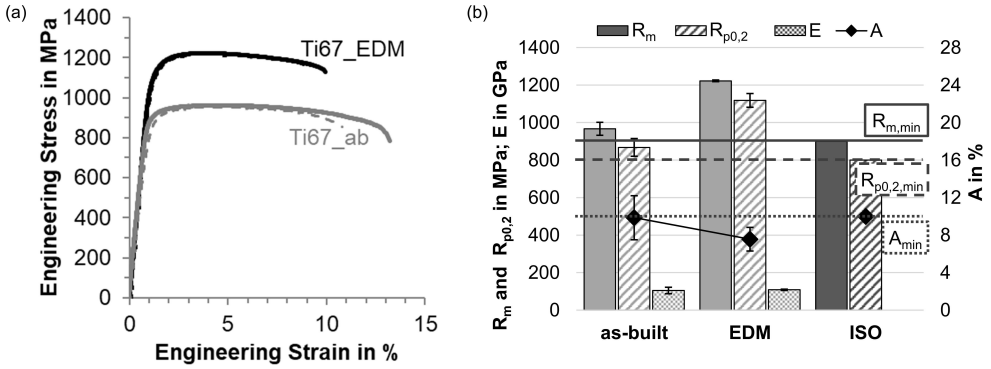

Figure 6. (a) Stress-strain curves of the laser beam melted, as-built (Ti67_ab, black lines) and electrical discharge machined (Ti67_EDM, black lines) TiAl6Nb7; (b) mechanical Properties of both states, as-built and electrical discharge machined out of a cuboid specimens (EDM) as well as minimum values for TiAl6Nb7 according ISO 5832-11 (ISO) [38]; mean values and standard deviations of ultimate tensile strength R_m (filled bars), yield strength $R_{p0.2}$ (striped bars), Young's modulus E (checkered bars) and breaking elongation A (black line).

spectively. The martensitic structure of the laser beam melted alloy leads to similar and higher mechanical properties regarding ultimate tensile and yield strength compared to wrought products (R_m = 984 MPa–1024 MPa; $R_{p0.2}$ = 933 MPa–952 MPa), as well as compared to casted products (R_m = 933 MPa, $R_{p0.2}$ = 817 MPa), especially with an α dominant equiaxed microstructure [7, 20, 23]. Nevertheless, the laser beam melted specimens lacked significantly in ductility and therefore plastic elongations are small [24, 25]. The different material behavior can be explained by the different microstructures, which have a strong impact on the mechanical properties of the alloys. Typically, in conventional material, the size and morphology of the α grains determine the mechanical properties, while in laser beam melted material the colony size and the size of the α or rather α' laths control the properties. Plastic deformation tends to be the movement of dislocations. The conventional material with the larger α grain size enables the deformation with less dislocation pile ups, whereas the smaller grain size in the laser beam melted material increases the dislocation pile ups [70]. As demonstrated by the Hall-Petch equation, there is an inverse relation between grain size and yield strength, resulting in the higher yield and ultimate tensile strength and the lower ductility of the laser beam melted specimens. Due to high cooling rate during laser beam melting and the resulting microstructure, a brittle material behavior occurs [24, 71, 72]. The increased mechanical properties of the laser beam melted specimens is caused by the higher residual stresses, the martensitic transformation during cooling to α' instead of α, as well as grain refinement as a strengthening mechanism [62]. As compared with TiAl6Nb7 castings, the properties of the laser beam melted specimens exceed the properties of casted specimens [22, 72]. According to ISO 5832-11, the mechanical properties of TiAl6Nb7 for biomedical applications should be at least 900 MPa (R_m), 800 MPa ($R_{p0.2}$) and 10 % (A) [38]. The different states only meet the requirements in some points. The laser beam melted TiAl6Nb7 has adequate values for tensile and yield strength, but not for the elongation. A comparison of the required demands to the determined mechanical properties for both states is summarized, Figure 6b. The investigations showed, that the Young's moduli of the alloy vary within a certain range between 105 GPa–116 GPa. Comparative values given in the literature according to ASM International Handbook is for TiAl6Nb7 105 GPa [38, 73]. The differences in stiffness of the two states may be influenced by the different distribution and levels of residual stress in the microstructure. Laser beam melted specimens tend to have high residual stresses due to the heat flow. The residual stresses in larger specimens are lower due to a better heat flow through a larger area, than in a small area, e. g. of an as-built tensile specimen. There is a strong dependency on the length of the scan vectors [74, 75]. The electrical discharge machined specimens have a significantly higher yield strength and ultimate tensile strength than the as-built specimens. The microstructure of the as-built specimens is strongly affected by the heat flow through the small exposure area as well as through the edge and the contiguous, non-melted powder surrounding the specimen [74, 75]. The microstructure of the electrical discharge machined specimens is affected less. Due to the subsequent machining after the laser beam melting process there is no influenced edge region, taking into account, that the rough surface and micro notches of the as-built surface are nuclei for crack initiation [76, 77]. The reasons for hardness enhancement could also influence the mechanical properties. Metallurgical transformation, surface hardening as well as the residual stress states could have an effect on the increased mechanical properties of the electrical discharge machined condition [55, 63–69]. The strength to hardness correlation for casted TiAl6V4, based on empirical relationships, is in good agreement, with the obtained results [78, 79]. For the as-built and the electrical discharge machined specimens the deviations between the experimental tensile strength $R_{m,\,\mathrm{exp}}$ ($\approx$967 MPa) and the tensile strength calculated from the hardness $R_{m,\,\mathrm{cal,\,HV\rightarrow Rm}}$ ($\approx$1024 MPa), respectively, $R_{m,\,\mathrm{exp}}$ ($\approx$1223 MPa) and $R_{m,\,\mathrm{cal,\,HV\rightarrow Rm}}$ ($\approx$1127 MPa), are quite large, but can be used as a approximation. Probably due to the process conditions the deviations occur. The hardness is strongly impacted by the underlying microstructure and the local crystallographic orientation of the α phase [78, 79]. As the laser beam melted specimens do not fulfil the demanded requirements for application as chirurgical implants according to ISO 5832-11, there are a few possibilities to increase the breaking elongation [38, 80]. The breaking

elongation can be increased by heat treatments which reduce the internal stresses [81]. Heat treatments could also lead to a homogeneous, decreased stress distribution inside the whole specimens, and to a partially decomposition of the α' martensite into equilibrium laminar α and β phases and therefore, to a relaxation of the tensed crystal lattice and to a decreased residual stress state [82–84]. Another possible thermomechanical treatment is hot isostatic pressing, minimizing residual porosity and fuses unmelted particles to increase the mechanical properties as described for TiAl6V4 [85]. Due to heat and thermomechanical treatments the average grains size increases. Sliding effects are mainly detected between grains and therefore, the breaking elongation will increase [86]. Another reason of increased breaking elongation is the presence of β phase titanium. An increased amount of body-centered cubic β titanium improves the ductile behavior [83, 86].

3.6 Fracture surfaces

After performing the tensile tests, secondary electron imaging on a scanning electron microscope was conducted to characterize the fractured surfaces. Both conditions, as-built and electrical discharge machined, show similar results, therefore only the fracture surface of the as-built specimens is shown. Additively processed titanium often exhibits brittle material behavior due to martensitic phase transformation. Nevertheless, TiAl6Nb7 demonstrates mainly ductile material and fracture behavior, *Figure 7*. The propensity of cleavage fracture decreases with decreasing grain size, so the fracture surface of the laser beam melted materials show cleavage facets with high amounts of dimples at the grain boundaries [87]. Fractured surfaces show small, shallow dimples on quasi-cleavage fracture surfaces, and transgranular facets, confirming the minor brittle fracture behavior of the additively processed material. Concentric features, as a

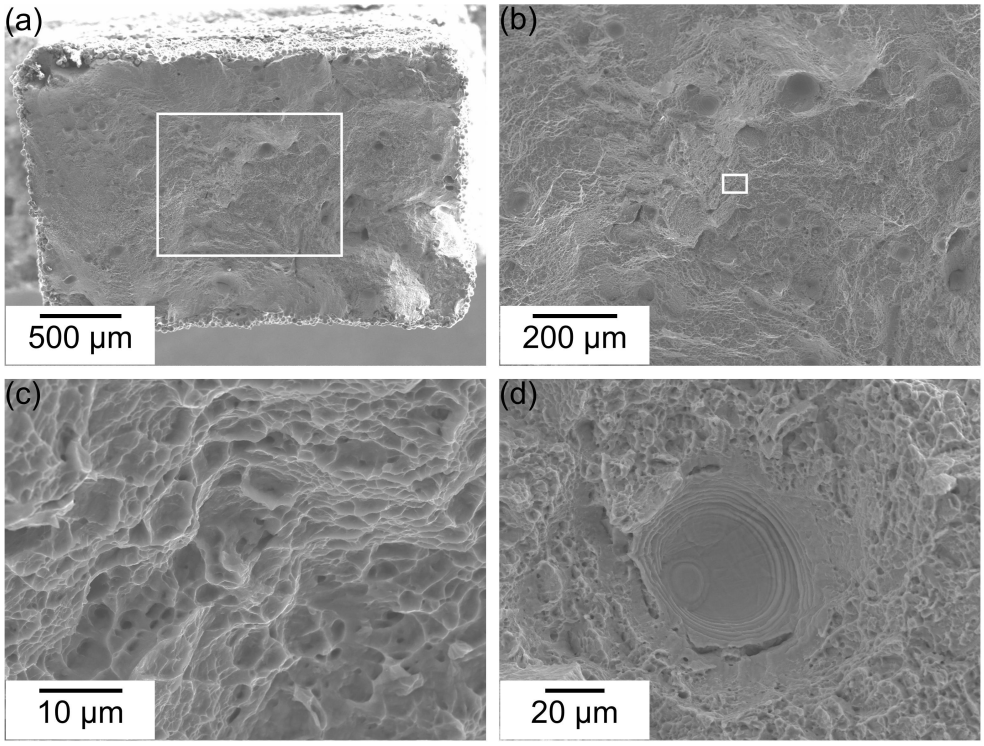

Figure 7. Scanning electron microscope-secondary electrons images of tensile fracture surface of the as-built TiAl6Nb7; (a) overall view; (b) enlarged view from the boxed region in (a); (c) enlarged view of the boxed region in (b); (d) concentric defect (gas pore).

result of the laser beam melting, like pores, unmelted powder particles and defects occur on fracture surfaces in laser beam melted and electrical discharge machined conditions, Figure 7a, b, d. These build defects are typically perpendicular to the build direction and pulled apart by the tensile load.

4 Conclusions

Different aspects of the titanium alloy TiAl6Nb7 have been addressed. The microstructure, chemical composition, as well as the mechanical properties like tensile strength and hardness were investigated. The following conclusions were made from these investigations:

- The microstructure shows fine, acicular α' martensite laths, which have growed inside the primary β grains. These prior β grains are elongated as a result of the epitaxial growth in build direction due to the layer wise fabrication during the laser beam melting process. The size and orientation of the α' martensite laths are determined by size and growth direction of prior β grains, which form due to the high energy input in the laser beam melting process.
- Only minor deviations in the chemical compositions regarding the powder and the laser beam melted material are noticeable. The compositions are within the range of ISO 5832-11.
- The indentation hardness, yield strength and ultimate tensile strength tends to be higher in the laser beam melted specimens compared to the conventional materials due to different microstructures. A finer microstructure leads to increased strength values due to grain-boundary strengthening. Decreasing grain sizes and therefore increased dislocation pile ups inside the grains lead to reduced breaking elongation.
- Small, shallow dimples on quasi-cleavage fracture surfaces, and transgranular facets, confirming the ductile behavior of the additively processed materials, characterize the fracture surface of the laser beam melted TiAl6Nb7.

Further investigations have to be conducted for biomedical applications of the alloy. The next steps are the ascertainment of differences between laser beam melted TiAl6Nb7 and TiAl6V4 as well as differences between conventionally and additively manufactured material. Different heat treatments and the resulting effects on the mechanical behaviour as well as the fatigue performances of these alloys will be investigated. Grain size and phase fraction have to be adapted, to fulfil the required properties. Corrosion properties in body-like conditions will be determined in further investigations. Furthermore, there will be examinations on applying physical vapour deposition coatings by the Institute of Materials Engineering (TU Dortmund, Germany) and their effects especially on fatigue and mechanical performance as well as on the biocompatible features. The biocompatibility of different coatings will be evaluated by determining cell viability and cell proliferation by the Department of Pharmacology, Toxicology and Pharmacy (TiHo Hanover, Germany).

Acknowledgements

The research was performed with the equipment and base of the LWK and DMRC research infrastructure. The authors are grateful to the staff members of the LWK and DMRC. The authors gratefully thank the German Research Foundation (DFG) for the financial support (SCHA 1484/45-1, ME 4991/2-1, TI 343/167-1). Open Access funding enabled and organized by Projekt DEAL.

5 References

[1] M. Schmidt, M. Merklein, D. Bourell, D. Dimitrov, T. Hausotte, K. Wegener, L. Overmeyer, F. Vollertsen, G.N. Levy, *CIRP Ann.* **2017**, *66*, 561.

[2] DIN Deutsches Institut für Normung e. V., *EN ISO 17296-2 : 2016*, **2016**.

[3] DIN Deutsches Institut für Normung e. V., *EN ISO/ASTM 52900 : 2018*, **2018**.

[4] D. Bourell, J.P. Kruth, M. Leu, G. Levy, D. Rosen, A.M. Beese, A. Clare, *CIRP Ann.* **2017**, *66*, 659.

[5] T.T. Wohlers, I. Campbell, O. Diegel, J. Kowen, Wohlers report 2018: 3D printing and additive manufacturing state of the industry: annual worldwide progress report, Wohlers Associates, Inc, Fort Collins, Colorado **2018**.

[6] H. Shipley, D. McDonnell, M. Culleton, R. Coull, R. Lupoi, G. O'Donnell, D. Trimble, *Int. J. Mach. Tools Manuf.* **2018**, *128*, 1.

[7] L.-C. Zhang, L.-Y. Chen, *Adv. Eng. Mater.* **2019**, *21*, 1801215.

[8] H. Attar, K.G. Prashanth, A.K. Chaubey, M. Calin, L.C. Zhang, S. Scudino, J. Eckert, *Mater. Lett.* **2015**, *142*, 38.

[9] N. Dai, L.-C. Zhang, J. Zhang, Q. Chen, M. Wu, *Corros. Sci.* **2016**, *102*, 484.

[10] Y. Yang, Y. Chen, J. Zhang, X. Gu, P. Qin, N. Dai, X. Li, J.-P. Kruth, L.-C. Zhang, *Mater. Des.* **2018**, *146*, 239.

[11] T. DebRoy, H.L. Wei, J.S. Zuback, T. Mukherjee, J.W. Elmer, J.O. Milewski, A.M. Beese, A. Wilson-Heid, A. De, W. Zhang, *Prog. Mater. Sci.* **2018**, *92*, 112.

[12] D. Buchbinder, W. Meiners, E. Brandl, F. Palm, K. Müller-Lohmeier, M. Wolter, C. Over, W. Moll, J. Weber, N. Skrynecki, J. Gradl, V. Neubert, *Generative Fertigung von Aluminiumbauteilen für die Serienproduktion: AluGenerativ, Fkz.: 01RIO639A-D* **2010**.

[13] M. Abdel-Hady Gepreel, M. Niinomi, *J. Mech. Behav. Biomed. Mater.* **2013**, *20*, 407.

[14] M. Geetha, A.K. Singh, R. Asokamani, A.K. Gogia, *Prog. Mater. Sci.* **2009**, *54*, 397.

[15] M. Long, H. Rack, *Biomaterials* **1998**, *19*, 1621.

[16] S.M. Kurtz, K.L. Ong, J. Schmier, F. Mowat, K. Saleh, E. Dybvik, J. Kärrholm, G. Garellick, L.I. Havelin, O. Furnes, H. Malchau, E. Lau, *J. Bone Jt. Surg., Am. Vol.* **2007**, *89 Suppl 3*, 144.

[17] E. Nes, K. Marthinsen, Y. Brechet, *Scr. Mater.* **2002**, *47*, 607.

[18] D. Kuroda, M. Niinomi, M. Morinaga, Y. Kato, T. Yashiro, *Mater. Sci. Eng., A* **1998**, *243*, 244.

[19] Y. Li, C. Yang, H. Zhao, S. Qu, X. Li, Y. Li, *Materials* **2014**, *7*, 1709.

[20] M. Niinomi, *Mater. Sci. Eng., A* **1998**, *243*, 231.

[21] D.A. Hollander, M. von Walter, T. Wirtz, R. Sellei, B. Schmidt-Rohlfing, O. Paar, H.-J. Erli, *Biomaterials* **2006**, *27*, 955.

[22] D. Iijima, *Biomaterials* **2003**, *24*, 1519.

[23] M. Niinomi, *J. Mech. Behav. Biomed. Mater.* **2008**, *1*, 30.

[24] L.E. Murr, S.A. Quinones, S.M. Gaytan, M.I. Lopez, A. Rodela, E.Y. Martinez, D.H. Hernandez, E. Martinez, F. Medina, R.B. Wicker, *J. Mech. Behav. Biomed. Mater.* **2009**, *2*, 20.

[25] B. Vandenbroucke, J.-P. Kruth, *Rapid Prototyp. J.* **2007**, *13*, 196.

[26] M. Navarro, A. Michiardi, O. Castaño, J.A. Planell, *J.R. Soc., Interface* **2008**, *5*, 1137.

[27] D.M. Dohan Ehrenfest, P.G. Coelho, B.-S. Kang, Y.-T. Sul, T. Albrektsson, *Trends Biotechnol.* **2010**, *28*, 198.

[28] J. Raphel, M. Holodniy, S.B. Goodman, S.C. Heilshorn, *Biomaterials* **2016**, *84*, 301.

[29] K.J. Bozic, S.M. Kurtz, E. Lau, K. Ong, V. Chiu, T.P. Vail, H.E. Rubash, D.J. Berry, *Clin. Orthop. Relat. Res.* **2010**, *468*, 45.

[30] M. Kutz, Standard handbook of biomedical engineering and design, McGraw-Hill, New York **2003**.

[31] M.J. Yaszemski, *Biomaterials in Orthopedics*, 2nd ed., Taylor and Francis, Hoboken **2013**.

[32] S.A. Ajeel, T.L. Alzubaydi, A.K. Swadi, *Engineering and Technology Journal* **2007**, *25*.

[33] T. Sercombe, N. Jones, R. Day, A. Kop, *Rapid Prototyp. J.* **2008**, *14*, 300.

[34] E. Chlebus, B. Kuźnicka, T. Kurzynowski, B. Dybała, *Mater. Charact.* **2011**, *62*, 488.

[35] X. Liu, P. Chu, C. Ding, *Mater. Sci. Eng., R* **2004**, *47*, 49.

[36] B. Schwilling, C. Fleck, D. Eifler, *Materialwiss. Werkstofftech.* **2002**, *33*, 453.

[37] M. López, A. Gutiérrez, J. Jiménez, *Electrochim. Acta* **2002**, *47*, 1359.

[38] DIN Deutsches Institut für Normung e. V., *ISO 5832-11 : 2014*, **2015**.

[39] A.A. Antonysamy, P.B. Prangnell, J. Meyer, *Mater. Sci. Forum* **2012**, *706*, 205.

[40] G. Lütjering, *Mater. Sci. Eng., A* **1998**, *243*, 32.

[41] G. Lütjering, J.C. Williams, *Titanium*, 2nd ed., Springer-Verlag, s.l. **2007**.

[42] C. Körner, *Int. Mater. Rev.* **2016**, *61*, 361.

[43] B. Baufeld, E. Brandl, O. van der Biest, *J. Mater. Process. Technol.* **2011**, *211*, 1146.

[44] P. Kobryn, S. Semiatin, *J. Mater. Process. Technol.* **2003**, *135*, 330.

[45] L. Thijs, F. Verhaeghe, T. Craeghs, J. van Humbeeck, J.-P. Kruth, *Acta Mater.* **2010**, *58*, 3303.

[46] B. Vrancken, L. Thijs, J.-P. Kruth, J. van Humbeeck, *J. Alloys Compd.* **2012**, *541*, 177.

[47] W.G. Burgers, *Physica* **1934**, 561.

[48] M. Peters, C. Leyens, *Titan und Titanlegierungen*, 3rd ed., Wiley-VCH, Weinheim **2002**.

[49] S. Banerjee, P. Mukhopadhyay, *Phase transformations: Examples from titanium and zirconium alloys*, Elsevier, Amsterdam, Oxford **2007**.

[50] I. Polmear, D. StJohn, J.-F. Nie, M. Qian, in *Light Alloys*, (Eds: I. Polmear, D. StJohn, J.-F. Nie, M. Qian), Elsevier **2017**, pp. 369–460.

[51] L.E. Murr, S.M. Gaytan, D.A. Ramirez, E. Martinez, J. Hernandez, K.N. Amato, P.W. Shindo, F.R. Medina, R.B. Wicker, *J. Mater. Sci. Technol.* **2012**, *28*, 1.

[52] O. Rehme, *Cellular Design for Laser Freeform Fabrication*, 1st ed., Cuvillier Verlag, Göttingen **2010**.

[53] P. Harcuba, K. Václavová, J. Čapek, J. Stráský, M. Janeček, M. Janovská, *Acta Phys. Pol., A* **2015**, *128*, 570.

[54] J. Sieniawski, W. Ziaja, K. Kubiak, M. Motyk, in *Titanium alloys - advances in properties control*, (Eds: J. Sieniawski, W. Ziaja), InTech, Rijeka, Croatia **2014**.

[55] J. Boban, A. Ahmed, *J. Mater. Process. Technol.* **2021**, *291*, 117013.

[56] SLM Solutions Group AG, Material Data Sheet - Ti-Alloy TiAl6Nb7 / F1295.

[57] E.O. Hall, *Proc. Phys. Soc., London, Sect. B* **1951**, *747*.

[58] N.J. Petch, *ISIJ Int.* **1953**, *25*.

[59] R.W. Armstrong, *Mater. Trans.* **2014**, *55*, 2.

[60] R. Filip, K. Kubiak, W. Ziaja, J. Sieniawski, *J. Mater. Process. Technol.* **2003**, *133*, 84.

[61] J. Sieniawski, R. Filip, W. Ziaja, *Mater. Des.* **1997**, *18*, 361.

[62] H. Attar, M. Calin, L.C. Zhang, S. Scudino, J. Eckert, *Mater. Sci. Eng., A* **2014**, *593*, 170.

[63] H. Tsukahara, H. Minami, K. Masui, T. Sone, K. Demizu, *Journal of The Japan Society of Electrical Machining Engineers* **2001**, *35*, 24.

[64] H. Tsukahara, H. Minami, K. Masui, K. Demizu, T. Sone, *Journal of The Japan Society of Electrical Machining Engineers* **1999**, *33*, 9.

[65] H. Tsukahara, H. Minami, K. Masui, T. Sone, K. Demizu, *Journal of The Japan Society of Electrical Machining Engineers* **2004**, *38*, 24.

[66] F. Ghanem, C. Braham, H. Sidhom, *J. Mater. Process. Technol.* **2003**, *142*, 163.

[67] M.B. Ndaliman, A.A. Khan, M.Y. Ali, *Proc. Inst. Mech. Eng., Part B* **2013**, *227*, 460.

[68] S. Kumar, R. Singh, T.P. Singh, B.L. Sethi, *J. Mater. Process. Technol.* **2009**, *209*, 3675.

[69] F. Klocke, D. Welling, J. Dieckmann, *Procedia Eng.* **2011**, *19*, 184.

[70] M. Shunmugavel, A. Polishetty, G. Littlefair, *Proc. Technol.* **2015**, *20*, 231.

[71] S. Leuders, T. Lieneke, S. Lammers, T. Tröster, T. Niendorf, *J. Mater. Res.* **2014**, *29*, 1911.

[72] E. Kobayashi, T.J. Wang, H. Doi, T. Yoneyama, H. Hamanaka, *J. Mater. Sci.: Mater. Med.* **1998**, *9*, 567.

[73] R. Boyer, G. Welsch, E.W. Collings, *Materials properties handbook: Titanium alloys*, 4th ed., ASM International, Materials Park, Ohio **2007**.

[74] J.-P. Kruth, J. Deckers, E. Yasa, R. Wauthlé, *Proc. Inst. Mech. Eng., Part B* **2012**, *226*, 980.

[75] L.A. Parry, I.A. Ashcroft, R.D. Wildman, *Addit. Manuf.* **2019**, *25*, 166.

[76] G. Kasperovich, J. Hausmann, *J. Mater. Process. Technol.* **2015**, *220*, 202.

[77] S. Liu, Y.C. Shin, *Mater. Des.* **2019**, *164*, 107552.

[78] J.S. Keist, T.A. Palmer, *Mater. Sci. Eng., A* **2017**, *693*, 214.

[79] C.F. Hickey, Tensile Strength-hardness Correlation for Titanium Alloys **1961**.

[80] DIN Deutsches Institut für Normung e. V., *EN ISO 5832-3 : 2016*, **2017**.

[81] M. Thöne, S. Leuders, A. Riemer, T. Tröster, H.A. Richard, in Proceedings of the 23rd Annual International Solid Freeform Fabrication Symposium – An Additive Manufacturing Conference 2013, **2013**.

[82] E. Sallica-Leva, R. Caram, A.L. Jardini, J.B. Fogagnolo, *J. Mech. Behav. Biomed. Mater.* **2016**, *54*, 149.
[83] P. Tao, H. Li, B. Huang, Q. Hu, S. Gong, Q. Xu, *China Foundry* **2018**, *15*, 243.
[84] F.X. Gil Mur, D. Rodríguez, J.A. Planell, *J. Alloys Compd.* **1996**, *234*, 287.
[85] G. Kasperovich, J. Hausmann, in Proceedings of the Materials Science & Technology Conference 2013, **2013**, 9.
[86] B. Gorny, T. Niendorf, J. Lackmann, M. Thoene, T. Troester, H.J. Maier, *Mater. Sci. Eng., A* **2011**, *528*, 7962.
[87] K.M. Ibrahim, M. Mhaede, L. Wagner, *J. Mater. Eng. Perform.* **2012**, *21*, 114.

Received in final form: May 7th 2021

Paper B

M. Hein, D. Kokalj, N. F. Lopes Dias, D. Stangier, H. Oltmanns, S. Pramanik, M. Kietzmann, K.-P. Hoyer, J. Meissner, W. Tillmann, and M. Schaper

Low Cycle Fatigue Performance of Additively Processed and Heat-Treated Ti-6Al-7Nb Alloy for Biomedical Applications

Metals, 12, 122, 2022 [296].

metals

MDPI

Article

Low Cycle Fatigue Performance of Additively Processed and Heat-Treated Ti-6Al-7Nb Alloy for Biomedical Applications

Maxwell Hein [1,2,*], David Kokalj [3], Nelson Filipe Lopes Dias [3], Dominic Stangier [3], Hilke Oltmanns [4], Sudipta Pramanik [1], Manfred Kietzmann [4], Kay-Peter Hoyer [1,2], Jessica Meißner [4], Wolfgang Tillmann [3] and Mirko Schaper [1,2]

1 Chair of Materials Science (LWK), Paderborn University, Warburger Str. 100, 33098 Paderborn, Germany; pramanik@lwk.upb.de (S.P.); hoyer@lwk.upb.de (K.-P.H.); schaper@lwk.upb.de (M.S.)
2 DMRC-Direct Manufacturing Research Center, University of Paderborn, Mersinweg 3, 33100 Paderborn, Germany
3 Institute of Materials Engineering (LWT), TU Dortmund University, Leonhard-Euler-Str. 2, 44227 Dortmund, Germany; david.kokalj@tu-dortmund.de (D.K.); filipe.dias@tu-dortmund.de (N.F.L.D.); dominic.stangier@tu-dortmund.de (D.S.); wolfgang.tillmann@udo.edu (W.T.)
4 Department of Pharmacology, Toxicology and Pharmacy, University of Veterinary Medicine, Bünteweg 17, 30559 Hannover, Germany; hilke.oltmanns@tiho-hannover.de (H.O.); manfred.kietzmann@tiho-hannover.de (M.K.); jessica.meissner@tiho-hannover.de (J.M.)
* Correspondence: hein@lwk.upb.de; Tel.: +49-5251-60-5447

Abstract: In biomedical engineering, laser powder bed fusion is an advanced manufacturing technology, which enables, for example, the production of patient-customized implants with complex geometries. Ti-6Al-7Nb shows promising improvements, especially regarding biocompatibility, compared with other titanium alloys. The biocompatible features are investigated employing cytocompatibility and antibacterial examinations on Al_2O_3-blasted and untreated surfaces. The mechanical properties of additively manufactured Ti-6Al-7Nb are evaluated in as-built and heat-treated conditions. Recrystallization annealing (925 °C for 4 h), β annealing (1050 °C for 2 h), as well as stress relieving (600 °C for 4 h) are applied. For microstructural investigation, scanning and transmission electron microscopy are performed. The different microstructures and the mechanical properties are compared. Mechanical behavior is determined based on quasi-static tensile tests and strain-controlled low cycle fatigue tests with total strain amplitudes ε_A of 0.35%, 0.5%, and 0.8%. The as-built and stress-relieved conditions meet the mechanical demands for the tensile properties of the international standard ISO 5832-11. Based on the Coffin–Manson–Basquin relation, fatigue strength and ductility coefficients, as well as exponents, are determined to examine fatigue life for the different conditions. The stress-relieved condition exhibits, overall, the best properties regarding monotonic tensile and cyclic fatigue behavior.

Keywords: laser powder bed fusion; Ti-6Al-7Nb; titanium alloy; biomedical engineering; low cycle fatigue; microstructure; nanostructure

check for updates

Citation: Hein, M.; Kokalj, D.; Lopes Dias, N.F.; Stangier, D.; Oltmanns, H.; Pramanik, S.; Kietzmann, M.; Hoyer, K.-P.; Meißner, J.; Tillmann, W.; et al. Low Cycle Fatigue Performance of Additively Processed and Heat-Treated Ti-6Al-7Nb Alloy for Biomedical Applications. *Metals* **2022**, *12*, 122. https://doi.org/10.3390/met12010122

Academic Editors: Martin Heilmaier, Martina Zimmermann and John Campbell

Received: 20 December 2021
Accepted: 7 January 2022
Published: 8 January 2022

Publisher's Note: MDPI stays neutral with regard to jurisdictional claims in published maps and institutional affiliations.

1. Introduction

Biomedical materials often are used for replacing lost or diseased biological structures [1–3]. Implants require adequate properties, including mechanical properties, such as high wear resistance, corrosion resistance, excellent biocompatibility, osseointegration, and non-cytotoxicity, to avoid revision surgeries [4].

Titanium and its alloys are generally used in biomedical applications due to their excellent biocompatibility, high corrosion resistance, and superb mechanical properties, such as low elastic modulus and high strength. Titanium alloys are the most widely used metallic materials for load-bearing biomedical applications [5–9]. Ti-6Al-7Nb is an (α + β) titanium alloy with high specific strength and corrosion resistance, accompanied

by excellent biocompatibility, and is used as an orthopedic and dental alloy [10–12]. Ti-6Al-4V, which already is of high interest in the biomedical industry, is commonly used but has slight disadvantages towards Ti-6Al-7Nb, regarding corrosion resistance and biocompatibility [13]. Previous studies showed that elements such as titanium, niobium, zirconium, gold, and tin are biocompatible, whereas aluminum, vanadium, chromium, and nickel are probably hazardous elements for the human body [14,15]. Vanadium was found to be cytotoxic and there are assumptions regarding vanadium ion release in service [16,17]. Various efforts have been carried out to address the issue of cytotoxicity of the alloying elements of Ti-6Al-4V, for example, by replacing all the alloying elements, as in the alloy Ti-35Nb-7Zr-5Ta [18]. Due to the hazardous vanadium in Ti-6Al-4V, the development of Ti-6Al-7Nb, through the substitution of vanadium by niobium, offered an alternative for load-bearing implant materials [16,19,20].

Laser powder bed fusion (LPBF), also called laser beam melting, is, regarding additive manufacturing (AM) of metals, one of the most established techniques [21–23]. In LPBF processes, the fast heating rates and cooling rates, respectively, result in a characteristic microstructure and therefore characteristic mechanical properties [24–26]. Conventional fabrication methods are limited due to manufacturing constraints producing patient-specific implants. Through AM, or rather LPBF, extraordinary biomedical implant topologies, such as porous and foam structures, are feasible [27–29].

Many available research results focus on the mechanical properties of different additively manufactured alloys, such as 316L, 17-4 PH, or Ti-6Al-4V [30,31]. However, there remains a significant gap in terms of fatigue properties analysis, since most available research on dynamic behavior is related to high cycle fatigue (HCF) testing and the crack growth analysis of additively manufactured parts of steel alloys [32–36] and titanium alloys [37–42]. Only few studies deal with the low cycle fatigue (LCF) properties of additively manufactured alloys in general [43–47]. Even fewer studies were performed with a focus on post-treatments for titanium alloys. Previous studies addressed the fatigue behavior of additively processed Ti-6Al-4V for different conditions and loading situations [38,42,48,49]. Examinations of the quasi-static behavior of Ti-6Al-7Nb are at hand but none of them include LCF behavior [17,50–53]. In previous studies, extremely high loads were reported during stumbling. Such load peaks during uncontrolled movements are difficult to investigate systematically. Implants are usually examined for high cycle fatigue, although the rare extreme loads could endanger the implant. Therefore, in addition to monotonic material characterization and high cycle fatigue tests, implants should also be investigated at low cycles with higher load levels [54,55]. Given that the physiological—sometimes extreme—loading during service life as an implant is cyclic, the fatigue performance of laser beam-melted Ti-6Al-7Nb requires attention. To combine LPBF with the promising quasi-static properties of Ti-6Al-7Nb, the microstructural and mechanical properties of additively manufactured Ti-6Al-7Nb in different conditions are investigated in this work. Heat treatments are an additional part of this examination, to initiate microstructural changes for the relaxation of the tensed crystal lattice and the beneficial crack growth behavior, as well as to achieve a homogenous, decreased residual stress state [56–58]. Generally, titanium alloys are heat-treated due to high residual stresses as well as due to the brittle α'-phase, occurring after LPBF. Moreover, thermal post-treatments induce an improvement of the quasi-static mechanical properties of different titanium alloys [52,59]. To sum up, since there is a lack of studies addressing fatigue behavior, it is necessary to focus on an investigation of the microstructure under different conditions, as-built and heat-treated, and their effect on quasi-static and LCF behaviors.

2. Materials and Methods

2.1. Manufacturing Procedure, Materials, and Mechanical Characterization

The specimens were fabricated using an LT12 SLM machine (DMG MORI AG, Bielefeld, Germany) with a beam spot size of 35 µm. For data preparation, the software Materialise Magics (Version 21.1, Materialise GmbH, Munich, Germany) was applied. To

obtain dense material with LPBF (relative density $\varphi > 99.9\%$), the following parameters were used: laser power P = 227 W, laser scanning speed v = 1.675 mm s^{-1}, hatch distance h = 0.077 mm. A constant scanning strategy of 5 mm stripes by layer-wise rotation of the scanning vectors of 67° alongside a defined layer thickness of 50 µm was applied. As contour parameters, a laser power P_c = 123 W and a scanning speed v_c = 0.512 mm s^{-1} were applied. The Ti-6Al-7Nb powder is supplied by ECKART TLS GmbH (Bitterfeld, Germany). The Ti-6Al-7Nb powder particles were examined concerning particle size distribution (PSD) with a Mastersizer 2000 (Malvern Panalytical GmbH, Kassel, Germany) using laser diffraction. The powder batch had a nominal PSD comprising 26.9 µm (D_{10}) and 52.1 µm (D_{90}) with a log-transformed normal distribution centered at 37.6 µm (D_{50}), see Figure 1a. Different heat treatments were performed under a vacuum atmosphere. Recrystallization annealing (HT1 = 925 °C for 4 h) was conducted to obtain equiaxed α with β at grain boundary triple points, β annealing (HT2 = 1050 °C for 2 h) to receive Widmanstätten α + β colony structures, and stress relieving (HT3 = 600 °C for 4 h) to decrease the undesirable residual stresses due to the LPBF process, as well as a decomposition of the martensitic α′ to α-phase [59,60]. The heat treatment process routes are presented in Figure 1c. The powder morphology was investigated employing the scanning electron microscope (SEM) Zeiss Ultra Plus (Carl Zeiss AG, Oberkochen, Germany). The powder consists of mainly spherical particles with a few agglomerations on bigger particles, see Figure 1b. Microstructural investigations were accomplished with the SEM equipped with an electron backscatter diffraction (EBSD) unit to detect phases and corresponding grain orientations. EBSD data was post-processed using the MATLAB-based (Version R2019a 9.6, The MathWorks, Inc., Natick, MA, USA) toolbox MTEX (Version 5.6.0) [61]. MTEX is a free available toolbox for analyzing and modelling crystallographic textures. Microscopic observations and classification of the fractured surfaces for quasi-static and fatigue tests were also carried out using SEM. Microstructural study of samples on nanoscale was undertaken by transmission electron microscopy (TEM). For TEM, thin-slice samples (≈ 400 µm) were cut by Struers Sectom-5 (Struers GmbH, Willich, Germany) and further polished to a thickness of ≈ 100 µm. At last, 3 mm diameter circular disc samples were punched from the thin samples. Twin jet electropolishing of the thin foils was performed with the Struers Tenupol-5 (Struers GmbH, Willich, Germany) using an electrolyte containing perchloric acid (60 mL), butanol (340 mL), and methanol (600 mL). Electropolishing was executed at a voltage of 21 V, a current of 35 mA, and a temperature of −22 °C. TEM investigations were executed using a cold field emission gun equipped with JEOL JEM-ARM 200F (JOEL Ltd., Tokyo, Japan). TEM, high-resolution TEM (HRTEM), and high-angle annular dark-field scanning transmission electron microscopy (HAADF-STEM) images were taken. Energy dispersive spectroscopy (EDS) was performed during HAADF-STEM imaging. EDS maps were collected with a 30 nm step size with 10 s dwell time per step. The crystalline phase composition of Ti-6Al-7Nb was characterized through X-ray diffraction (XRD; D8 Advance, Bruker, Madison, WI, USA) using a Cu-Kα radiation source (λ = 0.154187 nm) operating at a current of 40 mA and a voltage of 35 kV. The as-built and heat-treated Ti-6Al-7Nb parts were measured in θ-θ geometry within a scanning range from $2\theta = 30°$ to $2\theta = 90°$ applying a step width of 0.035° and an exposure time of 1.5 s per step. All tests for mechanical characterization were performed at an ambient temperature. Tensile specimens were built according to Figure 1d. The loading direction was parallel to the building direction (BD) of the samples.

Metals **2022**, *12*, 122

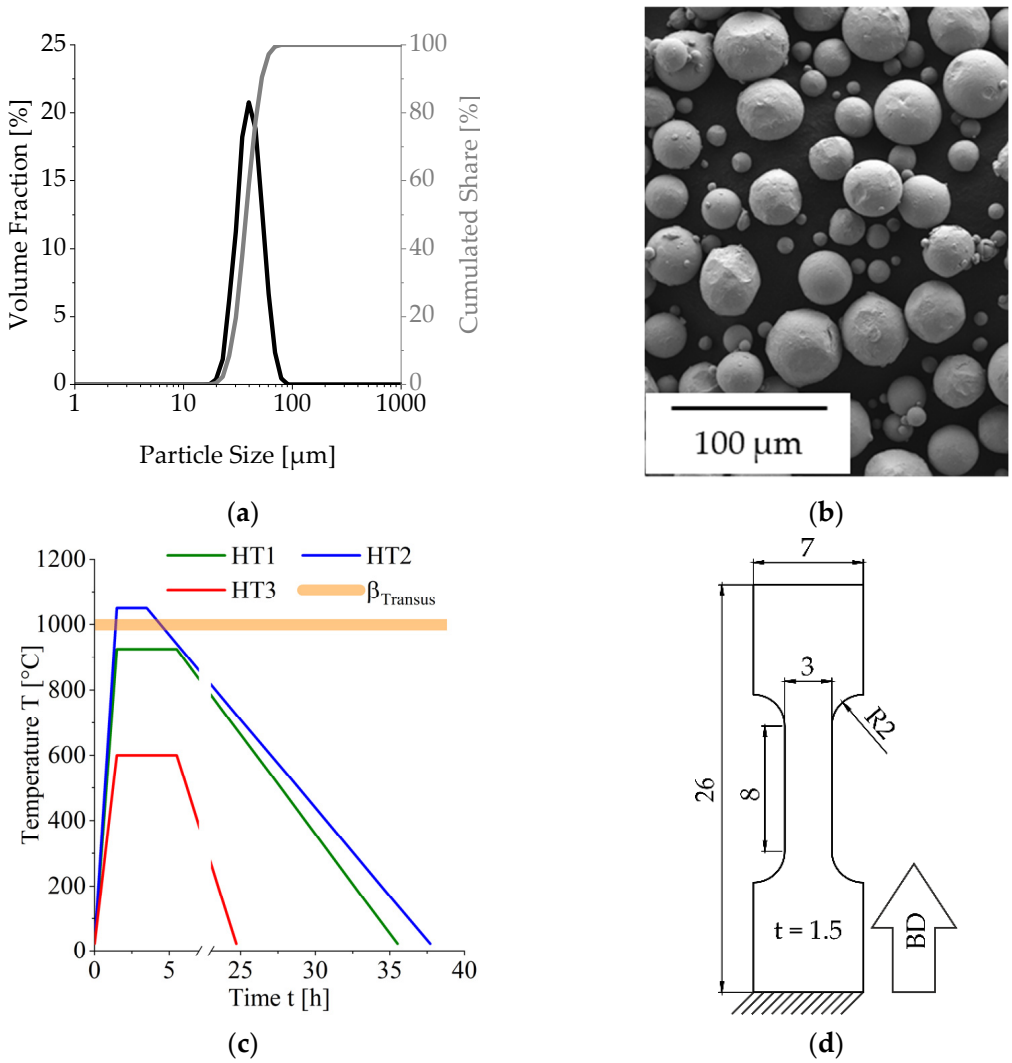

Figure 1. (**a**) Particle size distribution of Ti-6Al-7Nb; (**b**) powder morphology (SEM image); (**c**) schematic overview of the different heat treatments conducted—recrystallization annealing (HT1), β annealing (HT2), and stress relieving (HT3), as well as the $\beta_{transus}$ temperature for the alloy; (**d**) geometry and building direction (BD) of tensile and fatigue specimens.

All tensile specimens were blasted with high-grade Al_2O_3. The blasting material corresponded to a particle size of 70 µm–250 µm, used at 4 bar air pressure with a SMG 25 DUO (MHG Strahlanlagen GmbH, Düsseldorf, Germany). The tensile and LCF tests were performed utilizing a servo-hydraulic test-rig MTS 858 table-top system (MTS Systems Corporation, Eden Prairie, MN, USA) equipped with a 20 kN load cell and an extensometer 632.29F-30 (MTS Systems Corporation, Eden Prairie, MN, USA). The tensile test procedure corresponded to a displacement-controlled execution with a crosshead speed of1.5 mm min^{-1}, according to DIN EN ISO 6892-1. The LCF tests were strain-controlled, at total strain amplitudes ε_A of 0.35%, 0.5%, and 0.8%, with a R-ratio of −1 (compression–tensile fatigue), and a strain rate of 6×10^{-3} s^{-1}. At least three specimens per condition were tested with both monotonic and cyclic tests for each strain amplitude. The monotonic material properties, such as Young's moduli E, tensile yield strengths $R_{p0,2}$, ultimate tensile strengths R_m, and plastic elongations A, were obtained from the static tensile test. The determination

of the fatigue material constants requires the performance of several fatigue tests under cyclic loading and a R-ratio of −1. Cyclically loaded materials often have unstable and changing stress amplitude during the test, due to cyclic hardening or softening. Therefore, the stress amplitude for the stabilized state must be used, which occurs at the half number of cycles to fracture. The plastic strain amplitude can either be calculated with the stress amplitude, the Young´s modulus and the total strain amplitude (see Equation (4)), or by measuring the thickness of the recorded stable hysteresis loop recorded during the fatigue tests [62–65]. For evaluation of the total stress amplitude, σ_a, from the S–N curves, the Basquin relation is suitable, as follows:

$$\frac{\Delta\sigma}{2} = \sigma_a = \sigma'_f \cdot (2N_f)^b. \quad (1)$$

In Equation (1), σ'_f delineates the fatigue strength coefficient and b is the fatigue strength exponent. This equation fits the high-stress and low-stress fatigues [66]. For a better description of the high-stress fatigue region, the dependence between the number of reversals to failure $2N_f$ and the plastic strain amplitude $\Delta\varepsilon_p/2$, also called the Coffin–Manson relation, is used to describe the total fatigue life, as follows:

$$\frac{\Delta\varepsilon_p}{2} = \varepsilon'_f \cdot (2N_f)^c, \quad (2)$$

with the fatigue ductility coefficient, ε'_f, and the fatigue ductility exponent, c [66–68]. The total strain amplitude, $\Delta\varepsilon_A/2$, can be divided into two components, the plastic strain amplitude, $\Delta\varepsilon_p/2$, and the elastic strain amplitude, $\Delta\varepsilon_e/2$. The total strain amplitude, $\Delta\varepsilon/2$, of fatigue life curves is described as the sum of elastic and plastic strain amplitude, as follows, by Suresh [69]:

$$\frac{\Delta\varepsilon_A}{2} = \frac{\Delta\varepsilon_e}{2} + \frac{\Delta\varepsilon_p}{2}. \quad (3)$$

$\Delta\varepsilon_e/2$ is described by Hooke´s law as the quotient of σ_a to the Young′s modulus E as follows:

$$\frac{\Delta\varepsilon_e}{2} = \frac{\Delta\sigma}{2E} = \cdot \frac{\sigma_a}{E}. \quad (4)$$

Together with the modified Basquin equation and the Coffin–Manson relation, combining Equations (1)–(4), one obtains the following:

$$\varepsilon_A = \frac{\sigma'_f}{E} \cdot (2N_f)^b + \varepsilon'_f \cdot (2N_f)^c. \quad (5)$$

The first and second terms on the right-hand side of Equation (5) are the elastic ε_e and plastic ε_p components, respectively, of the total strain amplitude ε_A. Equation (5) can be used as the basis for the strain life approach to fatigue design. For determination of the fatigue life, a schematic illustration of the as-built condition is presented in Figure 2. The intersection of the curves for ε_e and ε_p describes the transition point, where the plastic and elastic strains are identical. From this point, the LCF life is governed more by elastic than plastic strain. For the as-built condition this point is around 110 cycles, see Figure 2. According to the Coffin–Manson–Basquin approximation, one is able to predict the fatigue life depending on the applied strain amplitude for the different conditions [66–68,70].

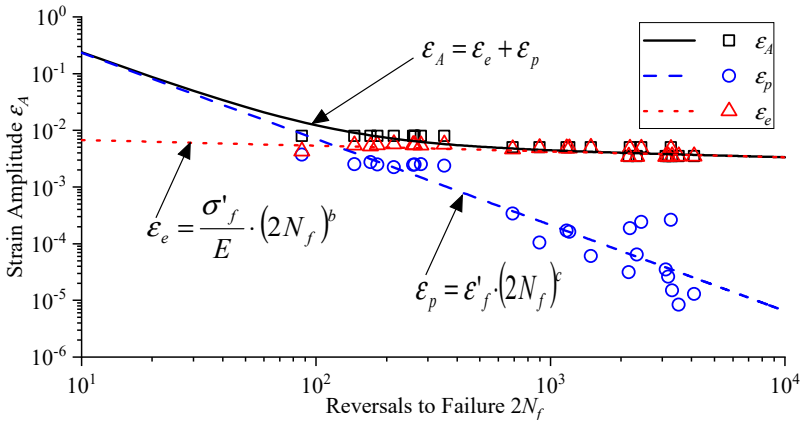

Figure 2. Example of the Coffin–Manson–Basquin curve according to Equation (5) for the as-built condition.

2.2. Biocompatibility Investigations

Two different surface conditions were analyzed to determine the optimum surface roughness for biocompatibility. On the one hand, the as-received surface was investigated without any post-treatment (NT). On the other hand, the surface was post-treated utilizing blasting with high-grade Al_2O_3 (ab). Blasting lead to rougher surfaces and to an increased surface area, resulting in faster osseointegration and higher survival rates for moderately rough implant surfaces: this was demonstrated by clinical studies [71–75]. The surface roughness was measured with an optical 3D macroscope VR-3100 (KEYENCE GmbH, Neu-Isenburg, Germany). The arithmetical mean roughness, Ra, and average roughness, Rz, were determined on the surfaces of the untreated and blasted specimens. A total of 5 specimens per condition were measured with 5 line measurements (length ≈ 6.8 mm) per side.

2.2.1. Cytocompatibility Testing

Biocompatibility studies were performed with different cell types. Therefore, murine fibroblasts (L-929; CLS Cell Lines Service, Eppelheim, Germany), human osteosarcoma cells (HOS 87070202; European Collection of Authenticated Cell Cultures, Merck, Germany), and human umbilical vein endothelial cells (HUVEC; Promocell, Heidelberg, Germany) were used. L-929 cells were grown and passaged in RPMI-1640 medium (Biochrom GmbH, Berlin, Germany), while HOS cells were grown and passaged in Eagle's MEM (EMEM)/Hanks' (Carl Roth GmbH + Co. KG, Karlsruhe, Germany). Both media were supplemented with fetal calf serum (FCS) superior (10%, Biochrom GmbH, Berlin, Germany) and penicillin/streptomycin (1%, Biochrom GmbH, Berlin, Germany). The EMEM/Hanks´ medium was also supplemented with non-essential amino acids (1%, Biochrom GmbH, Berlin, Germany) and L-glutamine (2 mmol, Biochrom GmbH, Berlin, Germany). HUVEC cells were grown and passaged in an endothelial cell grown medium kit (Promocell, Heidelberg, Germany) and were supplemented with penicillin/streptomycin (1%). All cell lines were grown and passaged in cell culture flasks or multi-well plates (Greiner Bio-One, Frickenhausen, Germany). For passaging, a trypsin (0.05%)/ethylene-diamine-tetraacetic (0.02%) acid solution (Biochrom GmbH, Berlin, Germany) was used. The cells were plated with a density of 50,000 cells per well in 24-well culture plates. After hot air sterilization of the test samples, the cells were seeded on the top of the samples (≈5 × 5 mm^2), which were embedded in agarose (2%, Agarose NEEO, Carl Roth GmbH + Co. KG, Karlsruhe, Germany) in respective culture mediums. After 72 h incubation (in a humidified atmosphere at 37 °C and 5% CO_2), cell proliferation was determined. Therefore, a crystal violet staining (CV) assay was performed [76]. After 72 h, the cells were fixed with glutaraldehyde (2%, Sigma-Aldrich, Merck KGaA, Darmstadt, Germany) in phosphate-buffered saline (PBS)

for 20 min. Subsequently, the supernatant was removed, and the cells were stained with CV (0.1%, Carl Roth GmbH + Co. KG, Karlsruhe, Germany) in deionized water. After 30 min, the pigment was removed, and the samples were removed from the agarose. After washing with deionized water, the test samples were air-dried. For 1 h, Triton X-100 (2%, Sigma-Aldrich, Merck KGaA, Darmstadt, Germany) in deionized water was added, so that CV was dissolved from the cells. Finally, the supernatant was transferred in a 96-well microtiter plate and the absorbance was determined at 570 nm using a 96-well microplate reader (MRX microplate reader, Dynatech Laboratories, Denkendorf, Germany). The experiments were carried out six times. Furthermore, the supernatant of L-929 and HOS was analyzed of the cytokine Il-6 expression (R&D Systems DuoSet, R&D Systems Inc., Minneapolis, MN, USA).

2.2.2. Antibacterial Examinations

To analyze the bacterial behavior on test samples, two different samples were used—*Escherichia coli* (ATCC 25922) and *Staphylococcus aureus* (ATCC 25923). The bacteria were cultivated on Columbia agar plates with sheep blood (7%, Fisher Scientific GmbH, Schwerte, Germany) for 24 h. The test samples were also embedded in agarose (2%, Agarose LM, Gerbu Biotechnik GmbH, Gailberg, Germany). Bacteria (10^{-6} CFU ml^{-1}) were seeded on the test samples. After 48 h of incubation at 37 °C, cell proliferation was analyzed, similarly to the cell proliferation, with a CV assay. The experiment was performed in four biological replicates.

3. Results and Discussion

3.1. Microstructure and Nanostructure of as-Built and Heat-Treated Ti-6Al-7Nb

The microstructure of (α + β) titanium strongly depends on the cooling rates and the quenching parameters, from the β-phase field at higher temperatures and the following heat treatment, respectively [77,78]. Figure 3 shows EBSD maps of the Ti-6Al-7Nb alloy after additive manufacturing and subsequent heat treatments. The EBSD map of the additively processed Ti-6Al-7Nb shows a very fine, acicular microstructure, see Figure 3a,c. The fine-lamellar α′ grain structures are strongly oriented inside the prior β grains. The size of these fine needles decreased with an increased cooling rate during solidification [37,79,80]. Figure 3b shows the reconstructed parent β grains using MTEX software. During solidification, the bcc β-phase preferentially grows in the <100> direction; therefore, the elongated, columnar primary β grains evolve parallel to the BD [81–83]. The resulting anisotropy and primary β grains affect the mechanical properties of the specimens [84]. Due to the fast cooling and passing the $\beta_{Transus}$ temperature, these β grains transform to α′-phase, according to the Burgers relation, in 12 possible transformation variants [81,85–87]. Due to the high cooling rate, the probability of α′ formation is very high [37,88,89]. The rapid cooling leads to a martensitic transformation and a limitation of diffusional transformation [90]. Figure 3c shows the cross-section perpendicular to the BD. Areas with similar crystallographic orientations are observable inside the grain boundaries of the probable parent β grains. Figure 3d demonstrates the microstructure for post-treatment HT1. An unexpected, coarse lamella-like microstructures evolved instead of equiaxed grains [60]. The microstructure is dependent on the initial microstructure and dislocations before the heat treatment. HT2 results in a coarse microstructure and huge grains due to temperatures above $\beta_{Transus}$ and grain growth. The grain orientation seems random, see Figure 3e. Figure 3f exhibits the microstructure after stress relief treatment (HT3). Only minor changes in the microstructure occurred compared with the as-built condition. Areas with similar grain orientation are present and the prior β grain boundaries are noticeable. The detected phase distribution of α, α′, and β titanium, respectively, is summarized in Table 1.

Metals **2022**, *12*, 122 8 of 19

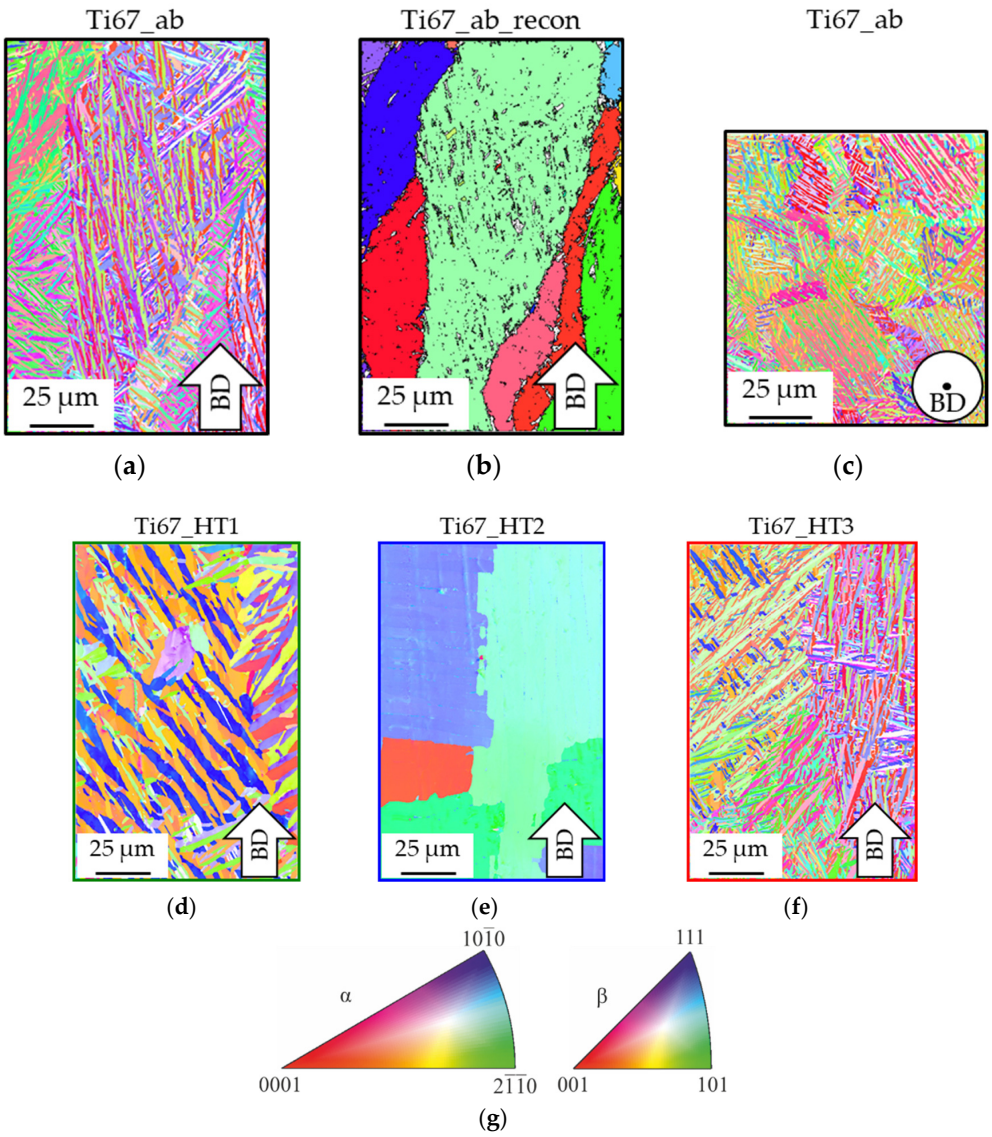

Figure 3. (**a**) Inverse pole figure (IPF) of as-built Ti-6Al-7Nb; (**b**) β parent grain reconstruction of (**a**); IPF of as-built (top view) (**c**); HT1 (**d**); HT2 (**e**); and HT3 (**f**) Ti-6Al-7Nb; and (**g**) color legend for inverse pole figure.

Figure 4 summarizes the TEM images, the HRTEM images, and the fast Fourier transformation (FFT) pattern of the as-built sample. The α' martensite laths are visible in Figure 4a. The width of the lath (dark contrast in Figure 4a) is 280 nm. Figure 4b is the FFT pattern from the white circular area in Figure 4a. Figure 4c is the FFT pattern from the yellow circular area in Figure 4b. The diffraction pattern confirms the hexagonal crystal structure of α' martensite in both laths. In addition, an HRTEM image of the interface between two laths (black square region in Figure 4a) is presented in Figure 4d. The red line highlights the interface between the two α' martensite laths. Figure 4e is the magnified HRTEM image of the black square region in Figure 4d. The $(0\bar{1}11)$ plane of one lath intersects the $(\bar{1}010)$ plane of another lath at 45°. Furthermore, Figure 4f shows the HAADF-STEM image and Figure 4g the EDS maps of the as-built sample. Here, laths of

α′ martensite are apparent. The EDS maps of the black square region in Figure 4g show that no segregation of alloying elements is observable, and the titanium, aluminum, and niobium distribution is homogenous in the laths.

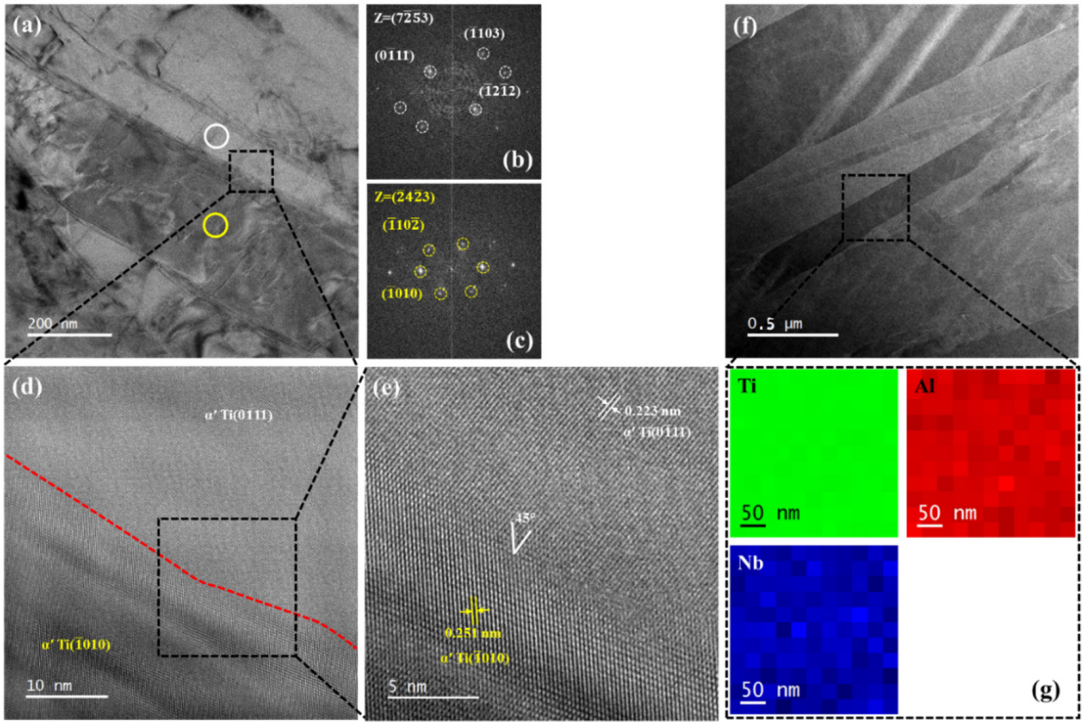

Figure 4. (**a**) TEM image of the as-built sample; (**b**,**c**) FFT pattern taken from the white and yellow circular areas in (**a**); (**d**) HRTEM image of the black square region in (**a**), the red line shows the boundary between two α′-martensite laths; (**e**) HRTEM image of the black square region in (**d**); (**f**) HAADF-STEM image of the as-built sample; (**g**) EDS maps of the black square region in (**f**).

Figure 5 shows the TEM images, HRTEM images, and diffraction pattern of the HT3 sample. The α laths are apparent in Figure 5a. In Figure 5a, some α laths are relatively coarse (≈170 nm). However, the α laths are relatively fine (≈ 40 nm). In this context, Figure 5b shows an HRTEM image taken from the region within the black square in Figure 5a. The lattice plane of two α laths is identified as $(\bar{1}010)$. The red lines point out the boundary between two α laths. For a deeper insight, Figure 5d is the magnified view of the black square region in Figure 5b. The interplanar spacing of the $(\bar{1}010)$ planes are measured as ≈ 0.252 nm. However, the two $(\bar{1}010)$ planes are misoriented by 18°. The diffraction pattern in Figure 5c confirms the zone axis to be $(\bar{1}2\bar{1}1)$. Again, the diffraction pattern shows the $(\bar{1}010)$ planes to be misoriented by 18°. Figure 5e shows the HAADF-STEM image and EDS maps of the stress relief treated sample, where α laths are visible. Finally, Figure 5f is the EDS maps of a triple junction between three α laths from the black square region in Figure 5e. An enrichment of niobium and a depletion of aluminum is observed at the triple junction. The α lath boundary regions are enriched in niobium and depleted in aluminum. This leads to the white contrast in the HAADF-STEM image in Figure 5e.

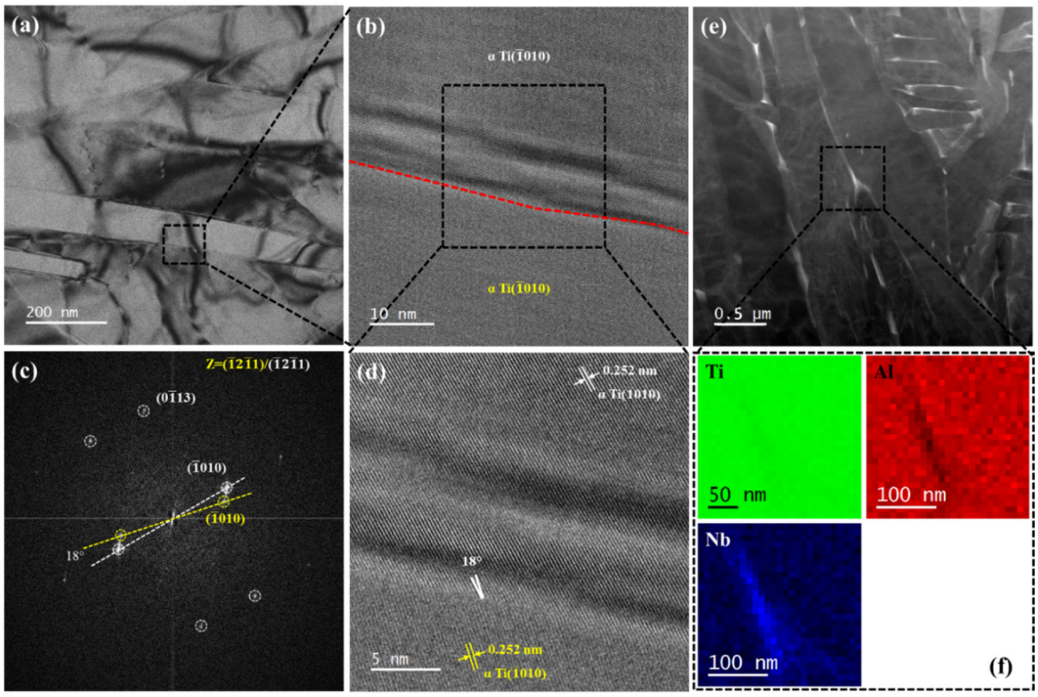

Figure 5. (**a**) TEM image of the HT3 sample; (**b**) HRTEM image from the black square area in (**a**), the red line indicates the boundary between two α-laths; (**c**) FFT pattern from the black square area in (**b**); (**d**) HRTEM image from the black square in (**b**); (**e**) HAADF-STEM image of the HT3 sample; (**f**) EDS maps of black square region in (**e**).

Figure 6 shows XRD patterns for the as-built and heat-treated Ti-6Al-7Nb samples. The XRD pattern of the sample in the as-built condition is characteristic for the hexagonal close-packed (hcp) α'/α structure of titanium alloys. Due to the hexagonal structure of both the α' and α phases with similar lattice parameters, a separation or distinction between both phases based on XRD is not possible [59]. Since additively manufactured alloys are characterized by high local cooling rates, the α' martensitic phase is assumed as dominating component, based on the findings of Xu et al. [52]. Stress relief heat treatment at 600 °C does not lead to any significant microstructural changes in the sample HT3, since the $\alpha' \rightarrow \alpha + \beta$ transformation is known to start at higher temperatures (≈760 °C) [59]. As shown for sample HT1, recrystallization annealing at 925 °C leads to the formation of the bcc β-structure of Ti and probably to a decomposition of α' to α. HT2 treatment was carried out above the $\beta_{Transus}$ temperature and did result in decomposition of the as-fabricated α'/α-phase [59]. Therefore, the β-phase is formed in the HT2 treated specimens. This is in good agreement with reported transformations and temperatures between 735 °C and 1050 °C for the $\alpha \rightarrow \beta$ reaction [59]. Post-treatment HT1 and HT2 lead to a decrease in the α'/α-Ti peak width, indicating grain growth. For the samples HT1 and HT2 additional peaks were observed between 2θ = 42–45°. Due to the large width of the peaks, several similar phases with small differences in stoichiometry are most likely. As reported by Bolzoni et al., titanium and aluminum can form binary phases, e.g., titanium aluminates, above 660 °C due to diffusion processes [91]. Therefore, the formation of small fractions of Ti_3Al, TiAl, and/or $TiAl_3$ is concluded for the heat treatments HT1 and HT2.

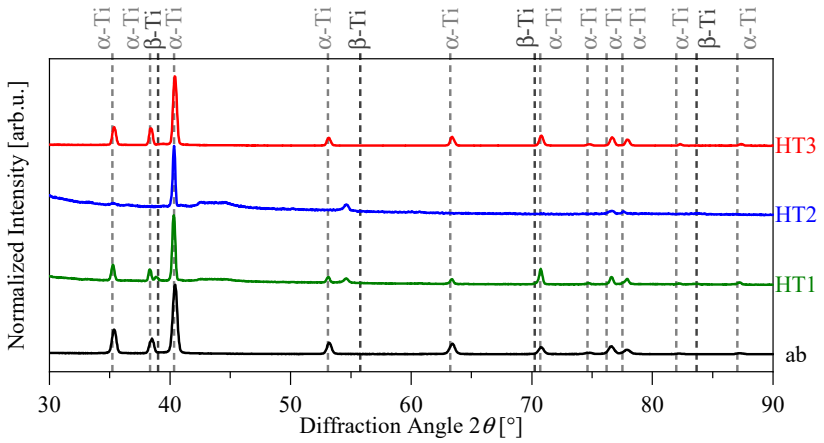

Figure 6. XRD patterns of as-built and heat-treated Ti-6Al-7Nb samples.

Table 1. Phase fraction detected by means of EBSD and results of quasi-static and fatigue tests of the LPBF fabricated, as-built, and heat-treated Ti-6Al-7Nb, including the minimum values regarding standard ISO 5832-11 [92].

State	Condition	α Phase	β Phase	$R_{p0.2}$ [MPa]	R_m [MPa]	E [GPa]	A [%]	σ'_f	b	ε'_f	c
ab	as-built	97.0%	3.0%	940 ± 14	1109 ± 3	105 ± 3	14.4 ± 0.9	89.7	−0.102	765.04	−1.518
HT1	925 °C/4 h	98.3%	1.7%	870 ± 11	934 ± 7	108 ± 6	8.8 ± 2.3	49.9	−0.027	191.97	−1.166
HT2	1050 °C/2 h	97.8%	2.2%	718 ± 4	791 ± 6	115 ± 3	12.0 ± 1.1	52.2	−0.036	10.103	−0.719
HT3	600 °C/4 h	97.7%	2.3%	1045 ± 9	1110 ± 10	116 ± 2	12.5 ± 0.9	100.7	−0.097	139.84	−1.167
ISO	–	–	–	800	900	–	10	–	–	–	–

3.2. Mechanical Properties of Ti-6Al-7Nb

Figure 7 displays the results for different mechanical properties of the monotonic tensile tests with images of fracture surfaces. The stress–strain curves for the monotonic test are presented in Figure 7a. For the different conditions, the mean values of Young´s moduli, E, tensile yield strengths, $R_{p0,2}$, ultimate tensile strengths, R_m, and plastic elongations, A, are compared to the international standard for implants for surgery ISO 5832-11 in Figure 7c and Table 1 [92]. The martensitic structure of the additively processed (α + β) titanium leads to high values for the mechanical properties regarding ultimate tensile and yield strength compared with wrought and conventionally processed materials, especially with an α-dominant equiaxed microstructure [7]. The different material behavior might be explained by the different microstructures and phase composition, which have a strong impact on the mechanical properties. Typically, in conventional material, the size and morphology of the α grains determine the mechanical properties, while in LPBF the colony size and the size of the α or rather α′ laths control the properties. Plastic deformation tends to be the movement of dislocations. Conventional material with larger α grains enables the deformation with less dislocation pileups, whereas the smaller grains in the additively processed material increase the dislocation pileups [93]. The tensile properties are, inter alia, caused by the higher residual stresses, the martensitic transformation during fast cooling to the α′ instead of the α phase, and grain refinement as a strengthening mechanism described by the Hall–Petch equation [94]. The Young´s moduli vary within a certain range between 105 GPa–116 GPa. Due to heat treatments and microstructural changes, the average grain size increases. Sliding effects are mainly detected between grains; therefore, the breaking elongation should increase [95]. Another reason for changes in breaking elongation is the presence of β titanium. An increased amount of bcc β titanium should improve the ductile behavior [57,95]. EBSD phase analysis showed the highest fraction of β titanium for as-built conditions (3.0%), the lowest fraction for HT1 (1.7%), and between for HT2 (2.2%)

and HT3 (2.3%), in accordance to the breaking elongation, see Figure 7c. According to the XRD analysis only for HT1 and HT2 β titanium is verified and may, therefore, explain the lower tensile strength for these conditions but not the reduced breaking elongations.

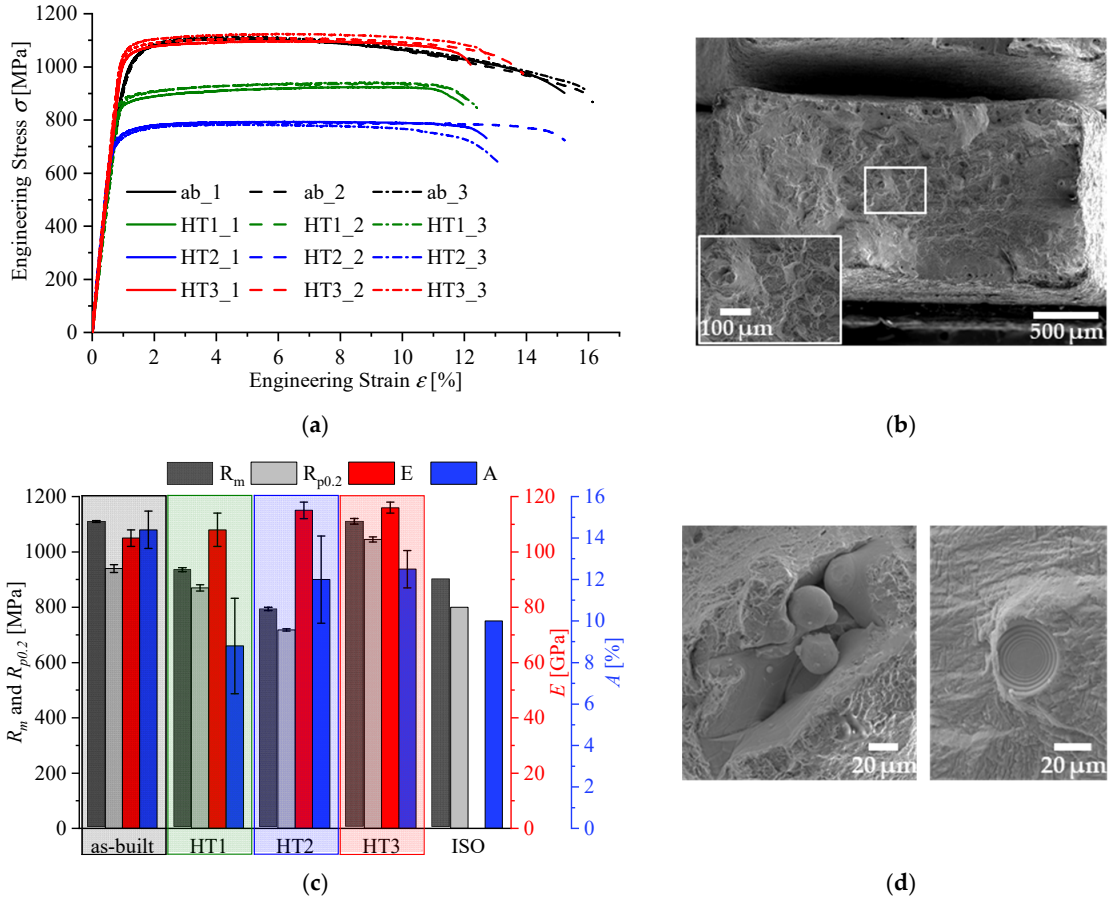

Figure 7. (**a**) Stress–strain curves of the as-built and heat-treated samples; (**b**) SEM images of the tensile fracture surface of an as-built Ti-6Al-7Nb specimen; (**c**) mechanical properties of the different conditions including minimum values for Ti-6Al-7Nb according to ISO 5832-11 (ISO) [92]; (**d**) SEM images of a characteristic LPBF defects, lack of fusion with unmelted powder particles (left) and gas pore (right), on a tensile fracture surface of an as-built Ti-6Al-7Nb specimen.

The ε_A-N_f plots for the different conditions are approximated with the Coffin–Manson–Basquin relation based on the elastic and plastic strain superposition explained in Figure 2. The results are depicted in Figure 8a. The approximations represent the relation between the total strain ε_A and the fatigue life N_f of Ti-6Al-7Nb alloy in different conditions. The Coffin–Manson–Basquin fatigue life approximation are determined as follows:

$$\varepsilon_{A,\,as-built} = 765.04 \cdot (2N_f)^{-1.518} + 0.8545 \cdot (2N_f)^{-0.102}; \quad (6)$$

$$\varepsilon_{A,HT1} = 191.97 \cdot (2N_f)^{-1.166} + 0.4616 \cdot (2N_f)^{-0.027}; \quad (7)$$

$$\varepsilon_{A,\,HT2} = 10.103 \cdot (2N_f)^{-0.719} + 0.4535 \cdot (2N_f)^{-0.036}; \quad (8)$$

$$\varepsilon_{A,\,HT3} = 139.84 \cdot (2N_f)^{-1.167} + 0.8677 \cdot (2N_f)^{-0.097}. \quad (9)$$

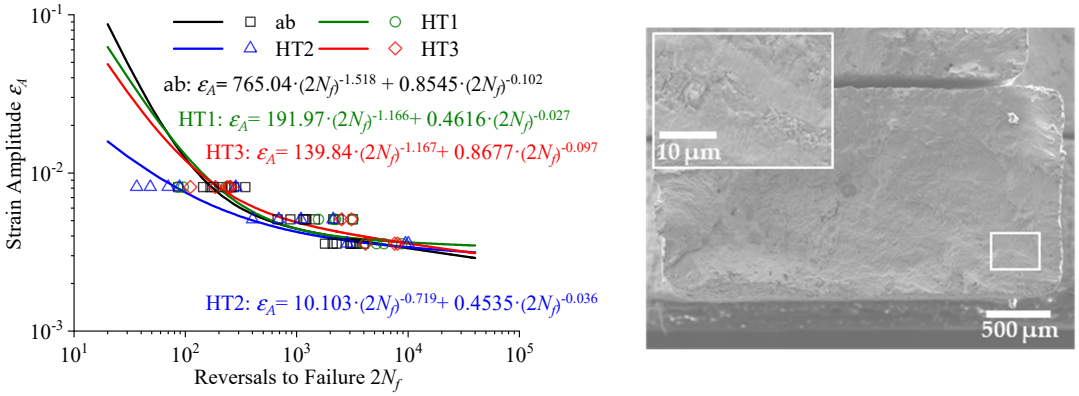

Figure 8. (**a**) Coffin–Manson–Basquin plots for Ti-6Al-7Nb samples in as-built, HT1, HT2, and HT3 conditions; (**b**) SEM images of a fracture surface of an as-built Ti-6Al-7Nb fatigue specimens, with fatigue striations, probably oriented perpendicular to the crack growth direction.

Figure 8a depicts the fatigue life of the different conditions. The fatigue performance for higher strain amplitudes ($2N_f < 10^2$ reversals) of the as-built condition is better, compared with the HT1, HT2, and HT3 conditions. The fatigue performance in LCF range is connected to the monotonic tensile performance in terms of tensile strength. Higher strengths tend to lead to higher, tolerable strain amplitudes and higher fatigue life. Fatigue strength is generally high as higher monotonic strength hinders microplasticity and eventually local damage [42]. The curves of the as-built HT1 and HT3 conditions intersect around 10^2 cycles and are comparable up to 10^4 cycles. While the performance for higher strain amplitudes ($2N_f < 10^4$ reversals) for the HT2 condition is the worst, the performance gets better for lower strain amplitudes. As the process-induced pores and defects are not affected by these post-treatments, other causes are likely to be decisive, such as the microstructures or residual stresses. For post treatment HT2 the reduced strength and the microstructural notches could lead to accumulation of local damage and finally results in early crack initiation [42]. The fatigue crack growth behavior of post-treated Ti-6Al-7Nb is affected by the microstructure. Depending on the crack growth direction and grain long axis different crack growth rates are probable [96–98]. For lower strain amplitudes, the three heat-treated conditions show superior fatigue behavior compared with the as-built conditions, attributed to the reduced residual stresses and microstructural features [52,56–59,94]. Corresponding to the fatigue ductility exponent c, the heat-treated specimens show smaller gradients, while the as-built condition has the lowest value resulting in the shortest fatigue life. HT1 and HT3 exhibit close fatigue ductility exponent c and, therefore, are probably favorable for HCF applications.

In general, due to miniaturization of samples the fatigue and monotonic tensile behavior could be affected [42]. The monotonic material properties, such as Young´s moduli E, tensile yield strengths $R_{p0,2}$, ultimate tensile strengths Rm, plastic elongations A, the fatigue parameters—such as fatigue strength coefficients σ'_f and exponents b—and fatigue ductility coefficients ε'_f and exponents c, of the Coffin–Manson–Basquin equation, are given in Table 1.

3.3. Fracture Behavior

The fracture surface of the as-built Ti-6Al-7Nb alloy demonstrates mainly ductile fracture behavior, see Figure 7b. The propensity of cleavage fracture decreases with decreasing grain size. Therefore, the fracture surface of the additively processed materials shows cleavage facets with high amounts of dimples at the grain boundaries [58]. These fractured surfaces show small, shallow dimples on quasi-cleavage fracture surfaces, and transgran-

ular facets, confirming the minor brittle fracture behavior of the additively processed specimens. Features, as a result of the LPBF fabrication, such as pores, unmelted powder particles, and defects occur on fracture surfaces in as-built and heat-treated conditions, see Figure 7d. These build defects typically are perpendicular to the build direction and pulled apart by the tensile load during monotonic and fatigue tests [99,100]. The fracture surfaces of fatigue tests tend to be smoother for lower strain amplitudes. Distinct fatigue striations, perpendicular to the crack growth direction, can be detected for all conditions and strain amplitudes, see Figure 8b. The striations are close to the probable crack initiation spot. Typical forced rupture areas are difficult to spot.

3.4. Characterization of Roughness, Cytocompatibility, and Antibacterial Effects

The roughness of the specimens without surface treatment (NT) exhibits values for Ra of 7.5 ± 0.3 µm and Rz of 49.6 ± 2.2 µm. Due to unmelted powder particles and the surface of the layer-wise fabrication, the roughness of NT specimens is higher than for the blasted specimens (ab) with Ra of 4.8 ± 0.2 µm and Rz of 34.3 ± 1.2 µm, which have smoother surfaces, on account of the mechanically post-processed treatment.

There was no effect of cell proliferation of the two examined samples on murine L-929 cells and human HUVEC cells. A slight tendency of diminished cell proliferation was observed in human HOS cells on blasted Ti-6Al-7Nb. Thus, the examined samples show a proper biocompatibility behavior for the different cell lines, used in the present study, see Figure 9. Furthermore, no increase in cytokine release of Il-6 was detected (data not shown). Concerning antibacterial effects, *E. coli* proliferation was not influenced by the different samples, while the proliferation of *S. aureus* was reduced by the blasted surface of Ti-6Al-7Nb, see Figure 9.

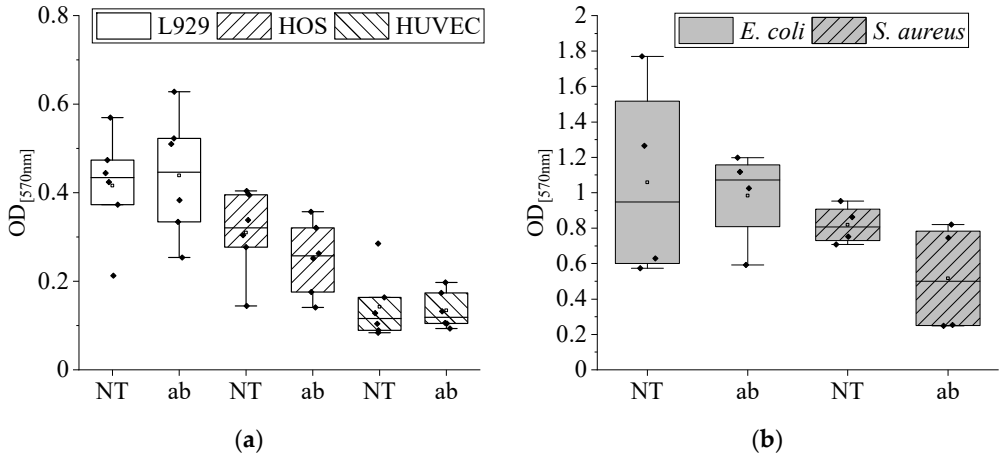

Figure 9. (**a**) Effects of different surfaces on the proliferation of L929, HOS and HUVEC cells after 72 h incubation, and (**b**) bacterial proliferation of *E. coli* and *S. aureus* after 24 h incubation; OD = optical density at 570 nm; n = 4–6.

As described by Schweikl et al., blasting with Al_2O_3 particles led to incorporation of Al into the outer surface layers [101]. Therefore, the increased concentration of Al on the specimens' surfaces could result in decreasing the proliferation behavior of HOS cells and *S. aureus* [102–104]. Rough sandblasted surfaces with sharp ridges and edges could influence the proliferation and it seems to appear that the quality of cell contact on rough surfaces is related to the minimum width of the cavity [101]. As reported in various studies, blasting leads to the presence of severely plastic deformed layers and, therefore, to strain-hardening, as well as to compressive residual stresses [105–107]. Due to the antibacterial effect regarding the proliferation of *S. aureus* and because of probably

better fatigue properties of blasted specimens, the specimens for the mechanical tests were blasted with Al_2O_3 particles.

4. Conclusions

The microstructure and the monotonic and fatigue behaviors of additively processed Ti-6Al-7Nb were investigated. Different surface conditions were examined regarding biocompatible properties, such as cytocompatibility and antibacterial effects. The following conclusions can be drawn from these investigations:

- Ti-6Al-7Nb shows significantly different microstructures in the as-built, stress-relieved, recrystallized, and β-annealed conditions. While the α'/α structure is dominant within the as-built state, the formation and precipitation of the β-phase are manageable by a vacuum heat treatment above 925 °C as analyzed using XRD and EBSD.
- There are significant differences in the monotonic tensile properties of the various conditions. Concerning the ISO values, the as-built and stress-relieved conditions (HT3) are favorable. Tensile and yield strength, as well as breaking elongation, are higher than the demanded values, but the specimens' dimensions have to be considered. HT1 and HT2 do not fulfill the requirements, probably due to the present β-phase. Heat treatments, such as HT1 and HT2, can significantly affect the microstructure and may tend to soften the lattice structures and decrease the residual stresses and, therefore, lead to significantly reduced tensile strength.
- LCF life is higher for lower strain amplitudes in the heat-treated specimens than in as-built conditions, which can be attributed to decreased residual stresses as well as to microstructural differences. HT2 shows the highest fatigue life for lower strain amplitudes, while the as-built condition has higher service life for higher strain amplitudes. Regarding overall performance, quasi-static results, and LCF performance, stress relief treatment (HT3) is favorable. The material behavior for HCF loading still has to be determined.
- Transgranular facets characterize the fracture surface of the additively processed Ti-6Al-7Nb, confirming the ductile behavior. Small, shallow dimples on quasi-cleavage fracture surfaces are visible. Fatigue fracture surfaces are characterized by fatigue striations and remaining forced rupture surfaces. Defects may have less impact on quasi-static but a high impact on fatigue behavior.
- Both surfaces, the untreated and the blasted, show good biocompatibility in different cell types (fibroblasts, osteosarcoma cells, and endothelial cells). Only a slight antiproliferative effect was observed for blasted Ti-6Al-7Nb in osteoblasts. An increase in cytokine release of Il-6 was not observed.
- Blasting with high-grade Al_2O_3 is preferable regarding biocompatibility and antibacterial effects. Blasted Ti-6Al-7Nb exhibits an antibacterial effect against *S. aureus* in comparison with not post-treated Ti-6Al-7Nb. *E. coli* was able to grow on both surfaces of Ti-6Al-7Nb similarly. On account of remaining aluminum on the blasted surface, glass bead blasting could be taken into consideration.

Author Contributions: Conceptualization, M.H., K.-P.H. and M.S.; data curation, M.H.; formal analysis, M.H., K.-P.H. and M.S.; funding acquisition, K.-P.H., J.M., W.T. and M.S.; investigation, M.H., D.K., N.F.L.D., D.S., H.O., S.P. and J.M.; methodology, M.H., K.-P.H. and M.S.; project administration, M.H.; resources, J.M., W.T. and M.S.; software, M.H. and D.K.; supervision, K.-P.H., J.M., W.T. and M.S.; validation, M.H., K.-P.H. and M.S.; visualization, M.H.; writing—original draft preparation, M.H.; writing—review and editing, M.H., D.K., N.F.L.D., D.S., H.O., S.P., M.K., K.-P.H., J.M., W.T. and M.S. All authors have read and agreed to the published version of the manuscript.

Funding: This research was funded by the Deutsche Forschungsgemeinschaft (DFG), grant numbers SCHA 1484/45-1, ME 4991/2-1 and TI 343/167-1.

Data Availability Statement: The data that support the findings of this study are available from the corresponding author upon reasonable request.

Acknowledgments: The research was performed with the equipment and base of the LWK and DMRC research infrastructure. The authors are grateful to the staff members of the LWK and DMRC.

Conflicts of Interest: The authors declare no conflict of interest. The funders had no role in the design of the study; in the collection, analyses, or interpretation of data; in the writing of the manuscript, or in the decision to publish the results.

References

1. Abdel-Hady Gepreel, M.; Niinomi, M. Biocompatibility of Ti-alloys for long-term implantation. *J. Mech. Behav. Biomed. Mater.* **2013**, *20*, 407–415. [CrossRef] [PubMed]
2. Geetha, M.; Singh, A.K.; Asokamani, R.; Gogia, A.K. Ti based biomaterials, the ultimate choice for orthopaedic implants—A review. *Prog. Mater. Sci.* **2009**, *54*, 397–425. [CrossRef]
3. Long, M.; Rack, H. Titanium alloys in total joint replacement—A materials science perspective. *Biomaterials* **1998**, *19*, 1621–1639. [CrossRef]
4. Kurtz, S.M.; Ong, K.L.; Schmier, J.; Mowat, F.; Saleh, K.; Dybvik, E.; Kärrholm, J.; Garellick, G.; Havelin, L.I.; Furnes, O.; et al. Future clinical and economic impact of revision total hip and knee arthroplasty. *J. Bone Jt. Surg. Am.* **2007**, *89* (Suppl. S3), 144–151. [CrossRef]
5. Vandenbroucke, B.; Kruth, J.-P. Selective laser melting of biocompatible metals for rapid manufacturing of medical parts. *Rapid Prototyp. J.* **2007**, *13*, 196–203. [CrossRef]
6. Iijima, D. Wear properties of Ti and Ti–6Al–7Nb castings for dental prostheses. *Biomaterials* **2003**, *24*, 1519–1524. [CrossRef]
7. Niinomi, M. Mechanical biocompatibilities of titanium alloys for biomedical applications. *J. Mech. Behav. Biomed. Mater.* **2008**, *1*, 30–42. [CrossRef]
8. Hollander, D.A.; von Walter, M.; Wirtz, T.; Sellei, R.; Schmidt-Rohlfing, B.; Paar, O.; Erli, H.-J. Structural, mechanical and in vitro characterization of individually structured Ti-6Al-4V produced by direct laser forming. *Biomaterials* **2006**, *27*, 955–963. [CrossRef] [PubMed]
9. Murr, L.E.; Quinones, S.A.; Gaytan, S.M.; Lopez, M.I.; Rodela, A.; Martinez, E.Y.; Hernandez, D.H.; Martinez, E.; Medina, F.; Wicker, R.B. Microstructure and mechanical behavior of Ti-6Al-4V produced by rapid-layer manufacturing, for biomedical applications. *J. Mech. Behav. Biomed. Mater.* **2009**, *2*, 20–32. [CrossRef]
10. Kobayashi, E.; Wang, T.J.; Doi, H.; Yoneyama, T.; Hamanaka, H. Mechanical properties and corrosion resistance of Ti-6Al-7Nb alloy dental castings. *J. Mater. Sci. Mater. Med.* **1998**, *9*, 567–574. [CrossRef]
11. Kobayashi, E.; Mochizuki, H.; Doi, H.; Yoneyama, T.; Hanawa, T. Fatigue Life Prediction of Biomedical Titanium Alloys under Tensile/Torsional Stress. *Mater. Trans.* **2006**, *47*, 1826–1831. [CrossRef]
12. Srimaneepong, V.; Yoneyama, T.; Kobayashi, E.; Doi, H.; Hanawa, T. Comparative study on torsional strength, ductility and fracture characteristics of laser-welded alpha+beta Ti-6Al-7Nb alloy, CP Titanium and Co-Cr alloy dental castings. *Dent. Mater.* **2008**, *24*, 839–845. [CrossRef]
13. Liu, X.; Chu, P.; Ding, C. Surface modification of titanium, titanium alloys, and related materials for biomedical applications. *Mater. Sci. Eng. R Rep.* **2004**, *47*, 49–121. [CrossRef]
14. Kuroda, D.; Niinomi, M.; Morinaga, M.; Kato, Y.; Yashiro, T. Design and mechanical properties of new β type titanium alloys for implant materials. *Mater. Sci. Eng. A Struct. Mater.* **1998**, *243*, 244–249. [CrossRef]
15. Li, Y.; Yang, C.; Zhao, H.; Qu, S.; Li, X.; Li, Y. New Developments of Ti-Based Alloys for Biomedical Applications. *Materials* **2014**, *7*, 1709–1800. [CrossRef]
16. López, M.; Gutiérrez, A.; Jiménez, J. In vitro corrosion behaviour of titanium alloys without vanadium. *Electrochim. Acta* **2002**, *47*, 1359–1364. [CrossRef]
17. Chlebus, E.; Kuźnicka, B.; Kurzynowski, T.; Dybała, B. Microstructure and mechanical behaviour of Ti—6Al—7Nb alloy produced by selective laser melting. *Mater. Charact.* **2011**, *62*, 488–495. [CrossRef]
18. Surmeneva, M.; Grubova, I.; Glukhova, N.; Khrapov, D.; Koptyug, A.; Volkova, A.; Ivanov, Y.; Cotrut, C.M.; Vladescu, A.; Teresov, A.; et al. New Ti–35Nb–7Zr–5Ta Alloy Manufacturing by Electron Beam Melting for Medical Application Followed by High Current Pulsed Electron Beam Treatment. *Metals* **2021**, *11*, 1066. [CrossRef]
19. Tamilselvi, S.; Raman, V.; Rajendran, N. Corrosion behaviour of Ti–6Al–7Nb and Ti–6Al–4V ELI alloys in the simulated body fluid solution by electrochemical impedance spectroscopy. *Electrochim. Acta* **2006**, *52*, 839–846. [CrossRef]
20. Metikoš-Huković, M.; Kwokal, A.; Piljac, J. The influence of niobium and vanadium on passivity of titanium-based implants in physiological solution. *Biomaterials* **2003**, *24*, 3765–3775. [CrossRef]
21. Schmidt, M.; Merklein, M.; Bourell, D.; Dimitrov, D.; Hausotte, T.; Wegener, K.; Overmeyer, L.; Vollertsen, F.; Levy, G.N. Laser based additive manufacturing in industry and academia. *CIRP Ann.* **2017**, *66*, 561–583. [CrossRef]
22. Bourell, D.; Kruth, J.P.; Leu, M.; Levy, G.; Rosen, D.; Beese, A.M.; Clare, A. Materials for additive manufacturing. *CIRP Ann.* **2017**, *66*, 659–681. [CrossRef]
23. Wohlers, T.T.; Campbell, I.; Diegel, O.; Kowen, J. *Wohlers Report 2018. 3D Printing and Additive Manufacturing State of the Industry: Annual Worldwide Progress Report*; Wohlers Associates, Inc.: Fort Collins, CO, USA, 2018; ISBN 0991333241.

24. Attar, H.; Prashanth, K.G.; Chaubey, A.K.; Calin, M.; Zhang, L.C.; Scudino, S.; Eckert, J. Comparison of wear properties of commercially pure titanium prepared by selective laser melting and casting processes. *Mater. Lett.* **2015**, *142*, 38–41. [CrossRef]
25. Dai, N.; Zhang, L.-C.; Zhang, J.; Chen, Q.; Wu, M. Corrosion behavior of selective laser melted Ti-6Al-4 V alloy in NaCl solution. *Corros. Sci.* **2016**, *102*, 484–489. [CrossRef]
26. Yang, Y.; Chen, Y.; Zhang, J.; Gu, X.; Qin, P.; Dai, N.; Li, X.; Kruth, J.-P.; Zhang, L.-C. Improved corrosion behavior of ultrafine-grained eutectic Al-12Si alloy produced by selective laser melting. *Mater. Des.* **2018**, *146*, 239–248. [CrossRef]
27. Melchels, F.P.; Domingos, M.A.; Klein, T.J.; Malda, J.; Bartolo, P.J.; Hutmacher, D.W. Additive manufacturing of tissues and organs. *Prog. Polym. Sci.* **2012**, *37*, 1079–1104. [CrossRef]
28. Herzog, D.; Seyda, V.; Wycisk, E.; Emmelmann, C. Additive manufacturing of metals. *Acta Mater.* **2016**, *117*, 371–392. [CrossRef]
29. Guo, N.; Leu, M.C. Additive manufacturing: Technology, applications and research needs. *Front. Mech. Eng.* **2013**, *8*, 215–243. [CrossRef]
30. Lewandowski, J.J.; Seifi, M. Metal Additive Manufacturing: A Review of Mechanical Properties. *Annu. Rev. Mater. Res.* **2016**, *46*, 151–186. [CrossRef]
31. Yap, C.Y.; Chua, C.K.; Dong, Z.L.; Liu, Z.H.; Zhang, D.Q.; Loh, L.E.; Sing, S.L. Review of selective laser melting: Materials and applications. *Appl. Phys. Rev.* **2015**, *2*, 41101. [CrossRef]
32. Tolosa, I.; Garciandía, F.; Zubiri, F.; Zapirain, F.; Esnaola, A. Study of mechanical properties of AISI 316 stainless steel processed by "selective laser melting", following different manufacturing strategies. *Int. J. Adv. Manuf. Technol.* **2010**, *51*, 639–647. [CrossRef]
33. Nezhadfar, P.D.; Burford, E.; Anderson-Wedge, K.; Zhang, B.; Shao, S.; Daniewicz, S.R.; Shamsaei, N. Fatigue crack growth behavior of additively manufactured 17-4 PH stainless steel: Effects of build orientation and microstructure. *Int. J. Fatigue* **2019**, *123*, 168–179. [CrossRef]
34. Kluczyński, J.; Śnieżek, L.; Grzelak, K.; Torzewski, J.; Szachogłuchowicz, I.; Wachowski, M.; Łuszczek, J. Crack Growth Behavior of Additively Manufactured 316L Steel-Influence of Build Orientation and Heat Treatment. *Materials* **2020**, *13*, 3259. [CrossRef]
35. Zhang, M.; Sun, C.-N.; Zhang, X.; Wei, J.; Hardacre, D.; Li, H. High cycle fatigue and ratcheting interaction of laser powder bed fusion stainless steel 316L: Fracture behaviour and stress-based modelling. *Int. J. Fatigue* **2019**, *121*, 252–264. [CrossRef]
36. Jerrard, P.G.E.; Hao, L.; Evans, K.E. Experimental investigation into selective laser melting of austenitic and martensitic stainless steel powder mixtures. *Proc. Inst. Mech. Eng. B J. Eng. Manuf.* **2009**, *223*, 1409–1416. [CrossRef]
37. Baufeld, B.; Brandl, E.; van der Biest, O. Wire based additive layer manufacturing: Comparison of microstructure and mechanical properties of Ti–6Al–4V components fabricated by laser-beam deposition and shaped metal deposition. *J. Mater. Process. Technol.* **2011**, *211*, 1146–1158. [CrossRef]
38. Brandl, E. *Microstructural and Mechanical Properties of Additive Manufactured Titanium (Ti-6Al-4V) Using Wire. Evaluation with Respect to Additive Processes Using Powder and Aerospace Material Specifications*; Dissertation, Brandenburg University of Technology Cottbus-Senftenberg: Cottbus, Germany, 2010; ISBN 978-3-8322-9530-1.
39. Khorasani, A.; Gibson, I.; Goldberg, M.; Littlefair, G. On the role of different annealing heat treatments on mechanical properties and microstructure of selective laser melted and conventional wrought Ti-6Al-4V. *Rapid Prototyp. J.* **2017**, *23*, 295–304. [CrossRef]
40. Liu, S.; Shin, Y.C. Additive manufacturing of Ti6Al4V alloy: A review. *Mater. Des.* **2019**, *164*, 107552. [CrossRef]
41. Riemer, A.; Richard, H.A. Crack Propagation in Additive Manufactured Materials and Structures. *Procedia Struct. Integr.* **2016**, *2*, 1229–1236. [CrossRef]
42. Leuders, S.; Lieneke, T.; Lammers, S.; Tröster, T.; Niendorf, T. On the fatigue properties of metals manufactured by selective laser melting—The role of ductility. *J. Mater. Res.* **2014**, *29*, 1911–1919. [CrossRef]
43. Tillmann, W.; Hagen, L.; Garthe, K.-U.; Hoyer, K.-P.; Schaper, M. Effect of substrate pre-treatment on the low cycle fatigue performance of tungsten carbide-cobalt coated additive manufactured 316 L substrates. *Mater. Werkst.* **2020**, *51*, 1452–1464. [CrossRef]
44. Romano, S.; Patriarca, L.; Foletti, S.; Beretta, S. LCF behaviour and a comprehensive life prediction model for AlSi10Mg obtained by SLM. *Int. J. Fatigue* **2018**, *117*, 47–62. [CrossRef]
45. Bressan, S.; Ogawa, F.; Itoh, T.; Berto, F. Low cycle fatigue behavior of additively manufactured Ti-6Al-4V under non-proportional and proportional loading. *Frat. Integrita Strutt.* **2019**, *13*, 18–25. [CrossRef]
46. Zhang, S.Q.; Li, S.J.; Jia, M.T.; Prima, F.; Chen, L.J.; Hao, Y.L.; Yang, R. Low-cycle fatigue properties of a titanium alloy exhibiting nonlinear elastic deformation behavior. *Acta Mater.* **2011**, *59*, 4690–4699. [CrossRef]
47. Awd, M.; Tenkamp, J.; Hirtler, M.; Siddique, S.; Bambach, M.; Walther, F. Comparison of Microstructure and Mechanical Properties of Scalmalloy®Produced by Selective Laser Melting and Laser Metal Deposition. *Materials* **2017**, *11*, 17. [CrossRef]
48. Leuders, S.; Thöne, M.; Riemer, A.; Niendorf, T.; Tröster, T.; Richard, H.A.; Maier, H.J. On the mechanical behaviour of titanium alloy TiAl6V4 manufactured by selective laser melting: Fatigue resistance and crack growth performance. *Int. J. Fatigue* **2013**, *48*, 300–307. [CrossRef]
49. Wycisk, E.; Siddique, S.; Herzog, D.; Walther, F.; Emmelmann, C. Fatigue Performance of Laser Additive Manufactured Ti–6Al–4V in Very High Cycle Fatigue Regime up to 109 Cycles. *Front. Mater.* **2015**, *2*, 72. [CrossRef]
50. Polozov, I.; Sufiiarov, V.; Popovich, A.; Masaylo, D.; Grigoriev, A. Synthesis of Ti-5Al, Ti-6Al-7Nb, and Ti-22Al-25Nb alloys from elemental powders using powder-bed fusion additive manufacturing. *J. Alloy. Compd.* **2018**, *763*, 436–445. [CrossRef]
51. Affolter, C.; Thorwarth, G.; Arabi-Hashemi, A.; Müller, U.; Weisse, B. Ductile Compressive Behavior of Biomedical Alloys. *Metals* **2020**, *10*, 60. [CrossRef]

52. Xu, C.; Sikan, F.; Atabay, S.E.; Muñiz-Lerma, J.A.; Sanchez-Mata, O.; Wang, X.; Brochu, M. Microstructure and mechanical behavior of as-built and heat-treated Ti–6Al–7Nb produced by laser powder bed fusion. *Mater. Sci. Eng. A Struct. Mater.* **2020**, *793*, 139978. [CrossRef]
53. Hein, M.; Hoyer, K.-P.; Schaper, M. Additively processed TiAl6Nb7 alloy for biomedical applications. *Mater. Werkst.* **2021**, *52*, 703–716. [CrossRef]
54. Bergmann, G.; Bender, A.; Dymke, J.; Duda, G.; Damm, P. Standardized Loads Acting in Hip Implants. *PLoS ONE* **2016**, *11*, e0155612. [CrossRef]
55. Bergmann, G.; Graichen, F.; Rohlmann, A.; Bender, A.; Heinlein, B.; Duda, G.N.; Heller, M.O.; Morlock, M.M. Realistic loads for testing hip implants. *Biomed. Mater. Eng.* **2010**, *20*, 65–75. [CrossRef] [PubMed]
56. Sallica-Leva, E.; Caram, R.; Jardini, A.L.; Fogagnolo, J.B. Ductility improvement due to martensite α′ decomposition in porous Ti-6Al-4V parts produced by selective laser melting for orthopedic implants. *J. Mech. Behav. Biomed. Mater.* **2016**, *54*, 149–158. [CrossRef] [PubMed]
57. Tao, P.; Li, H.; Huang, B.; Hu, Q.; Gong, S.; Xu, Q. Tensile behavior of Ti-6Al-4V alloy fabricated by selective laser melting: Effects of microstructures and as-built surface quality. *China Foundry* **2018**, *15*, 243–252. [CrossRef]
58. Gil Mur, F.X.; Rodríguez, D.; Planell, J.A. Influence of tempering temperature and time on the α′-Ti-6Al-4V martensite. *J. Alloy. Compd.* **1996**, *234*, 287–289. [CrossRef]
59. Liang, Z.; Sun, Z.; Zhang, W.; Wu, S.; Chang, H. The effect of heat treatment on microstructure evolution and tensile properties of selective laser melted Ti6Al4V alloy. *J. Alloy. Compd.* **2019**, *782*, 1041–1048. [CrossRef]
60. Donachie, M.J. *Titanium. A Technical Guide*, 2nd ed.; ASM International: Materials Park, OH, USA, 2000; ISBN 9780871706867.
61. Bachmann, F.; Hielscher, R.; Schaeben, H. Texture Analysis with MTEX—Free and Open Source Software Toolbox. *Solid State Phenom.* **2010**, *160*, 63–68. [CrossRef]
62. Plumtree, A. Cyclic stress–Strain response and substructure. *Int. J. Fatigue* **2001**, *23*, 799–805. [CrossRef]
63. Rice, R.C. *Fatigue Design Handbook*, 2nd ed.; Society of Automotive Engineers: Warrendale, PA, USA, 1988; ISBN 9780898830118.
64. Skelton, R.P.; Maier, H.J.; Christ, H.-J. The Bauschinger effect, Masing model and the Ramberg–Osgood relation for cyclic deformation in metals. *Mater. Sci. Eng. A Struct. Mater.* **1997**, *238*, 377–390. [CrossRef]
65. Nieslony, A.; Dsoki, C.; Kaufmann, H.; Krug, P. New method for evaluation of the Manson–Coffin–Basquin and Ramberg–Osgood equations with respect to compatibility. *Int. J. Fatigue* **2008**, *30*, 1967–1977. [CrossRef]
66. Basquin, O.H. The exponential law of endurance tests. *Am. Soc. Test. Mater.* **1910**, *10*, 625–630.
67. Coffin, L.F. A Study of the Effects of Cyclic Thermal Stresses on a Ductile Metal. *Trans. Am. Soc. Mech.* **1954**, *76*, 931–950.
68. Manson, S.S. *Behavior of Materials Under Conditions of Thermal Stress*; National Advisory Committee for Aeronautics: Edwards, CA, USA, 1953.
69. Suresh, S. *Fatigue of Materials*, 2nd ed.; Reprint; Cambridge Univ. Press: Cambridge, UK, 2004; ISBN 978-0-521-57847-9.
70. ASM International. *Fatigue and Fracture*, 10th ed.; 3. Print; ASM International: Materials Park, OH, USA, 2002; ISBN 9780871703859.
71. Schupbach, P.; Glauser, R.; Bauer, S. Al_2O_3 Particles on Titanium Dental Implant Systems following Sandblasting and Acid-Etching Process. *Int. J. Biomater.* **2019**, *2019*, 6318429. [CrossRef]
72. Le Guéhennec, L.; Soueidan, A.; Layrolle, P.; Amouriq, Y. Surface treatments of titanium dental implants for rapid osseointegration. *Dent. Mater.* **2007**, *23*, 844–854. [CrossRef] [PubMed]
73. Wennerberg, A.; Albrektsson, T.; Chrcanovic, B. Long-term clinical outcome of implants with different surface modifications. *Eur. J. Oral Implantol.* **2018**, *11* (Suppl. S1), S123–S136.
74. Yuda, A.W.; Supriadi, S.; Saragih, A.S. Surface modification of Ti-alloy based bone implant by sandblasting. In *The 4th Biomedical Engineering's Recent Progress in Biomaterials, Drugs Development, Health, and Medical Devices, Proceedings of the International Symposium of Biomedical Engineering (ISBE), Padang, Indonesia, 22–24 July 2019*; AIP Publishing: Melville, NY, USA, 2019; p. 20015.
75. Yurttutan, M.E.; Keskin, A. Evaluation of the effects of different sand particles that used in dental implant roughened for osseointegration. *BMC Oral Health* **2018**, *18*, 47. [CrossRef]
76. Gillies, R.J.; Didier, N.; Denton, M. Determination of cell number in monolayer cultures. *Anal. Biochem.* **1986**, *159*, 109–113. [CrossRef]
77. Sercombe, T.; Jones, N.; Day, R.; Kop, A. Heat treatment of Ti-6Al-7Nb components produced by selective laser melting. *Rapid Prototyp. J.* **2008**, *14*, 300–304. [CrossRef]
78. Ajeel, S.A.; Alzubaydi, T.L.; Swadi, A.K. Influence of Heat Treatment Conditions on Microstructure of Ti-6Al-7Nb Alloy as Used Surgical Implant Materials. *Eng. Technol.* **2007**, *25*, 431–442.
79. DebRoy, T.; Wei, H.L.; Zuback, J.S.; Mukherjee, T.; Elmer, J.W.; Milewski, J.O.; Beese, A.M.; Wilson-Heid, A.; De, A.; Zhang, W. Additive manufacturing of metallic components—Process, structure and properties. *Prog. Mater. Sci.* **2018**, *92*, 112–224. [CrossRef]
80. Körner, C. Additive manufacturing of metallic components by selective electron beam melting—A review. *Int. Mater. Rev.* **2016**, *61*, 361–377. [CrossRef]
81. Banerjee, S.; Mukhopadhyay, P. *Phase Transformations. Examples from Titanium and Zirconium Alloys*; Elsevier: Amsterdam, The Netherlands; Oxford, UK, 2007; ISBN 9780080421452.
82. Thijs, L.; Verhaeghe, F.; Craeghs, T.; van Humbeeck, J.; Kruth, J.-P. A study of the microstructural evolution during selective laser melting of Ti–6Al–4V. *Acta Mater.* **2010**, *58*, 3303–3312. [CrossRef]

83. Kobryn, P.; Semiatin, S. Microstructure and texture evolution during solidification processing of Ti–6Al–4V. *J. Mater. Process. Technol.* **2003**, *135*, 330–339. [CrossRef]
84. Lütjering, G. Influence of processing on microstructure and mechanical properties of (α + β) titanium alloys. *Mater. Sci. Eng. A Struct. Mater.* **1998**, *243*, 32–45. [CrossRef]
85. Lütjering, G.; Williams, J.C. *Titanium*, 2nd ed.; Springer: Berlin, Germany, 2007; ISBN 9783540713975.
86. Burgers, W.G. On the process of transition of the cubic-body-centered modification into the hexagonal-close-packed modification of zirconium. *Physica* **1934**, *1*, 561–586. [CrossRef]
87. Peters, M.; Leyens, C. *Titan und Titanlegierungen*, 3rd ed.; Wiley-VCH: Weinheim, Germany, 2002; ISBN 9783527611089.
88. Murr, L.E.; Gaytan, S.M.; Ramirez, D.A.; Martinez, E.; Hernandez, J.; Amato, K.N.; Shindo, P.W.; Medina, F.R.; Wicker, R.B. Metal Fabrication by Additive Manufacturing Using Laser and Electron Beam Melting Technologies. *J. Mater. Sci. Technol.* **2012**, *28*, 1–14. [CrossRef]
89. Rehme, O. *Cellular Design for Laser Freeform Fabrication*, 1st ed.; Cuvillier Verlag: Göttingen, Germany, 2010; ISBN 9783869552736.
90. Sieniawski, J.; Ziaja, W.; Kubiak, K.; Motyk, M. Microstructure and Mechanical Properties of High Strength Two-Phase Titanium Alloys. In *Titanium Alloys—Advances in Properties Control*; Sieniawski, J., Ziaja, W., Eds.; InTech: Rijeka, Croatia, 2014; ISBN 978-953-51-1110-8.
91. Bolzoni, L.; Weissgaerber, T.; Kieback, B.; Ruiz-Navas, E.M.; Gordo, E. Mechanical behaviour of pressed and sintered CP Ti and Ti-6Al-7Nb alloy obtained from master alloy addition powder. *J. Mech. Behav. Biomed. Mater.* **2013**, *20*, 149–161. [CrossRef] [PubMed]
92. *ISO 5832-11:2014*; Chirurgische Implantate—Metallische Werkstoffe—Teil 11: Titan Aluminium-6 Niob-7 Knetlegierung. DIN Deutsches Institut für Normung e. V.: Berlin, Germany, 2015.
93. Shunmugavel, M.; Polishetty, A.; Littlefair, G. Microstructure and Mechanical Properties of Wrought and Additive Manufactured Ti-6Al-4V Cylindrical Bars. *Procedia Technol.* **2015**, *20*, 231–236. [CrossRef]
94. Attar, H.; Calin, M.; Zhang, L.C.; Scudino, S.; Eckert, J. Manufacture by selective laser melting and mechanical behavior of commercially pure titanium. *Mater. Sci. Eng. A Struct. Mater.* **2014**, *593*, 170–177. [CrossRef]
95. Gorny, B.; Niendorf, T.; Lackmann, J.; Thoene, M.; Troester, T.; Maier, H.J. In situ characterization of the deformation and failure behavior of non-stochastic porous structures processed by selective laser melting. *Mater. Sci. Eng. A Struct. Mater.* **2011**, *528*, 7962–7967. [CrossRef]
96. Blochwitz, C.; Jacob, S.; Tirschler, W. Grain orientation effects on the growth of short fatigue cracks in austenitic stainless steel. *Mater. Sci. Eng. A Struct. Mater.* **2008**, *496*, 59–66. [CrossRef]
97. Rao, K.T.V.; Yu, W.; Ritchie, R.O. Fatigue crack propagation in aluminum-lithium alloy 2090: Part II. small crack behavior. *Metall. Mater. Trans. A Phys. Metall. Mater. Sci.* **1988**, *19*, 563–569. [CrossRef]
98. Riemer, A.; Leuders, S.; Thöne, M.; Richard, H.A.; Tröster, T.; Niendorf, T. On the fatigue crack growth behavior in 316 L stainless steel manufactured by selective laser melting. *Eng. Fract. Mech.* **2014**, *120*, 15–25. [CrossRef]
99. Zerbst, U.; Bruno, G.; Buffiere, J.-Y.; Wegener, T.; Niendorf, T.; Wu, T.; Zhang, X.; Kashaev, N.; Meneghetti, G.; Hrabe, N.; et al. Damage tolerant design of additively manufactured metallic components subjected to cyclic loading: State of the art and challenges. *Prog. Mater. Sci.* **2021**, *121*, 100786. [CrossRef] [PubMed]
100. Afkhami, S.; Dabiri, M.; Alavi, S.H.; Björk, T.; Salminen, A. Fatigue characteristics of steels manufactured by selective laser melting. *Int. J. Fatigue* **2019**, *122*, 72–83. [CrossRef]
101. Schweikl, H.; Müller, R.; Englert, C.; Hiller, K.-A.; Kujat, R.; Nerlich, M.; Schmalz, G. Proliferation of osteoblasts and fibroblasts on model surfaces of varying roughness and surface chemistry. *J. Mater. Sci. Mater. Med.* **2007**, *18*, 1895–1905. [CrossRef] [PubMed]
102. Jeffery, E.H.; Abreo, K.; Burgess, E.; Cannata, J.; Greger, J.L. Systemic aluminum toxicity: Effects on bone, hematopoietic tissue, and kidney. *J. Toxicol. Environ. Health* **1996**, *48*, 649–665. [CrossRef] [PubMed]
103. Daley, B.; Doherty, A.T.; Fairman, B.; Case, C.P. Wear debris from hip or knee replacements causes chromosomal damage in human cells in tissue culture. *J. Bone Jt. Surg. Br.* **2004**, *86-B*, 598–606. [CrossRef]
104. Weng, Y.; Liu, H.; Ji, S.; Huang, Q.; Wu, H.; Li, Z.; Wu, Z.; Wang, H.; Tong, L.; Fu, R.K.; et al. A promising orthopedic implant material with enhanced osteogenic and antibacterial activity: Al2O3-coated aluminum alloy. *Appl. Surf. Sci.* **2018**, *457*, 1025–1034. [CrossRef]
105. Cattoni, D.; Ferrari, C.; Lebedev, L.; Pazos, L.; Svoboda, H. Effect of Blasting on the Fatigue Life of Ti-6Al-7Nb and Stainless Steel AISI 316 LVM. *Proc. Mater. Sci.* **2012**, *1*, 461–468. [CrossRef]
106. Javier Gil, F.; Planell, J.A.; Padrós, A.; Aparicio, C. The effect of shot blasting and heat treatment on the fatigue behavior of titanium for dental implant applications. *Dent. Mater.* **2007**, *23*, 486–491. [CrossRef] [PubMed]
107. Pazos, L.; Corengia, P.; Svoboda, H. Effect of surface treatments on the fatigue life of titanium for biomedical applications. *J. Mech. Behav. Biomed. Mater.* **2010**, *3*, 416–424. [CrossRef] [PubMed]

Paper C

M. Hein, N. F. Lopes Dias, D. Kokalj, D. Stangier, K.-P. Hoyer, W. Tillmann, and M. Schaper

On the Influence of Physical Vapor Deposited Thin Coatings on the Low-cycle Fatigue Behavior of Additively Processed Ti-6Al-7Nb Alloy

International Journal of Fatigue, 166, 2023 [226].

International Journal of Fatigue 166 (2023) 107235

Contents lists available at ScienceDirect

International Journal of Fatigue

journal homepage: www.elsevier.com/locate/ijfatigue

On the influence of physical vapor deposited thin coatings on the low-cycle fatigue behavior of additively processed Ti-6Al-7Nb alloy

Maxwell Hein [a,b,*], Nelson Filipe Lopes Dias [c], David Kokalj [c], Dominic Stangier [c], Kay-Peter Hoyer [a,b], Wolfgang Tillmann [c], Mirko Schaper [a,b]

[a] Chair of Materials Science, Paderborn University, Warburger Straße 100, 33098 Paderborn, Germany
[b] Direct Manufacturing Research Center, Paderborn University, Mersinweg 3, 33100 Paderborn, Germany
[c] Institute of Materials Engineering, TU Dortmund University, Leonhard-Euler, Straße 2, 44227 Dortmund, Germany

ARTICLE INFO

Keywords:
Laser powder bed fusion
Ti-6Al-7Nb
Physical vapor deposition
Mechanical properties
Low-cycle fatigue

ABSTRACT

The tensile and fatigue properties of laser powder bed fused Ti-6Al-7Nb are improved by physical vapor deposition (PVD). Thin coatings of titanium nitride (TiN), titanium carbonitride (TiCN), and silver-containing amorphous carbon (a-C:Ag) are deposited by magnetron sputtering. Tensile and strain-controlled low-cycle fatigue tests with various total strain amplitudes are performed. The coatings increase the tensile strength and decrease the breaking elongation. The low-cycle fatigue performance of the PVD-coated conditions, except for the a-C:Ag coating, is improved. The coatings considerably enhance tensile strength and fatigue resistance due to their high residual compressive stresses and increased surface hardness.

1. Introduction

Additive manufacturing (AM), also known as 3D printing, is an advanced manufacturing technique, where the material is added layer by layer to form complex geometries and structures, based on 3D data [1]. Various AM techniques are available, such as stereolithography, selective laser sintering, and selective laser melting, also known as laser powder bed fusion (LPBF) or laser beam melting. Numerous materials, like ceramics, polymers, metals, and even living cells, can be processed [2]. Besides the opportunity for near-net-shape fabrication of complex parts, which cannot be produced with conventional manufacturing methods, AM technologies can be cost-effective, time-saving, and resource-saving [3,4].

Due to these advantages, AM technologies are increasingly used in the biomedical industry, mainly because of the possibility of individualizing medical devices [5,6]. Specific biomedical implant topologies, such as porous or foam structures, can be manufactured by LPBF [7–9]. For load-bearing applications, like hip and knee implants, metallic materials - e.g., titanium and its alloys, stainless steels, and cobalt-chromium alloys - are often used [10–12]. Because of their excellent biocompatibility, high corrosion resistance, and outstanding mechanical properties - like increased strength and fracture toughness, plus low elastic modulus - titanium and its alloys are used in biomedical applications [13–17]. Ti-6Al-4V was initially developed for aeronautical applications and is the most frequently used titanium alloy in the biomedical field. Although this alloy exhibits superb corrosion properties, the effect of its alloying elements is questionable, concerning the cytotoxicity and the impact on aseptic loosening [18–22]. For this reason, Ti-6Al-7Nb was established as an alternative to Ti-6Al-4V for load-bearing implants. Substituting vanadium with niobium resulted in increased corrosion resistance and biocompatibility, with similar mechanical properties to Ti-6Al-4V [21,23,24].

Several studies focus on the mechanical properties of different, additively processed alloys, such as steel or titanium alloys [25,26]. High-cycle fatigue (HCF) analysis is usually applied for implants, and sometimes extreme loading could occur through stumbling and endanger the implant. In addition to HCF and monotonic material characterization, implants should be examined at low cycles with higher load levels, imitating the physiological loading during service life [27,28]. In terms of fatigue analysis of additively manufactured alloys, there is still a lack of knowledge since most available research is related to HCF and crack growth analysis of titanium [29–34] and steel [35–39]. So far, little research has analyzed the low-cycle fatigue of additively manufactured alloys [40–44]. Other studies addressed the fatigue behavior of additively processed titanium alloys, such as Ti-6Al-4V [30,34,45,46] and Ti-6Al-7Nb [47].

* Corresponding author at: Chair of Materials Science, Paderborn University, Warburger Straße 100, 33098 Paderborn, Germany.
E-mail address: hein@lwk.upb.de (M. Hein).

https://doi.org/10.1016/j.ijfatigue.2022.107235
Received 4 April 2022; Received in revised form 8 August 2022; Accepted 30 August 2022
Available online 6 September 2022

Under physiological loading, artificial titanium-based implants show high friction and low wear resistance against various counterpart materials [48]. Some functional physical vapor deposition (PVD) thin coatings, such as titanium nitride (TiN), titanium carbonitride (TiCN), and amorphous carbon (a-C; also referred to as diamond-like carbon, DLC) based coating systems, can be applied on titanium for biomedical applications, thus improving the tribological behavior and tailoring the biocompatible features significantly [49–52]. Different studies show that PVD thin coatings on bulk or wrought material enhance the fatigue performance for LCF and HCF [53–57]. The hard surface layer possesses high mechanical strength, good adhesion to the substrate, and high compressive residual stresses and, therefore, inhibits the plastic deformation on the substrate material. As a result, PVD coatings improve the tensile and fatigue properties [55,58–61].

The PVD deposition of bio-functional thin coatings on additively manufactured Ti-6Al-7Nb alloys is an innovative approach to enhance wear resistance, biocompatibility, and mechanical properties, particularly the LCF behavior. Therefore, TiN, TiCN, and Ag-containing a-C (a-C:Ag) coatings are deposited on LPBF processed Ti-6Al-7Nb. The effects of the PVD coatings on the monotonic tensile and LCF behavior of laser beam melted Ti-6Al-7Nb are focused and analyzed.

2. Experimental details

The (α + β) titanium alloy Ti-6Al-7Nb was used to produce the specimens by LPBF. The powder was supplied by ECKART TLS GmbH (Bitterfeld, Germany). The chemical compositions of the powder and the as-built samples, as well as the powder particle investigations, are presented in previous examinations [62]. The chemical composition of the powder was: 6.03 wt% Al, 6.75 wt% Nb, 0.09 wt%Fe, and 0.1 wt%O, Ti is balanced and in agreement with ISO 5832-11 [63]. The powder particle morphology was mainly spherical, with a nominal Gaussian particle size distribution between 26.9 µm (D10) and 52.1 µm (D90), centered at 37.6 µm. The powder was dried by cyclic, alternating evacuation and flooding with argon to reduce the relative humidity to below 5%. An LT12 SLM machine (DMG MORI AG, Bielefeld, Germany) with a beam spot size of 35 µm was used for specimen fabrication. The software Magics (Version 21.1, Materialise GmbH, Munich, Germany) was used for data preparation. The following parameters were applied for low porosity and high relative density: laser power P = 185 W, laser scanning speed v = 1,675 mm s^{-1}, hatch distance h = 0.077 mm. A constant scanning strategy of 5 mm stripes by layer-wise rotation of the scanning vectors of 67° alongside a layer thickness of 50 µm was applied. A laser power Pc = 123 W and scanning speed vc = 512 mm s-1 were applied as contour parameters. The process took place in an inert argon atmosphere with an oxygen content between 0.08% and 0.13% to prevent the oxidation of titanium. The building platform temperature was kept at 200 °C. All specimens were subsequently blasted with high-grade Al_2O_3. The blasting material had a particle size of 70 µm–250 µm, used at 4 bar air pressure with an SMG 25 DUO (MHG Strahlanlagen GmbH, Düsseldorf, Germany). Before the PVD deposition, the Ti-6Al-7Nb substrates were cleaned in an ultrasonic ethanol bath for 30 min.

The PVD coatings were deposited in a magnetron sputtering process using an industrial device CC800/9 Custom (CemeCon AG, Würselen, Germany). Three different coatings were applied: TiN, TiCN, and a-C:Ag. TiN had a chemical composition of 49.1 ± 0.2 at.% Ti and 50.9 ± 0.2 at.% N, whereas TiCN had 38.4 ± 1.5 at.% Ti, 30.4 ± 0.5 at.% C, and 31.2 ± 1.0 at.% N [64]. Interlayers of Ti for TiN and bilayered Ti/TiN for TiCN were grown to improve the adhesion. The amorphous carbon coating a-C:Ag containing 7.5 at.% Ag was deposited with a chemically graded titanium carbide (Ti_xC_y) interlayer [51].

The residual stresses of the different PVD coatings were determined from the substrate curvature using Stoney's equation [65]. P-doped Si wafers with a preferred orientation along the (1 0 0) plane served as substrate material for this analysis. The radius of curvature of the coated silicon wafers was measured using a contour measurer MarSurf XC 20 (Mahr GmbH, Göttingen, Germany). For the evaluation of the hardness, an Agilent Nano Indenter G200 (Agilent Technologies Inc., Santa Clara, CA, USA) with a Berkovich indenter was employed. An indentation depth of approximately 10% of the PVD coating thickness was defined to minimize the effects of the interlayers and substrate. A total of 49 indentations (7 × 7) were performed on each coating to calculate an average hardness value. The hardness measurements were performed on metallographically lapped and polished surfaces to avoid roughness effects on the measures [66]. The adhesion of the PVD coatings on the sandblasted Ti-6Al-7Nb substrates was evaluated in Rockwell C indentation tests according to DIN 4856 [67]. A load of 588.6 N (weight of 60 kg) was applied to generate the Rockwell C indents. The adhesion of the PVD coatings was classified into the adhesion classes from HF1 (excellent adhesion) to HF6 (poor adhesion).

The monotonic tensile and LCF tests were performed using a servo-hydraulic MTS 858 tabletop test system equipped with a 661.19F-03 load cell (capacity 15 ± 0.15 kN, MTS Systems Corporation, Eden Prairie, MN, USA). An extensometer 632.29F-20 was used for the tensile tests, and an extensometer 632.29F-20 was used for the LCF tests (gage length 3 mm, ±8% ± 0.08%; both MTS Systems Corporation, Eden Prairie, MN, USA). A displacement-controlled execution with a cross-head speed of 1.5 mm min^{-1} was used for the tensile tests, according to DIN EN ISO 6892–1 [68]. The strain-controlled LCF tests were performed according to ASTM E606, with total strain amplitudes ε_A of 0.35%, 0.5%, and 0.8%, with an R-ratio of R = −1 (compression-tensile fatigue), and a strain rate of 6×10^{-3} s^{-1} [69]. For the tensile tests, five specimens per condition were assayed. For the LCF tests, at least three specimens per condition were examined at each strain amplitude. The monotonic material properties, such as Younǵs moduli (E), tensile yield strengths (YS), ultimate tensile strengths (UTS), and elongations at fracture (A), were obtained from dog-bone test specimens. All specimens were loaded along the initial building direction. The ratio "cross-section to gauge length" in the tested specimens was less than 5.65, which is the standard value for tensile specimens [68]. Thus, the elongation values should be critically considered.

Several fatigue tests under cyclic loading were required to determine the fatigue material constants. Due to cyclic hardening or softening, cyclically loaded materials often have unstable and changing stress amplitude during the test. The stress amplitude for the stabilized state was used, which was determined to be at the half number of cycles to fracture. In addition to the Younǵs moduli E determined by the tensile tests, the Younǵs moduli (E_{LCF}) were determined for the different conditions at their stabilized hysteresis loops. The plastic strain amplitude can either be calculated or determined by measuring the thickness of the stable hysteresis loop recorded during fatigue testing [70–73]. The Coffin-Manson-Basquin approximation was used to predict the fatigue life depending on the applied strain amplitude for the different conditions. By combining the modified Basquin [74] and the Coffin-Manson relation [75,76] one obtains the approximation [77]:

$$\varepsilon_A = \frac{\sigma'_f}{E} \cdot (2N_f)^b + \varepsilon'_f \cdot (2N_f)^c \quad (1)$$

with the total strain amplitude ε_A, fatigue strength coefficient σ'_f, the Young′s modulus E, the number of reversals to failure $2N_f$, the fatigue strength exponent b, the fatigue ductility coefficient ε'_f, and the fatigue ductility exponent c. The summands in Equation (1) are the elastic ε_e and plastic ε_p components, respectively, of the total strain amplitude ε_A. The equation can be used as a basic strain-life approach to fatigue design [47,74–78].

The interface between the PVD coatings and the substrate, the nanoindentations, and the fracture surfaces of the monotonic and low-cycle fatigue tests were investigated employing the scanning electron microscope (SEM) Zeiss Ultra Plus (Carl Zeiss AG, Oberkochen, Germany).

3. Results

The morphology of the different PVD coatings and SEM micrographs of the Rockwell C indents on the PVD-coated Ti-6Al-7Nb substrates are depicted in Fig. 1 (a-c). The stress state of the PVD coatings was analyzed using Stoney's equation. It is worth mentioning that this method determines the macroscopic stresses of the entire coating structure. The coating surface of the coated silicon wafers was convex, indicating compressive stresses for all PVD coatings. The TiN and TiCN coatings exhibit residual stresses of -0.32 ± 0.01 GPa and -0.59 ± 0.04 GPa. The addition of carbon to TiN is generally linked with an increase in compressive stresses due to the high lattice strain caused by the substitution of nitrogen atoms with larger carbon atoms in the cubic TiN lattice structure [79]. For a–C:Ag, a value of -1.15 ± 0.03 GPa was determined in a previous study by the authors for Ag-containing a–C coatings [51]. The silver addition to a–C reduces the compressive stresses, but the magnitude of the stresses remains higher compared to TiN and TiCN. The hardness of the as-built Ti-6Al-7Nb samples is 5.3 ± 0.3 GPa (540 ± 31 HV). The PVD thin coatings increase the hardness. For a-C:Ag coating the hardness is 13.2 ± 1.3 GPa (1346 ± 133 HV), for TiCN 9.6 ± 0.9 GPa (979 ± 92 HV), and for TiN 17.8 ± 1.4 GPa (1815 ± 143 HV) [64]. The TiN, TiCN, and a–C:Ag layers exhibit a high adhesion strength on the sandblasted substrates without any adhesive failure. For all thin coatings, the adhesion class corresponds to HF1, see Fig. 1 (d-f).

The geometry and building direction of the tensile specimens is presented in Fig. 2 (a). No delamination between the coating and substrate was observed under monotonic tension or cyclic loading. Fig. 2 (b) depicts conditions of the different PVD coatings after the tests. Fig. 2 (c) summarizes the stress–strain curves of the monotonic tensile tests. The Youngs moduli of the coated specimens are higher. The mean YS and UTS are higher for the coated conditions, whereas the average breaking elongation is lower than for the as-built state. TiCN coating improves the monotonic tensile behavior and results in the highest YS and UTS of all conditions, and the highest elongation at fracture for the coated variants, slightly below the as-built samples. a-C:Ag coated samples show the lowest YS and UTS among the PVD-coated samples, but a higher elongation at break than TiN coated specimens. The monotonic material properties are given in Table 1.

The results of the LCF tests, which are the cycles to failure N_f over total strain amplitudes ε_A, are presented in Fig. 3 (a). With increasing strain amplitude, the cycles to failure decrease for all conditions. The mean lifetime of the as-built state is the lowest among all strain amplitudes compared to the PVD-coated conditions. The standard deviation of the a-C:Ag coated specimens at a strain amplitude of 0.5% is relatively high, compared to the other deviations. The ε_A-N_f plots of the different conditions are approximated with the Coffin–Manson–Basquin relation, see Fig. 3 (b). The approximations characterize the relation between the total strain ε_A and the fatigue life N_f of the different conditions. The Coffin–Manson–Basquin fatigue life approximations are determined as follows:

$$\varepsilon_{A,as-built} = 765.04 \cdot (2N_f)^{-1.518} + 0.8545 \cdot (2N_f)^{-0.102} \quad (2)$$

$$\varepsilon_{A,+TiN} = 985.18 \cdot (2N_f)^{-1.507} + 1.6743 \cdot (2N_f)^{-0.177} \quad (3)$$

$$\varepsilon_{A,+TiCN} = 390.42 \cdot (2N_f)^{-1.323} + 1.6384 \cdot (2N_f)^{-0.17} \quad (4)$$

$$\varepsilon_{A,+a-C:Ag} = 180.95 \cdot (2N_f)^{-1.28} + 1.2492 \cdot (2N_f)^{-0.142} \quad (5)$$

Fig. 3 (b) depicts the fatigue life curves of the different conditions. The approximations show an increased lifetime among all PVD coatings between 10^2 and 10^4 reversals and between the strain amplitudes ε_A (0.35% −0.8%), respectively.

The fatigue properties in terms of the fatigue strength coefficients σ'_f and exponents b and fatigue ductility coefficients ε'_f and exponents c of the Coffin-Manson-Basquin equation are given in Table 1. Corresponding to the fatigue ductility exponents c, the PVD-coated specimens show larger gradients. The TiN coating results in the highest fatigue ductility coefficients ε'_f. The TiN and TiCN coatings exhibit the highest fatigue strength coefficients σ'_f. Regarding the fatigue strength exponent b, the as-built condition has the largest gradient. In terms of the overall performance in the tested reversals range for $10^2 < 2N_f < 10^4$, the coated conditions are to be favored, corresponding to the Coffin-Manson approximation. The PVD-coated specimens, except for the a-C:Ag coating, show a larger fatigue ductility coefficient ε'_f, compared to as-built Ti-6Al-7Nb. The initial slopes are smaller for PVD-coated conditions, represented by lower fatigue ductility exponents c. Among all conditions, the fatigue strength coefficients σ'_f are higher for the PVD-

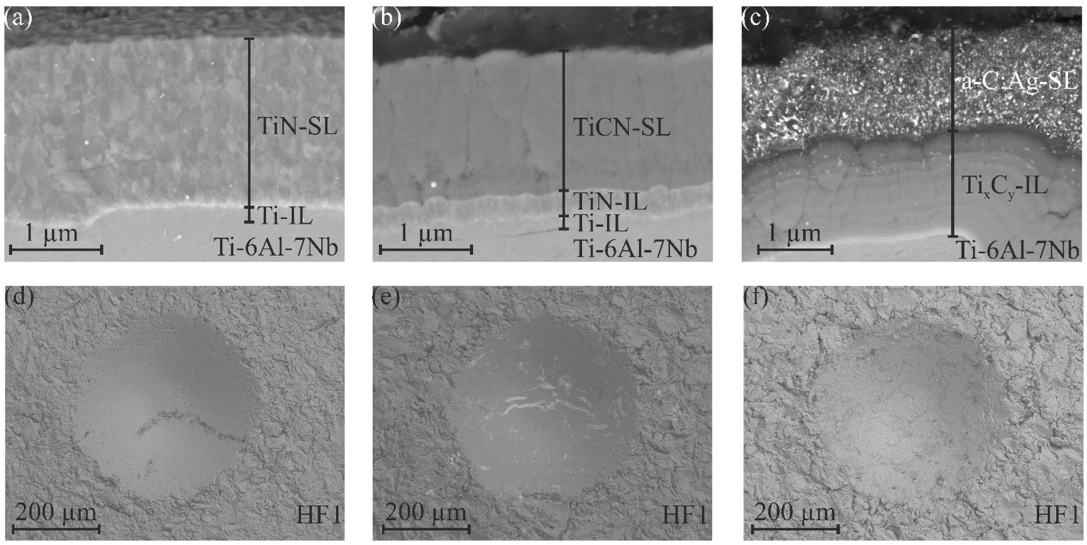

Fig. 1. Secondary electron images of PVD-coatings on Ti-6Al-7Nb substrate with different interlayers (IL) and surface layers (SL); (a) TiN-SL on Ti-IL; (b) TiCN-SL on bilayered Ti-IL and TiN-IL; and (c) a-C:Ag-SL on chemically graded Ti_xC_y-IL; backscattered electron images of nanoindentation on different coatings with adhesion classification for (d) TiN, (e) TiCN, and (f) a-C:Ag.

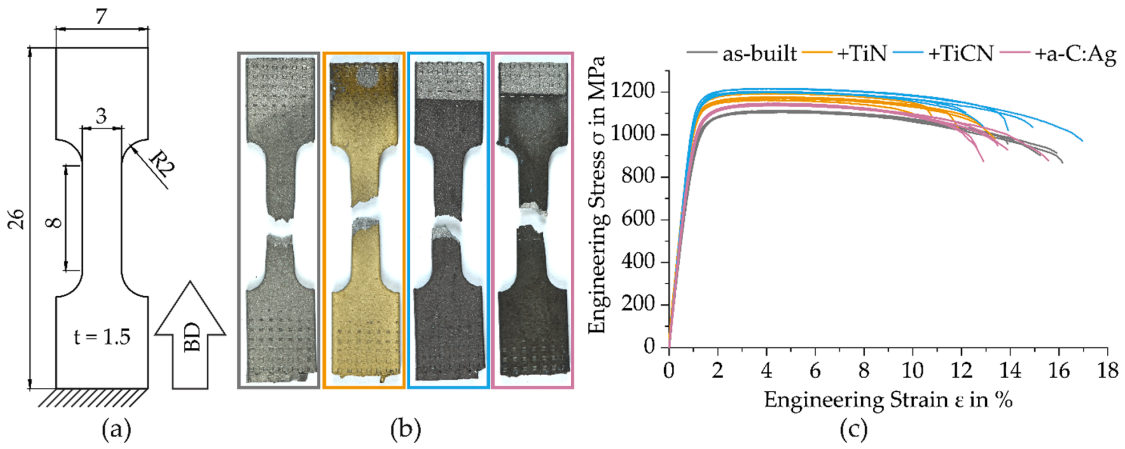

Fig. 2. (a) Geometry and building direction (BD) of tensile and fatigue specimens; (b) overview of different PVD coatings on Ti-6Al-7Nb specimens after tensile testing, coatings from left to right: as-built, TiN, TiCN, a-C:Ag; (c) stress–strain curves of the as-built and PVD-coated samples.

Table 1
Results of hardness measurements [64], monotonic tensile and fatigue tests of the LPBF fabricated, as-built, and PVD-coated Ti-6Al-7Nb, including the minimum values regarding standard ISO 5832-11 [63].

Condition	Hardness (GPa)	YS (MPa)	UTS (MPa)	A (%)	E (GPa)	E_{LCF} (GPa)	σ'_f	b	ε'_f	c
as-built	5.3 ± 0.3	940 ± 14	1109 ± 3	14.4 ± 0.9	105 ± 3	147 ± 8	89.7	−0.102	765.04	−1.518
+TiN	17.8 ± 1.4	1055 ± 20	1175 ± 10	10.9 ± 1.0	117 ± 5	143 ± 3	195.9	−0.177	985.18	−1.507
+TiCN	9.6 ± 0.9	1107 ± 13	1207 ± 8	13.3 ± 1.7	116 ± 2	143 ± 3	190.1	−0.170	390.42	−1.323
+a-C:Ag	13.2 ± 1.3	984 ± 9	1141 ± 4	12.9 ± 1.0	109 ± 1	141 ± 6	136.2	−0.142	180.95	−1.28
ISO	–	800	900	10	–	–	–	–	–	–

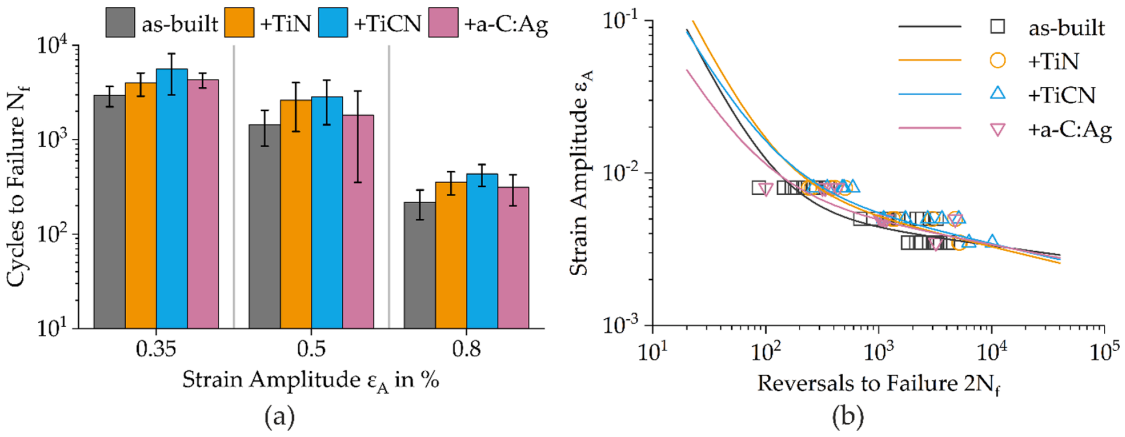

Fig. 3. (a) Cycles to failure for different conditions and strain amplitudes; (b) Coffin-Manson-Basquin plots for Ti-6Al-7Nb samples in as-built and PVD-coated conditions.

coated samples. In contrast, the fatigue strength exponents b are lower, resulting in a reduced fatigue performance for higher cycles.

The fracture surfaces of the monotonic tensile tests show similar, mainly ductile fracture behavior for all conditions since the substrate material is similar (Fig. 4 (a-c)). The fracture surface is divided into two areas, a primarily forced fracture in the inner fracture surface areas and a ductile fracture at the outer regions, see Fig. 4 (d-f). Fig. 4 (d-f) also depict the TiN, TiCN, and a-C:Ag PVD coatings at the edges of the fracture surfaces.

The SEM images of the LCF tests also indicate divided fracture surfaces (Fig. 5 (a-c)). Here, the inner surfaces mainly consist of forced fracture, see, for instance, Fig. 5 (d). In contrast to the monotonic tests' surfaces, the LCF tests' fracture surfaces depict distinct fatigue striations, highlighted by white arrows in Fig. 5 (e) and (f). The cracks typically propagate perpendicular to the fatigue striations and from the crack initiation spot. Since cracks often start at the outer surfaces and propagate to the center, the crack growth direction can be assumed, see black arrows in Fig. 5 (e) and (f). Characteristic LPBF defects, like gas pores and unmelted powder particles, are visible in all conditions and on all fracture surfaces (Fig. 5 (f)).

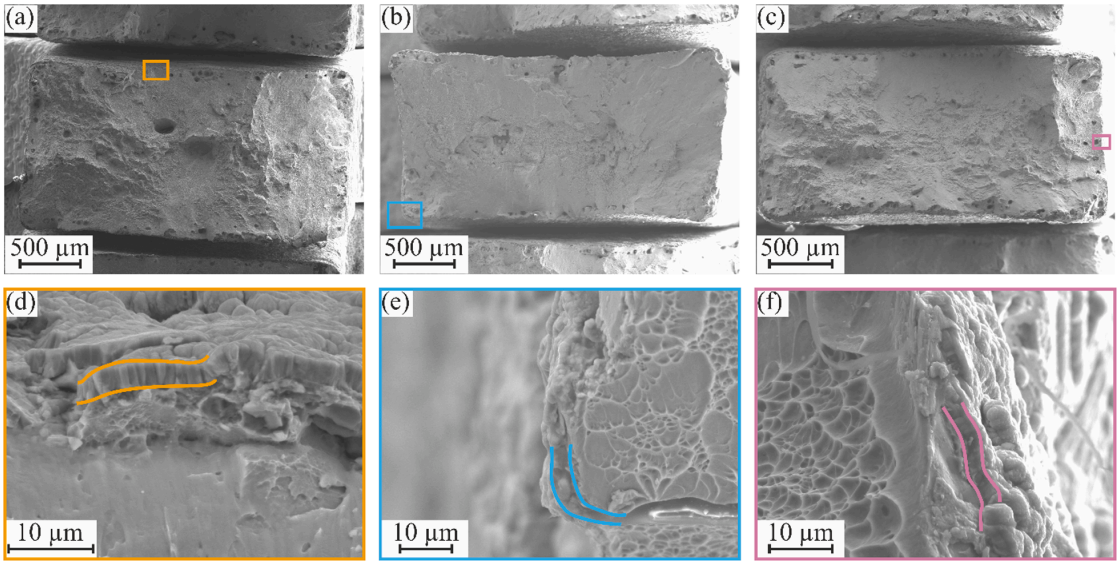

Fig. 4. SEM images of the tensile fracture surfaces of (a) TiN-; (b) TiCN-; and (c) a-C:Ag coated Ti-6Al-7Nb; (d) close-up of the orange box in (a) with markings of the TiN coating; (e) close-up of the blue box in (b) with markings of the TiCN coating; and (f) close-up of the pink box in (c) with markings of the a-C:Ag coating. (For interpretation of the references to colour in this figure legend, the reader is referred to the web version of this article.)

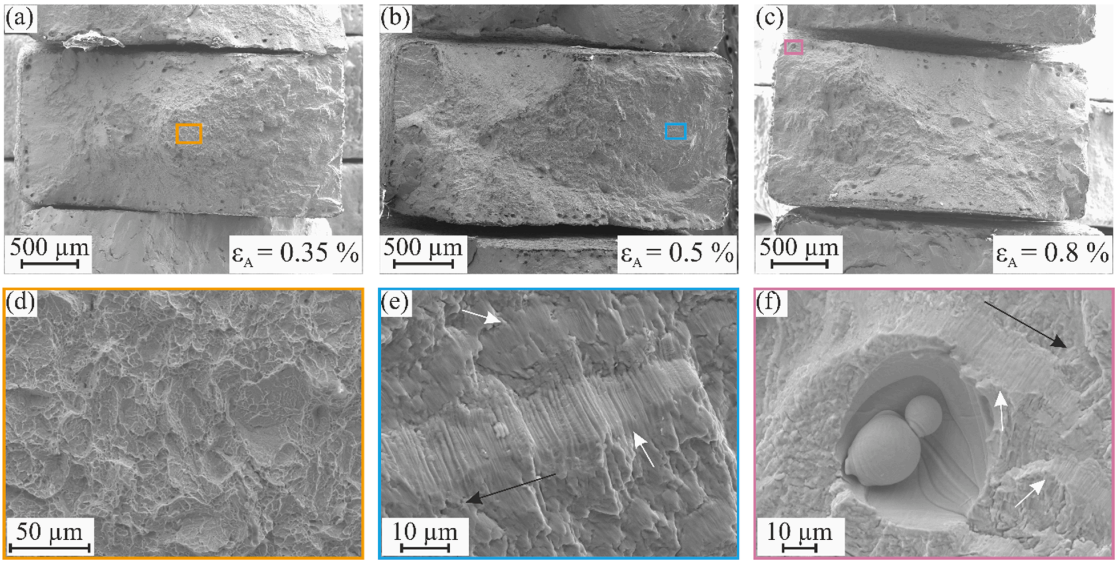

Fig. 5. SEM images of the LCF fracture surfaces of (a) TiN-; (b) TiCN-; and (c) a-C:Ag coated Ti-6Al-7Nb tested with different total strain amplitudes; (d) close-up of the orange box in (a) depicting the residual fracture face; (e) close-up of the blue box in (b) with fatigue striations (white arrows) and probable crack grow direction (black arrow); and (f) close-up of the pink box in (c) with fatigue striations (white arrows), probable crack grow direction (black arrow), and pore with unmelted powder particles. (For interpretation of the references to colour in this figure legend, the reader is referred to the web version of this article.)

4. Discussion

The hardness of the PVD coatings is significantly higher than that of the substrate material. The TiN, TiCN, and a–C:Ag layers exhibit high adhesion on the sandblasted Ti-6Al-7Nb substrate (adhesion class HF1). In a previous study, these PVD coatings exhibited a sufficiently good adhesion on the additively manufactured Ti-6Al-7Nb alloy with polished surfaces, with TiN, TiCN, and a-C:Ag having the adhesion classes HF1, HF3, and HF4, respectively [64]. The improved adhesion behavior is related to the rough, sandblasted surface since the roughness asperities ensure a mechanical interlocking of the thin coatings on the substrates [80].

In this study, the tensile and LCF samples are manufactured and blasted with the same parameters. Process-induced defects and a similar microstructure are present in the as-built and PVD-coated specimens and can therefore be neglected. The miniaturization of samples could affect fatigue and monotonic tensile behavior [34].

The monotonic tensile properties of all conditions fulfill the required ISO values [63]. These are comparable to each other and tests with the same geometry, but the comparison to the ISO values remains difficult.

The deposition of PVD coatings increases the YS and UTS in all coated states, accompanied by a decreased elongation at fracture. The effect of the coatings on the mechanical properties can be explained by changes in the structural surface state. The microplastic deformation in the subsurface layer leads to an increased dislocation density close to the surface, suppressing the movement of slip bands. This results in a barrier to the occurrence of dislocations on the surface and the formation of inhibited groups of dislocations, which again results in the appearance of internal compressive stresses working against dislocations formation and decreasing the effect of applied tensile stresses [58].

Similar to the monotonic tensile behavior and expectably based on the average service life, the TiCN coating presents the best fatigue performance in the tested strain amplitude range. For higher strain amplitudes and lower reversals ($2N_f < 10^2$ reversals), the fatigue performance can only be approximated rudimentarily. For high strain amplitudes, the as-built condition and the TiN coating reveal the best performance, although the TiCN coating shows the best monotonic and fatigue performance in the tested strain amplitude range. According to the fatigue ductility exponents c, the as-built condition would be favorable for lower reversals ($2N_f < 10$) and higher strain amplitudes, respectively. Concerning higher reversals ($2N_f > 10^4$), the as-built condition is preferable due to the larger fatigue strength exponent b. The larger fatigue ductility coefficients ε'_f of the PVD coatings, except for a-C:Ag, result in better fatigue performance for fewer cycles.

As the standard deviation of the a-C:Ag coated specimens at a strain amplitude of 0.5% is relatively high, particular attention should be given to the DLC coating. Although the coatings seem to have a predominantly positive effect on fatigue behavior, the a-C:Ag coating results and other studies show adverse effects. Bai et al. observed a reduction of the fatigue limit of Ti-6Al-4V coated with CrAlN and TiN coatings, due to impeded deformation at the beginning of fatigue tests and cracks inducing micro damages. These cracks typically initiate in the coating and propagate to the substrate [81]. Sundaram observed a slightly coating-induced fatigue degradation in Ti-6Al-4V due to DLC coatings [82]. Costa et al. showed decreasing fatigue life for coated conditions with TiN, CrN, and a-C:H:W (tungsten-containing amorphous carbon) compared to the base material. Nevertheless, the DLC coating results in the highest fatigue strength among the three coatings due to lower defect density, considering the sputtering technique, and a Cr interlayer, acting as fatigue crack propagation barrier [83]. In this study, the coatings were applied with the same sputtering technique, therefore, the defects density should be equivalent. As the a-C:Ag coating contains Ag nanocrystallites [51], these particles may act as crack nucleation sites, resulting in a decreased fatigue performance. In the case of an engineering application or mechanical design, the most critical case or worst test result should be assumed rather than the average life. However, in the case of LCF loading, applying the a-C:Ag coating should be avoided as it appears to harm the fatigue performance.

The surface conditions play a significant role in fatigue behavior. Mechanical surface treatments improve fatigue life by altering the roughness, hardness, and residual stress state [84]. The LCF performance is usually strongly connected to the monotonic tensile performance in terms of UTS, where higher strength leads to higher, tolerable strain amplitudes and higher fatigue life. The PVD-coated specimens, except for the a-C:Ag coating, show a superior LCF performance compared to as-built and heat-treated Ti-6Al-7Nb, due to microstructural changes and different surface conditions [47,84]. The fatigue strength is generally increased as higher monotonic strength hinders microplasticity and eventually local damage [34]. Studies show improvements in the LCF behavior by PVD coatings. These enhanced properties are attributed to the residual compressive stresses resulting from the coating deposition process and its hardening effect [55]. Other studies confirm the adverse effects of PVD coatings on LCF performance. Costa et al. performed fatigue tests with coated specimens, claiming decreased fatigue performance through arc evaporated coatings by coating defects and voids as crack nucleation sites. Nevertheless, processes with lower defect densities, like magnetron sputtering and ductile interlayer, improve performances [83]. According to Baragetti et al., the brittle nature of the coatings might generate cracks, which could behave like micro notches for the substrate [85]. PVD coatings may lead to decreased fatigue performance for smooth surfaces. In the case of rough, as-built, and blasted surfaces, as desired for biomedical applications [47], the PVD coatings increase the monotonic tensile properties and improve fatigue performance.

5. Conclusions

In this study, PVD thin coating surface modifications were applied to improve the mechanical properties of Ti-6Al-7Nb for biomedical applications. Various PVD coatings, namely TiN, TiCN, and a-C:Ag, were deposited on laser beam melted, blasted Ti-6Al-7Nb. The tensile and fatigue properties of Ti-6Al-7Nb could be enhanced to a certain extent after surface modification. The effect of depositing TiN, TiCN, and a-C:Ag PVD coatings on the hardness, monotonic tensile, and LCF performance of LPBF Ti-6Al-7Nb has been determined experimentally. The findings can be summarized as follows:

- The hardness of PVD-coated specimens has increased by factor 2 to 3, compared to the uncoated substrate material. TiN coating possesses the highest hardness.
- The TiN, TiCN, and a–C:Ag layers exhibit high adhesion on the sandblasted Ti-6Al-7Nb substrate (adhesion class HF1).
- The PVD-coated conditions reveal better strength characteristics compared to the as-built condition. Among the PVD coatings, TiCN shows the highest tensile strength, with slightly lower elongation at break compared to the as-built state.
- The deposition of PVD coatings leads to increased fatigue strengths. The PVD thin coatings improve the average number of cycles to failure for all tested strain amplitudes by 60% (TiN), 95% (TiCN), and 39% (a-C:Ag), as compared to the uncoated substrate material by altering the hardness and residual stress state. The a-C:Ag coated specimens show significant deviation for the medium strain amplitude (0.5%) even below the level of the as-built condition.

Concluding, the investigations underline that PVD coatings are highly effective in improving the tensile performance of additively manufactured Ti-6Al-7Nb. The PVD coatings enhance the fatigue performance, except for the medium strain amplitude of the a-C:Ag coated specimens. In summary, PVD coatings can be advantageous in the design of load-bearing implants. In a crucial application, such as an implant or prosthesis in the human body, the most critical load case or the worst-case scenario should be decisive. Accordingly, the a-C:Ag coating should only be considered to a limited extent in such an application since the influence of this coating does not seem to be consistently positive on the material behavior.

CRediT authorship contribution statement

Maxwell Hein: Conceptualization, Data curation, Formal analysis, Investigation, Project administration, Visualization, Writing – original draft. **Nelson Filipe Lopes Dias:** Writing – review & editing. **David Kokalj:** Writing – review & editing. **Dominic Stangier:** Writing – review & editing. **Kay-Peter Hoyer:** Supervision, Writing – review & editing. **Wolfgang Tillmann:** Funding acquisition, Resources, Writing – review & editing. **Mirko Schaper:** Funding acquisition, Resources, Supervision, Writing – review & editing.

Declaration of Competing Interest

The authors declare that they have no known competing financial interests or personal relationships that could have appeared to influence the work reported in this paper.

Acknowledgments

This work was supported by the German Research Foundation (DFG) within the project SCHA 1484/45-1 and TI 343/167-1.

References

[1] Gross BC, Erkal JL, Lockwood SY, Chen C, Spence DM. Evaluation of 3D printing and its potential impact on biotechnology and the chemical sciences. Anal Chem 2014;86(7):3240–53. https://doi.org/10.1021/ac403397r.
[2] Gebhardt A, Hötter J-S. Additive manufacturing: 3D printing for prototyping and manufacturing. Cincinnati, OH, Munich, Cincinnati: Hanser Publications; Hanser Publishers; 2016.
[3] Gibson I, Rosen D, Stucker B. Additive manufacturing technologies: 3D printing, rapid prototyping and direct digital manufacturing. New York, Heidelberg, Dodrecht, London: Springer; 2015.
[4] Dutta B, Froes FH. Additive manufacturing of titanium alloys: State of the art, challenges, and opportunities. Amsterdam, Boston, Heidelberg: Butterworth-Heinemann is an imprint of Elsevier; 2016. und 9 weitere:.
[5] Kumar R, Kumar M, Chohan JS. The role of additive manufacturing for biomedical applications: A critical review. J Manuf Process 2021;64:828–50. https://doi.org/10.1016/j.jmapro.2021.02.022.
[6] Javaid M, Haleem A. Additive manufacturing applications in medical cases: A literature based review. Alexandria J Med 2018;54(4):411–22. https://doi.org/10.1016/j.ajme.2017.09.003.
[7] Melchels FP, Domingos MA, Klein TJ, Malda J, Bartolo PJ, Hutmacher DW. Additive manufacturing of tissues and organs. Prog Polym Sci 2012;37(8):1079–104. https://doi.org/10.1016/j.progpolymsci.2011.11.007.
[8] Herzog D, Seyda V, Wycisk E, Emmelmann C. Additive manufacturing of metals. Acta Mater 2016;117:371–92. https://doi.org/10.1016/j.actamat.2016.07.019.
[9] Guo N, Leu MC. Additive manufacturing: technology, applications and research needs. Front. Mech. Eng. 2013;8(3):215–43. https://doi.org/10.1007/s11465-013-0248-8.
[10] Fazel-Rezai R. Biomedical Engineering - From Theory to Applications: From Theory to Applications. Erscheinungsort nicht ermittelbar: IntechOpen; 2011.
[11] Zaman HA, Sharif S, Idris MH, Kamarudin A. Metallic Biomaterials for Medical Implant Applications: A Review. AMM 2015;735:19–25. https://doi.org/10.4028/www.scientific.net/AMM.735.19.
[12] Festas AJ, Ramos A, Davim JP. Medical devices biomaterials – A review. Proc Institut Mech Eng, Part L: J Mater: Des Appl 2020;234(1):218–28. https://doi.org/10.1177/1464420719882458.
[13] Vandenbroucke B, Kruth JP. Selective laser melting of biocompatible metals for rapid manufacturing of medical parts. Rapid Prototyp J 2007;13(4):196–203. https://doi.org/10.1108/13552540710776142.
[14] Iijima D. Wear properties of Ti and Ti–6Al–7Nb castings for dental prostheses. Biomaterials 2003;24(8):1519–24. https://doi.org/10.1016/S0142-9612(02)00533-1.
[15] Niinomi M. Mechanical biocompatibilities of titanium alloys for biomedical applications. J Mech Behav Biomed Mater 2008;1(1):30–42. https://doi.org/10.1016/j.jmbbm.2007.07.001.
[16] Hollander DA, von Walter M, Wirtz T, Sellei R, Schmidt-Rohlfing B, Paar O, et al. Structural, mechanical and in vitro characterization of individually structured Ti-6Al-4V produced by direct laser forming. Biomaterials 2006;27(7):955–63. https://doi.org/10.1016/j.biomaterials.2005.07.041.
[17] Murr LE, Quinones SA, Gaytan SM, Lopez MI, Rodela A, Martinez EY, et al. Microstructure and mechanical behavior of Ti-6Al-4V produced by rapid-layer manufacturing, for biomedical applications. J Mech Behav Biomed Mater 2009;2(1):20–32. https://doi.org/10.1016/j.jmbbm.2008.05.004.
[18] Browne RC. Vanadium poisoning from gas turbines. Br J Ind Med 1955;12(1):57–9. https://doi.org/10.1136/oem.12.1.57.
[19] Laing P.G. Clinical experience with prosthetic materials: Historical perspectives, current problems, and future directions. In: Syrett B.C, Acharya A, editors. Corrosion and degradation of implant materials. 100 Barr Harbor Drive, PO Box C700. West Conshohocken, PA: 19428-2959: ASTM International; 1979. p. 199–211.
[20] Sjoberg S-G. Vanadium dust, chronic bronchitis and possible risk of emphysema; a follow-up investigation of workers at a vanadium factory. Acta Med Scand 1956;154(5):381–6.
[21] López M, Gutiérrez A, Jiménez J. In vitro corrosion behaviour of titanium alloys without vanadium. Electrochim Acta 2002;47(9):1359–64. https://doi.org/10.1016/S0013-4686(01)00860-X.
[22] Chlebus E, Kuźnicka B, Kurzynowski T, Dybała B. Microstructure and mechanical behaviour of Ti-6Al-7Nb alloy produced by selective laser melting. Mater Charact 2011;62(5):488–95. https://doi.org/10.1016/j.matchar.2011.03.006.
[23] Tamilselvi S, Raman V, Rajendran N. Corrosion behaviour of Ti–6Al–7Nb and Ti–6Al–4V ELI alloys in the simulated body fluid solution by electrochemical impedance spectroscopy. Electrochim Acta 2006;52(3):839–46. https://doi.org/10.1016/j.electacta.2006.06.018.
[24] Metikoš-Huković M, Kwokal A, Piljac J. The influence of niobium and vanadium on passivity of titanium-based implants in physiological solution. Biomaterials 2003;24(21):3765–75. https://doi.org/10.1016/S0142-9612(03)00252-7.
[25] Lewandowski JJ, Seifi M. Metal Additive Manufacturing: A Review of Mechanical Properties. Annu. Rev. Mater. Res. 2016;46(1):151–86. https://doi.org/10.1146/annurev-matsci-070115-032024.
[26] Yap CY, Chua CK, Dong ZL, Liu ZH, Zhang DQ, Loh LE, et al. Review of selective laser melting: Materials and applications. Appl Phys Rev 2015;2(4):41101. https://doi.org/10.1063/1.4935926.
[27] Bergmann G, Graichen F, Rohlmann A, Bender A, Heinlein B, Duda GN, et al. Realistic loads for testing hip implants. Biomed Mater Eng 2010;20(2):65–75. https://doi.org/10.3233/BME-2010-0616.
[28] Bergmann G, Bender A, Dymke J, Duda G, Damm P. Standardized Loads Acting in Hip Implants. PLoS ONE 2016;11(5):e0155612. https://doi.org/10.1371/journal.pone.0155612.
[29] Baufeld B, Brandl E, van der Biest O. Wire based additive layer manufacturing: Comparison of microstructure and mechanical properties of Ti–6Al–4V components fabricated by laser-beam deposition and shaped metal deposition. J Mater Process Technol 2011;211(6):1146–58. https://doi.org/10.1016/j.jmatprotec.2011.01.018.
[30] Brandl E. Microstructural and mechanical properties of additive manufactured titanium (Ti-6Al-4V) using wire: Evaluation with respect to additive processes using powder and aerospace material specifications. Zugl.: Cottbus, Techn. Univ., Diss., 2010. Aachen: Shaker; 2010.
[31] Khorasani A, Gibson I, Goldberg M, Littlefair G. On the role of different annealing heat treatments on mechanical properties and microstructure of selective laser melted and conventional wrought Ti-6Al-4V. Rapid Prototyp J 2017;23(2):295–304. https://doi.org/10.1108/RPJ-02-2016-0022.
[32] Liu S, Shin YC. Additive manufacturing of Ti6Al4V alloy: A review. Mater Des 2019;164:107552. https://doi.org/10.1016/j.matdes.2018.107552.
[33] Riemer A, Richard HA. Crack Propagation in Additive Manufactured Materials and Structures. Procedia Struct. Integ. 2016;2:1229–36. https://doi.org/10.1016/j.prostr.2016.06.157.
[34] Leuders S, Lieneke T, Lammers S, Tröster T, Niendorf T. On the fatigue properties of metals manufactured by selective laser melting – The role of ductility. J. Mater. Res. 2014;29(17):1911–9. https://doi.org/10.1557/jmr.2014.157.
[35] Tolosa I, Garciandía F, Zubiri F, Zapirain F, Esnaola A. Study of mechanical properties of AISI 316 stainless steel processed by "selective laser melting", following different manufacturing strategies. Int J Adv Manuf Technol 2010;51(5–8):639–47. https://doi.org/10.1007/s00170-010-2631-5.
[36] Nezhadfar PD, Burford E, Anderson-Wedge K, Zhang B, Shao S, Daniewicz SR, et al. Fatigue crack growth behavior of additively manufactured 17–4 PH stainless steel: Effects of build orientation and microstructure. Int J Fatigue 2019;123:168–79. https://doi.org/10.1016/j.ijfatigue.2019.02.015.
[37] Kluczyński J, Śnieżek L, Grzelak K, Torzewski J, Szachogłuchowicz I, Wachowski M, et al. Crack Growth Behavior of Additively Manufactured 316L Steel-Influence of Build Orientation and Heat Treatment. Materials (Basel) 2020;13(15). https://doi.org/10.3390/ma13153259.
[38] Zhang M, Sun C-N, Zhang X, Wei J, Hardacre D, Li H. High cycle fatigue and ratcheting interaction of laser powder bed fusion stainless steel 316L: Fracture behaviour and stress-based modelling. Int J Fatigue 2019;121:252–64. https://doi.org/10.1016/j.ijfatigue.2018.12.016.
[39] Jerrard PGE, Hao L, Evans KE. Experimental investigation into selective laser melting of austenitic and martensitic stainless steel powder mixtures. Proc Inst Mech Eng B J Eng Manuf 2009;223(11):1409–16. https://doi.org/10.1243/09544054JEM1574.
[40] Tillmann W, Hagen L, Garthe K-U, Hoyer K-P, Schaper M. Effect of substrate pre-treatment on the low cycle fatigue performance of tungsten carbide-cobalt coated additive manufactured 316 L substrates. Mat.-wiss. u. Werkstofftech. 2020;51(11):1452–64. https://doi.org/10.1002/mawe.202000109.
[41] Romano S, Patriarca L, Foletti S, Beretta S. LCF behaviour and a comprehensive life prediction model for AlSi10Mg obtained by SLM. Int J Fatigue 2018;117:47–62. https://doi.org/10.1016/j.ijfatigue.2018.07.030.
[42] Bressan S, Ogawa F, Itoh T, Berto F. Low cycle fatigue behavior of additively manufactured Ti-6Al-4V under non-proportional and proportional loading. Frat. ed Integrita Strutt. 2019;13(48):18–25. https://doi.org/10.3221/IGF-ESIS.48.03.
[43] Zhang SQ, Li SJ, Jia MT, Prima F, Chen LJ, Hao YL, et al. Low-cycle fatigue properties of a titanium alloy exhibiting nonlinear elastic deformation behavior. Acta Mater 2011;59(11):4690–9. https://doi.org/10.1016/j.actamat.2011.04.015.
[44] Awd M, Tenkamp J, Hirtler M, Siddique S, Bambach M, Walther F. Comparison of Microstructure and Mechanical Properties of Scalmalloy® Produced by Selective Laser Melting and Laser Metal Deposition. Materials (Basel) 2017;11(1). https://doi.org/10.3390/ma11010017.
[45] Leuders S, Thöne M, Riemer A, Niendorf T, Tröster T, Richard HA, et al. On the mechanical behaviour of titanium alloy TiAl6V4 manufactured by selective laser melting: Fatigue resistance and crack growth performance. Int J Fatigue 2013;48:300–7. https://doi.org/10.1016/j.ijfatigue.2012.11.011.
[46] Wycisk E, Siddique S, Herzog D, Walther F, Emmelmann C. Fatigue Performance of Laser Additive Manufactured Ti–6Al–4V in Very High Cycle Fatigue Regime up to 109 Cycles. Front. Mater. 2015;2. https://doi.org/10.3389/fmats.2015.00072.
[47] Hein M, Kokalj D, Lopes Dias NF, Stangier D, Oltmanns H, Pramanik S, et al. Low Cycle Fatigue Performance of Additively Processed and Heat-Treated Ti-6Al-7Nb Alloy for Biomedical Applications. Metals (Basel) 2022;12(1):122. https://doi.org/10.3390/met12010122.
[48] Brunette DM. Titanium in Medicine: Material Science, Surface Science, Engineering, Biological Responses and Medical Applications. Berlin, Heidelberg: Springer; 2001.
[49] Liu X, Chu P, Ding C. Surface modification of titanium, titanium alloys, and related materials for biomedical applications. Mater Sci Eng R Rep 2004;47(3–4):49–121. https://doi.org/10.1016/j.mser.2004.11.001.

[50] Kulkarni M, Mazare A, Schmuki P, Iglič A. Biomaterial surface modification of titanium and titanium alloys for medical applications. In: One Central Press, editor. Nanomedicine; 2014, p. 111–136.

[51] Tillmann W, Lopes Dias NF, Franke C, Kokalj D, Stangier D, Filor V, et al. Tribo-mechanical properties and biocompatibility of Ag-containing amorphous carbon films deposited onto Ti6Al4V. Surf Coat Technol 2021;421:127384. https://doi.org/10.1016/j.surfcoat.2021.127384.

[52] Tillmann W, Lopes Dias NF, Stangier D, Hagen L, Schaper M, Hengsbach F, et al. Tribo-mechanical properties and adhesion behavior of DLC coatings sputtered onto 36NiCrMo16 produced by selective laser melting. Surf Coat Technol 2020;394:125748. https://doi.org/10.1016/j.surfcoat.2020.125748.

[53] Glodež S, Podgrajšek M, Podgornik B, Ren Z. The influence of PVD coating on the low cycle fatigue behaviour of Cr-Mo-V steel at elevated temperatures. Surf Coat Technol 2017;321:358–65. https://doi.org/10.1016/j.surfcoat.2017.05.008.

[54] Gopkalo AP, Muzyka NR, Rutkovskii AV, Shvets VP. Effect of PVD coatings on the strain and low-cycle fatigue resistance of stainless steel and titanium alloys. Strength Mater 2011;43(6):604–14. https://doi.org/10.1007/s11223-011-9333-6.

[55] Gopkalo AP, Rutkovskyy AV. The effect of PVD coatings on the tensile strength and low-cycle fatigue resistance of stainless steel and titanium alloys. Fatigue Fract Eng Mater Struct 2011;34(12):1012–20. https://doi.org/10.1111/j.1460-2695.2011.01590.x.

[56] Twu MJ, Hu CC, Liu DW, Hsu CY, Kuo CG. Effects of TiN, CrN and TiAlN coatings using reactive sputtering on the fatigue behaviour of AA2024 and medium carbon steel specimens. J Exp Nanosci 2016;11(7):581–92. https://doi.org/10.1080/17458080.2015.1100332.

[57] Correa Jácome JF, Caicedo Angulo JC, Castro YA. PVD coatings influence (TiCN, BCN, and CrAlN) on the fatigue life behavior of AISI 1045 steel for automotive applications. Int J Adv Manuf Technol 2022. https://doi.org/10.1007/s00170-021-08455-8.

[58] Rutkovskii AV, Lyashenko BA, Gopkalo AP, Soroka EB. On the hardening effect of plasma-deposited coatings. Strength Mater 1999;31(6):616–8. https://doi.org/10.1007/BF02510898.

[59] Puchi-Cabrera ES, Matínez F, Herrera I, Berríos J, Dixit S, Bhat D. On the fatigue behavior of an AISI 316L stainless steel coated with a PVD TiN deposit. Surf Coat Technol 2004;182(2–3):276–86. https://doi.org/10.1016/j.surfcoat.2003.07.003.

[60] Kim KR, Suh CM, Murakami RI, Chung CW. Effect of intrinsic properties of ceramic coatings on fatigue behavior of Cr–Mo–V steels. Surf Coat Technol 2003;171(1–3):15–23. https://doi.org/10.1016/S0257-8972(03)00229-9.

[61] Berríos JA, Teer DG, Puchi-Cabrera ES. Fatigue properties of a 316L stainless steel coated with different TiNx deposits. Surf Coat Technol 2001;148(2–3):179–90. https://doi.org/10.1016/S0257-8972(01)01346-9.

[62] Hein M, Hoyer K-P, Schaper M. Additively processed TiAl6Nb7 alloy for biomedical applications. Mat.-wiss. u. Werkstofftech. 2021;52(7):703–16. https://doi.org/10.1002/mawe.202000288.

[63] DIN Deutsches Institut für Normung e. V. Chirurgische Implantate – Metallische Werkstoffe – Teil 11: Titan Aluminium-6 Niob-7 Knetlegierung (ISO 5832-11:2014). ISO 5832-11:2014 2015(5832-11:2015-12).

[64] Tillmann W, Lopes Dias NF, Kokalj D, Stangier D, Hein M, Hoyer K-P, et al. Tribo-functional PVD thin films deposited onto additively manufactured Ti6Al7Nb for biomedical applications. under review. Mater Lett 2022.

[65] Janssen G, Abdalla MM, van Keulen F, Pujada BR, van Venrooy B. Celebrating the 100th anniversary of the Stoney equation for film stress: Developments from polycrystalline steel strips to single crystal silicon wafers. Thin Solid Films 2009;517(6):1858–67. https://doi.org/10.1016/j.tsf.2008.07.014.

[66] Tillmann W, Lopes Dias NF, Franke C, Kokalj D, Stangier D, Thomann CA, et al. Mechanical properties and adhesion behavior of amorphous carbon films with bias voltage controlled TixCy interlayers on Ti6Al4V. Diam Relat Mater 2021;115:108361. https://doi.org/10.1016/j.diamond.2021.108361.

[67] DIN 4856:2018-02, Kohlenstoffschichten und andere Hartstoffschichten_-Rockwell-Eindringprüfung zur Bewertung der Haftung. Berlin: Beuth Verlag GmbH. https://doi.org/10.31030/2795562.

[68] DIN EN ISO 6892-1:2020-06, Metallische Werkstoffe_- Zugversuch_- Teil_1: Prüfverfahren bei Raumtemperatur (ISO_6892-1:2019); Deutsche Fassung EN_ISO_6892-1:2019. Berlin: Beuth Verlag GmbH. https://doi.org/10.31030/3132591.

[69] ASTM International. ASTM Standard E606/E606M-12 - Standard Test Method for Strain-Controlled Fatigue Testing. West Conshohocken, PA: ASTM International. https://doi.org/10.1520/E0606-04E01.

[70] Plumtree A. Cyclic stress–strain response and substructure. Int J Fatigue 2001;23(9):799–805. https://doi.org/10.1016/S0142-1123(01)00037-8.

[71] Rice R.C. Fatigue design handbook. 2nd ed. Pa: Warrendale; 1988.

[72] Skelton RP, Maier HJ, Christ H-J. The Bauschinger effect, Masing model and the Ramberg-Osgood relation for cyclic deformation in metals. Mater Sci Eng A Struct Mater 1997;238(2):377–90. https://doi.org/10.1016/s0921-5093(97)00465-6.

[73] Nieslony A, Dsoki C, Kaufmann H, Krug P. New method for evaluation of the Manson–Coffin–Basquin and Ramberg-Osgood equations with respect to compatibility. Int J Fatigue 2008;30(10–11):1967–77. https://doi.org/10.1016/j.ijfatigue.2008.01.012.

[74] Basquin OH. The exponential law of endurance tests. Am. Soc. Test. Mater. 1910;10:625–30.

[75] Coffin LF. A Study of the Effects of Cyclic Thermal Stresses on a Ductile Metal. Trans. Am. Soc. Me. 1954;76.

[76] Manson SS. Behavior of Materials Under Conditions of Thermal Stress. National Advisory Committee for Aeronautics 1953.

[77] Suresh S. Fatigue of materials. 2nd ed. Cambridge: Cambridge Univ. Press; 2004.

[78] ASM International. Fatigue and fracture. 10th ed. Materials Park, Ohio: ASM International; 2002.

[79] Cheng YH, Browne T, Heckerman B. Influence of CH4 fraction on the composition, structure, and internal stress of the TiCN coatings deposited by LAFAD technique. Vacuum 2010;85(1):89–94. https://doi.org/10.1016/j.vacuum.2010.04.007.

[80] Weiss H. Adhesion of advanced overlay coatings: mechanisms and quantitative assessment. Surf Coat Technol 1995;71(2):201–7. https://doi.org/10.1016/0257-8972(94)01022-B.

[81] Bai Y, Xi Y, Gao K, Yang H, Pang X, Yang X, et al. Brittle coating effects on fatigue cracks behavior in Ti alloys. Int J Fatigue 2019;125:432–9. https://doi.org/10.1016/j.ijfatigue.2019.04.017.

[82] Sundaram VS. Diamond like carbon film as a protective coating for high strength steel and titanium alloy. Surf Coat Technol 2006;201(6):2707–11. https://doi.org/10.1016/j.surfcoat.2006.05.046.

[83] Costa M, Venditti M, Cioffi M, Voorwald H, Guimarães VA, Ruas R. Fatigue behavior of PVD coated Ti–6Al–4V alloy. Int J Fatigue 2011;33(6):759–65. https://doi.org/10.1016/j.ijfatigue.2010.11.007.

[84] Donachie MJ. Titanium: A technical guide. 2nd ed. Materials Park, OH: ASM International; 2000.

[85] Baragetti S, Lusvarghi L, Pighetti Mantini F, Tordini F. Fatigue Behaviour of Notched PVD-Coated Titanium Components. KEM 2007;348–349:313–6. https://doi.org/10.4028/www.scientific.net/KEM.348-349.313.

Paper D

M. Hein

Influence of Physical Vapor Deposition on High-cycle Fatigue Performance of Additively Manufactured Ti-6Al-7Nb Alloy

Crystals, 12, 1190, 2022 [297].

crystals

MDPI

Article

Influence of Physical Vapor Deposition on High-Cycle Fatigue Performance of Additively Manufactured Ti-6Al-7Nb Alloy

Maxwell Hein [1,2]

[1] Chair of Materials Science (LWK), Paderborn University, Warburger Str. 100, 33098 Paderborn, Germany; hein@lwk.upb.de
[2] DMRC—Direct Manufacturing Research Center, Paderborn University, Mersinweg 3, 33100 Paderborn, Germany

Abstract: Load-bearing permanent implants, such as hip or knee joint replacements, are permanently loaded in the human body and must withstand considerable high loading cycles. The characteristic properties of additively manufactured Ti-6Al-7Nb, manufactured by laser powder bed fusion (LPBF), such as a rough surface and high residual stresses, have a detrimental effect on the fatigue behavior of such components. Functional physical vapor deposition (PVD) coatings and heat treatments offer the possibility to influence these properties. For this reason, the effects of stress-relief heat treatment (SR; 600 °C/4 h) and three PVD coatings (titanium nitride (TiN), titanium carbonitride (TiCN), and silver-containing amorphous carbon (a-C:Ag)) on the mechanical properties, in terms of high-cycle fatigue, are identified. Wöhler curves are determined and the staircase procedure ascertains the fatigue strengths. The fatigue strengths increase compared to the as-built condition by 105.4% (SR), 44.2% (TiN), 31.1% (TiCN), and 2.6% (a-C:Ag). Fracture surfaces are analyzed by scanning electron microscopy and show LPBF characteristic defects such as pores. The surfaces are partially divided into forced and fatigue fracture, the latter characterized by fatigue striations. Overall, PVD coatings, and especially SR, lead to an improved high-cycle fatigue behavior.

Keywords: laser powder bed fusion; Ti-6Al-7Nb; titanium alloy; biomedical engineering; high-cycle fatigue

Citation: Hein, M. Influence of Physical Vapor Deposition on High-Cycle Fatigue Performance of Additively Manufactured Ti-6Al-7Nb Alloy. *Crystals* **2022**, *12*, 1190. https://doi.org/10.3390/cryst12091190

Academic Editor: Umberto Prisco

Received: 21 July 2022
Accepted: 17 August 2022
Published: 24 August 2022

1. Introduction

Additive manufacturing (AM) encompasses various near-net-shape manufacturing techniques, including binder jetting, direct energy deposition, and laser powder bed fusion (LPBF). In these techniques, complex geometries and structures are formed layer by layer [1]. Thereof, LPBF is the most established method for AM of metals [2–4]. With it, it is possible to fabricate cost-effective and economic near-net-shape parts that are normally quite challenging to fabricate via conventional methods [5,6]. Accordingly, this technique has many applications in different sectors, such as aerospace, automobile, and biomedical. In the latter, LPBF has especially great potential in arthroplasty to produce patient-specific prostheses, such as hip or knee implants [7,8]. These load-bearing implants use various metallic materials, such as stainless steel alloys, cobalt-chromium alloys, or titanium alloys [9–11]. Compared to other biomaterials, titanium and its alloys have excellent mechanical properties—high specific strength, favorable lower elastic modulus, and excellent biocompatibility [12–16]. Despite the variety of used alloys, there is still room for enhancement. For instance, replacing alloying elements can further enhance biocompatibility [17–19]. Comparing Ti-6Al-4V vs. Ti-6Al-7Nb, in the former alloy, replacing the cytotoxic vanadium with niobium further enhances the local biocompatibility, increases corrosion resistance, and at the same time, preserves the mechanical properties, such as tensile strength [20–22]. This makes the Ti-6Al-7Nb alloy the optimal candidate as a biomaterial. However, like other additively manufactured alloys, achieving optimal mechanical properties of Ti-6Al-7Nb requires further optimization. Various research focused

on the mechanical performance of additively manufactured alloys, such as steels (316L, 17-4 PH) or titanium alloys (Ti-6Al-4V, Ti-6Al-7Nb, Ti-24Nb-4Zr-8Sn) [23–27]. Some of those studies focus on fatigue properties in terms of low-cycle fatigue (LCF) and high-cycle fatigue (HCF), as well as crack growth analysis of additively manufactured specimens of steels [28–33] and titanium alloys [34–40], with no further processing steps. One of these processing steps is applying functional physical vapor deposition (PVD) thin coatings. This technique is very beneficial since it improves strength, wear, tribological properties, corrosion resistance, and biocompatibility [41–44]. Different layer types are appropriate for biomedical applications, including nitride-based coatings, such as titanium nitride (TiN) or titanium carbonitride (TiCN), and amorphous carbon (a-C) [45,46]. In the latter, antibacterial activity and cell proliferation can be tailored by adding silver particles and adjusting the chemical composition of the silver-containing amorphous carbon coating (a-C:Ag) [44]. Although these improve wear properties, PVD coatings may reduce fatigue life by creating crack-initiating sites. Subsequently, instead of three stages for failure to occur, just two are required: propagation and saturation [47]. However, PVD coatings may also introduce compressive residual stresses. These compressive stresses enhance fatigue performance and they, therefore, can potentially increase fatigue life [48]. Therefore, PVD coatings were successfully applied on different base materials to increase the fatigue performance. For example, Puchi-Cabrera et al. deposited a-C (diamond-like carbon; DLC) and TiN on 1.4404 stainless steel. Compared to base steel, these coatings increased both fatigue life and limit. This increase was due to compressive residual stresses and good adhesion to the substrate, which delayed crack initiation [49,50]. Fatigue properties were also improved in other base steel alloys. For example, Jácome et al. deposited TiCN, boron carbonitride (BCN), and chromium aluminum nitride (CrAlN) on 1.1191 steel [51]. As stated before, deposition does not necessarily improve fatigue life at all times, depending on the layer chemical composition, substrate, layer thickness, and fatigue stress amplitude (low vs. high). In some cases, fatigue properties deteriorate. For example, Ferreira et al. deposited tungsten (W), tungsten nitride (WN), tungsten titanium (WTi), and tungsten titanium nitride (WTiN) on 1.7225 steel to enhance mechanical properties. In these trials, while only the WTi coating increased fatigue life at low amplitudes, all coatings decreased fatigue life at high amplitudes [52]. Therefore, it can be deduced that the interaction between the deposited layer and the substrate could affect the resulting properties. Consequently, to study the influence of substrate material on fatigue properties, Baragetti et al. deposited chromium nitride (CrN) on 1.4462 duplex stainless steel, 1.2343 tool steel, and EN AW-6082 aluminum alloy. In this work, while CrN increased the fatigue limit of the coated steel specimens, no enhancement in the coated aluminum specimens was detectable [48]. This increase in the former can be attributed to the increase in the critical crack length resulting from the coating adhering well to the substrate [53]. This does not necessarily mean that other types of layers could adhere well to steel. Another coating seems to affect its fatigue life negatively. DLC coating, for example, decreases the fatigue properties. The use of these coatings could, nonetheless, improve other properties, such as corrosion resistance and corrosion fatigue [54]. Therefore, optimizing a certain alloy requires careful selection and finetuning of the deposited layer. The encouraging results and versatility of PVD coatings led it being employed for other alloys. For example, it can improve titanium alloys' performance and properties. Compared to the base materials, Gopkalo et al. showed that coatings with TiN, chromium (Cr), (Cr+TiN), (TiC)N, (TiAl)N on Ti-6Al-4V, Ti-10V-2Fe-3Al, Ti-5Al-2.5Sn, and 1.4541 steel alloy could increase fatigue life [55]. Nonetheless, depending on the titanium alloys, other coatings can, however, have adverse effects. For example, Costa et al. showed that TiN, CrN, and DLC coatings deposited on a Ti-6Al-4V substrate could decrease fatigue performance [56,57]. This seems to be consistent with Bai et al. [58]. They showed TiN or CrAlN decreases the fatigue limit of Ti-6Al-4V by approximately 38%. In all these tests, the integrity of the deposited layer is essential to enhance fatigue properties. The resulting defects in the coating can act as crack-initiation locations.

Despite all the benefits and versatility of PVD to biomedical applications, there is a lack of research on the effects of PVD coatings on additively manufactured materials. Accordingly, this research aims to bridge this knowledge gap, particularly for the biomedical Ti-6Al-7Nb titanium alloy. In this research, the effects of various deposited PVD coatings—TiN, TiCN, and a-C:Ag—on the mechanical behavior in terms of HCF are investigated.

2. Materials and Methods

Gas-atomized pre-alloyed powder of (α + β)-phase Ti-6Al-7Nb was used to study the effects of PVD on the fatigue performance of samples manufactured using LPBF. ECKART TLS GmbH (ECKART TLS GmbH, Bitterfeld, Germany) provided this powder. A previous publication studied and reported its morphology and chemical composition [25]. Before fabricating the samples, different steps were employed. First, a pre-processing drying step was used to reduce residual humidity. The resulting powder relative humidity was below 5%. Following this step, Materialise Magics software (V 21.1, Materialise GmbH, Munich, Germany) was utilized for data and building job preparations. These build jobs were performed in LT12 SLM machine (DMG MORI AG, Bielefeld, Germany). It is equipped with a 1067 nm Nd:YAG laser source with power up to 400 W and a 35 µm spot diameter. This machine uses an inert argon atmosphere with an oxygen content between 0.08 and 0.13% to prevent undesired oxidation and contamination of the melt pool. Depending on the region, contour, or hatch, two constant parameter sets were used to obtain the fatigue samples' high relative densities, see Table 1. The hatch was exposed with 5 mm stripes, rotated layer by layer by 67°. During this process, the building platform temperature was kept at 200 °C.

Table 1. LPBF parameters for the hatch and contour of Ti-6Al-7Nb; 5 mm stripe exposure, rotated layer by layer by 67°; constant building platform temperature at 200 °C.

Parameter Sets	Layer Thickness t in µm	Laser Power P in W	Scanning Speed in m s^{-1}	Hatch Distance h in mm
Hatch	50	185	1.675	0.077
Contour	50	123	0.512	-

The dimensions and geometry of the fatigue specimens were fabricated according to Niendorf [59], see Figure 1a. Simulation showed that stress distribution in the notch root is homogenous and without any significant stress gradients. The specimens, therefore, can be considered notch free and are applied for HCF tests [59]. As described by Hein et al., shot peening with Al_2O_3 may be beneficial in terms of antibacterial effects and low-cycle fatigue performance [60]. Therefore, all specimens were blasted with high-grade Al_2O_3. For that, an SMG 25 DUO (MHG Strahlanlagen GmbH, Düsseldorf, Germany) machine was used. The utilized Al_2O_3 particle sizes ranged from 70 to 250 µm. These particles were blasted on the surface with an air pressure of 4 bar. The as-built specimen is depicted in Figure 1b. Additionally, stress-relief heat treatment (SR) was employed. SR was implemented under vacuum at 600 °C for 4 h to reduce residual stresses, characteristic of the LPBF process, and decomposition of α′ to α phase [61,62]. The SR specimen is shown in Figure 1c. This treatment is implemented for one condition to determine the effect of SR on the HCF behavior as it is beneficial for quasi-static and low-cycle fatigue performance [60].

The PVD coatings were deposited on the substrate via magnetron sputtering using a CC800/9 Custom (CemeCon AG, Würselen, Germany). The TiN and TiCN coatings were deposited with Ti targets and bipolarly pulsed with a cathode power of 4 kW at a mid-frequency of 50 kHz. For TiN, an interlayer of Ti was applied by sputtering Ti targets in a reactive-free atmosphere, following the introduction of reactive N_2 to the deposition chamber. The TiCN coating was deposited with a bilayered Ti/TiN interlayer. The surface layer of TiCN was sputtered in a reactive atmosphere by keeping the N_2 flow constant and injecting acetylene (C_2H_2) into the chamber. During the deposition of the TiN and TiCN coatings, the bias voltage was set to −70 V, the base pressure was 5 mPa, and the working

pressure was Ar controlled and kept constant at 450 mPa. The chamber was heated with a heating power of 5 kW, which equals about 400 °C. The a-C:Ag coating was deposited with a chemically graded titanium carbide (Ti_XC_Y) interlayer, deposited by simultaneously sputtering Ti and graphite targets. A detailed explanation of the deposition process is provided in [63]. The a-C:Ag coating was deposited with two graphite targets with Ag pellets, bipolarly pulsed at a mid-frequency of 20 kHz, with an average cathode power of 2 kW and a bias voltage of −100 V. The base pressure was 5 mPa and the working pressure was Ar controlled and set to 300 mPa. The chamber was not actively heated during the deposition of a-C:Ag, but the chamber temperature was about 120 °C due to the plasma. A detailed description of the a-C:Ag deposition process is given in [44]. Tillmann et al. summarized the properties of the three deposited coatings [43]. The different conditions are depicted in Figure 1—as built (Figure 1b), stress relieved (Figure 1c), TiN (Figure 1d), TiCN (Figure 1e), and a 7.5 at.% silver-containing a-C coating (a-C:Ag, Figure 1f).

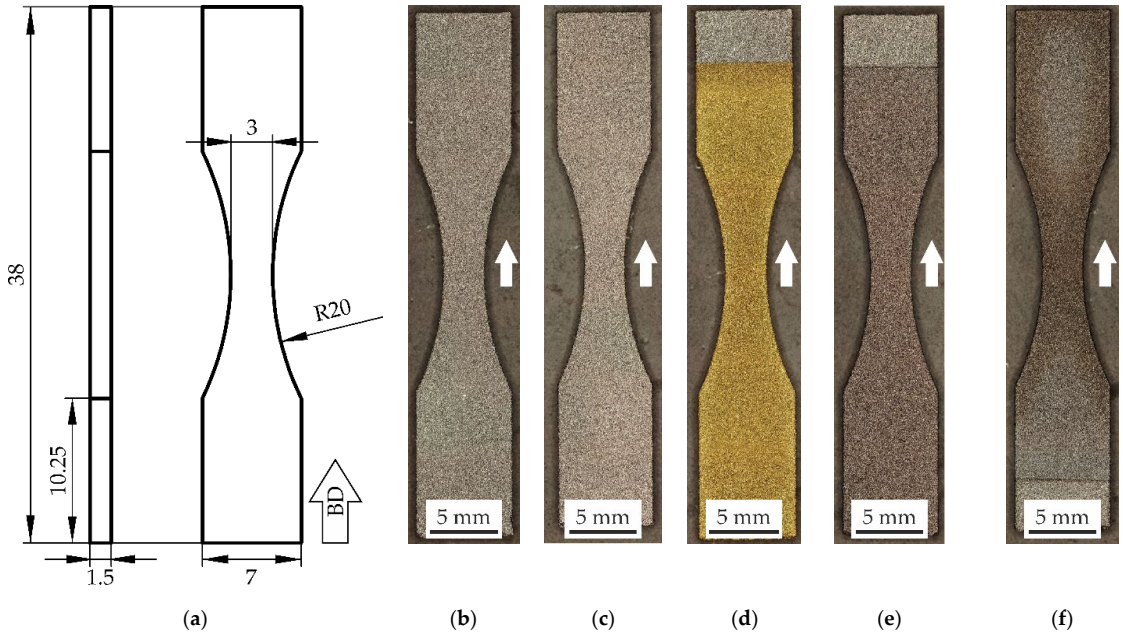

Figure 1. (**a**) Geometry and build direction (BD) of the fatigue specimens; overview of specimens in different conditions (**b**) as built; (**c**) stress relieved (SR); (**d**) titanium nitride (TiN); (**e**) titanium carbonitride (TiCN); (**f**) silver-containing amorphous carbon (a-C:Ag).

The surface roughness of the specimens was measured using the tactile profile method. In it, the diamond tip is equipped with a profilometer Hommel Etamic T8000 (Jenoptic AG, Jena, Germany). According to DIN EN ISO 4288, five roughness measurements were performed per specimen [64]. Ten specimens per condition were evaluated to determine the average roughness depth, Rz, and the arithmetical mean roughness, Ra.

Regarding the HCF, two kinds of testing could be used: stress-controlled loading and strain-controlled fatigue testing. As healthy bones usually respond to different types of loading by elastic stress and strain [65], stress-controlled testing is a good way to test prostheses. Accordingly, ambient temperature HCF tests were performed with sinusoidal loading on a high-frequency testing machine ElectroForce3550 (Bose Corporation ElectroForce Systems Group, Eden Prairie, MN, USA) according to DIN 50100 [66]. The stress-controlled testing was conducted using a 25 kN load cell 647.02B (MTS Systems Corporation, Eden Prairie, MN, USA). The test was controlled via winTest Analysis software (Version 4.1, The Testometric Company Ltd.; Rochdale, UK). These performed stress-controlled fatigue tests had a stress ratio of R = −1 (completely reversed cycling) and a test frequency of 100 Hz using

hydraulic wedge grips. The specimens were axially loaded parallel to the build direction (BD) with a sinusoidal loading. In these tests, a maximum number of cycles N_G was set at 10^7 cycles. The fatigue behavior was determined based on the Wöhler curve by testing different stress amplitudes between finite life and long-life strength range. To describe the finite life strength range, the following equation is used:

$$N = C \cdot (\sigma_a)^{-k} \quad (1)$$

where k is the Wöhler line slope and C is the location parameter, which is the theoretical tolerable number of cycles at a stress amplitude of σ_a = 1 MPa. The curve was determined by decreasing the stress amplitude step by step. For each stress state, three specimens were tested. Using a statistical approach, the probability of survival, P_S, or the probability of failure, P_F, was ascertained. A scatter band can be obtained by performing several tests at the same stress amplitude. This scatter band is an extension of the Wöhler curve with the failure probability of 10% ($P_{F10\%}$), 50% ($P_{F50\%}$), and 90% ($P_{F90\%}$). The Wöhler curve transforms into a horizontal line, which describes the long-life fatigue strength, σ_F. The fatigue strength was determined by the staircase test procedure (SC). The SC, according to Hück, is a fast and robust method to determine the average endurance limit/fatigue strength [67].

Fracture surfaces and surface analyses allow conclusions to be drawn about the failure of specimens. Features are detectable, which can provide information about the failure causes. The fracture surfaces of the HCF specimens were investigated using a scanning electron microscope (SEM) Zeiss Ultra Plus (Carl Zeiss AG, Oberkochen, Germany). The SEM images were created by the use of secondary electrons (SE) and an in-lens detector. The fracture surfaces were classified into forced and fatigue fractures. The interface between the PVD coatings and the substrate was also inspected to obtain information on delamination or crack origins in or near the coatings.

3. Results and Discussion

3.1. Roughness

As described by Nakatani et al., the surface roughness significantly affects the fatigue performance in terms of fatigue strength [68], particularly HCF behavior. The surface roughness was measured to study the effect of PVD coatings on the roughness and determine the influence of the roughness on the overall fatigue performance. While in the as-built condition, the mean roughness depth, Rz, is 33.12 ± 3.76 µm, and the arithmetic average roughness, Ra, is 4.64 ± 0.45 µm; for the SR condition, Rz is 30.77 ± 0.87 µm, and Ra is of 4.52 ± 0.24 µm. For the nitride-based PVD coatings, Rz is 33.74 ± 1.98 µm, and Ra is 4.80 ± 0.23 µm for TiN, and 32.11 ± 1.78 µm as well as 4.63 ± 0.22 µm for TiCN, respectively. The a-C:Ag PVD coating possesses an Rz of 32.73 ± 2.70 µm and an Ra of 4.65 ± 0.35 µm. The results indicate that PVD coatings have little to no effect on the Ra and Rz values. As a near-net-shape coating procedure, the PVD coating does not alter the surface roughness; therefore, the fatigue properties in terms of roughness variations will not change [69]. Nonetheless, the SR heat treatment slightly reduces the roughness and may enhance the fatigue performance [68,70,71]. In general, the roughness is comparable to former research and may be beneficial and preferred for biomedical applications in terms of cell growth [60]. As the roughness values of all conditions are in a certain range (Rz = 30.77 µm–33.12 µm; Ra = 4.52 µm–4.80 µm), it can be assumed that the different roughness values do not cause the significant differences in fatigue behavior.

3.2. High-Cycle Fatigue

To obtain information on the effect of the different conditions and coatings on the fatigue behavior, in terms of fatigue strength and long-term fatigue strength, HCF tests were performed for several cycles from 10^4 to 10^7. The HCF test results are tabulated in Table 2.

Table 2. Overview of the fatigue test results of the as-built, SR, TiN-coated, TiCN-coated, and a-C:Ag-coated conditions, with different stress amplitudes, σ_a, and cycles to failure, N, for different test procedures, Wöhler curve and staircase test procedure (SC), 10^7 = run-outs.

	Condition	**As-Built**		**SR**		**+TiN**		**+TiCN**		**+a-C:Ag**	
	Test	σ_a	**N**	σ_a	**N**	σ_a	**N**	σ_a	**N**	σ_a	**N**
Wöhler	1	400	9243	400	30,576	400	14,141	400	12,244	400	11,259
	2	400	9456	400	30,292	400	13,121	400	10,483	400	9294
	3	400	8123	400	30,201	400	15,663	400	10,624	400	9131
	4	350	11,462	300	97,779	300	26,428	300	16,029	300	17,525
	5	350	9979	300	73,048	300	20,530	300	18,132	300	12,786
	6	350	10,211	300	86,040	300	17,525	300	19,386	300	12,477
	7	300	13,979	300	74,281	200	76,525	200	62,671	200	41,585
	8	300	13,462	200	1,250,876	200	71,204	200	51,996	200	45,665
	9	300	13,782	200	764,148	200	77,222	200	57,180	200	31,088
	10	200	39,514	200	945,842	150	152,991	150	137,682	150	85,630
	11	200	42,166	200	675,594	150	171,897	150	144,485	150	100,463
	12	200	31,930	175	10^7	150	168,327	150	117,362	150	102,704
	13	100	486,130	175	10^7	125	10^7	125	10^7	125	139,143
	14	100	396,010	175	10^7	125	10^7	125	306,679	125	114,243
	15	100	560,428	-	-	125	10^7	125	10^7	125	138,871
	16	150	69,036	-	-	-	-	125	10^7	100	268,655
	17	150	91,714	-	-	-	-	-	-	100	390,224
	18	150	66,932	-	-	-	-	-	-	100	328,678
	19	125	205,157	-	-	-	-	-	-	75	10^7
	20	125	137,410	-	-	-	-	-	-	75	10^7
	21	125	128,867	-	-	-	-	-	-	75	10^7
	22	75	10^7	-	-	-	-	-	-	-	-
	23	75	10^7	-	-	-	-	-	-	-	-
	24	75	10^7	-	-	-	-	-	-	-	-
SC	1	98	257,290	192	369,262	131	10^7	144	184,074	99	417,474
	2	90	10^7	183	10^7	137	169,586	137	196,359	90	10^7
	3	98	411,817	192	460,000	131	245,437	131	354,125	99	390,952
	4	90	429,664	192	10^7	125	10^7	125	256,334	90	10^7
	5	82	10^7	200	10^7	131	10^7	119	10^7	99	430,847
	6	90	10^7	-	-	137	10^7	125	10^7	90	10^7
	7	98	9,519,363	-	-	144	205,177	131	298,425	99	289,494
	8	-	-	-	-	-	-	125	281,170	-	-
	9	-	-	-	-	-	-	119	270,714	-	-

The HCF test results are summarized in Figure 2. Figure 2 shows double-logarithmic stress-life plots (stress amplitude over cycles to failure). The test points for the Wöhler curves (solid points) and the staircase test procedure (SC, open points) are illustrated. Specimens that withstand the loading over 10^7 cycles are classified as run outs. Run outs are indicated by black, horizontal arrows. In addition, failure bands described by the failure probability curves $P_{F10\%}$, $P_{F50\%}$, and $P_{F90\%}$ are plotted. The diagrams present the different conditions (Figure 2 (a) as built, (b) SR, (c) TiN, (d) TiCN, and (e) a-C:Ag) as well as the overview of the $P_{F50\%}$ curves for all conditions (Figure 2f). The curves of the as-built and a-C:Ag-coated conditions are similar in terms of the fatigue strength, indicated by the horizontal solid and dash-dot-dot lines in Figure 2f. TiCN (dash-dot horizontal line) and, in particular, TiN (dashed horizontal line) coatings improve the fatigue performance, resulting in higher fatigue strength, compared to the uncoated, as-built condition (solid horizontal line), demonstrated in Figure 2f. SR heat treatment significantly improves the fatigue strength (dotted horizontal line) compared to all other conditions, see Figure 2f. The Wöhler line slope k describes the slope in the fatigue strength range. The slopes are similar for the as-built and the coated specimens; they range between 2.5 and 2.7 and only the fatigue strength is higher for the coated samples. For the SR condition (Figure 2b), the slope

is at 5. Therefore, the curve is less steep and the fatigue strength is significantly higher than all other conditions.

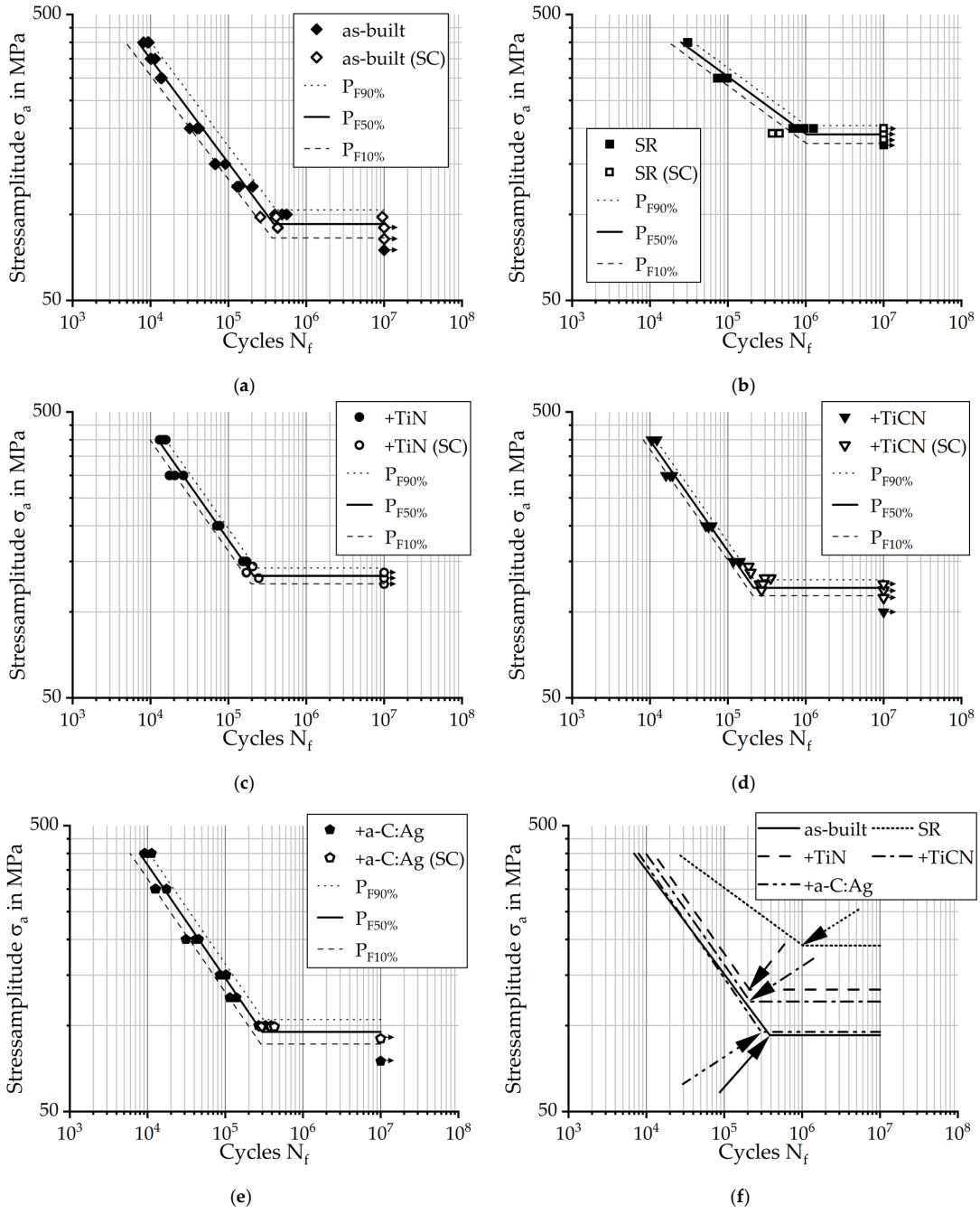

Figure 2. Experimental stress-life curves of the different conditions showing the results of the Wöhler tests (filled symbols) and staircase tests (SC, hollow symbols); failure bands described by the failure probability curves $P_{F10\%}$, $P_{F50\%}$, and $P_{F90\%}$; horizontal arrows indicate the run-out specimens (after 10^7 cycles); (**a**) as-built condition; (**b**) SR condition; (**c**) PVD coated with TiN; (**d**) PVD coated with TiCN; (**e**) PVD coated with a-C:Ag; (**f**) comparison of the failure probability curves $P_{F50\%}$ of the different conditions.

The fatigue strength σ_F of the as-built condition (Figure 2a) is similar to the a-C:Ag condition (Figure 2e) with 92.6 MPa and 95.0 MPa, respectively. The fatigue strength σ_F of the TiCN-coated state (Figure 2d) is 121.4 MPa and above the as-built and a-C:Ag-coated conditions. The TiN-coated condition (Figure 2c) has the highest fatigue strength σ_F of 133.5 MPa. For the SR condition, the fatigue strength σ_F is 190.2 MPa and more than two-times higher than for the initial, as-built condition. SR treatment results in a 42% increase in fatigue strength compared to the highest fatigue strength of the PVD-coated samples. The cycles at the knee point of the 50% failure probability curve are slightly lower for the a-C:Ag coating (298,870 cycles) compared to the as-built condition (385,153 cycles), see solid and dash-dot-dot arrows in Figure 2f, respectively. Although the TiN-coated condition has the highest fatigue strength among the coatings, the knee point cycles are lower (210,470 cycles), see dashed arrow in Figure 2f. The knee point of the TiCN-coated condition is at 214,018 cycles, see dash-dot arrow in Figure 2f. For the SR condition, the cycles at the knee point are at 1,025,238 cycles (see dotted arrow in Figure 2f) and the k value is about two-times higher than for all conditions. The higher the Wöhler line slope, in general, the better the fatigue strength characteristics. The results of the fatigue tests are summarized in Table 3.

Table 3. Overview of the fatigue properties of the as-built, SR, TiN-coated, TiCN-coated, and a-C:Ag-coated conditions; fatigue strength, σ_F, cycles at the knee point, N_K of the failure probability curves, $P_{F50\%}$, Wöhler line slope, k.

Condition	As-Built	SR	+TiN	+TiCN	+a-C:Ag
σ_F in MPa	92.6	190.2	133.5	121.4	95.0
N_K	385,153	1,025,238	210,470	214,018	298,870
k	2.7	5.0	2.6	2.6	2.5

3.3. Fracture Analysis

The fracture analysis is performed for the different conditions after fatigue testing. The analysis is used to determine the failure causes and mechanisms. Concerning the various coatings, the characteristics of the coatings and the crack initiation points are of special interest. Fatigue fracture surfaces often have typical observable characteristics, such as crack origins and fatigue striations. The fatigue fracture surface of an as-built specimen is shown in Figure 3a. The fracture surface is divisible into three areas, separated by dotted lines in Figure 3a. The area between both lines depicts the final, forced fracture area. The fatigue crack seems to be nucleated on both sides of the final fracture. The Roman numerals (I–V) indicate multiple possible crack nucleation sites where the crack initiation likely begins. As the fatigue test progresses, the multiple cracks may grow together to form one critical crack. The divided fracture surface—fatigue fracture (right) and a residual forced fracture (left)—is depicted in Figure 3b. Typically, the higher the stress amplitude, the larger the forced fracture area. The fatigue fracture surface is shown in Figure 3c. Fatigue striations are observable on the fatigue fracture surface (right side in Figure 3b,d, white arrows) and are perpendicular to the crack propagation direction (indicated with a red arrow). Distinct fatigue striations are observable for all conditions and stress amplitudes. The residual fracture surface typically shows areas with forced transgranular facets associated with brittle fracture mechanisms and ductile fracture with dimples (Figure 3e, black arrows). Defects, characteristic of the LPBF process, are often perpendicular to the build direction and pulled apart by loading. Typical defects are, for example, pores and unmelted powder particles, which are depicted in Figure 3f,g, respectively. These defects are detrimental when it comes to fatigue performance of additively manufactured specimens, as they are probable fatigue crack initiation points [40,72–74].

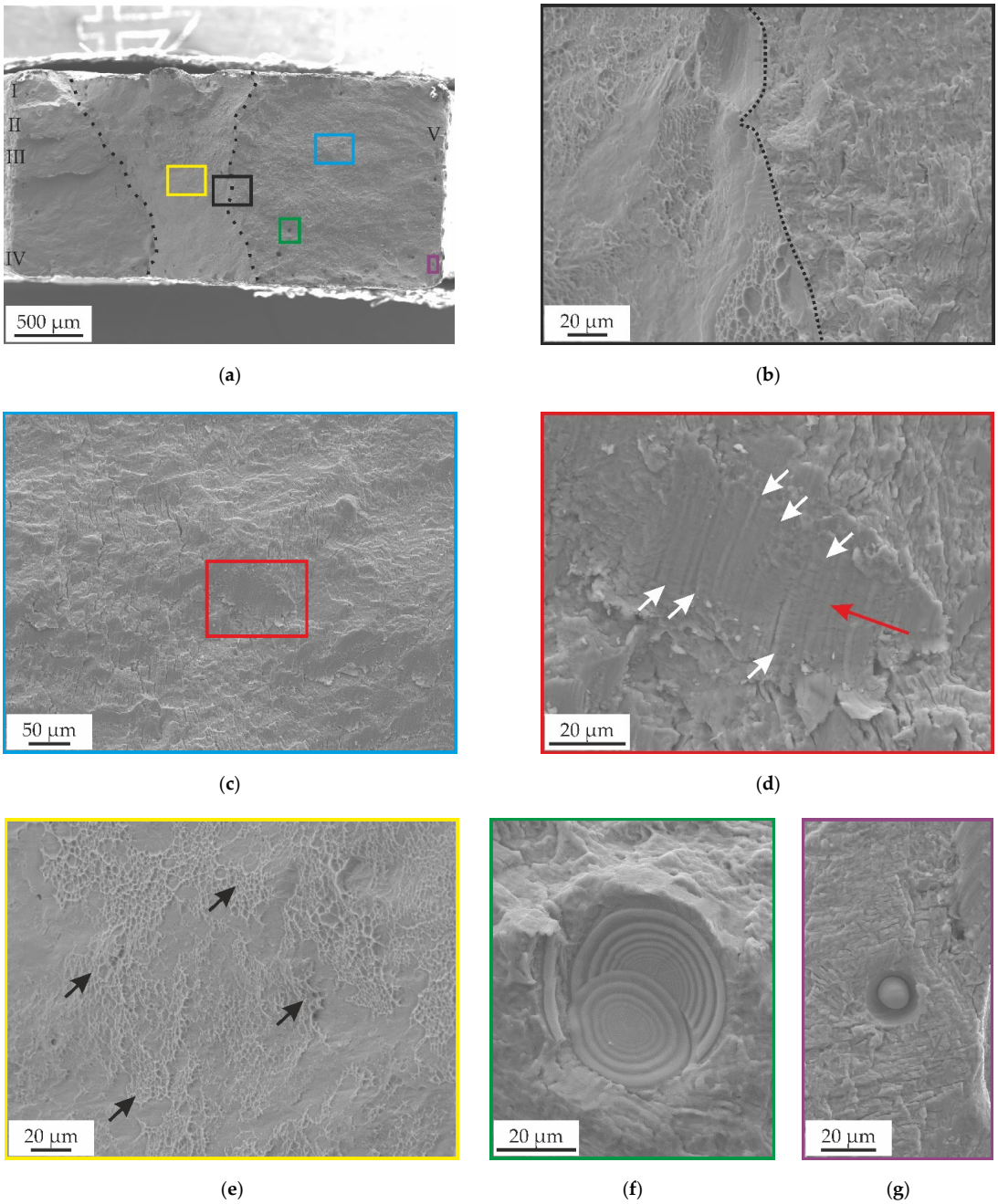

(**a**) (**b**) (**c**) (**d**) (**e**) (**f**) (**g**)

Figure 3. SEM images of a fatigue fracture surface on an as-built Ti-6Al-7Nb fatigue specimen; (**a**) overview image of the fracture surface, forced fracture occurs between the dashed, black lines; (**b**) fracture surface from the black square in (**a**), divided by the dashed line into fatigue fracture (right of the dashed line) and residual forced fracture (left of the dashed line); (**c**) fatigue fracture surface from the blue square in (**a**); (**d**) detailed view of the red square in (**c**) of the fatigue striations (white arrows) and the probable crack propagation direction (red arrow); (**e**) detailed view on the residual forced fracture surface with shallow dimples (black arrows) resulting from ductile material behavior; (**f**) laser powder bed fusion (LPBF) characteristic gas pore; (**g**) LPBF characteristic lack of fusion defect with unmelted powder particle.

Figure 4a shows the fracture surface of a TiN-coated specimen. The fracture surface is divided into the fatigue fracture (left side) and the forced fracture area surrounded by the dashed line. Crack nucleation sites are probably on the left side of the fracture surface, marked with red circles in Figure 4a. The crack can originate at different spots and propagate to a single fatigue crack. The crack propagation direction is marked with a red arrow in Figure 4a,b. Figure 4b shows the magnified area within the black rectangle in Figure 4a. Fatigue striations are visible, which are perpendicular to the crack propagation direction, see white arrows in Figure 4b. Figure 4c depicts a coated powder particle on the surface of the specimens. PVD coatings are known to be near-net shaped, which reproduce the underlying surface topography and roughness [69]. The particle is probably partially melted on the back side. The PVD coating of undercuts, such as the back side of the particle, is challenging [75]. As a result, the surface gets inhomogeneous from right to left (substrate on the right), probably due to a thinner coating on the undercut side of the coating direction (left to right). The TiN coating shows a smooth fracture surface, see Figure 4d,e. In Figure 4d, the TiN coating is highlighted by the dashed, yellow lines, whereby the visual appearance of the fractured coating differs from the fatigue fracture surface of the substrate on the left side. After a fracture, occasional artifacts, such as cracks through the coating, are observable, see Figure 4e. The thickness of the coating is around 3 µm, but the Ti interlayer described by Tillmann et al. is not observable [43]. Figure 4f shows the morphology of the TiN coating, which consists of angular and edgy, pyramid-like structures [76].

Figure 5 shows the SEM images of the TiCN coating, including fracture surfaces. Figure 5a shows that the fracture surface may be divided into the fatigue fracture (left side) and the forced fracture area (dashed line). The red circles indicate the probable crack nucleation sites (Figure 5a). The crack may originate from different spots, typically from defects, such as pores or cracks, and propagate to a single fatigue crack. A red arrow marks the possible crack propagation direction in Figure 5a,b. Figure 5b shows the magnified area within a black rectangle in Figure 5a. In Figure 5b (white arrows), several fatigue striations are visible, which are usually perpendicular to the crack propagation direction. The fracture surface of the Ti-6Al-7Nb, subsequently coated with TiCN, shows, similar to the other conditions, characteristic fatigue fracture features, such as fatigue striations, see white arrows in Figure 5b,c. The TiCN coating is highlighted with black arrows in Figure 5c and dashed, yellow lines in Figure 5d. The fracture surface is in the bottom area of Figure 5d. A closeup of the TiCN coating shows the multilayer layout of the TiCN coating, consisting of the Ti interlayer (Ti-IL), the TiN interlayer (TiN-IL), and the TiCN surface layer (TiCN-SL) in Figure 5e. At this position, the coating is around 1.74 µm thick. The TiCN coating has a hemispherical structure, also described as a cauliflower-like appearance, see Figure 5f [77,78].

The fracture surface of a specimen with diamond-like carbon a-C:Ag coating, including LPBF characteristic defects, such as pores (Figure 6a, black arrows) and characteristic fatigue striations (Figure 6b, white arrows), is depicted in Figure 6. Fatigue striations (white arrows) are visible on the fracture surface, see Figure 6b–d. The areas marked with the Roman numerals (I–III) could be crack nucleation sites. The area (white circle) in Figure 6c indicates a conspicuous spot for the crack origin. Crack initiation likely begins at different points and, as the test progresses, the individual cracks grow together to form one crack. The probable crack propagation direction is marked with a red arrow in Figure 6a,b. Figure 6d shows the around 2 µm thick a-C:Ag coating, see yellow arrows. The a-C:Ag coating exhibits a cluster-like structure, commonly observed for a-C films [79]. Nano-sized particles (green arrows) are noted coating the surface, especially in the undercut region of the powder particle. As reported by previous studies, these particles are assumed to be Ag nanocrystallites dispersed on the surface of the coating [44,80,81].

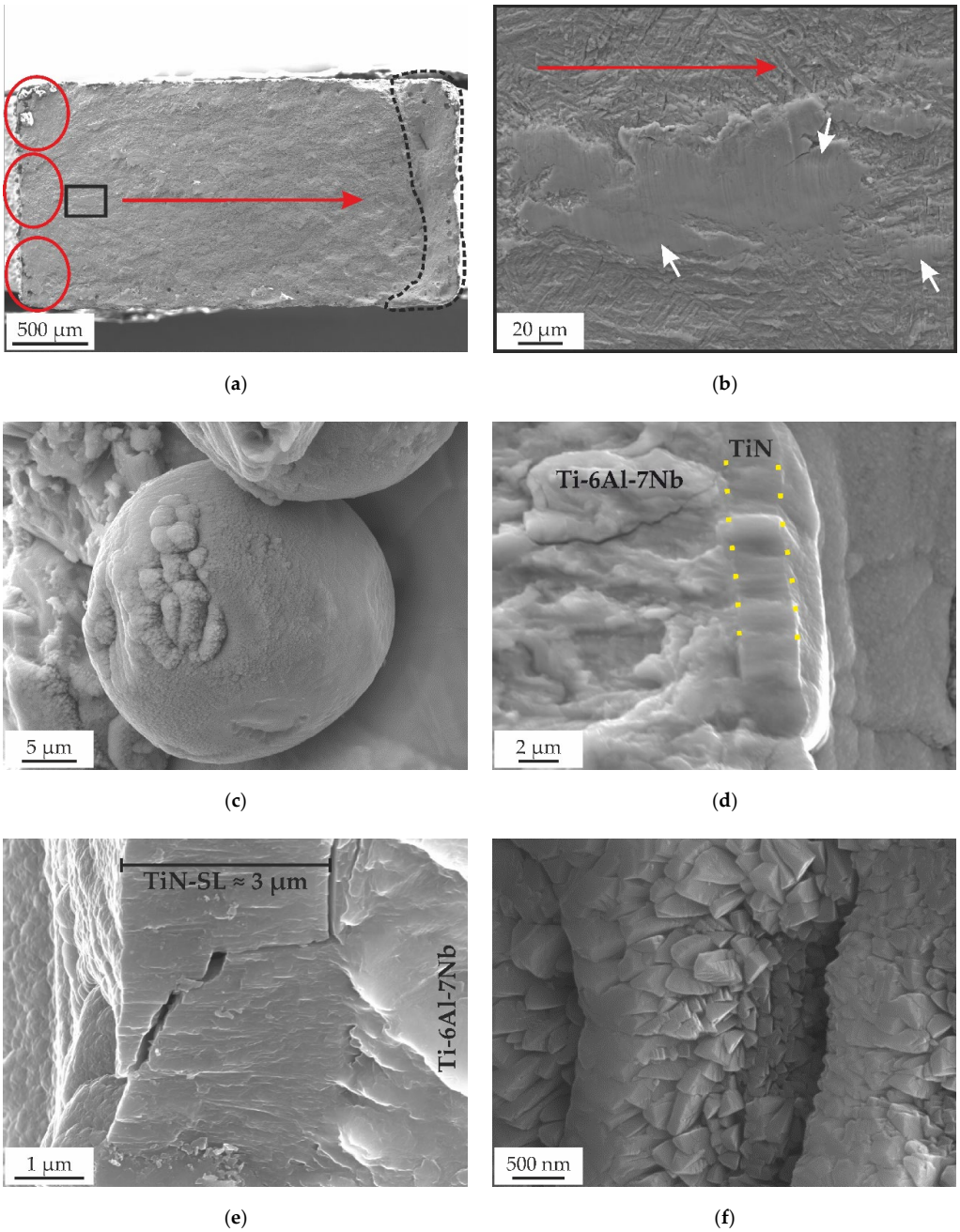

(**a**) (**b**)

(**c**) (**d**)

(**e**) (**f**)

Figure 4. SEM images of the fracture surface of a TiN-coated specimen; (**a**) overview SE image of the fracture surface, forced fracture surface indicated with the dashed line, possible crack nucleation sites within the red circles, where the red arrow indicates crack propagation direction; (**b**) SE image of fracture surface from the black square in (**a**), with crack propagation direction (red arrow) and fatigue striations (white arrows); (**c**) SE image of coated powder particle on the surface of the specimen; (**d**) SE image of TiN coating (dashed, yellow lines) in the boundary region of the fatigue fracture surface of the substrate (left area); (**e**) in-lens image of TiN surface layer (TiN-SL) at the edge of a fractured surface (right area) after fatigue testing, showing emerged cracks in the coating; (**f**) in-lens image of the TiN surface with edgy and angular, pyramid-like growth structure.

Crystals **2022**, *12*, 1190 12 of 18

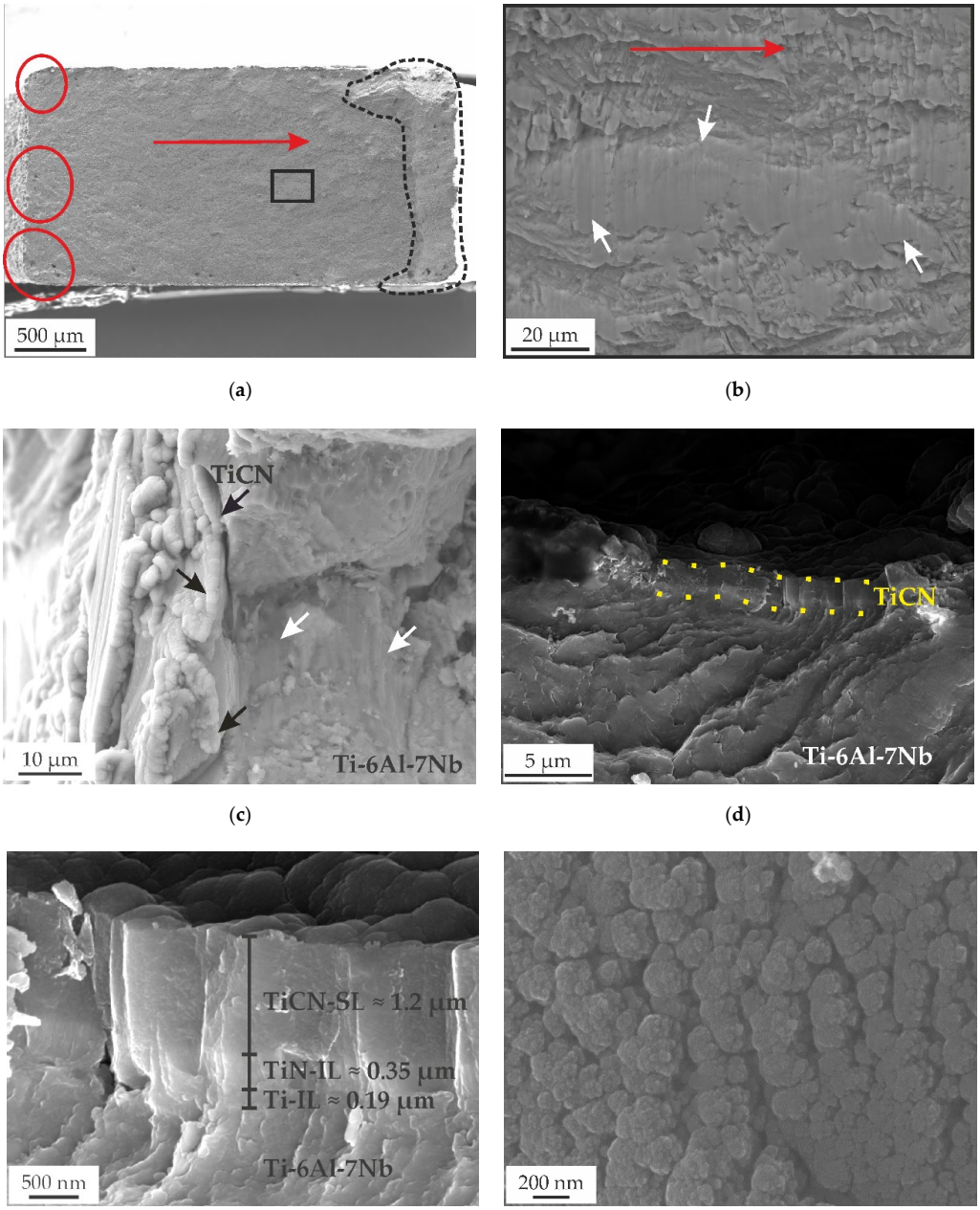

Figure 5. SEM images of the fracture surface of a TiCN-coated specimen; (**a**) overview SE image of the fracture surface, forced fracture surface indicated with the dashed line, possible crack nucleation sites within the red circles, the red arrow indicates crack propagation direction; (**b**) fracture surface from the black square in (**a**), with crack propagation direction (red arrow) and fatigue striations (white arrows); (**c**) TiCN coating (black arrows) on the substrate material (right area) and fatigue striations on the fracture surface (white arrows); (**d**) in-lens image of the TiCN coating (yellow dashed lines) in the edge region of the fatigue fracture surface of the substrate (bottom area); (**e**) in-lens image of TiCN surface layer (TiCN-SL), TiN interlayer (TiN-IL), and Ti interlayer (Ti-IL) at the edge of a fractured surface (bottom area) after fatigue testing; (**f**) TiCN surface with cauliflower-like structure.

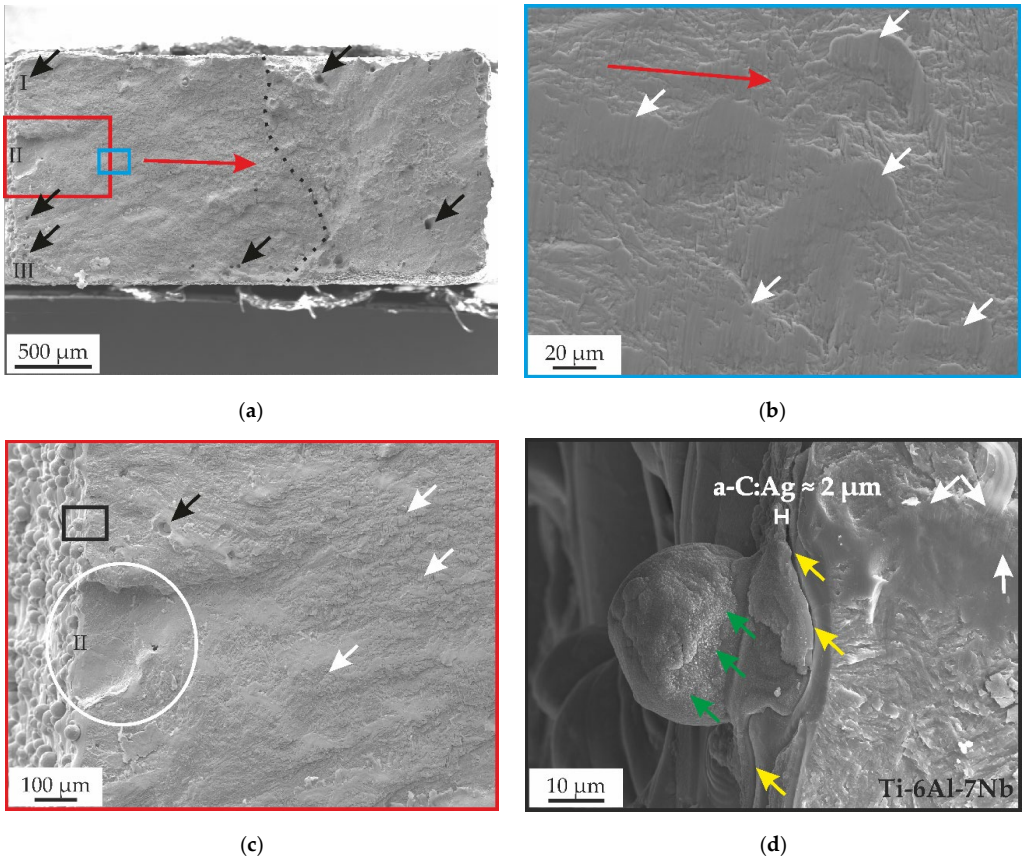

Figure 6. SEM images of the fracture surface of an a-C:Ag-coated specimen; (**a**) overview SE image of the fracture surface, dashed line separating fatigue (left) and forced fracture (right), Roman numerals indicating the possible crack nucleation sites, black arrows marking pores; (**b**) detailed view of the blue rectangle in (**a**), showing the fatigue characteristic striations (white arrows) and the crack propagation direction (red arrow); (**c**) overview of the fatigue fracture surface with fatigue striations (white arrows) and LPBF characteristic defects such as pores (black arrow); (**d**) detailed in-lens image of the black square in (**c**) showing the a-C:Ag coating on the surface (yellow arrows) and the fatigue fracture surface (right area) with fatigue striations (white arrows), a coated powder particle on the surface of the specimen with Ag particles (green arrows).

Fracture surfaces were analyzed to identify crack-initiation spots and to determine whether the cracks started in the substrate or the coating. Unfortunately, the identification of crack-initiation points is quite challenging and was not successful, probably due to the specimen geometry (flat, rectangular) and size (miniature size) [70,82]. As the crack-initiation points are challenging to determine, it was impossible to distinguish whether the crack originated in the substrate or at the surface (coating). Nonetheless, where it starts is dictated by different factors. For example, if the crack originates from the substrate, then it is assumed to happen at defects close to the surface [83–85]. The different coatings did not flake on the specimen surfaces. Only local delamination that occurred near the fatigue crack was observable. As described by Tillmann et al., this confirms the assumption that the adhesion between substrate and coating is strong, especially for the TiN and TiCN coating [43].

4. Conclusions

This study addresses the effects of PVD coating on the mechanical properties of additively manufactured Ti-6Al-7Nb biomedical alloy. The change in fatigue strength properties is determined for specimens with different substrate conditions (as-built and SR heat-treated) and PVD-coated states (TiN, TiCN, and a-C:Ag). The results indicate PVD coatings can improve fatigue behavior and SR heat treatment results in a more significant improvement in fatigue performance. The findings can be summarized as follows:

- The deposition of the PVD coatings improves fatigue strength. The PVD coatings improve the fatigue strength for all conditions by 44.2% (TiN), 31.1% (TiCN), and 2.6% (a-C:Ag) compared to the uncoated substrate material. SR heat treatment leads to a significant fatigue strength improvement of 105.4%.
- The Wöhler curve knee points of the PVD-coated specimens are lower than the as-built condition and the Wöhler line slopes are similar but less steep. Therefore, the Wöhler curves of the PVD-coated specimens are shifted parallel to the as-built Wöhler curves to higher fatigue strengths. An exception is the SR-heat-treated condition, which has a higher knee point (166.2% more cycles) and two-times higher Wöhler line slope. In combination with a higher fatigue strength, this results in a significant change in position and angle of the SR Wöhler curve.
- The fracture surfaces can be divided into fatigue fracture and forced fracture, whereby the fatigue-forced-fracture ratio depends on the applied stress amplitude. The forced fracture surfaces of the different conditions are characterized by transgranular facets. Brittle and ductile fracture features, such as dimples are present on the fracture surface.
- The fatigue fracture surfaces are characterized by fatigue striations perpendicular to the crack propagation direction.
- LPBF-characteristic defects (e.g., pores, unmelted powder) are visible for all conditions and have a high impact on fatigue performance. Defects often can act as crack origins but could not be identified. Delamination or flaking of the TiN, TiCN, and C:Ag coatings was not observable, assuming a high adhesion of the various coatings on the Ti-6Al-7Nb substrate.

In conclusion, this work illustrates the significant improvement in SR heat treatment and PVD coatings on the HCF performance of additively manufactured Ti-6Al-7Nb. Therefore, PVD coatings can be advantageous in the design of load-bearing implants. Further research should focus on the deposition of PVD coatings on SR specimens to combine the significant improvement in the heat treatment of the substrate with the surface improvement in the PVD coatings in terms of hardness, wear resistance, and tailoring of biocompatibility features.

Funding: This research was funded by the Deutsche Forschungsgemeinschaft (DFG), grant numbers SCHA 1484/45-1.

Data Availability Statement: The data that support the findings of this study are available from the corresponding author upon reasonable request.

Acknowledgments: The author gratefully acknowledges the German Research Foundation (DFG) for the financial support and the Institute of Materials Engineering (TU Dortmund University, Dortmund, Germany) for providing the coated samples. The research was performed with the equipment and base of the LWK and DMRC research infrastructure. The authors are grateful for the support of the LWK and DMRC staff members, especially thankful to Kay-Peter Hoyer and Mirko Schaper for the project acquisition, support, and supervision, as well as to Mostafa Jamel and Tobias Schulz for the valuable discussions.

Conflicts of Interest: The author declares no conflict of interest. The funders had no role in the design of the study; in the collection, analyses, or interpretation of data; in the writing of the manuscript, or in the decision to publish the results.

References

1. Gross, B.C.; Erkal, J.L.; Lockwood, S.Y.; Chen, C.; Spence, D.M. Evaluation of 3D printing and its potential impact on biotechnology and the chemical sciences. *Anal. Chem.* **2014**, *86*, 3240–3253. [CrossRef] [PubMed]
2. Schmidt, M.; Merklein, M.; Bourell, D.; Dimitrov, D.; Hausotte, T.; Wegener, K.; Overmeyer, L.; Vollertsen, F.; Levy, G.N. Laser based additive manufacturing in industry and academia. *CIRP Ann.* **2017**, *66*, 561–583. [CrossRef]
3. Bourell, D.; Kruth, J.P.; Leu, M.C.; Levy, G.N.; Rosen, D.; Beese, A.M.; Clare, A. Materials for additive manufacturing. *CIRP Ann.* **2017**, *66*, 659–681. [CrossRef]
4. Wohlers, T.T.; Campbell, I.; Diegel, O.; Kowen, J. *Wohlers Report 2018. 3D Printing and Additive Manufacturing State of the Industry: Annual Worldwide Progress Report*; Wohlers Associates, Inc.: Fort Collins, CL, USA, 2018; ISBN 0991333241.
5. Gibson, I.; Rosen, D.; Stucker, B. *Additive Manufacturing Technologies. 3D Printing, Rapid Prototyping and Direct Digital Manufacturing*, 2nd ed.; Springer: Berlin/Heidelberg, Germany, 2015; ISBN 978-1493921126.
6. Dutta, B.; Froes, F.H. *Additive Manufacturing of Titanium Alloys. State of the Art, Challenges, and Opportunities*; Butterworth-Heinemann is an Imprint of Elsevier: Amsterdam, The Netherlands, 2016; ISBN 9780128047835.
7. Kumar, R.; Kumar, M.; Chohan, J.S. The role of additive manufacturing for biomedical applications: A critical review. *J. Manuf. Process.* **2021**, *64*, 828–850. [CrossRef]
8. Javaid, M.; Haleem, A. Additive manufacturing applications in medical cases: A literature based review. *Alex. J. Med.* **2018**, *54*, 411–422. [CrossRef]
9. Fazel-Rezai, R. *Biomedical Engineering—From Theory to Applications*; IntechOpen: London, UK, 2011; ISBN 9789533076379.
10. Zaman, H.A.; Sharif, S.; Idris, M.H.; Kamarudin, A. Metallic Biomaterials for Medical Implant Applications: A Review. *Appl. Mech. Mater.* **2015**, *735*, 19–25. [CrossRef]
11. Festas, A.J.; Ramos, A.; Davim, J.P. Medical devices biomaterials—A review. *Proc. Inst. Mech. Eng. Part L J. Mater. Des. Appl.* **2020**, *234*, 218–228. [CrossRef]
12. Vandenbroucke, B.; Kruth, J.P. Selective laser melting of biocompatible metals for rapid manufacturing of medical parts. *Rapid Prototyp. J.* **2007**, *13*, 196–203. [CrossRef]
13. Iijima, D. Wear properties of Ti and Ti–6Al–7Nb castings for dental prostheses. *Biomaterials* **2003**, *24*, 1519–1524. [CrossRef]
14. Niinomi, M. Mechanical biocompatibilities of titanium alloys for biomedical applications. *J. Mech. Behav. Biomed. Mater.* **2008**, *1*, 30–42. [CrossRef]
15. Hollander, D.A.; von Walter, M.; Wirtz, T.; Sellei, R.; Schmidt-Rohlfing, B.; Paar, O.; Erli, H.-J. Structural, mechanical and in vitro characterization of individually structured Ti-6Al-4V produced by direct laser forming. *Biomaterials* **2006**, *27*, 955–963. [CrossRef] [PubMed]
16. Murr, L.E.; Quinones, S.A.; Gaytan, S.M.; Lopez, M.I.; Rodela, A.; Martinez, E.Y.; Hernandez, D.H.; Martinez, E.; Medina, F.; Wicker, R.B. Microstructure and mechanical behavior of Ti-6Al-4V produced by rapid-layer manufacturing, for biomedical applications. *J. Mech. Behav. Biomed. Mater.* **2009**, *2*, 20–32. [CrossRef] [PubMed]
17. Khrunyk, Y.Y.; Ehnert, S.; Grib, S.V.; Illarionov, A.G.; Stepanov, S.I.; Popov, A.A.; Ryzhkov, M.A.; Belikov, S.V.; Xu, Z.; Rupp, F.; et al. Synthesis and Characterization of a Novel Biocompatible Alloy, Ti-Nb-Zr-Ta-Sn. *Int. J. Mol. Sci.* **2021**, *22*, 10611. [CrossRef]
18. Surmeneva, M.; Grubova, I.; Glukhova, N.; Khrapov, D.; Koptyug, A.; Volkova, A.; Ivanov, Y.; Cotrut, C.M.; Vladescu, A.; Teresov, A.; et al. New Ti–35Nb–7Zr–5Ta Alloy Manufacturing by Electron Beam Melting for Medical Application Followed by High Current Pulsed Electron Beam Treatment. *Metals* **2021**, *11*, 1066. [CrossRef]
19. Surmeneva, M.A.; Koptyug, A.; Khrapov, D.; Ivanov, Y.F.; Mishurova, T.; Evsevleev, S.; Prymak, O.; Loza, K.; Epple, M.; Bruno, G.; et al. In situ synthesis of a binary Ti–10at% Nb alloy by electron beam melting using a mixture of elemental niobium and titanium powders. *J. Mater. Process. Technol.* **2020**, *282*, 116646. [CrossRef]
20. Tamilselvi, S.; Raman, V.; Rajendran, N. Corrosion behaviour of Ti–6Al–7Nb and Ti–6Al–4V ELI alloys in the simulated body fluid solution by electrochemical impedance spectroscopy. *Electrochim. Acta* **2006**, *52*, 839–846. [CrossRef]
21. Metikoš-Huković, M.; Kwokal, A.; Piljac, J. The influence of niobium and vanadium on passivity of titanium-based implants in physiological solution. *Biomaterials* **2003**, *24*, 3765–3775. [CrossRef]
22. López, M.; Gutiérrez, A.; Jiménez, J. In vitro corrosion behaviour of titanium alloys without vanadium. *Electrochim. Acta* **2002**, *47*, 1359–1364. [CrossRef]
23. Lewandowski, J.J.; Seifi, M. Metal Additive Manufacturing: A Review of Mechanical Properties. *Annu. Rev. Mater. Res.* **2016**, *46*, 151–186. [CrossRef]
24. Yap, C.Y.; Chua, C.K.; Dong, Z.L.; Liu, Z.H.; Zhang, D.Q.; Loh, L.E.; Sing, S.L. Review of selective laser melting: Materials and applications. *Appl. Phys. Rev.* **2015**, *2*, 41101. [CrossRef]
25. Hein, M.; Hoyer, K.-P.; Schaper, M. Additively processed TiAl6Nb7 alloy for biomedical applications. *Mater. Und Werkst.* **2021**, *52*, 703–716. [CrossRef]
26. Hein, M.; Lopes Dias, N.F.; Pramanik, S.; Stangier, D.; Hoyer, K.-P.; Tillmann, W.; Schaper, M. Heat Treatments of Metastable β Titanium Alloy Ti-24Nb-4Zr-8Sn Processed by Laser Powder Bed Fusion. *Materials* **2022**, *15*, 3774. [CrossRef] [PubMed]
27. Leuders, S.; Thöne, M.; Riemer, A.; Niendorf, T.; Tröster, T.; Richard, H.A.; Maier, H.J. On the mechanical behaviour of titanium alloy TiAl6V4 manufactured by selective laser melting: Fatigue resistance and crack growth performance. *Int. J. Fatigue* **2013**, *48*, 300–307. [CrossRef]

28. Tolosa, I.; Garciandía, F.; Zubiri, F.; Zapirain, F.; Esnaola, A. Study of mechanical properties of AISI 316 stainless steel processed by "selective laser melting", following different manufacturing strategies. *Int. J. Adv. Manuf. Technol.* **2010**, *51*, 639–647. [CrossRef]
29. Nezhadfar, P.D.; Burford, E.; Anderson-Wedge, K.; Zhang, B.; Shao, S.; Daniewicz, S.R.; Shamsaei, N. Fatigue crack growth behavior of additively manufactured 17-4 PH stainless steel: Effects of build orientation and microstructure. *Int. J. Fatigue* **2019**, *123*, 168–179. [CrossRef]
30. Kluczyński, J.; Śnieżek, L.; Grzelak, K.; Torzewski, J.; Szachogłuchowicz, I.; Wachowski, M.; Łuszczek, J. Crack Growth Behavior of Additively Manufactured 316L Steel-Influence of Build Orientation and Heat Treatment. *Materials* **2020**, *13*, 3259. [CrossRef] [PubMed]
31. Zhang, M.; Sun, C.-N.; Zhang, X.; Wei, J.; Hardacre, D.; Li, H. High cycle fatigue and ratcheting interaction of laser powder bed fusion stainless steel 316L: Fracture behaviour and stress-based modelling. *Int. J. Fatigue* **2019**, *121*, 252–264. [CrossRef]
32. Jerrard, P.G.E.; Hao, L.; Evans, K.E. Experimental investigation into selective laser melting of austenitic and martensitic stainless steel powder mixtures. *Proc. Inst. Mech. Eng. B J. Eng. Manuf.* **2009**, *223*, 1409–1416. [CrossRef]
33. Riemer, A.; Leuders, S.; Thöne, M.; Richard, H.A.; Tröster, T.; Niendorf, T. On the fatigue crack growth behavior in 316L stainless steel manufactured by selective laser melting. *Eng. Fract. Mech.* **2014**, *120*, 15–25. [CrossRef]
34. Baufeld, B.; Brandl, E.; van der Biest, O. Wire based additive layer manufacturing: Comparison of microstructure and mechanical properties of Ti–6Al–4V components fabricated by laser-beam deposition and shaped metal deposition. *J. Mater. Process. Technol.* **2011**, *211*, 1146–1158. [CrossRef]
35. Brandl, E. *Microstructural and Mechanical Properties of Additive Manufactured Titanium (Ti-6Al-4V) Using Wire. Evaluation with Respect to Additive Processes Using Powder and Aerospace Material Specifications*; Zugl.: Cottbus, Germany; Shaker: Aachen, Germany, 2010; ISBN 978-3-8322-9530-1.
36. Khorasani, A.; Gibson, I.; Goldberg, M.; Littlefair, G. On the role of different annealing heat treatments on mechanical properties and microstructure of selective laser melted and conventional wrought Ti-6Al-4V. *Rapid Prototyp. J.* **2017**, *23*, 295–304. [CrossRef]
37. Liu, S.; Shin, Y.C. Additive manufacturing of Ti6Al4V alloy: A review. *Mater. Des.* **2019**, *164*, 107552. [CrossRef]
38. Riemer, A.; Richard, H.A. Crack Propagation in Additive Manufactured Materials and Structures. *Procedia Struct. Integ.* **2016**, *2*, 1229–1236. [CrossRef]
39. Leuders, S.; Lieneke, T.; Lammers, S.; Tröster, T.; Niendorf, T. On the fatigue properties of metals manufactured by selective laser melting—The role of ductility. *J. Mater. Res.* **2014**, *29*, 1911–1919. [CrossRef]
40. Popov, V.V.; Katz-Demyanetz, A.; Garkun, A.; Bamberger, M. The effect of powder recycling on the mechanical properties and microstructure of electron beam melted Ti-6Al-4 V specimens. *Addit. Manuf.* **2018**, *22*, 834–843. [CrossRef]
41. Wood, M.I. The mechanical properties of coatings and coated systems. *Mater. Sci. Eng. A Struct. Mater.* **1989**, *120-121*, 633–643. [CrossRef]
42. Mehran, Q.M.; Fazal, M.A.; Bushroa, A.R.; Rubaiee, S. A Critical Review on Physical Vapor Deposition Coatings Applied on Different Engine Components. *Crit. Rev. Solid State Mater. Sci.* **2018**, *43*, 158–175. [CrossRef]
43. Tillmann, W.; Lopes Dias, N.F.; Kokalj, D.; Stangier, D.; Hein, M.; Hoyer, K.-P.; Schaper, M.; Gödecke, D.; Oltmanns, H.; Meißner, J. Tribo-functional PVD thin films deposited onto additively manufactured Ti6Al7Nb for biomedical applications. *Mater. Lett.* **2022**, 132384. [CrossRef]
44. Tillmann, W.; Lopes Dias, N.F.; Franke, C.; Kokalj, D.; Stangier, D.; Filor, V.; Mateus-Vargas, R.H.; Oltmanns, H.; Kietzmann, M.; Meißner, J.; et al. Tribo-mechanical properties and biocompatibility of Ag-containing amorphous carbon films deposited onto Ti6Al4V. *Surf. Coat. Technol.* **2021**, *421*, 127384. [CrossRef]
45. Liu, X.; Chu, P.; Ding, C. Surface modification of titanium, titanium alloys, and related materials for biomedical applications. *Mater. Sci. Eng. R Rep.* **2004**, *47*, 49–121. [CrossRef]
46. Fuentes, E.; Alves, S.; López-Ortega, A.; Mendizabal, L.; Sáenz de Viteri, V. Advanced Surface Treatments on Titanium and Titanium Alloys Focused on Electrochemical and Physical Technologies for Biomedical Applications. In *Biomaterial-Supported Tissue Reconstruction or Regeneration*; Barbeck, M., Jung, O., Smeets, R., Koržinskas, T., Eds.; IntechOpen: London, UK, 2019; ISBN 978-1-83880-377-3.
47. Nascimento, M. Effects of surface treatments on the fatigue strength of AISI 4340 aeronautical steel. *Int. J. Fatigue* **2001**, *23*, 607–618. [CrossRef]
48. Baragetti, S.; Lavecchia, G.; Terranova, A. Variables affecting the fatigue resistance of PVD-coated components. *Int. J. Fatigue* **2005**, *27*, 1541–1550. [CrossRef]
49. Puchi-Cabrera, E.S.; Matínez, F.; Herrera, I.; Berríos, J.; Dixit, S.; Bhat, D. On the fatigue behavior of an AISI 316L stainless steel coated with a PVD TiN deposit. *Surf. Coat. Technol.* **2004**, *182*, 276–286. [CrossRef]
50. Puchi-Cabrera, E.S.; Staia, M.H.; Ochoa-Pérez, E.A.; Teer, D.G.; Santana-Méndez, Y.Y.; La Barbera-Sosa, J.G.; Chicot, D.; Lesage, J. Fatigue behavior of a 316L stainless steel coated with a DLC film deposited by PVD magnetron sputter ion plating. *Mater. Sci. Eng. A Struct. Mater.* **2010**, *527*, 498–508. [CrossRef]
51. Correa Jácome, J.F.; Caicedo Angulo, J.C.; Castro, Y.A. PVD coatings influence (TiCN, BCN, and CrAlN) on the fatigue life behavior of AISI 1045 steel for automotive applications. *Int. J. Adv. Manuf. Technol.* **2022**, *119*, 3995–4009. [CrossRef]
52. Ferreira, J.; Costa, J.; Lapa, V. Fatigue behaviour of 42Cr Mo4 steel with PVD coatings. *Int. J. Fatigue* **1997**, *19*, 293–299. [CrossRef]
53. Baragetti, S. Fatigue resistance of steel and titanium PVD coated spur gears. *Int. J. Fatigue* **2007**, *29*, 1893–1903. [CrossRef]

54. Baragetti, S.; Borzini, E.; Božic, Ž.; Arcieri, E.V. On the fatigue strength of uncoated and DLC coated 7075-T6 aluminum alloy. *Eng. Fail. Anal.* **2019**, *102*, 219–225. [CrossRef]
55. Gopkalo, A.P.; Rutkovskyy, A.V. The effect of PVD coatings on the tensile strength and low-cycle fatigue resistance of stainless steel and titanium alloys. *Fatigue Fract. Eng. Mater. Struct.* **2011**, *34*, 1012–1020. [CrossRef]
56. Costa, M.Y.P.; Cioffi, M.O.H.; Venditti, M.L.R.; Voorwald, H.J.C. Fatigue fracture behavior of Ti-6Al-4V PVD coated. *Procedia Eng.* **2010**, *2*, 1859–1864. [CrossRef]
57. Costa, M.; Venditti, M.; Cioffi, M.; Voorwald, H.; Guimarães, V.A.; Ruas, R. Fatigue behavior of PVD coated Ti–6Al–4V alloy. *Int. J. Fatigue* **2011**, *33*, 759–765. [CrossRef]
58. Bai, Y.; Xi, Y.; Gao, K.; Yang, H.; Pang, X.; Yang, X.; Volinsky, A.A. Brittle coating effects on fatigue cracks behavior in Ti alloys. *Int. J. Fatigue* **2019**, *125*, 432–439. [CrossRef]
59. Niendorf, T. Ermüdungseigenschaften Ultrafeinkörniger Kubisch Raumzentrierter Werkstoffe. Ph.D. Thesis, Paderborn Univercity, Paderborn, Germany, 2010.
60. Hein, M.; Kokalj, D.; Lopes Dias, N.F.; Stangier, D.; Oltmanns, H.; Pramanik, S.; Kietzmann, M.; Hoyer, K.-P.; Meißner, J.; Tillmann, W.; et al. Low Cycle Fatigue Performance of Additively Processed and Heat-Treated Ti-6Al-7Nb Alloy for Biomedical Applications. *Metals* **2022**, *12*, 122. [CrossRef]
61. Donachie, M.J. *Titanium. A technical Guide*, 2nd ed.; ASM International: Materials Park, OH, USA, 2000; ISBN 9780871706867.
62. Liang, Z.; Sun, Z.; Zhang, W.; Wu, S.; Chang, H. The effect of heat treatment on microstructure evolution and tensile properties of selective laser melted Ti6Al4V alloy. *J. Alloys Compd.* **2019**, *782*, 1041–1048. [CrossRef]
63. Tillmann, W.; Lopes Dias, N.F.; Franke, C.; Kokalj, D.; Stangier, D.; Thomann, C.A.; Debus, J. Mechanical properties and adhesion behavior of amorphous carbon films with bias voltage controlled TixCy interlayers on Ti6Al4V. *Diam. Relat. Mater.* **2021**, *115*, 108361. [CrossRef]
64. *DIN EN ISO 4288:1998-04*; Geometrische Produktspezifikation (GPS)_-Oberflächenbeschaffenheit: Tastschnittverfahren_-Regeln und Verfahren für die Beurteilung der Oberflächenbeschaffenheit (ISO_4288:1996); Deutsche Fassung EN_ISO_4288:1997. Beuth Verlag GmbH: Berlin, Germany, 1998. [CrossRef]
65. Lin, C.-Y.; Kang, J.-H. Mechanical Properties of Compact Bone Defined by the Stress-Strain Curve Measured Using Uniaxial Tensile Test: A Concise Review and Practical Guide. *Materials* **2021**, *14*, 4224. [CrossRef]
66. *DIN 50100:2016-12*; DIN Deutsches Institut für Normung e. V. Schwingfestigkeitsversuch—Durchführung und Auswertung von zyklischen Versuchen mit konstanter Lastamplitude für metallische Werkstoffproben und Bauteile. DIN 50100: 2016-12. Beuth Verlag GmbH: Berlin, Germany, 2016. [CrossRef]
67. Hück, M. Ein verbessertes Verfahren für die Auswertung von Treppenstufenversuchen. *Mat. Werkstofftech.* **1983**, *14*, 406–417. [CrossRef]
68. Nakatani, M.; Masuo, H.; Tanaka, Y.; Murakami, Y. Effect of Surface Roughness on Fatigue Strength of Ti-6Al-4V Alloy Manufactured by Additive Manufacturing. *Procedia Struct. Integr.* **2019**, *19*, 294–301. [CrossRef]
69. Korhonen, A.S. Corrosion of thin hard PVD coatings. *Vacuum* **1994**, *45*, 1031–1034. [CrossRef]
70. Mertová, K.; Džugan, J.; Roudnická, M.; Daniel, M.; Vojtěch, D.; Seifi, M.; Lewandowski, J.J. Build Size and Orientation Influence on Mechanical Properties of Powder Bed Fusion Deposited Titanium Parts. *Metals* **2020**, *10*, 1340. [CrossRef]
71. Kasperovich, G.; Hausmann, J. Improvement of fatigue resistance and ductility of TiAl6V4 processed by selective laser melting. *J. Mater. Processing Technol.* **2015**, *220*, 202–214. [CrossRef]
72. Liu, Q.C.; Elambasseril, J.; Sun, S.J.; Leary, M.; Brandt, M.; Sharp, P.K. The Effect of Manufacturing Defects on the Fatigue Behaviour of Ti-6Al-4V Specimens Fabricated Using Selective Laser Melting. *Adv. Mat. Res.* **2014**, *891–892*, 1519–1524. [CrossRef]
73. Murakami, Y. *Metal Fatigue. Effects of Small Defects and Nonmetallic Inclusions*, 2nd ed.; Academic Press: Amsterdam, The Netherlands, 2019; ISBN 9780128138779.
74. Sercombe, T.; Jones, N.; Day, R.; Kop, A. Heat treatment of Ti-6Al-7Nb components produced by selective laser melting. *Rapid Prototyp. J.* **2008**, *14*, 300–304. [CrossRef]
75. Von Niessen, K.; Gindrat, M.; Refke, A. Vapor Phase Deposition Using Plasma Spray-PVD™. *J. Therm. Spray Tech.* **2010**, *19*, 502–509. [CrossRef]
76. Cheng, Z.; Yang, J.; Shao, F.; Zhong, X.; Zhao, H.; Zhuang, Y.; Sheng, J.; Ni, J.; Tao, S. Thermal Stability of PS-PVD YSZ Coatings with Typical Dense Layered and Columnar Structures. *Crystals* **2020**, *10*, 826. [CrossRef]
77. Deng, Z.-Q.; Mao, J.; Liu, M.; Deng, C.-M.; Ma, J.-T. Regional characteristic of 7YSZ coatings prepared by plasma spray-physical vapor deposition technique. *Rare Met.* **2021**, *40*, 3308–3315. [CrossRef]
78. Zhao, H.; Zhang, X.; Deng, C.; Deng, Z.; Chen, X. Performance Evaluation and Thermal Shock Behavior of PS-PVD (Gd0.9Yb0.1)2Zr2O7/YSZ Thermal Barrier Coatings. *Coatings* **2022**, *12*, 323. [CrossRef]
79. Tillmann, W.; Lopes Dias, N.F.; Stangier, D.; Nienhaus, A.; Thomann, C.A.; Wittrock, A.; Moldenhauer, H.; Debus, J. Effect of the bias voltage on the structural and tribo-mechanical properties of Ag-containing amorphous carbon films. *Diam. Relat. Mater.* **2020**, *105*, 107803. [CrossRef]
80. Baba, K.; Hatada, R.; Flege, S.; Ensinger, W. Preparation and Properties of Ag-Containing Diamond-Like Carbon Films by Magnetron Plasma Source Ion Implantation. *Adv. Mater. Sci. Eng.* **2012**, *2012*, 1–5. [CrossRef]

81. Bociaga, D.; Komorowski, P.; Batory, D.; Szymanski, W.; Olejnik, A.; Jastrzebski, K.; Jakubowski, W. Silver-doped nanocomposite carbon coatings (Ag-DLC) for biomedical applications—Physiochemical and biological evaluation. *Appl. Surf. Sci.* **2015**, *355*, 388–397. [CrossRef]
82. Kumar, K.; Pooleery, A.; Madhusoodanan, K.; Singh, R.N.; Chakravartty, J.K.; Dutta, B.K.; Sinha, R.K. Use of Miniature Tensile Specimen for Measurement of Mechanical Properties. *Procedia Eng.* **2014**, *86*, 899–909. [CrossRef]
83. Paik, J.K.; Melchers, R.E. *Condition Assessment of Aged Structures*; CRC Press: Boca Raton, FL, USA, 2008; ISBN 978-1-84569-334-3.
84. Lumley, R. *Fundamentals of Aluminium Metallurgy. Production, Processing and Applications*; Elsevier Science & Technology: Cambridge, UK, 2011; ISBN 978-1-84569-654-2.
85. Pfeifer, M. *Degradation and Reliability of Materials. Materials Enabled Designs*; Elsevier: Amsterdam, The Netherlands, 2009; pp. 161–187. ISBN 9780750682879.

Paper E

M. Hein, N. F. Lopes Dias, S. Pramanik, D. Stangier, K.-P. Hoyer, W. Tillmann, and M. Schaper

Heat Treatments of Metastable β Titanium Alloy Ti-24Nb-4Zr-8Sn Processed by Laser Powder Bed Fusion

Materials, 15, 3774, 2022 [229].

materials

MDPI

Article

Heat Treatments of Metastable β Titanium Alloy Ti-24Nb-4Zr-8Sn Processed by Laser Powder Bed Fusion

Maxwell Hein [1,2,*], Nelson Filipe Lopes Dias [3], Sudipta Pramanik [1], Dominic Stangier [3], Kay-Peter Hoyer [1,2], Wolfgang Tillmann [3] and Mirko Schaper [1,2]

[1] Chair of Materials Science (LWK), Paderborn University, Warburger Str. 100, 33098 Paderborn, Germany; pramanik@lwk.upb.de (S.P.); hoyer@lwk.upb.de (K.-P.H.); schaper@lwk.upb.de (M.S.)
[2] DMRC—Direct Manufacturing Research Center, Paderborn University, Mersinweg 3, 33100 Paderborn, Germany
[3] Institute of Materials Engineering (LWT), TU Dortmund University, Leonhard-Euler-Str. 2, 44227 Dortmund, Germany; filipe.dias@tu-dortmund.de (N.F.L.D.); dominic.stangier@tu-dortmund.de (D.S.); wolfgang.tillmann@udo.edu (W.T.)
* Correspondence: hein@lwk.upb.de; Tel.: +49-5251-60-5447

Abstract: Titanium alloys, especially β alloys, are favorable as implant materials due to their promising combination of low Young's modulus, high strength, corrosion resistance, and biocompatibility. In particular, the low Young's moduli reduce the risk of stress shielding and implant loosening. The processing of Ti-24Nb-4Zr-8Sn through laser powder bed fusion is presented. The specimens were heat-treated, and the microstructure was investigated using X-ray diffraction, scanning electron microscopy, and transmission electron microscopy. The mechanical properties were determined by hardness and tensile tests. The microstructures reveal a mainly β microstructure with α" formation for high cooling rates and α precipitates after moderate cooling rates or aging. The as-built and α" phase containing conditions exhibit a hardness around 225 HV5, yield strengths (YS) from 340 to 490 MPa, ultimate tensile strengths (UTS) around 706 MPa, fracture elongations around 20%, and Young's moduli about 50 GPa. The α precipitates containing conditions reveal a hardness around 297 HV5, YS around 812 MPa, UTS from 871 to 931 MPa, fracture elongations around 12%, and Young's moduli about 75 GPa. Ti-24Nb-4Zr-8Sn exhibits, depending on the heat treatment, promising properties regarding the material behavior and the opportunity to tailor the mechanical performance as a low modulus, high strength implant material.

Keywords: laser powder bed fusion; Ti-24Nb-4Zr-8Sn; titanium alloy; biomedical engineering; mechanical properties; microstructure; X-ray diffraction

Citation: Hein, M.; Lopes Dias, N.F.; Pramanik, S.; Stangier, D.; Hoyer, K.-P.; Tillmann, W.; Schaper, M. Heat Treatments of Metastable β Titanium Alloy Ti-24Nb-4Zr-8Sn Processed by Laser Powder Bed Fusion. *Materials* **2022**, *15*, 3774. https://doi.org/10.3390/ma15113774

Academic Editors: Wai Yee Yeong and Swee Leong Sing

Received: 19 April 2022
Accepted: 22 May 2022
Published: 25 May 2022

1. Introduction

Nowadays, there is still a lack of individualized implants, facing safety and risk concerns [1]. Individually adapted implants may reduce revision surgeries and rehabilitation times. They can also restore joint kinetics and improve implant fixation during healing [2]. Patient-specific, customized implants can significantly increase the success rate of the medical treatment of a patient [3,4]. Additive manufacturing (AM) and, specifically, laser powder bed fusion (LPBF) provide the possibility to manufacture these customized implants [5]. LPBF is a powder-based AM technology in which parts are built layer by layer using a laser beam melting the specified area. This layer-wise fabrication of parts leads to geometrical freedom, with few design constraints, and the possibility to manufacture, economically, down to a batch size of one [6,7].

Titanium and titanium alloys are receiving increasing attention in different industries such as aerospace and especially medical industries, due to their superior mechanical performance, as well as their excellent corrosion resistance and biocompatibility [8–10]. For most applications and biomedical use cases, (α + β) phase titanium alloys, such as Ti-6Al-4V

or Ti-6Al-7Nb, are used with the main disadvantage of a relatively high Young's modulus around 110 GPa, which is over 3 to 4 times higher compared to the cortical human bone [11]. Titanium alloys are often used for load-bearing implants, where this mismatch between the implant and surrounding bone leads to stress shielding [12]. The difference in stiffness leads to a reduced loading of the bone. Stress shielding is an adaption of bone cells to varying stress states in the bone and, therefore, may result in bone density reduction and implant loosening [13]. Recent studies reflect the development of titanium alloys towards low elastic moduli accompanied by high strengths, and non-toxic and non-allergic elements [14–17]. Trying to increase the biocompatibility by substituting the toxic elements aluminum and vanadium, and still obtaining sufficient mechanical properties, the β titanium alloy Ti-24Nb-4Zr-8Sn (Ti2448) was developed. The Ti2448 alloy exhibits a low Young's modulus of 42 GPa to 55 GPa and a high strength of 800 MPa to 1200 MPa, depending on processing and heat treatment routes [18–21]. The biocompatibility and corrosion behavior are improved through the substitution of the hazardous alloying elements with non-toxic elements such as niobium, zirconium, and tin. Ti2448 is a promising alloy, containing non-toxic, biocompatible elements, but is also compromised in terms of microstructural features and mechanical properties, due to the high concentration of β phase stabilizing elements. Analogous to pure titanium, the α phase has a hexagonal closed packed (hcp) structure at ambient temperature. Above 882 °C, titanium consists of body-centered cubic (bcc) structures, which is the β phase. The β phase becomes stable and can be maintained in the metastable state below 882 °C by adding β stabilizers. The amount of β stabilizer to obtain purely β phases at ambient temperature depends on the molybdenum equivalency Mo_{eq}, which is an empirical rule derived from an analysis of binary titanium alloys, and can be described as follows [22–26]:

$$Mo_{eq} = 1.0\,Mo + 0.67\,V + 0.44\,W + 0.28\,Nb + 0.22\,Ta + 1.6\,Cr + 2.5\,Fe... - 1.0\,Al\ [wt.\ \%]. \quad (1)$$

In general, the addition of 10 wt. % molybdenum suppresses the transformation from β to α upon quenching. Below a Mo_{eq} of 10, the alloy is metastable [22,26]. The effect of molybdenum is, on the one hand, a reduction in the critical cooling rate to retain the β phase and, on the other hand, a significant reduction in the martensitic start temperature $M_{S\alpha'}$ [25]. Bania's equation for the Mo_{eq} includes a factor for aluminum. The aluminum equivalent Al_{eq} is added to reflect the tendency to support the formation of the α phase concerning the α stabilizers aluminum, tin, oxygen, and nitrogen as follows [26,27]:

$$Al_{eq} = 1.0\,Al + 0.17\,Zr + 0.33\,Sn + 10\,O + 10\,N\ [wt.\ \%]. \quad (2)$$

In the condition of energy disturbance, such as heat treatment and deformation, the metastable bcc β phase decomposes into the hcp α phase, the hcp α′ martensite phase, the orthorhombic α″ martensite, or/and the ω phase [27–32]. The α′ martensite formation in titanium alloys, in general, results in increasing tensile strength and hardness accompanied by decreasing plasticity [33,34]. The formation of α″ martensite under rapid quenching tends to reduce hardness, tensile, and fatigue strength [18,35–38]. Additionally, the ω phase is strengthening the titanium alloy in a certain volume fraction range, but also can lead to embrittlement [39,40]. Heat treatments of metastable β titanium alloys show promising features to improve and enhance the mechanical properties and are considered for different fields of applications, including aerospace or medical applications [22,26,41,42].

Various titanium alloys have already been manufactured by LPBF, such as Ti-6Al-4V [43–45] and Ti-6Al-7Nb [46–50]. As described, these alloys obtain high elastic moduli compared to human bones, which could lead to stress shielding, and contain, in part, hazardous elements such as aluminum and vanadium, which are referred to allergic reactions, neurotoxic effects, and probably Alzheimer's disease [51–53]. Therefore, in this study, the low-modulus metastable β titanium alloy Ti2448 is manufactured by LPBF and investigated. The complex phase transformation in combination with the LPBF is unknown

and these investigations are to contribute to understanding the mechanisms. Subsequent heat treatments are applied to modify and adjust the mechanical properties. To tailor the material behavior and to achieve sufficient mechanical properties, different heat treatments are conducted. Conclusively, the effects of different microstructures in the as-built and heat-treated conditions on the mechanical behavior is determined.

2. Materials and Methods

The Ti2448 powder was gas atomized by GfE Metalle und Materialien GmbH (Nürnberg, Germany) and examined concerning particle size distribution with a Mastersizer 2000 (Malvern Panalytical GmbH, Kassel, Germany) using laser diffraction. The powder is mainly spherical, see Figure 1a. It has a nominal particle size distribution between 28.5 µm (D_{10}) and 73.9 µm (D_{90}) with a log-transformed normal distribution centered at 45.9 µm (D_{50}). The chemical composition of the initial Ti2448 powder was determined by the Revierlabor (Chemische Laboratorien für Industrie und Umwelt GmbH, Essen, Germany) by X-ray fluorescence analysis, combustion analysis with infrared detection, and standard carrier gas hot extraction. The measured composition is compared to the target values and the LPBF manufactured specimens. The chemical composition of the as-built specimens was determined using the Bruker Q4 Tasman optical emission spectrometer (OES, Bruker AXS GmbH, Karlsruhe, Germany).

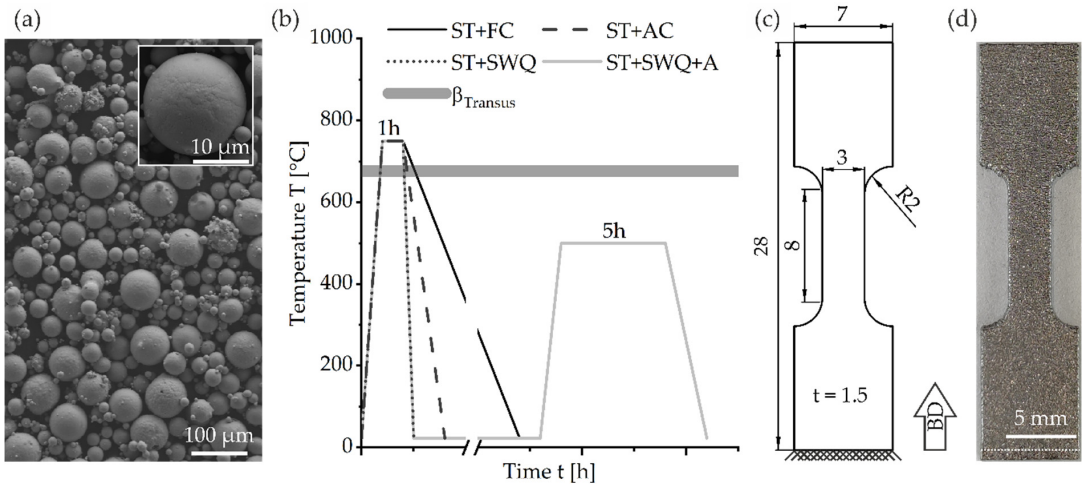

Figure 1. (**a**) SEM image of the morphology of initial Ti2448 powder, inset showing a spherical powder particle in higher magnification; (**b**) schematic overview of the heat treatments (ST = solution treatment, FC = furnace cooling, AC = air cooling, SWQ = slow water quenching in a glass ampule, A = aging) as well as the $\beta_{Transus}$ temperature; (**c**) geometry in reference to the building direction (BD) of the tensile specimens; (**d**) image of an as-built sample, support structure below the white dashed line.

The specimens were manufactured using an LT12 SLM machine (DMG MORI AG, Bielefeld, Germany) in an inert argon atmosphere containing less than 1000 ppm oxygen to minimize oxidation of the molten pool and the risk of introducing contaminants. The machine is equipped with a 400 W fiber laser with a spot size of 35 µm. Specimens were manufactured using a laser power P = 225 W, with a laser scanning speed v = 1.5 m s^{-1} and hatch distance h = 0.1 mm to obtain a relative density of more than 99.5%. As the contour parameters, a laser power P_c = 150 W and a scanning speed v_c = 0.4 m s^{-1} were applied. The layer thickness was kept constant at 50 µm, while the layer-wise rotation of the scanning vectors of 67°, and 5 mm stripes were applied. The building platform was preheated to 200 °C.

The as-built specimens were studied and compared to heat-treated specimens to analyze the differences in microstructure and mechanical properties. For identification of the effects of heat treatments, four different treatments were conducted in evacuated glass ampules in a Nabertherm furnace N41/13 (Nabertherm GmbH, Lilienthal, Germany). Solution treatment (ST) was performed at 750 °C for 1 h for all heat treatments followed by different cooling rates. Furnace cooling (FC), air cooling (AC), and slow water quenching (SWQ) of the glass ampules in water were applied. Additional specimens were aged at 500 °C for 4 h after SWQ (SWQ+A) with subsequent AC, see Figure 1b [54].

The crystalline phases were analyzed by X-ray diffraction (XRD) using a D8 Advance diffractometer (Bruker AXS GmbH, Karlsruhe, Germany) equipped with a polycapillary parallel X-ray lens of 2 mm and a LynxEye silicon strip detector (Bruker AXS GmbH, Karlsruhe, Germany). The specimens were ground with sandpaper (grain size 2500) and then vibration polished for 24 h on a VibroMet (Buehler, ITW Test & Measurement GmbH, Düsseldorf, Germany). The XRD measurements were performed with Cu-Kα1 radiation (λ = 1.5406 Å) at an acceleration voltage of 40 kV and a current of 40 mA. The diffractograms were obtained in Bragg-Brentano geometry over a scanning range of 2θ within 30° and 90° with a scan step of $\Delta 2\theta = 0.034°$ and an exposure time of 1 s. In addition, the lattice parameters of the hcp α, orthorhombic α'', and bcc β phases were determined.

For microstructural and hardness investigations, the specimens were ground and vibration polished. KOH-solution (32% H_2O; 8% H_2O_2; 60% KOH (40%)) was used for etching the specimens from 2.5 min to 5 min. The etched specimens were investigated with a light microscope (LiMi) Zeiss Axiophot (Carl Zeiss AG, Oberkochen, Germany). Powder morphology and microstructure were examined with a scanning electron microscope (SEM) Zeiss Ultra Plus (Carl Zeiss AG, Oberkochen, Germany).

Further examination of the microstructure was performed using transmission electron microscopy (TEM). Thin foils were prepared. Slices of ≈400 µm thickness were cut employing the Struers Sectom-5 (Struers GmbH, Willich, Germany). The slices were ground using SiC abrasive papers to a thickness of ≈100 µm. Then, 3 mm diameter discs were punched out of the slices. The discs were further thinned with Struers Tenupol-5 (Struers GmbH, Willich, Germany) using an electrolyte containing 5% perchloric acid-methanol solution at a voltage of 21 V, a current of 16 mA, and at a solution temperature of −23 °C. TEM was performed using a JEOL JEM-ARM 200F (JOEL Ltd., Tokyo, Japan). TEM, high-resolution TEM (HRTEM), high angle annular dark-field scanning TEM (HAADF-STEM), and energy dispersive spectroscopy (EDS) was performed. EDS maps were measured on selected regions of the HAADF-STEM images with a 5 nm step size and 2 s dwell time per step.

The Vickers hardness was measured on surfaces perpendicular to the build direction with a hardness tester KB 30 FA (KB Prüftechnik GmbH, Hochdorf-Assenheim, Germany) according to Vickers HV5. A minimum of two specimens per condition were tested with 30 hardness indentions across the surface of each specimen.

The monotonic tensile tests were performed utilizing a servo-hydraulic test-rig MTS 858 Tabletop System (MTS Systems Corporation, Eden Prairie, MN, USA) equipped with a 20 kN load cell and an extensometer 632.29F-30 (MTS Systems Corporation, Eden Prairie, MN, USA). The design of the miniature dogbone specimens is according to DIN EN ISO 6892-1, but does not fulfill the proportional specimen criterium [55]. The loading direction was parallel to the building direction (BD). The geometry and the BD are depicted in Figure 1c. An as-built sample is shown in Figure 1d. The tensile test procedure corresponded to a displacement-controlled execution with a crosshead speed of 1.5 mm min^{-1} according to DIN EN ISO 6892-1 [55].

3. Results and Discussion

3.1. Chemical Composition

The chemical composition of the initial Ti2448 powder was determined and compared to the target values and the LPBF manufactured specimens, see Table 1. The initial powder niobium content is slightly higher than prescribed, whereas the tin content is slightly lower.

Due to the different melting temperatures of the alloying elements, it is challenging to obtain the desired chemical configuration of the initial powder. The contents of zirconium and tin in the as-built specimens are in the prescribed range, the content of niobium is above 9 wt. %. The chemical composition could be affected by the vaporization of the alloying elements during the fabrication process [56–60]. Nevertheless, the oxygen content could be increased due to residual oxygen in the process chamber and the oxygen affinity of titanium at elevated temperatures [61,62]. Based on Equations (1) and (2), the Mo_{eq} is calculated for the initial powder state to be 2.94. Based on the chemical composition of the alloy, one may assume that the alloy is a metastable β to β rich titanium alloy [22,26].

Table 1. Chemical composition of initial powder and LPBF manufactured Ti2448 alloy in wt. %.

Condition	Ti	Nb	Zr	Sn	O	Mo_{eq}
Target Value	Bal.	23.5–24.5	3.5–4.5	7.5–8.5	<0.12	2.32
Initial Powder	Bal.	25.2	4.2	7.1	0.11	2.94
as-built	Bal.	>9.0	3.5	8.2	0.37	-

3.2. Phase Constituents and Microstructure

The microstructure of Ti2448 highly depends on the processing route and the heat treatment. The XRD diffractograms of the LPBF processed Ti2448 in the initial powder, as-built, and heat-treated conditions are shown in Figure 2. It can be observed that Ti2448 mainly consists of the cubic β phase (space group $Im\bar{3}m$) and, depending on the condition, also contains low amounts of the hexagonal α phase (space group $P6_3/mmc$), orthorhombic α″ martensite (space group *Cmcm*), or presumably hexagonal ω phase (space group *P6/mmm*). Compared to the β phase, the Bragg reflections of the remaining phases are broader, indicating a high degree of microstrain (deformed crystal lattice) and/or small grain sizes [63,64]. The Ti2248 powder contains the α″ phase next to the β phase. For Ti2248 in the as-built state, the Bragg reflections of the β (200) and β (211) planes show a shoulder formation towards higher angles, indicating a superposition with another Bragg reflection. At these angles, the Bragg reflections may originate from the ω phase. A clear assignment is not possible due to the overlapping and broad reflections. Contrarily, the heat-treated Ti2248 alloys possess either the α″ or α phase. The microstructure and subsequent transformation behavior are highly sensitive to the chemical composition and various cooling rates from the β phase field. In general, metastable β decomposes in the α (hcp), the α′ martensite (hcp), the α″ martensite (orthorhombic), and the ω phases [27–30]. The transformation can be tailored by employing heat treatments, thereby controlling the content of β stabilizers in the β phase through the cooling conditions [64–66]. For niobium concentrations less than 13 wt. % in Ti-Nb alloys, the α′ martensite is usually present [37]. Therefore, the Ti2248 alloy with its higher niobium content is expected to contain the ω or α″ phase inside a β matrix. With decreasing temperature, the instability of the bcc lattice in β phase alloys increases. As described by Moffat and Larbalestier for Ti-Nb alloys, the α″ and ω phases compete to evolve in an unstable lattice [67]. The β phase decomposition is determined by the quench rate, while the two decomposition modes to α″ or ω phase are mutually exclusive, due to the different transformation variants in metastable titanium alloys, as observed by Duering et al. [68]. For higher cooling rates, the formation of α″ martensite is favorable, while material cooled with lower rates comprise β and ω phase. The lower the cooling rate, the more complete is the collapse of the $\{222\}_\beta$ planes and the larger the ω precipitates should be [67]. It is assumed that the cooling condition in the LPBF process fosters the formation of the ω phase. As already proposed by Qi et al., a continuous diffusional-displacive $\beta \rightarrow \alpha'' \rightarrow \alpha$ transformation may be present [69]. High cooling rates, such as in SWQ, AC, and during the powder fabrication process, promote the α″ phase formation, while for slow cooling rates such as in FC or for aging treatments, the α″ phase was not detected, see Figure 2. The α″ phase can be regarded as the intermediate stage in between the transformation from bcc to hcp. In the as-built condition, only minor reflections of the α″ phase are observable and, in addition, some of the peaks of other

Materials **2022**, *15*, 3774

phases are broadened, probably due to the overlay with the α″ phase peaks, see black arrows in Figure 2. It is assumed, that due to insufficient undercooling during the process and/or decomposition through in situ heat treatments, the formation of α″ martensite is inhibited, suppressed, or reversed [34,70,71]. Heat treatments, including slow cooling or aging, enable the decomposition of α″ and the precipitation of the α phase [72]. In summary, slow cooling from the β phase-field, as well as aging, results in the formation of α precipitates. Higher cooling rates result in the martensitic formation of the α″ phase, while in the as-built state, at intermediate cooling rates and/or in-process heat treatment, the formation of the ω and α″ phases seems to be supported, which is mutually competitive.

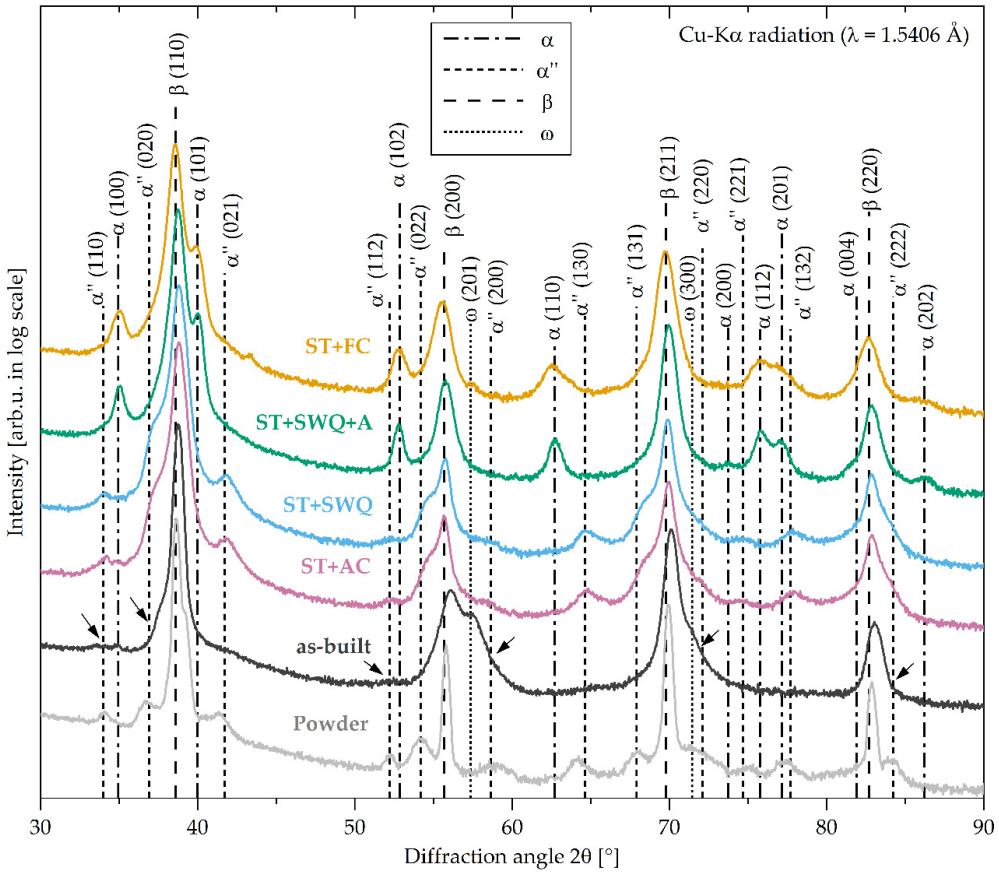

Figure 2. X-ray diffractograms of Ti2448 in as-built, ST+FC, ST+AC, ST+SWQ, and ST+SWQ+A conditions as well as the initial powder; black arrows indicating overlay of α″ phase peaks in the as-built condition; not depicted in the diagram: α″ orthorhombic (111) (superposition with β (110)), α″ orthorhombic (113) (superposition with β (211)); α hexagonal (002) (superposition with β (110)), and α hexagonal (103) (superposition with β (211)).

The lattice parameters of the hcp α phase, orthorhombic α″ martensite, and bcc β phase of Ti2448 in different conditions were determined from the XRD diffractograms and are summarized in Table 2. For the hexagonal ω phase, the calculation of the lattice parameters was not possible due to the overlapping of the Bragg reflections. The lattice parameter of the β phase is in the range between 3.287 Å and 3.303 Å. Deviations can be caused by distortions of the lattices, interference between phases, different chemical compositions, and therefore various atom radii. As calculated by XRD, the α phase exhibits lattice parameters of a = 2.959 Å and c = 4.758 Å for the furnace cooled condition and a = 2.959 Å and c = 4.726 Å for the aged condition. The obtained values for the α and the β phase follow

the results of previous studies [62,73]. The α phase lattice parameters of the furnace-cooled determined by TEM are a = 3.191 Å and c = 5.045 Å and deviate from the other values. The orthorhombic α″ phase shows lattice parameters of approximately a = 3.1 Å, b = 4.9 Å, and c = 4.7 Å for the XRD calculation and about a = 3.28 Å, b = 4.88 Å, and c = 4.617 Å for the TEM analysis, which slightly differ from reported values of deformation-induced α″ martensitic transformation [74,75]. It is assumed that the thermal formation of the α″ phase differs from mechanically induced transformations, leading to slightly different lattice parameters.

Table 2. Lattice parameters, determined by XRD, for hcp α, orthorhombic α″, and bcc β of Ti2448 in the as-built, ST+FC, ST+AC, ST+SWQ, and ST+SWQ+A condition as well as the initial powder; lattice parameters determined by TEM (marked in brackets).

Condition	Hcp α		Orthorhombic α″			Bcc β
	a = b [Å]	c [Å]	a [Å]	b [Å]	c [Å]	a = b = c [Å]
Initial Powder	-	-	3.107	4.924	4.716	3.298
as-built	-	-	-	-	-	3.287
as-built (TEM)	-	-	3.28	4.88	4.617	3.297
ST+FC	2.959	4.758	-	-	-	3.303
ST+FC (TEM)	3.191	5.045	-	-	-	3.294
ST+AC	-	-	3.110	4.860	4.716	3.294
ST+SWQ	-	-	3.121	4.871	4.679	3.295
ST+SWQ+A	2.959	4.726	-	-	-	3.294

The KOH-etched surfaces of the different conditions are depicted in Figure 3. Figure 3a,b demonstrate the as-built condition. β grain boundaries are observable in the LiMi and SEM images. Laths are visible in the grains and in the inset in (a), which is presumably referred to as the α″ martensitic phase. The ω phase was not detected. The air-cooled and water quenched conditions have a similar microstructure, see Figure 3c–f, respectively. Coarse grains are observed for both conditions. In contrast to the as-built condition, no α″ phase laths are observable in the microscopic images for the AC and SWQ condition, although the XRD measurements suggest this. Figure 3g,h show the LiMi and SEM images of the aged specimen. The prior β grains are not as clearly visible as in the other conditions. A very fine, diffuse microstructure is visible in the LiMi, which turned out to be α precipitates at a higher magnification in the SEM. Primary β grain boundaries are visible in the SEM image of the aged condition, see Figure 3h. The initial microstructure, such as in the as-built condition, is visible in the furnace cooled specimen, see Figure 3i. Yet, the SEM close-up in Figure 3j indicates α precipitates similar to those in the aged specimens, but not as homogeneous distributed. As observed by Ren et al., aging has a significant effect on the precipitation behavior of the secondary α phase in titanium alloys [76]. The ST+FC specimens exhibit an irregular distribution and heterogeneous size of intra-granular α precipitates (white arrows) with grain boundary α (black arrows), see Figure 3j. An adapted heat treatment (ST+SWQ+A) can modify the microstructure to achieve a uniform size and orientation (approximately 60°, white triangle) of the acicular α precipitations, see Figure 3h. Varying the aging time and temperature can tailor the morphology of the intra-granular α precipitates and the grain boundary α phase can be coarsened and, therefore, adjust the mechanical behavior [76,77].

A uniform microstructure with grain sizes less than 50 nm was observed by Hao et al. and Li et al. in cold-rolled sheets of Ti2448 [18,20]. The microstructure of hot-forged and cold-rolled Ti2448 was investigated and compared by Li et al. [19]. The hot-forged material consists of equiaxed β grains with a grain size of around 5 µm, divided into subgrains with sizes less than 1 µm. Aging of the hot-forged alloy resulted in α phase precipitations with a needle-like shape. The cold-rolled Ti2448 has a β + α″ microstructure with coarse grains but also nanostructured regions. Yang et al. cold-rolled previous hot-forged Ti2448 cylinder and performed subsequent solution treatment at 900 °C with water quenching (ST) or flash treatment at 700 °C with air cooling (FT). The resulting microstructures were

Materials **2022**, *15*, 3774

homogenous single β phase with grain sizes about 50 µm and 7 µm, respectively [78]. The microstructure of Ti2448 processed by warm swaging and warm rolling is presented by Hao et al. [79]. The hot-forged alloy showed an equiaxed β phase microstructure with grain sizes of 100 µm, consisting of equiaxed subgrains with sizes of around 1 µm. After warm swaging, the microstructure became swirled marble-like, with differences from the surface to the core. Subsequent warm rolling resulted in a homogeneous microstructure comprising β phase with grain sizes less than 200 nm and nanosized α phase. Zhang et al. observed a microstructure for as-hot-rolled Ti2448 with grains around tens of microns, containing subgrains of the sizes of hundreds of nanometers, and consisting of single β phase without the formation of ω phase or α″ martensite [21].

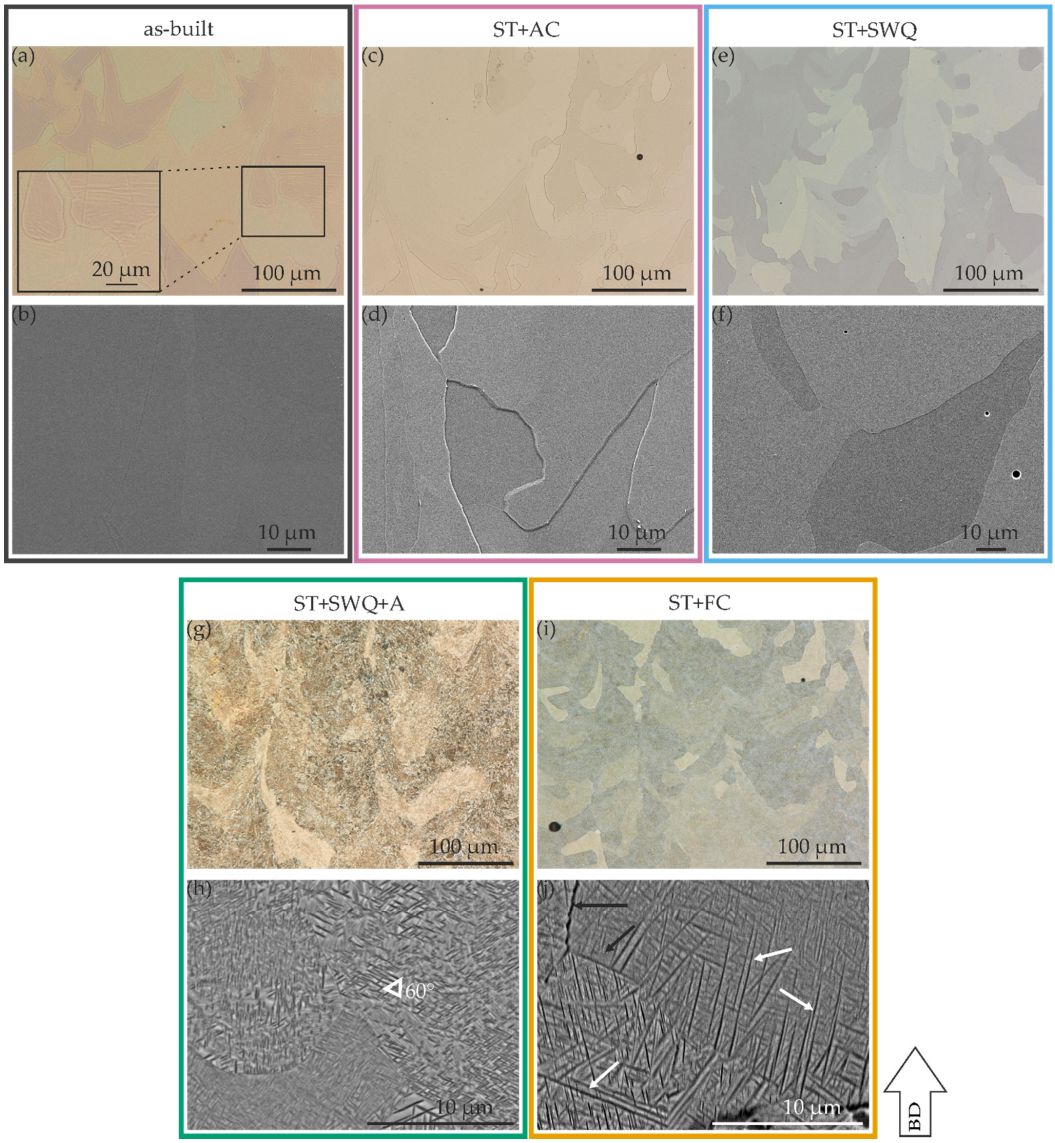

Figure 3. LiMi images of KOH-etched as-built (**a**) inset showing the black box in higher magnification), ST+AC (**c**), ST+SWQ (**e**), ST+SWQ+A (**g**), and ST+FC (**i**) conditions; and SEM images of KOH-etched as-built (**b**), ST+AC (**d**), ST+SWQ (**f**), ST+SWQ+A (**h**), and ST+FC (**j**) conditions; building direction (BD) for all conditions is indicated by the arrow.

Figure 4 shows the HAADF-STEM images and EDS maps of the as-built specimen. Figure 4a,b illustrate the nanostructure consisting of alternately α″ martensite and β titanium laths. Figure 4b is the magnification of the white square region in (a). The images prove the presence of parallel plates. The thickness of the plates varies between 42 and 85 nm. The plates are orthorhombic α″ martensite phase (bright laths) and the surrounding matrix is β phase (dark laths). The EDS maps for titanium, niobium, zirconium, and tin are depicted in Figure 4c–f and are taken from the white, dashed square in (b). The composition of the alloying elements is uniform in the α″ plates and β matrix. This indicates the diffusion-free nature of the orthorhombic α″ martensite phase formation.

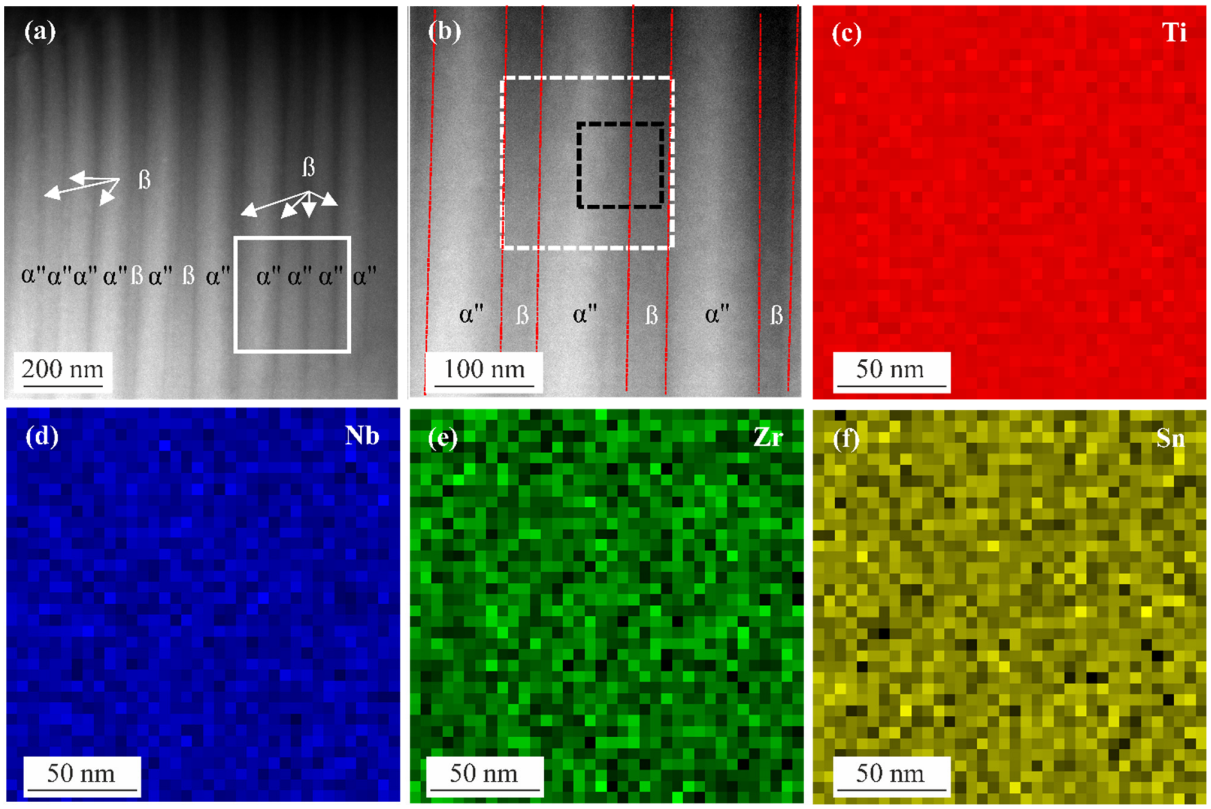

Figure 4. (**a**) HAADF STEM image of the as-built specimen, (**b**) HAADF STEM image of the white square region in (**a**), brighter laths are α″ martensite phase, while the surrounding area is the β matrix, red, dashed lines demarcate the boundary between α″ martensite and β phase; EDS maps from the white, dashed square in (**b**) and chemical distribution of (**c**) titanium, (**d**) niobium, (**e**) zirconium, and (**f**) tin.

HRTEM, FFT, and Fourier filtered HRTEM images of the as-built specimen from the black, dashed square region in Figure 4b are shown in Figure 5. Figure 5a–c are from the β phase, whereas Figure 5d–f are from the α″/β interface region. The HRTEM image in Figure 5a highlights the lattice of the β phase. The corresponding FFT image in (b) is captured from the [011]β zone axis and shows the $0\bar{1}1\beta$, $\bar{2}00\beta$ and $\bar{2}\bar{1}1\beta$ spots. Figure 5c is the zoomed-in image of (a), indicating the (110)β and (200)β planes. Figure 5d shows the HRTEM image from the lattice fringes of the orthorhombic α″ martensite phase and β phase lattice planes. Figure 5e is taken from the [011]β and [001]α″ zone axis. The FFT image in (e) presents the $0\bar{1}1\beta$, $\bar{2}00\beta$, and $\bar{2}\bar{1}1\beta$ spots as well as the $0\bar{2}0\alpha''$, $200\alpha''$, $2\bar{2}0\alpha''$, and $1\bar{1}0\alpha''$ spots. Multiple spots are observed to overlap with each other: (i) $0\bar{2}0\alpha''$ and $0\bar{1}1\beta$, (ii) $200\alpha''$ and $\bar{2}00\beta$ and (iii) $2\bar{2}0\alpha''$ and $\bar{2}\bar{1}1\beta$. From the FFT image, the orientation

relationship between the β and α″ martensite phase is [001]α″||[011]β, [0$\bar{2}$0]α″||[0$\bar{1}$1]β, [2$\bar{2}$0]α″||[$\bar{2}$1$\bar{1}$]β and [200]α″||[$\bar{2}$00]β. Figure 5f illustrates a magnified HRTEM marking the fringes from the (200)β, (200)α″, (110)β, (020)α″, and (110)α″ lattice planes.

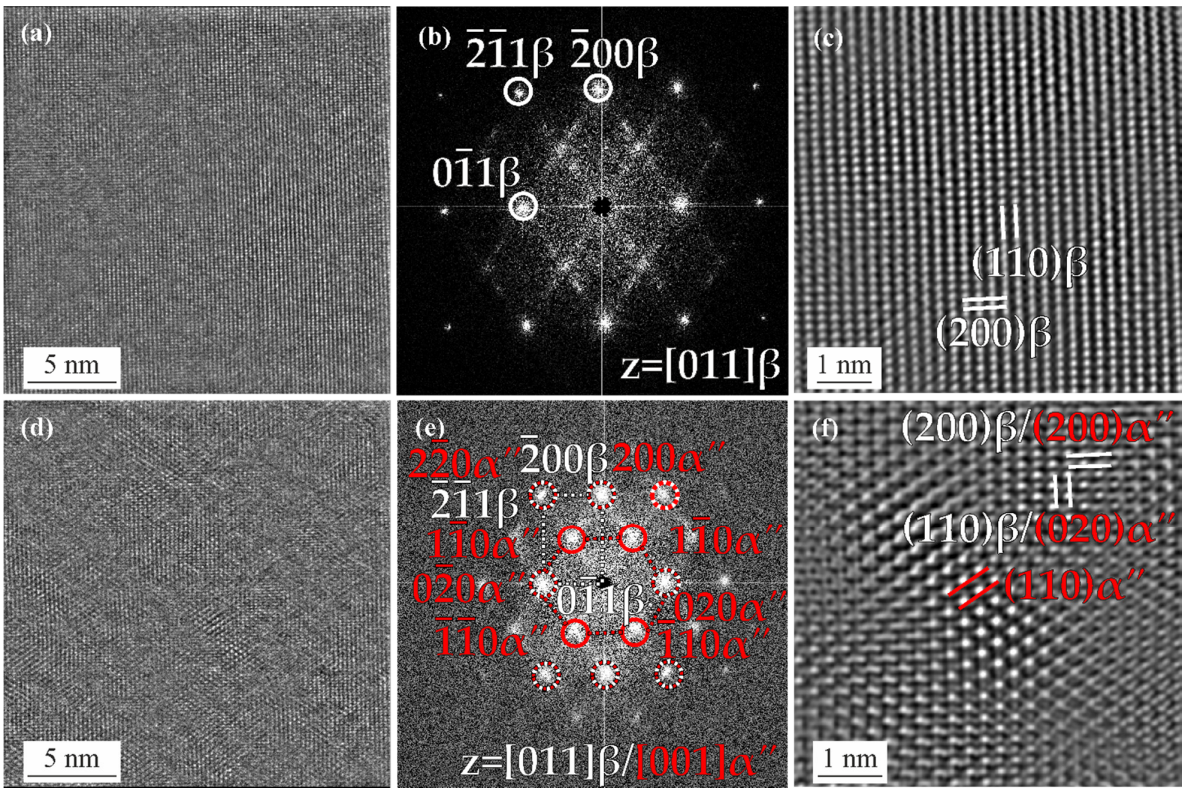

Figure 5. HRTEM, FFT, and Fourier filtered HRTEM images from the black, dashed square region in Figure 4b; (**a**) HRTEM and (**b**) FFT images of the β phase in (**a**), zone axis is [011]β; (**c**) higher magnification Fourier filtered HRTEM image of the β matrix in (**a**); (**d**) HRTEM and (**e**) FFT images of the α″ and β phase in Figure 4b, zone axis in is [011]β/[001]α″; (**f**) higher magnification Fourier filtered HRTEM image of the α″ and β phase in (**d**).

HAADF-STEM images of the ST+FC specimens are depicted in Figure 6a,b, showing the α and β phases. The α phase is present in the form of plates (white arrows) inside the β matrix. The EDS maps in Figure 6c–f are taken from the region in (b), showing the distribution of titanium, niobium, zirconium, and tin in the α and β phases. A depletion (lower color intensity) of niobium and an enrichment (higher color intensity) of titanium is observed in the α phase, indicating a diffusional mechanism of α phase formation due to the diffusion of mainly niobium. Zirconium and tin are stabilizing or neutral to the β phase-formation of titanium [80,81]. Minor differences in the distribution of zirconium and tin in terms of depletion can be observed between the α and β phases.

The TEM image of the ST+FC specimen depicted in Figure 7a shows the α phase plates and the β phase matrix. Figure 7b illustrates the HRTEM image of the α plate taken from the white square region in (a). Figure 7c is a magnified view of the top β/α interface in (b). The FFT image in Figure 7d is calculated from (c) with the zone axis of [$\bar{1}$13]β. The 0002α spot overlaps with the 110β spot, indicating that (0002)α||(110)β. Figure 7e is a close-up HRTEM image of the β/α interface of (c), marking the fringes from the (0002)α, (110)β, (2$\bar{2}$00)α, (1$\bar{2}$1)β, and (2$\bar{1}$1)β lattice planes. At the β/α interface, the lattice fringe of (0002)α is parallel to (110)β. A magnified Fourier filtered image of the β/α interface is presented in Figure 7f, illustrating the (0002)α||(110)β relationship.

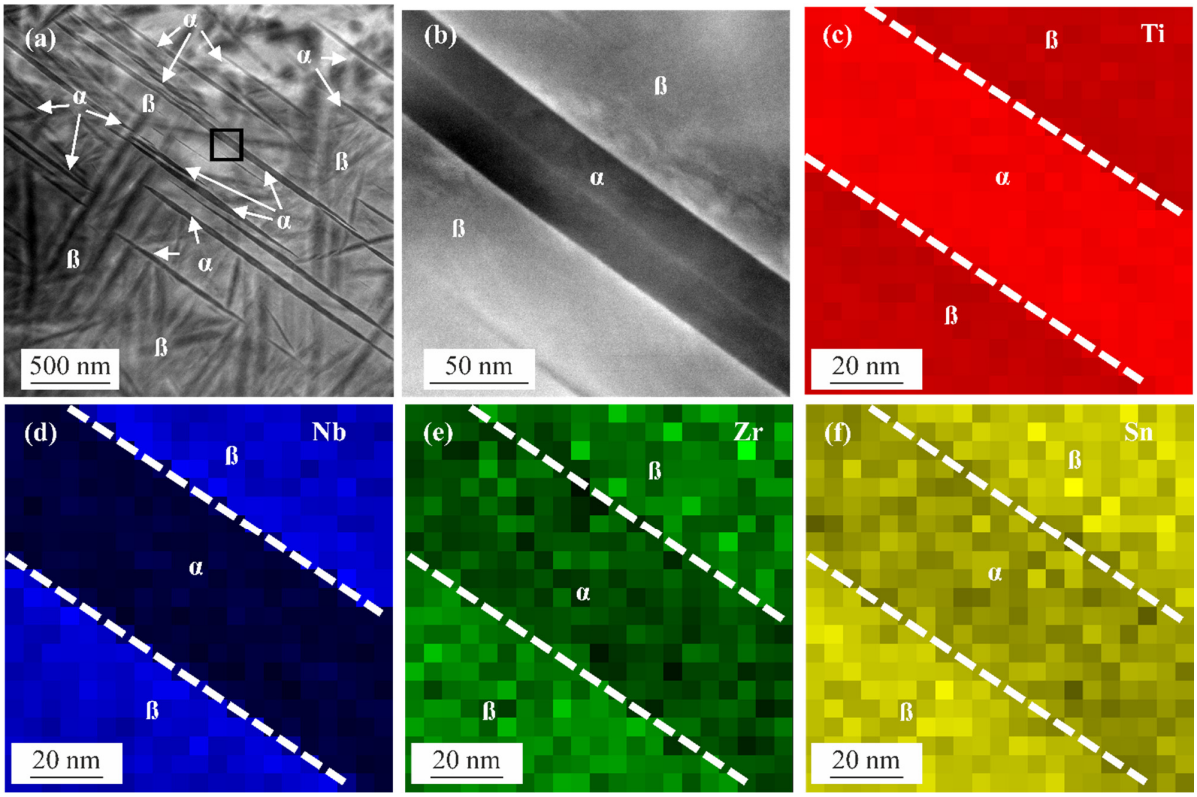

Figure 6. (**a**) HAADF STEM image of the ST+FC specimen with α phase laths inside the β phase matrix; (**b**) HAADF STEM image of the black square in (**a**), showing a higher magnification of an α phase lath surrounded by the β phase; EDS maps and chemical distribution of (**c**) titanium, (**d**) niobium, (**e**) zirconium, and (**f**) tin, demonstrating titanium enrichment inside the α phase (higher color intensity) and titanium depletion inside β phase, and enrichment of niobium, zirconium, and tin inside the β phase (higher color intensity) and depletion inside α phase, respectively.

Metastable β titanium alloys tend to decompose to the ω, α, and α″ phases. The ω phase probably occurs at lower temperatures, as described by Ohmori et al. [82]. In the as-built condition, the ω phase was not observed during TEM investigations, but, due to the XRD results, is assumed to be present in this condition. For the furnace cooled conditions, nevertheless, the α phase laths probably nucleate at the ω/β interfaces and grow in the β matrix, consuming the ω phase particles, as described by Ohmori et al. during quenching from the β phase region. The α″ martensite plates nucleated preferentially at the β grain boundaries [82].

Materials **2022**, *15*, 3774

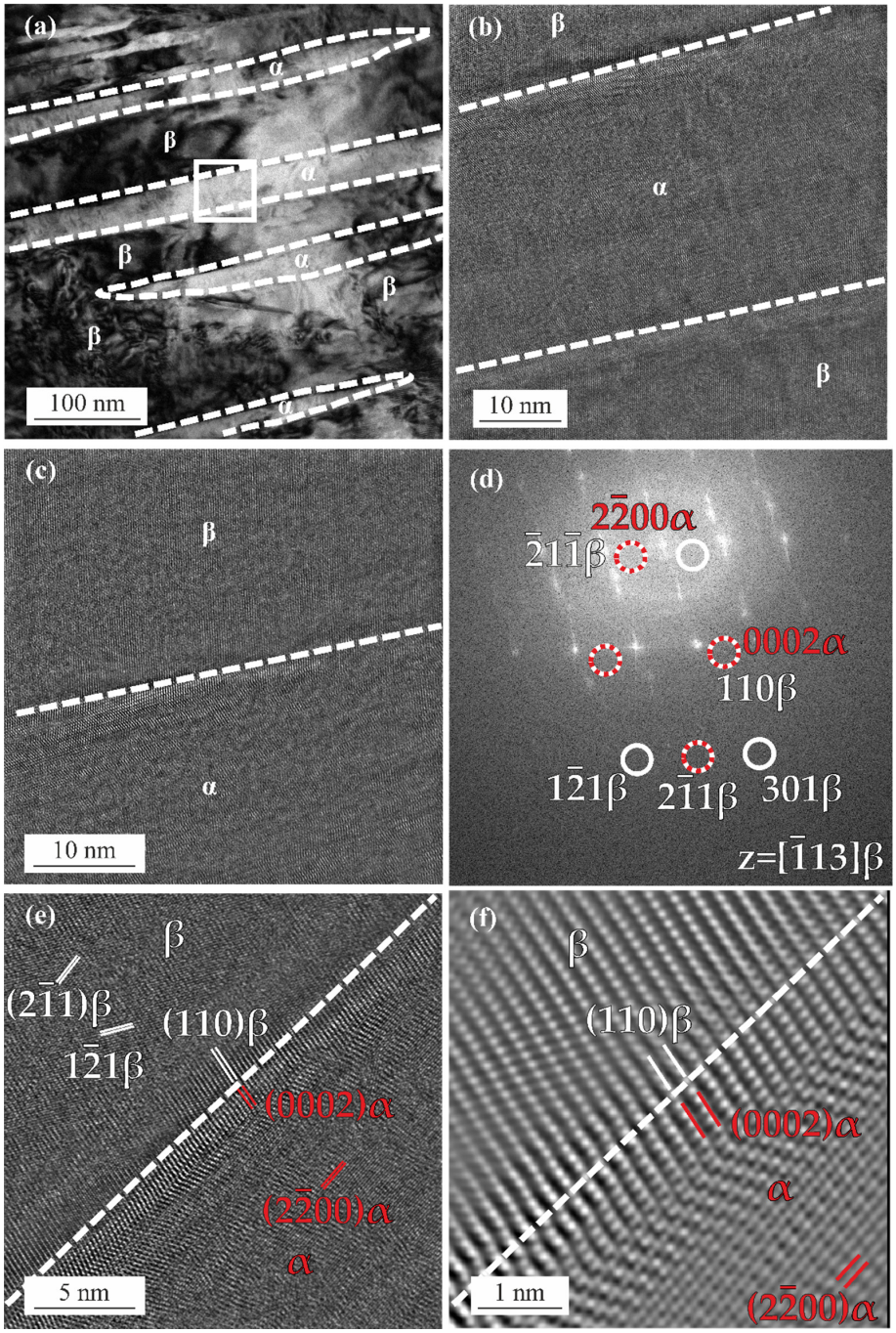

Figure 7. (**a**) TEM image of α phase and β phase in the ST+FC specimen; (**b**) HRTEM image of the α lath and β phase; (**c**) HRTEM image of the upper α/β interface in (**b**); (**d**) FFT image of the area in (**c**) with [113]β zone axis; (**e**) magnified HRTEM image of the α/β interface in (**c**) with the $(2\bar{1}\bar{1})\beta$, $(1\bar{2}1)\beta$, (110)β, (0002)α, and $(2\bar{2}00)\alpha$ planes marked; (**f**) Fourier filtered HRTEM image showing the α/β interface in (**e**) with the (110)β, (0002)α, and $(2\bar{2}00)\alpha$ planes marked.

3.3. Mechanical Properties

The hardness of the additively manufactured Ti2448 in as-built and heat-treated conditions is summarized in Figure 8a. In the as-built condition, the hardness is 219 ± 8 HV5 and slightly lower but in good agreement with other research on LPBF-fabricated Ti2448 with near full dense (230 HV0.5 [83], 240 HV1 [54], 230 HV0.5 [84]), and lower than for EBM-fabricated Ti2448 (255 HV [85]). For conventional conditions, the hardness varies between 215 HV (hot-forged), 230 HV (warm swaged), and 265 HV (warm rolled) [79]. For ST+AC and ST+SWQ conditions, the hardness is slightly higher, 232 ± 5 HV5 and 230 ± 5 HV5, respectively, compared to the as-built condition, probably due to the presence of α″ martensite [18,35–38]. The ST+SWQ+A heat treatment leads to a hardness of 290 ± 4 HV5. The highest hardness results in ST+FC condition with 305 ± 3 HV5. The increased hardness of the aged and furnace cooled condition is assumed to be precipitation hardening due to α precipitates formation in the β matrix [69,86]. The hardness values are summarized in Table 3.

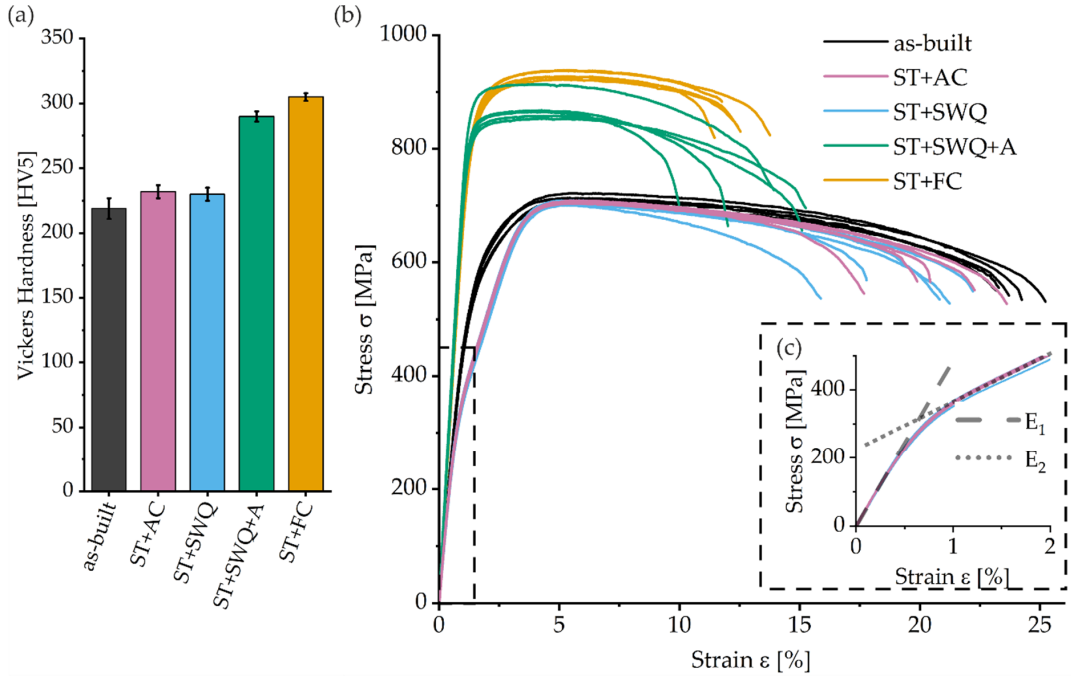

Figure 8. (**a**) Vickers hardness for different conditions; (**b**) stress–strain curves of different conditions; (**c**) inset of the dashed boxed in (**b**) presenting the nonlinear elastic behavior of the ST+AC and ST+SWQ conditions.

The stress–strain curves of the as-built and heat-treated specimens of Ti2448 are depicted in Figure 8b. The lowest ultimate tensile strength (UTS) of 700 ± 6 MPa and the highest fracture elongation A of 22 ± 1% were measured for the as-built condition. AC or SWQ after ST result in similar UTS of approximately 705 MPa and elongations of around 20%. The Young's moduli E_1 of the as-built, ST+AC, and ST+SWQ conditions are similar at the beginning of the elastic deformation, until a strain of 0.5%. The tensile tests of the ST+AC and ST+SWQ conditions show significant and continuous elastic softening with increasing strain and, therefore, stress. The slope changes for strain values higher than 1% to E_2 of approximately 14 ± 0.11 GPa, see Figure 8c. The α″ martensite phase is present in these two conditions. Kolli et al. propose deformation mechanisms by conventional slip and stress-induced transformation due to α′ martensite, α″ martensite, ω phase, and deformation twinning, whereas the mechanisms depend on the β phase stability of the titanium

alloy [42,87]. With increasing Mo_{eq}, the stress-induced deformation mechanisms follow the sequence $\alpha' \rightarrow \alpha'' \rightarrow \omega$ + twinning $\rightarrow$ twinning $\rightarrow$ twinning + slip $\rightarrow$ slip. With a Mo_{eq} of around 2.94 and a niobium content higher than 13 wt. %, the alloys are expected to contain the α'' phase and the deformation mechanism is likely to be based on α'' formation [37]. The presence of metastable α'' martensite or ω phase can promote stress-induced transformation and serve as nucleation sites during deformation [42,87]. As described by Furuta et al., both conditions show pseudo-elastic deformation. This behavior is based on stress-induced α'' martensite, which is determined through in situ XRD measurements during tensile tests. Along with increasing tensile strain and stress, the α'' phase retransforms to β and can be explained by reversible martensitic transformation, also known as "pseudo-elastic deformation" [88]. Hao et al. assume stress-induced phase transformation and/or incipient kink bands as the origin of the peculiar elastic behavior [89]. Although the LPFB process leads to α'' martensite microstructure, shown by the TEM investigations, this exceptional pseudo-elastic deformation behavior was not detectable for the as-built condition. The thermal history of each layer during the process may result in a characteristic microstructure of the as-built specimen and, therefore, a unique material behavior. The material undergoes a series of thermal cycles, where the previously fabricated material can be partially re-melted and re-solidified [90,91]. Non-linear elastic behavior of the as-built condition may be attributed to the microstructure, probably characterized by localized distorted region with the elastic strain being located hierarchically in the alloy, as assumed by Furuta et al. [88]. Subsequent aging or FC after ST led to higher strengths, 871 $\pm$ 22 MPa and 931 $\pm$ 7 MPa, a significant reduction of elongations, 12 $\pm$ 2% and 11 $\pm$ 1 MPa, and increased Young's moduli E_1, 76 $\pm$ 3 GPa and 73 $\pm$ 1 GPa, respectively. These treatments produce fine dispersion of α precipitates as the principal strengthening mechanism. The aging temperature and time have a significant effect on the size and spacing of the α phase formed and, therefore, on the mechanical performance [92].

Table 3. Comparison of average mechanical properties, including the hardness and monotonic tensile properties, of the as-built and heat-treated Ti2448, as well as literature values including conventional processing methods: yield strength YS, ultimate tensile strength UTS, fracture elongation A, and Young's Moduli E_1 and E_2.

Condition	Hardness [HV5]	YS [MPa]	UTS [MPa]	A [%]	E_1/E_2 [GPa]
as-built	219 $\pm$ 8	490 $\pm$ 16	700 $\pm$ 6	22 $\pm$ 1	49 $\pm$ 1/-
ST+AC	232 $\pm$ 5	362 $\pm$ 7	707 $\pm$ 2	20 $\pm$ 2	51 $\pm$ 2/14 $\pm$ 0.1
ST+SWQ	230 $\pm$ 5	339 $\pm$ 10	705 $\pm$ 3	19 $\pm$ 2	50 $\pm$ 2/14 $\pm$ 0.1
ST+SWQ+A	290 $\pm$ 4	819 $\pm$ 27	871 $\pm$ 22	12 $\pm$ 2	76 $\pm$ 3/-
ST+FC	305 $\pm$ 3	805 $\pm$ 11	931 $\pm$ 7	11 $\pm$ 1	73 $\pm$ 1/-
LPBF [83]	220–230	563 $\pm$ 38	665 $\pm$ 18	14 $\pm$ 4	53 $\pm$ 1/-
Hot rolled [21]	-	700	830	15	46
Hot-forged [19]	230–370	570	750	13	55
Hot-forged [79]	215	-	800	18	52
Warm swaged [79]	230	-	850	14	55
Warm rolled [79]	265	-	1150	8	56

The mechanical properties are summarized in Table 3. Rapid cooling during fabrication or heat treatment results in lower strength properties. High cooling rates from above the $\beta_{Transus}$ temperature result in the formation of the α'' martensite and, consequently, lower strength and elongation, compared to the as-built condition. Previous studies have shown that the α'' martensite phase reduces hardness, tensile, and fatigue properties [36,93]. Through slow cooling or aging treatments at temperatures below $\beta_{Transus}$, α phase laths can evolve and grow. Annealing treatments and slower cooling lead to strengthening due to enhanced nucleation of the α precipitates [20,94]. Compared to other research on additively manufactured Ti2448, the properties are in good agreement regarding the hardness and UTS, whereas the YS and fracture elongation slightly differ, due to varying proportionality factors concerning the specimen geometry [83]. In comparison to other processing

routes, the different heat treatments, in particular the aging and FC, enhance the mechanical properties in terms of UTS and hardness. The properties of the warm swaging and rolling treatments are caused by the ultrafine-grained microstructures, not achievable by the applied treatments [79]. Further work shows similar properties, depending on the processing routes and heat treatment strategy [95], although, for the additively manufactured Ti2448, different treatments show huge potential in improving the mechanical behavior and properties, especially aging or FC. Besides improved UTS and YS remaining similar elongation compared to the conventional process routes, the Young's moduli increase for these conditions due to the presence of α precipitations. The hardness of conventional processed Ti2448 can be outperformed by the additively processed and heat-treated conditions [19]. Nevertheless, additively manufactured and heat-treated (FC or SWQ+A) Ti2448 achieves similar or better mechanical performances than conventional processed Ti2448 regarding UTS and YS, with slightly increased Young's moduli and still retained good ductility.

The possibility of in situ α″ martensitic transformations during deformation of the β phase for air-cooled and slow water quenched specimens, during hardness or tensile tests, could be present. The determination is challenging and would require the observation of the specimens at the nanoscopic level during the tests. Further investigations on the stress-induced deformation and formation of the α″ phase are necessary for a comprehensive understanding of the mechanical behavior, exclusively concerning the fatigue behavior and the utilization as an implant alloy. In addition, the individual tailoring of the mechanical properties by adapting the aging heat treatment parameters has to be considered for further research.

4. Conclusions

Micro- and nanostructure, as well as Vickers hardness and monotonic tensile properties of Ti2448 manufactured with LPBF, have been studied in the as-built state and heat-treated conditions. Solution heat treatment at 750 °C with various cooling rates (AC, FC, and SWQ) or ST with subsequent aging at 500 °C were performed and compared to the as-built additively manufactured condition. The effect of different heat treatments is determined as follows:

- The as-built condition shows mainly β phase containing acicular α″ martensite phase, as detected via TEM. Air-cooled and water-quenched states exhibit similar microstructures consisting of β grains, investigated by LiMi and SEM. The aged condition exhibits a diffuse microstructure with homogeneous and uniform α precipitates inside the β matrix. The furnace-cooled specimens have a microstructure comparable to the aged conditions but have heterogeneously distributed and coarser α precipitates within the β phase.
- The nanostructure, determined by TEM, of the as-built condition is compared to the furnace cooled condition, which exhibits the best tensile properties regarding hardness, UTS, and YS. The α″ martensite laths were detected inside the β matrix. Based on FFT images, the orientation relationship of the α″ martensite and β phase is determined. The homogeneous distribution of alloying elements in the EDS maps indicates a diffusion-free phase transformation during cooling. The furnace-cooled specimens consist of α precipitates inside a β phase matrix. Based on crystallographic relation, the precipitates are oriented approximately 60° to each other.
- X-ray diffractograms are sensitive to the various heat treatments and, in particular, the cooling rates. High cooling rates, e.g., AC, SWQ, and the powder fabrication process, lead to the formation of the martensitic α″ phase. Low cooling rates (FC) or aging after ST result in the formation of the α phase.
- FC or aging after solution treatment results in a microstructure containing acicular α precipitates in the β matrix, leading to high tensile strength with relatively low ductility. Phase transformation, such as stress-induced α″ phase transformation, probably leads to pseudo-elastic deformation behavior in the air-cooled and slow water-quenched conditions. As the α″ phase was not detected with XRD in the furnace cooled and

aged conditions, a linear stress–strain relationship was observable in the elastic range. The as-built conditions show elastic anomaly, which is attributed to the LPBF resulting microstructure. The furnace cooled condition exhibits the best mechanical properties regarding UTS, YS, and hardness with a slightly worse fracture elongation compared to the aged conditions.

Controlling the development and refinement of precipitated α phase in metastable β titanium alloys allows the achievement of an excellent combination of strength and ductility, including superb biocompatible properties. In this work, the furnace-cooled specimens obtain the best mechanical properties regarding hardness, UTS, and YS. Nevertheless, the aged condition has to be considered for further investigations regarding the possibility of tailoring the material properties. Adapted heat treatments enable adjusting the microstructural features in terms of the α precipitates. Furthermore, in situ investigations at the nanoscopic level should be performed to determine and understand the material behavior and possible α'' phase transformation behavior during the tensile tests of the air-cooled and water-quenched conditions. If fully understood, the two-part Young's modulus can be utilized. Regarding the overall performance, Ti2448 shows promising features regarding the tailoring of mechanical properties and applying an implant material with a low Young's modulus, as well as adequate and adaptable strength properties.

Author Contributions: Conceptualization, M.H., K.-P.H. and M.S.; methodology, M.H., K.-P.H. and M.S.; software, M.H. and N.F.L.D.; validation, M.H., N.F.L.D., K.-P.H. and M.S.; formal analysis, M.H., K.-P.H. and M.S.; investigation, M.H., N.F.L.D. and S.P.; resources, W.T. and M.S.; data curation, M.H.; writing—original draft preparation, M.H.; writing—review and editing, M.H., N.F.L.D., S.P., D.S., K.-P.H., W.T. and M.S.; visualization, M.H.; supervision, K.-P.H., D.S., W.T. and M.S.; project administration, M.H.; funding acquisition, K.-P.H., W.T. and M.S. All authors have read and agreed to the published version of the manuscript.

Funding: This research was funded by the Deutsche Forschungsgemeinschaft (DFG), grant numbers SCHA 1484/45-1, and TI 343/167-1.

Data Availability Statement: The data that support the findings of this study are available from the corresponding author upon reasonable request.

Acknowledgments: The research was performed with the equipment and base of the LWK and DMRC research infrastructure. The authors are grateful to the staff members of the LWK and DMRC.

Conflicts of Interest: The authors declare no conflict of interest. The funders had no role in the design of the study; in the collection, analyses, or interpretation of data; in the writing of the manuscript, or in the decision to publish the results.

References

1. Gubin, A.V.; Kuznetsov, V.P.; Borzunov, D.Y.; Koryukov, A.A.; Reznik, A.V.; Chevardin, A.Y. Challenges and Perspectives in the Use of Additive Technologies for Making Customized Implants for Traumatology and Orthopedics. *Biomed. Eng.* **2016**, *50*, 285–289. [CrossRef]
2. Bechtold, J.E. Application of Computer Graphics in the Design of Custom Orthopedic Implants. *Orthop. Clin. N. Am.* **1986**, *17*, 605–612. [CrossRef]
3. Heller, M.; Bauer, H.-K.; Goetze, E.; Gielisch, M.; Roth, K.E.; Drees, P.; Maier, G.S.; Dorweiler, B.; Ghazy, A.; Neufurth, M.; et al. Applications of patient-specific 3D printing in medicine. *Int. J. Comput. Dent.* **2016**, *19*, 323–339. [PubMed]
4. Munsch, M. Laser additive manufacturing of customized prosthetics and implants for biomedical applications. In *Laser Additive Manufacturing*; Elsevier: Amsterdam, The Netherlands, 2017; pp. 399–420, ISBN 9780081004333.
5. Narra, S.P.; Mittwede, P.N.; DeVincent Wolf, S.; Urish, K.L. Additive Manufacturing in Total Joint Arthroplasty. *Orthop. Clin. N. Am.* **2019**, *50*, 13–20. [CrossRef] [PubMed]
6. Gebhardt, A.; Hötter, J.-S. *Additive Manufacturing: 3D Printing for Prototyping and Manufacturing*; Hanser Publishers: Cincinnati, OH, USA; Munich, Germany, 2016; ISBN 978-1-56990-582-1.
7. AlMangour, B. (Ed.) *Additive Manufacturing of Emerging Materials*; Springer: Cham, Switzerland, 2019; ISBN 978-3-319-91713-9.
8. Long, M.; Rack, H. Titanium alloys in total joint replacement—A materials science perspective. *Biomaterials* **1998**, *19*, 1621–1639. [CrossRef]
9. Niinomi, M. Recent metallic materials for biomedical applications. *Metall. Mater. Trans.* **2002**, *33*, 477–486. [CrossRef]

10. Blakey-Milner, B.; Gradl, P.; Snedden, G.; Brooks, M.; Pitot, J.; Lopez, E.; Leary, M.; Berto, F.; Du Plessis, A. Metal additive manufacturing in aerospace: A review. *Mater. Des.* **2021**, *209*, 110008. [CrossRef]
11. Niinomi, M. Mechanical properties of biomedical titanium alloys. *Mater. Sci. Eng.* **1998**, *243*, 231–236. [CrossRef]
12. Sumitomo, N.; Noritake, K.; Hattori, T.; Morikawa, K.; Niwa, S.; Sato, K.; Niinomi, M. Experiment study on fracture fixation with low rigidity titanium alloy: Plate fixation of tibia fracture model in rabbit. *J. Mater. Sci. Mater. Med.* **2008**, *19*, 1581–1586. [CrossRef] [PubMed]
13. Cheruvu, B.; Venkatarayappa, I.; Goswami, T. Stress Shielding in Cemented Hip Implants Assessed from Computed Tomography. *Biomed. J. Sci. Tech. Res.* **2019**, *18*, 13637–13641. [CrossRef]
14. Liu, Y.J.; Li, S.J.; Wang, H.L.; Hou, W.T.; Hao, Y.L.; Yang, R.; Sercombe, T.B.; Zhang, L.C. Microstructure, defects and mechanical behavior of beta-type titanium porous structures manufactured by electron beam melting and selective laser melting. *Acta Mater.* **2016**, *113*, 56–67. [CrossRef]
15. Bahl, S.; Suwas, S.; Chatterjee, K. Comprehensive review on alloy design, processing, and performance of β Titanium alloys as biomedical materials. *Int. Mater. Rev.* **2021**, *66*, 114–139. [CrossRef]
16. Geetha, M.; Singh, A.K.; Asokamani, R.; Gogia, A.K. Ti based biomaterials, the ultimate choice for orthopaedic implants—A review. *Prog. Mater. Sci.* **2009**, *54*, 397–425. [CrossRef]
17. Niinomi, M. Mechanical biocompatibilities of titanium alloys for biomedical applications. *J. Mech. Behav. Biomed. Mater.* **2008**, *1*, 30–42. [CrossRef]
18. Hao, Y.L.; Li, S.J.; Sun, S.Y.; Zheng, C.Y.; Hu, Q.M.; Yang, R. Super-elastic titanium alloy with unstable plastic deformation. *Appl. Phys. Lett.* **2005**, *87*, 91906. [CrossRef]
19. Li, S.J.; Cui, T.C.; Hao, Y.L.; Yang, R. Fatigue properties of a metastable beta-type titanium alloy with reversible phase transformation. *Acta Biomater.* **2008**, *4*, 305–317. [CrossRef]
20. Li, S.J.; Zhang, Y.W.; Sun, B.B.; Hao, Y.L.; Yang, R. Thermal stability and mechanical properties of nanostructured Ti–24Nb–4Zr–7.9Sn alloy. *Mater. Sci. Eng.* **2008**, *480*, 101–108. [CrossRef]
21. Zhang, S.Q.; Li, S.J.; Jia, M.T.; Hao, Y.L.; Yang, R. Fatigue properties of a multifunctional titanium alloy exhibiting nonlinear elastic deformation behavior. *Scr. Mater.* **2009**, *60*, 733–736. [CrossRef]
22. Bania, P.J. Beta titanium alloys and their role in the titanium industry. *JOM* **1994**, *46*, 16–19. [CrossRef]
23. Collings, E.W. *The Physical Metallurgy of Titanium Alloys*; American Society for Metals: Metals Park, OH, USA, 1984; ISBN 9780871701817.
24. Sing, S.L.; Yeong, W.Y.; Wiria, F.E. Selective laser melting of titanium alloy with 50 wt% tantalum: Microstructure and mechanical properties. *J. Alloys Compd.* **2016**, *660*, 461–470. [CrossRef]
25. Vrancken, B.; Thijs, L.; Kruth, J.-P.; van Humbeeck, J. Microstructure and mechanical properties of a novel β titanium metallic composite by selective laser melting. *Acta Mater.* **2014**, *68*, 150–158. [CrossRef]
26. Chen, L.-Y.; Cui, Y.-W.; Zhang, L.-C. Recent Development in Beta Titanium Alloys for Biomedical Applications. *Metals* **2020**, *10*, 1139. [CrossRef]
27. Jaffee, R.I.; Promisel, N.E. *The Science, Technology and Application of Titanium*; Elsevier: Amsterdam, The Netherlands, 1970; ISBN 9780080065649.
28. Burgers, W.G. On the process of transition of the cubic-body-centered modification into the hexagonal-close-packed modification of zirconium. *Physica* **1934**, *1*, 561–586. [CrossRef]
29. Newkirk, J.B.; Geisler, A.H. Crystallographic aspects of the beta to alpha transformation in titanium. *Acta Metall.* **1953**, *1*, 370–374. [CrossRef]
30. Schmidt, F.F.; Wood, R.A. Heat Treatment of Titanium and Titanium Alloys: Heat Treatments and Tensile Properties of Titanium and Titanium Alloys for Structures. 1966. Available online: https://ntrs.nasa.gov/citations/19660015720 (accessed on 19 February 2022).
31. Ehtemam-Haghighi, S.; Liu, Y.; Cao, G.; Zhang, L.-C. Influence of Nb on the β→α″ martensitic phase transformation and properties of the newly designed Ti-Fe-Nb alloys. *Mater. Sci. Eng. Mater. Biol. Appl.* **2016**, *60*, 503–510. [CrossRef]
32. Haghighi, S.E.; Lu, H.B.; Jian, G.Y.; Cao, G.H.; Habibi, D.; Zhang, L.C. Effect of α″ martensite on the microstructure and mechanical properties of beta-type Ti–Fe–Ta alloys. *Mater. Des.* **2015**, *76*, 47–54. [CrossRef]
33. He, J.; Li, D.; Jiang, W.; Ke, L.; Qin, G.; Ye, Y.; Qin, Q.; Qiu, D. The Martensitic Transformation and Mechanical Properties of Ti6Al4V Prepared via Selective Laser Melting. *Materials* **2019**, *12*, 321. [CrossRef]
34. Motyka, M. Martensite Formation and Decomposition during Traditional and AM Processing of Two-Phase Titanium Alloys—An Overview. *Metals* **2021**, *11*, 481. [CrossRef]
35. Banumathy, S.; Mandal, R.K.; Singh, A.K. Structure of orthorhombic martensitic phase in binary Ti–Nb alloys. *J. Appl. Phys.* **2009**, *106*, 93518. [CrossRef]
36. Hao, Y.L.; Yang, R.; Niinomi, M.; Kuroda, D.; Zhou, Y.L.; Fukunaga, K.; Suzuki, A. Young's modulus and mechanical properties of Ti-29Nb-13Ta-4.6Zr in relation to α″ martensite. *Metall. Mater. Trans.* **2002**, *33*, 3137–3144. [CrossRef]
37. Tang, X.; Ahmed, T.; Rack, H.J. Phase transformations in Ti-Nb-Ta and Ti-Nb-Ta-Zr alloys. *J. Mater. Sci.* **2000**, *35*, 1805–1811. [CrossRef]
38. Li, S.J.; Niinomi, M.; Akahori, T.; Kasuga, T.; Yang, R.; Hao, Y.L. Fatigue characteristics of bioactive glass-ceramic-coated Ti-29Nb-13Ta-4.6Zr for biomedical application. *Biomaterials* **2004**, *25*, 3369–3378. [CrossRef] [PubMed]

39. Hickman, B.S. The formation of omega phase in titanium and zirconium alloys: A review. *J. Mater. Sci.* **1969**, *4*, 554–563. [CrossRef]
40. Williams, J.C.; Hickman, B.S.; Marcus, H.L. The effect of omega phase on the mechanical properties of titanium alloys. *Metall. Mater. Trans.* **1971**, *2*, 1913–1919. [CrossRef]
41. Colombo-Pulgarín, J.C.; Biffi, C.A.; Vedani, M.; Celentano, D.; Sánchez-Egea, A.; Boccardo, A.D.; Ponthot, J.-P. Beta Titanium Alloys Processed by Laser Powder Bed Fusion: A Review. *J. Mater. Eng. Perform.* **2021**, *30*, 6365–6388. [CrossRef]
42. Kolli, R.; Devaraj, A. A Review of Metastable Beta Titanium Alloys. *Metals* **2018**, *8*, 506. [CrossRef]
43. Murr, L.E.; Gaytan, S.M.; Ramirez, D.A.; Martinez, E.; Hernandez, J.; Amato, K.N.; Shindo, P.W.; Medina, F.R.; Wicker, R.B. Metal Fabrication by Additive Manufacturing Using Laser and Electron Beam Melting Technologies. *J. Mater. Sci. Technol.* **2012**, *28*, 1–14. [CrossRef]
44. Murr, L.E.; Quinones, S.A.; Gaytan, S.M.; Lopez, M.I.; Rodela, A.; Martinez, E.Y.; Hernandez, D.H.; Martinez, E.; Medina, F.; Wicker, R.B. Microstructure and mechanical behavior of Ti-6Al-4V produced by rapid-layer manufacturing, for biomedical applications. *J. Mech. Behav. Biomed. Mater.* **2009**, *2*, 20–32. [CrossRef]
45. Thijs, L.; Verhaeghe, F.; Craeghs, T.; van Humbeeck, J.; Kruth, J.P. A study of the microstructural evolution during selective laser melting of Ti–6Al–4V. *Acta Mater.* **2010**, *58*, 3303–3312. [CrossRef]
46. Polozov, I.; Sufiiarov, V.; Popovich, A.; Masaylo, D.; Grigoriev, A. Synthesis of Ti-5Al, Ti-6Al-7Nb, and Ti-22Al-25Nb alloys from elemental powders using powder-bed fusion additive manufacturing. *J. Alloys Compd.* **2018**, *763*, 436–445. [CrossRef]
47. Xu, C.; Sikan, F.; Atabay, S.E.; Muñiz-Lerma, J.A.; Sanchez-Mata, O.; Wang, X.; Brochu, M. Microstructure and mechanical behavior of as-built and heat-treated Ti–6Al–7Nb produced by laser powder bed fusion. *Mater. Sci. Eng. Struct. Mater.* **2020**, *793*, 139978. [CrossRef]
48. Sercombe, T.; Jones, N.; Day, R.; Kop, A. Heat treatment of Ti-6Al-7Nb components produced by selective laser melting. *Rapid Prototyp. J.* **2008**, *14*, 300–304. [CrossRef]
49. Hein, M.; Hoyer, K.-P.; Schaper, M. Additively processed TiAl6Nb7 alloy for biomedical applications. *Mater. Und Werkst.* **2021**, *52*, 703–716. [CrossRef]
50. Hein, M.; Kokalj, D.; Lopes Dias, N.F.; Stangier, D.; Oltmanns, H.; Pramanik, S.; Kietzmann, M.; Hoyer, K.-P.; Meißner, J.; Tillmann, W.; et al. Low Cycle Fatigue Performance of Additively Processed and Heat-Treated Ti-6Al-7Nb Alloy for Biomedical Applications. *Metals* **2022**, *12*, 122. [CrossRef]
51. Mold, M.; Linhart, C.; Gómez-Ramírez, J.; Villegas-Lanau, A.; Exley, C. Aluminum and Amyloid-β in Familial Alzheimer's Disease. *J. Alzheimers Dis.* **2020**, *73*, 1627–1635. [CrossRef]
52. Engelhart, S.; Segal, R.J. Allergic reaction to vanadium causes a diffuse eczematous eruption and titanium alloy orthopedic implant failure. *Cutis* **2017**, *99*, 245–249.
53. Klotz, K.; Weistenhöfer, W.; Neff, F.; Hartwig, A.; van Thriel, C.; Drexler, H. The Health Effects of Aluminum Exposure. *Dtsch. Arztebl. Int.* **2017**, *114*, 653–659. [CrossRef]
54. Yang, C.L.; Zhang, Z.J.; Li, S.J.; Liu, Y.J.; Sercombe, T.B.; Hou, W.T.; Zhang, P.; Zhu, Y.K.; Hao, Y.L.; Zhang, Z.F.; et al. Simultaneous improvement in strength and plasticity of Ti-24Nb-4Zr-8Sn manufactured by selective laser melting. *Mater. Des.* **2018**, *157*, 52–59. [CrossRef]
55. *DIN EN ISO 6892-1:2020-06*; Metallische Werkstoffe_-Zugversuch_-Teil_1: Prüfverfahren bei Raumtemperatur (ISO_6892-1:2019), Deutsche Fassung EN_ISO_6892-1:2019. Beuth Verlag GmbH: Berlin, Germany, 2020.
56. Bidare, P.; Bitharas, I.; Ward, R.M.; Attallah, M.M.; Moore, A.J. Laser powder bed fusion at sub-atmospheric pressures. *Int. J. Mach. Tools Manuf.* **2018**, *130*, 65–72. [CrossRef]
57. Collur, M.M.; Paul, A.; DebRoy, T. Mechanism of alloying element vaporization during laser welding. *MTB* **1987**, *18*, 733–740. [CrossRef]
58. Dai, D.; Gu, D. Effect of metal vaporization behavior on keyhole-mode surface morphology of selective laser melted composites using different protective atmospheres. *Appl. Surf. Sci.* **2015**, *355*, 310–319. [CrossRef]
59. Santecchia, E.; Spigarelli, S.; Cabibbo, M. Material Reuse in Laser Powder Bed Fusion: Side Effects of the Laser—Metal Powder Interaction. *Metals* **2020**, *10*, 341. [CrossRef]
60. Yin, J.; Zhang, W.; Ke, L.; Wei, H.; Wang, D.; Yang, L.; Zhu, H.; Dong, P.; Wang, G.; Zeng, X. Vaporization of alloying elements and explosion behavior during laser powder bed fusion of Cu–10Zn alloy. *Int. J. Mach. Tools Manuf.* **2021**, *161*, 103686. [CrossRef]
61. Hryha, E.; Shvab, R.; Bram, M.; Bitzer, M.; Nyborg, L. Surface chemical state of Ti powders and its alloys: Effect of storage conditions and alloy composition. *Appl. Surf. Sci.* **2016**, *388*, 294–303. [CrossRef]
62. Lütjering, G.; Williams, J.C. *Titanium*, 2nd ed.; Springer: Berlin/Heidelberg, Germany, 2007; ISBN 9783540713975.
63. Li, C.; Chen, J.H.; Wu, X.; van der Zwaag, S. Effect of strain rate on stress-induced martensitic formation and the compressive properties of Ti–V–(Cr,Fe)–Al alloys. *Mater. Sci. Eng. Struct. Mater.* **2013**, *573*, 111–118. [CrossRef]
64. Neelakantan, S. Tailoring the Mechanical Properties of Titanium Alloys via Plasticity Induced Transformations. Ph.D. Dissertation, Delft University of Technology, Delft, The Netherlands, 2010.
65. Meng, F.; Yan, J.-Y.; Olson, G.B. TRIP Titanium Alloy Design. *MATEC Web Conf.* **2020**, *321*, 11070. [CrossRef]
66. Yan, J.-Y. TRIP Titanium Alloy Design. Ph.D. Dissertation, Northwestern University, Evanston, IL, USA, 2014.
67. Moffat, D.L.; Larbalestier, D.C. The compctition between martensite and omega in quenched Ti-Nb alloys. *Metall. Mater. Trans.* **1988**, *19*, 1677–1686. [CrossRef]

68. Duerig, T.W.; Albrecht, J.; Richter, D.; Fischer, P. Formation and reversion of stress induced martensite in Ti-10V-2Fe-3Al. *Acta Metall.* **1982**, *30*, 2161–2172. [CrossRef]
69. Qi, L.; He, S.; Chen, C.; Jiang, B.; Hao, Y.; Ye, H.; Yang, R.; Du, K. Diffusional-displacive transformation in a metastable β titanium alloy and its strengthening effect. *Acta Mater.* **2020**, *195*, 151–162. [CrossRef]
70. Dutta, B.; Froes, F.H. The Additive Manufacturing (AM) of titanium alloys. *Metall. Powder Rep.* **2017**, *72*, 96–106. [CrossRef]
71. Barriobero-Vila, P.; Gussone, J.; Haubrich, J.; Sandlöbes, S.; Da Silva, J.C.; Cloetens, P.; Schell, N.; Requena, G. Inducing Stable α + β Microstructures during Selective Laser Melting of Ti-6Al-4V Using Intensified Intrinsic Heat Treatments. *Materials* **2017**, *10*, 268. [CrossRef] [PubMed]
72. Mantani, Y.; Tajima, M. Phase transformation of quenched α″ martensite by aging in Ti–Nb alloys. *Mater. Sci. Eng. Struct. Mater.* **2006**, *438*, 315–319. [CrossRef]
73. Zwicker, U. *Titan und Titanlegierungen*; Springer: Berlin/Heidelberg, Germany, 1974; ISBN 978-3-642-80588-2.
74. Liu, J.P.; Wang, Y.D.; Hao, Y.L.; Wang, H.L.; Wang, Y.; Nie, Z.H.; Su, R.; Wang, D.; Ren, Y.; Lu, Z.P.; et al. High-energy X-ray diffuse scattering studies on deformation-induced spatially confined martensitic transformations in multifunctional Ti–24Nb–4Zr–8Sn alloy. *Acta Mater.* **2014**, *81*, 476–486. [CrossRef]
75. Yang, Y.; Castany, P.; Bertrand, E.; Cornen, M.; Lin, J.X.; Gloriant, T. Stress release-induced interfacial twin boundary ω phase formation in a β type Ti-based single crystal displaying stress-induced α″ martensitic transformation. *Acta Mater.* **2018**, *149*, 97–107. [CrossRef]
76. Ren, L.; Xiao, W.; Han, W.; Ma, C.; Zhou, L. Influence of duplex ageing on secondary α precipitates and mechanical properties of the near β-Ti alloy Ti-55531. *Mater. Charact.* **2018**, *144*, 1–8. [CrossRef]
77. Mantri, S.A.; Choudhuri, D.; Alam, T.; Viswanathan, G.B.; Sosa, J.M.; Fraser, H.L.; Banerjee, R. Tuning the scale of α precipitates in β-titanium alloys for achieving high strength. *Scr. Mater.* **2018**, *154*, 139–144. [CrossRef]
78. Yang, Y.; Castany, P.; Cornen, M.; Prima, F.; Li, S.J.; Hao, Y.L.; Gloriant, T. Characterization of the martensitic transformation in the superelastic Ti–24Nb–4Zr–8Sn alloy by in situ synchrotron X-ray diffraction and dynamic mechanical analysis. *Acta Mater.* **2015**, *88*, 25–33. [CrossRef]
79. Hao, Y.L.; Zhang, Z.B.; Li, S.J.; Yang, R. Microstructure and mechanical behavior of a Ti–24Nb–4Zr–8Sn alloy processed by warm swaging and warm rolling. *Acta Mater.* **2012**, *60*, 2169–2177. [CrossRef]
80. Peters, M.; Leyens, C. *Titan und Titanlegierungen*, 3rd ed.; Wiley-VCH: Weinheim, Germany, 2002; ISBN 9783527611089.
81. Sibum, H. Titanium and Titanium Alloys—From Raw Material to Semi-finished Products. *Adv. Eng. Mater.* **2003**, *5*, 393–398. [CrossRef]
82. Ohmori, Y.; Ogo, T.; Nakai, K.; Kobayashi, S. Effects of ω-phase precipitation on β→α, α″ transformations in a metastable β titanium alloy. *Mater. Sci. Eng. Struct. Mater.* **2001**, *312*, 182–188. [CrossRef]
83. Zhang, L.C.; Klemm, D.; Eckert, J.; Hao, Y.L.; Sercombe, T.B. Manufacture by selective laser melting and mechanical behavior of a biomedical Ti–24Nb–4Zr–8Sn alloy. *Scr. Mater.* **2011**, *65*, 21–24. [CrossRef]
84. Zhang, L.C.; Sercombe, T.B. Selective Laser Melting of Low-Modulus Biomedical Ti-24Nb-4Zr-8Sn Alloy: Effect of Laser Point Distance. *KEM* **2012**, *520*, 226–233. [CrossRef]
85. Hernandez, J.; Li, S.J.; Martinez, E.; Murr, L.E.; Pan, X.M.; Amato, K.N.; Cheng, X.Y.; Yang, F.; Terrazas, C.A.; Gaytan, S.M.; et al. Microstructures and Hardness Properties for β-Phase Ti–24Nb–4Zr–7.9Sn Alloy Fabricated by Electron Beam Melting. *J. Mater. Sci. Technol.* **2013**, *29*, 1011–1017. [CrossRef]
86. Ardell, A.J. Precipitation hardening. *Metall. Mater. Trans.* **1985**, *16*, 2131–2165. [CrossRef]
87. Kolli, R.P.; Joost, W.J.; Ankem, S. Phase Stability and Stress-Induced Transformations in Beta Titanium Alloys. *JOM* **2015**, *67*, 1273–1280. [CrossRef]
88. Furuta, T.; Kuramoto, S.; Hwang, J.; Nishino, K.; Saito, T. Elastic Deformation Behavior of Multi-Functional Ti–Nb–Ta–Zr–O Alloys. *Mater. Trans.* **2005**, *46*, 3001–3007. [CrossRef]
89. Hao, Y.L.; Li, S.J.; Sun, S.Y.; Zheng, C.Y.; Yang, R. Elastic deformation behaviour of Ti-24Nb-4Zr-7.9Sn for biomedical applications. *Acta Biomater.* **2007**, *3*, 277–286. [CrossRef]
90. Pantawane, M.V.; Dasari, S.; Mantri, S.A.; Banerjee, R.; Dahotre, N.B. Rapid thermokinetics driven nanoscale vanadium clustering within martensite laths in laser powder bed fused additively manufactured Ti6Al4V. *Mater. Res. Lett.* **2020**, *8*, 383–389. [CrossRef]
91. Cao, S.; Zou, Y.; Lim, C.V.S.; Wu, X. Review of laser powder bed fusion (LPBF) fabricated Ti-6Al-4V: Process, post-process treatment, microstructure, and property. *Gxjzz* **2021**, *2*, 1. [CrossRef]
92. Froes, F.H.; Bomberger, H.B. The Beta Titanium Alloys. *JOM* **1985**, *37*, 28–37. [CrossRef]
93. Lin, D.J.; Chern Lin, J.H.; Ju, C.P. Structure and properties of Ti–7.5Mo–xFe alloys. *Biomaterials* **2002**, *23*, 1723–1730. [CrossRef]
94. Rajan Soundararajan, S.; Vishnu, J.; Manivasagam, G.; Rao Muktinutalapati, N. Heat Treatment of Metastable Beta Titanium Alloys. In *Welding—Modern Topics*; Crisóstomo Absi Alfaro, S., Borek, W., Tomiczek, B., Eds.; IntechOpen: Rijeka, Croatia, 2021; ISBN 978-1-83881-895-1.
95. Coakley, J.; Rahman, K.M.; Vorontsov, V.A.; Ohnuma, M.; Dye, D. Effect of precipitation on mechanical properties in the β-Ti alloy Ti–24Nb–4Zr–8Sn. *Mater. Sci. Eng. Struct. Mater.* **2016**, *655*, 399–407. [CrossRef]

5 Conclusions

This chapter summarizes and correlates the main findings of the presented publications A – E. The research hypotheses from Chapter 3 are falsified or verified accordingly, and the resulting conclusions are presented.

The LPBF-processed Ti-6Al-7Nb in the as-built condition has higher mechanical properties in hardness, YS, and UTS in comparison to conventionally manufactured components. On the one hand, as given for the as-built condition, a finer microstructure results in increased strength values due to grain boundary strengthening, also known as the Hall-Petch relation. On the other hand, the decreasing grain size shows adverse effects on the breaking elongation. Reduced grain sizes lead to increased dislocation pile-ups within the grains and, therefore, to reduced elongation at break. As the strength and hardness values of LPBF processed material exceed the values of conventional Ti-6Al-7Nb, the breaking elongation is lower. Therefore the sub-hypothesis **H1a** is partly confirmed by Paper A and Paper B.

The LPBF and subsequent post-treatments, such as heat treatments, significantly affect the microstructure. The as-built condition of Ti-6Al-4V and Ti-6Al-7Nb show fine, acicular α' martensite laths. These laths are formed by phase transformation during rapid cooling from primary β grains. These grains first form during solidification from the melt and are elongated along the building direction due to the layer-wise fabrication and the resulting epitaxial grain growth. The fine acicular α' martensite grain size and orientation depend on the size and growth direction of the β grains, which depend on the manufacturing process and the process parameters. The investigations and results show the apparent dependence of the microstructure on the different heat treatment variants. On the one hand, the α phase and α' martensite are dominant within the as-built and stress-relieved condition. On the other hand, the β phase forms and precipitates at higher temperatures during heat treatments. Particularly for temperatures above the $\beta_{transus}$ temperature, the grains significantly start to grow. The as-built and stress-relieved conditions are favorable regarding YS, UTS, and breaking elongation, compared to those heat-treated at higher temperatures with a larger amount of β phase. Generally, the heat treatments, especially at higher temperatures, tend to soften the crystal lattice structures, reduce the process and phase formation induced residual stresses, and enhance the β phase formation. Consequently, the mechanical properties, particularly the strength values, are reduced. The sub-hypothesis **H1b** claims the possibility of tailoring the microstructure and quasi-static mechanical properties, which is confirmed by the results from Paper B.

The LCF behavior is strongly related to the material strength, as the loading situation leads to plastic deformation. Additionally, the LCF performance is connected to the residual stress state. The fatigue life is longer for heat-treated states at lower strain amplitudes and stresses. The reduction of residual stresses and changes in the microstructures show significant improvement in the LCF regime. In contrast, the strength values

dictate the LCF performance for higher strain amplitudes and stresses, whereas higher strength leads to higher fatigue life. Paper B shows different LCF behavior for different microstructures and confirms the sub-hypothesis **H1c**.
The deposition of PVD thin coatings strongly affects and enhances the material behavior, especially the quasi-static properties. The thin coatings, TiN, TiCN, and a-C:Ag, exhibit high adhesion on the blasted Ti-6Al-7Nb substrate surface. The hardness of PVD-coated surfaces is increased by the factor 2 to 3 compared to the blasted, as-built surface of Ti-6Al-7Nb, whereas TiN thin coating results in the highest hardness. In addition, the tensile properties are improved by PVD coatings. The PVD-coated conditions have higher tensile strength (YS and UTS) but show a slightly reduced breaking elongation compared to the as-built condition. Due to changes in the structural surface state by increased dislocation density close to the surface, increased surface hardness and strengthening are subjected to PVD coating-induced residual compressive stresses. On the one hand, the material behavior is affected, particularly strength and hardness values are higher compared to the as-built condition of Ti-6Al-7Nb. However, on the other hand, the elongation at break is slightly reduced by the deposition of PVD thin coatings, as presented in Paper C. The sub-hypothesis **H1d**, therefore, can only be partially verified.
The fatigue properties illustrate the improving effect of PVD thin films on the mechanical behavior of Ti-6Al-7Nb. Besides the quasi-static properties, the LCF properties can be enhanced to a certain extent by applying PVD coatings. The deposition of PVD coatings significantly improves the LCF performance. The average number of cycles to failure is increased for all conditions and all strain amplitudes within the LCF tests. Mainly by altering the surface hardness, the plastic deformation and, therefore, the crack initiation near the specimen's surface is delayed. Changes in the residual stress states in terms of increased compression stresses lead to crack closure tendencies at the crack tips during crack growth. Based on the same mechanisms, the HCF properties are also improved compared to the as-built condition of Ti-6Al-7Nb. The fatigue strength is enhanced by 2.6 % to 44.2 % by PVD coatings. The most significant improvement in fatigue performance (+105.4 %) is generated by stress relieving. The improvement in HCF performance can be attributed to recovery processes leading to reduced process-induced stresses. The sub-hypothesis **H1e** that PVD thin coatings and stress-relieving can improve LCF and HCF behavior is confirmed by Paper C and Paper D. On the one hand, the fatigue life within the LCF and HCF regime is increased; on the other hand, the fatigue strength is improved.
Overall the main hypothesis **H1**, that LPBF-manufactured Ti-6Al-7Nb in combination with HT and PVD thin coatings offers improved biocompatibility and mechanical performance, is mainly confirmed. Additionally to the effects and improvements in the mechanical performance described above, Ti-6Al-7Nb shows good biocompatibility on the as-built and blasted surfaces for different cell types, such as fibroblasts, osteosarcoma cells, and endothelial cells. Within the biological investigations, no cytokine release of Interleukin-6 (Il-6) was observable for any conditions. Il-6 is a cytokine involved in a variety of biological functions, in particular in immune responses and inflammation. Only slightly anti-proliferative effects on osteoblasts and anti-bacterial effects against *Staphylococcus aureus* were observable on blasted Ti-6Al-7Nb, probably due to the aluminum-containing blasting material.
The LPBF-processed Ti-24Nb-4Zr-8Sn alloy shows significantly different microstructures

and mechanical properties than Ti-6Al-7Nb. In the as-built state and after solution treatment with following air-cooling or slow water quenching, the microstructure comprises mainly β phase with sporadic acicular α'' martensite. This structure results from the high cooling rates of these conditions. For the lower cooling rates, such as furnace cooled or the subsequently aged condition, the microstructure contains α precipitates within the β matrix. The former condition has heterogeneously distributed and coarser α precipitates compared to the aged condition. As the strengthening mechanisms for metastable β titanium Ti-24Nb-4Zr-8Sn are primarily based on precipitation hardening due to the α precipitates, the α-containing conditions exhibit a significantly higher strength. The α precipitates also have an embrittling effect, resulting in a relatively low ductility and decreased breaking elongation. During the deformation of Ti-24Nb-4Zr-8Sn, a stress-induced phase transformation of α'' occurs, leading to a pseudo-elastic deformation behavior of the solution-treated and air-cooled or water-quenched conditions. This phase transformation results in a divided elastic modulus (50 GPa $\rightarrow$ 14 GPa), which is promising in reducing stress shielding. For Ti-24Nb-4Zr-8Sn, the mechanical properties (strength, elastic modulus) can be adjusted by heat treatments due to tailoring the α precipitates size in the β matrix. The main hypothesis H2 claims that the metastable β Ti-24Nb-4Z-r8Sn alloy has advantages regarding biocompatibility and material performance compared to Ti-6Al-7Nb. As the mechanical properties do not achieve the requirements according to the standards for Ti-6Al-7Nb, they are still promising in terms of tailoring and adjusting to the needs of implant material. As the chemical composition does not contain hazardous elements, such as aluminum or vanadium, it can be assumed that the biocompatibility is similar or better compared to Ti-6Al-7Nb. Therefore hypothesis **H2** is neither verified nor falsified.

In terms of overall performance, quasi-static and fatigue material behavior, the stress-relieved conditions show the most favorable properties. The investigations underline the features of PVD coatings and their significant improvement of the quasi-static and fatigue properties of Ti-6Al-7Nb. This work indicates the significant advancement of the mechanical properties of additively manufactured Ti-6Al-7Nb in combination with post-treatments, such as stress relief heat treatments or deposition of PVD coatings. The Ti-24Nb-4Zr-8Sn alloy shows promising approaches regarding its tailoring of mechanical properties and which is helpful for further biomedical applications. Nevertheless, the deposition of functional PVD coatings in combination with heat treatments is the most promising method to improve mechanical and biocompatible performance for the design of load-bearing implants.

Bibliography

[1] United Nations Department of Economic and Social Affairs, Population Division. „World Population Prospects 2022: Summary of Results“. In: (2022). URL: https://population.un.org/wpp/Publications/.

[2] D. G. Wan He and P. Kowal. *An Aging World: 2015: International Population Reports*. P95-16-1. Washington DC: U.S. Government Printing Office, 2016. URL: https://www.census.gov/library/publications/2016/demo/P95-16-1.html.

[3] Max Planck Institute for Demographic Research. *Glossary of Demographic Terms*. URL: https://www.demogr.mpg.de/en/about_us_6113/what_is_demography_6674/glossary_of_demographic_terms_6982/. (accessed: 21.09.2022).

[4] German Federal Ministry of the Interior and Community. „Demography Report – Federal Government Report on the Demographic Situation and Future Development of Germany“. In: (2011). URL: https://www.bmi.bund.de/SharedDocs/downloads/EN/themen/demography/demografiebericht_kurz_en.html.

[5] European Commission. *Report on the impact of demographic change*. 2020. URL: https://ec.europa.eu/commission/presscorner/detail/en/ip_20_1056.

[6] H. Ritchie and M. Roser. „Age Structure“. In: *Our World in Data* (2019). URL: https://ourworldindata.org/age-structure.

[7] E. Ortiz-Ospina. „Global Health“. In: *Our World in Data* (2019). URL: https://ourworldindata.org/health-meta.

[8] P. Thomas. „Patch testing and hypersensitivity reactions to metallic implants: still many open questions“. In: *Dermatitis : contact, atopic, occupational, drug* 24.3 (2013), pp. 106–107. DOI: 10.1097/DER.0b013e31829796f8.

[9] D. W. Hutmacher. „Scaffolds in tissue engineering bone and cartilage“. In: *Biomaterials* 21.24 (2000), pp. 2529–2543. ISSN: 01429612. DOI: 10.1016/S0142-9612(00)00121-6.

[10] T. Dixon, M. Shaw, S. Ebrahim, and P. Dieppe. „Trends in hip and knee joint replacement: socioeconomic inequalities and projections of need“. In: *Annals of the rheumatic diseases* 63.7 (2004), pp. 825–830. ISSN: 0003-4967. DOI: 10.1136/ard.2003.012724.

[11] R. D. Crowninshield, A. G. Rosenberg, and S. M. Sporer. „Changing demographics of patients with total joint replacement“. In: *Clinical orthopaedics and related research* 443 (2006), pp. 266–272. ISSN: 0009-921X. DOI: 10.1097/01.blo.0000188066.01833.4f.

[12] F. Birrell, O. Johnell, and A. Silman. „Projecting the need for hip replacement over the next three decades: influence of changing demography and threshold for surgery“. In: *Annals of the rheumatic diseases* 58.9 (1999), pp. 569–572. ISSN: 0003-4967. DOI: 10.1136/ard.58.9.569.

[13] H. W. Elani, J. R. Starr, J. D. Da Silva, and G. O. Gallucci. „Trends in Dental Implant Use in the U.S., 1999-2016, and Projections to 2026“. In: *Journal of dental research* 97.13 (2018), pp. 1424–1430. DOI: 10.1177/0022034518792567.

[14] C. Pabinger, H. Lothaller, N. Portner, and A. Geissler. „Projections of hip arthroplasty in OECD countries up to 2050“. In: *Hip international : the journal of clinical and experimental research on hip pathology and therapy* 28.5 (2018), pp. 498–506. DOI: 10.1177/1120700018757940.

[15] J. Kärrholm, H. Lindahl, H. Malchau, M. Mohaddes, S. Nemes, C. Rogmark, and O. Rolfson. *The Swedish Hip Arthroplasty Register Annual Report 2016*. 2017. DOI: 10.18158/SJy6jKyrM.

[16] M. Tsukanaka, V. Halvorsen, L. Nordsletten, I. Ø. EngesæTer, L. B. EngesæTer, A. Marie Fenstad, and S. M. Röhrl. „Implant survival and radiographic outcome of total hip replacement in patients less than 20 years old“. In: *Acta orthopaedica* 87.5 (2016), pp. 479–484. DOI: 10.1080/17453674.2016.1212180.

[17] W. Bonfield. „Designing porous scaffolds for tissue engineering“. In: *Philosophical transactions. Series A, Mathematical, physical, and engineering sciences* 364.1838 (2006), pp. 227–232. ISSN: 1364-503X. DOI: 10.1098/rsta.2005.1692.

[18] L. E. Murr, S. M. Gaytan, E. Martinez, F. Medina, and R. B. Wicker. „Next generation orthopaedic implants by additive manufacturing using electron beam melting“. In: *International journal of biomaterials* 2012 (2012), p. 245727. DOI: 10.1155/2012/245727.

[19] S. A. Yavari, R. Wauthle, J. van der Stok, A. C. Riemslag, M. Janssen, M. Mulier, J. P. Kruth, J. Schrooten, H. Weinans, and A. A. Zadpoor. „Fatigue behavior of porous biomaterials manufactured using selective laser melting“. In: *Materials science & engineering. C, Materials for biological applications* 33.8 (2013), pp. 4849–4858. DOI: 10.1016/j.msec.2013.08.006.

[20] S. van Bael, Y. C. Chai, S. Truscello, M. Moesen, G. Kerckhofs, H. van Oosterwyck, J.-P. Kruth, and J. Schrooten. „The effect of pore geometry on the in vitro biological behavior of human periosteum-derived cells seeded on selective laser-melted Ti6Al4V bone scaffolds“. In: *Acta biomaterialia* 8.7 (2012), pp. 2824–2834. DOI: 10.1016/j.actbio.2012.04.001.

[21] C. M. Murphy and F. J. O'Brien. „Understanding the effect of mean pore size on cell activity in collagen-glycosaminoglycan scaffolds“. In: *Cell adhesion & migration* 4.3 (2010), pp. 377–381. DOI: 10.4161/cam.4.3.11747.

[22] B. Dabrowski, W. Swieszkowski, D. Godlinski, and K. J. Kurzydlowski. „Highly porous titanium scaffolds for orthopaedic applications“. In: *Journal of biomedical materials research. Part B, Applied biomaterials* 95.1 (2010), pp. 53–61. DOI: 10.1002/jbm.b.31682.

[23] L. Wang. „Investigation of PVD and CVD Coatings for Manufacturing, Fuel Cell and Biomedical Applications“. Ph.D. Thesis. Windsor, ON, Canada: University of Windsor, 2010. URL: https://scholar.uwindsor.ca/etd/470.

[24] G. Qiu and Y. Guo. „Current situation and development trend of titanium metal industry in China“. In: *International Journal of Minerals, Metallurgy and Materials* 29.4 (2022), pp. 599–610. ISSN: 1674-4799. DOI: 10.1007/s12613-022-2455-y.

[25] C. Leyens and M. Peters. *Titanium and Titanium Alloys*. Wiley, 2003. ISBN: 9783527305346. DOI: 10.1002/3527602119.

[26] C. Veiga, J. Davim, and A. Loureiro. „Properties and applications of titanium alloys: a brief review“. In: *Reviews on Advanced Materials Science* 32.2 (2012), pp. 133–148.

[27] M. J. Donachie. *Titanium: A technical guide*. 2. ed., 1. printing. Materials Park, Ohio: ASM International, 2000. ISBN: 978-0-87170-686-7.

[28] R. R. Boyer. „An overview on the use of titanium in the aerospace industry“. In: *Materials Science and Engineering: A* 213.1-2 (1996), pp. 103–114. ISSN: 09215093. DOI: 10.1016/0921-5093(96)10233-1.

[29] A. Naim, R. Kumar, and S. Bhatia. „A review paper on materials used for manufacturing of alloy wheels“. In: *IOP Conference Series: Materials Science and Engineering* 1136.1 (2021), p. 012006. ISSN: 1757-8981. DOI: 10.1088/1757-899X/1136/1/012006.

[30] O. Schauerte. „Titanium in Automotive Production“. In: *Advanced Engineering Materials* 5.6 (2003), pp. 411–418. ISSN: 14381656. DOI: 10.1002/adem.200310094.

[31] D. Bombač, M. Brojan, P. Fajfar, F. Kosel, and R. Turk. „Review of materials in medical applications Pregled materialov v medicinskih aplikacijah“. In: *RMZ–Materials and Geoenvironment* 54.4 (2007), pp. 471–499.

[32] M. Balazic, J. Kopac, M. J. Jackson, and W. Ahmed. „Review: titanium and titanium alloy applications in medicine“. In: *International Journal of Nano and Biomaterials* 1.1 (2007), p. 3. ISSN: 1752-8933. DOI: 10.1504/IJNBM.2007.016517.

[33] C. N. Elias, J. H. C. Lima, R. Valiev, and M. A. Meyers. „Biomedical applications of titanium and its alloys“. In: *JOM* 60.3 (2008), pp. 46–49. ISSN: 1047-4838. DOI: 10.1007/s11837-008-0031-1.

[34] J. Breme, E. Eisenbarth, and V. Biehl. „Titanium and its Alloys for Medical Applications“. In: *Titanium and Titanium Alloys*. Ed. by C. Leyens and M. Peters. Weinheim, FRG: Wiley-VCH Verlag GmbH & Co. KGaA, 2003, pp. 423–451. ISBN: 9783527602117. DOI: 10.1002/3527602119.ch16.

[35] M. Peters, J. Hemptenmacher, J. Kumpfert, and C. Leyens. „Structure and Properties of Titanium and Titanium Alloys“. In: *Titanium and Titanium Alloys*. Ed. by C. Leyens and M. Peters. Weinheim, FRG: Wiley-VCH Verlag GmbH & Co. KGaA, 2003, pp. 1–36. ISBN: 9783527602117. DOI: 10.1002/3527602119.ch1.

[36] V. A. Joshi. *Titanium alloys: An atlas of structures and fracture features*. Boca Raton, Fla.: Taylor & Francis, 2006. ISBN: 9780849350108. URL: http://www.loc.gov/catdir/enhancements/fy0668/2005022915-d.html.

[37] L. M. Gammon, R. D. Briggs, J. M. Packard, K. W. Batson, R. Boyer, C. W. Domby, et al. „Metallography and microstructures of titanium and its alloys“. In: *ASM handbook* 9 (2004), pp. 899–917. DOI: 10.1361/asmhba0003779.

[38] G. Lütjering and J. C. Williams. *Titanium: With 51 tables*. 2. ed. Engineering materials and processes. Berlin, Heidelberg: Springer-Verlag, 2007. ISBN: 978-3-540-73036-1. DOI: 10.1007/978-3-540-73036-1.

[39] U. Zwicker. *Titan und Titanlegierungen*. Berlin, Heidelberg: Springer Berlin Heidelberg, 1974. ISBN: 978-3-642-80588-2. DOI: 10.1007/978-3-642-80587-5.

[40] R. I. Jaffee and N. E. Promisel, eds. *The science, technology, and application of titanium: Proceedings*. [1st ed.] Oxford and New York: Published for the organizing societies by Pergamon Press, 1970. ISBN: 9780080065649.

[41] I. Polmear. *Light alloys: Metallurgy of the light metals*. Fifth edition. Oxford, England and Cambridge, Massachusetts: Butterworth-Heinemann, 2017. ISBN: 9780080994307. URL: https://ebookcentral.proquest.com/lib/kxp/detail.action?docID=4833918.

[42] L.-Y. Chen, Y.-W. Cui, and L.-C. Zhang. „Recent Development in Beta Titanium Alloys for Biomedical Applications“. In: *Metals* 10.9 (2020), p. 1139. DOI: 10.3390/met10091139.

[43] P. J. Bania. „Beta Titanium Alloys and Their Role in the Titanium Industry“. In: *Beta titanium alloys in the 1990's: Proceedings of a Symposium on Beta Titanium Alloys*. Ed. by D. Eylon. Warrendale, Pa.: Minerals Metals & Materials Society, 1993, pp. 3–14. ISBN: 0-87339-200-0.

[44] P. J. Bania. „Beta titanium alloys and their role in the titanium industry“. In: *JOM* 46.7 (1994), pp. 16–19. ISSN: 1047-4838. DOI: 10.1007/BF03220742.

[45] E. W. Collings. *The physical Metallurgy of titanium alloys*. Vol. 3. ASM Series for metal processing. Metals Park, Ohio: American Society for Metals, 1984. ISBN: 9780871701817.

[46] B. Koch. *Zum Ermüdungsverhalten der metastabilen [beta]-Titanlegierung Ti-6,8Mo-4,5Fe-1,5Al (Timetal LCB): Mechanische und mikrostrukturelle Untersuchungen: Zugl.: Bochum, Univ., Diss., 2007*. Vol. Bd. 28. BAM-Dissertationsreihe. Berlin: Bundesanstalt für Materialforschung und -prüfung (BAM), 2007. ISBN: 978-3-9811655-7-9.

[47] R. Boyer, ed. *Materials properties handbook: Titanium alloys*. Materials Park, Ohio: ASM International, 1994. ISBN: 978-0-87170-481-8.

[48] R. Kolli and A. Devaraj. „A Review of Metastable Beta Titanium Alloys“. In: *Metals* 8.7 (2018), p. 506. DOI: 10.3390/met8070506.

[49] W. G. Burgers. „On the process of transition of the cubic-body-centered modification into the hexagonal-close-packed modification of zirconium“. In: *Physica* 1.7-12 (1934), pp. 561–586. ISSN: 00318914. DOI: 10.1016/S0031-8914(34)80244-3.

[50] A. J. Williams, R. W. Cahn, and C. S. Barrett. „The crystallography of the β-α transformation in titanium“. In: *Acta Metallurgica* 2.1 (1954), pp. 117–128. ISSN: 00016160. DOI: 10.1016/0001-6160(54)90101-7.

[51] M. K. McQuillan. „PHASE TRANSFORMATIONS IN TITANIUM AND ITS ALLOYS“. In: *Metallurgical Reviews* 8.1 (1963), pp. 41–104. ISSN: 0076-6690. DOI: 10.1179/mtlr.1963.8.1.41.

[52] T. W. Duerig, G. T. Terlinde, and J. C. Williams. „Phase transformations and tensile properties of Ti-10V-2Fe-3AI“. In: *Metallurgical Transactions A* 11.12 (1980), pp. 1987–1998. ISSN: 0360-2133. DOI: 10.1007/BF02655118.

[53] C. G. Rhodes and J. C. Williams. „The precipitation of α-phase in metastable β-phase Ti alloys“. In: *Metallurgical Transactions A* 6.11 (1975), pp. 2103–2114. ISSN: 0360-2133. DOI: 10.1007/BF03161837.

[54] Y. L. Hao, R. Yang, M. Niinomi, D. Kuroda, Y. L. Zhou, K. Fukunaga, and A. Suzuki. „Young's modulus and mechanical properties of Ti-29Nb-13Ta-4.6Zr in relation to αstrich-strich martensite“. In: *Metallurgical and Materials Transactions A* 33.10 (2002), pp. 3137–3144. ISSN: 1073-5623. DOI: 10.1007/s11661-002-0299-7.

[55] W. Xu, K. B. Kim, J. Das, M. Calin, and J. Eckert. „Phase stability and its effect on the deformation behavior of Ti-Nb-Ta-In/Cr β alloys“. In: *Scripta Materialia* 54.11 (2006), pp. 1943–1948. ISSN: 13596462. DOI: 10.1016/j.scriptamat.2006.02.002.

[56] F04 Committee. *ASTM F67-13, Specification for Unalloyed Titanium, for Surgical Implant Applications (UNS R50250, UNS R50400, UNS R50550, UNS R50700)*. West Conshohocken, PA, 2017. DOI: 10.1520/F0067-13.

[57] M. Könönen and J. Kivilahti. „Fusing of dental ceramics to titanium“. In: *Journal of dental research* 80.3 (2001), pp. 848–854. DOI: 10.1177/00220345010800030101.

[58] J. Emsley. *Nature's building blocks: Everything you need to know about the elements*. New ed., completely rev. and updated. Oxford: Oxford University Press, 2011. ISBN: 9780199605637.

[59] S. L. Semiatin, V. Seetharaman, and I. Weiss. „The thermomechanical processing of alpha/beta titanium alloys“. In: *JOM* 49.6 (1997), pp. 33–39. ISSN: 1047-4838. DOI: 10.1007/BF02914711.

[60] J. Kumpfert and C. Leyens. „Orthorhombic Titanium Aluminides: Intermetallics with Improved Damage Tolerance“. In: *Titanium and Titanium Alloys*. Ed. by C. Leyens and M. Peters. Weinheim, FRG: Wiley-VCH Verlag GmbH & Co. KGaA, 2003, pp. 59–88. ISBN: 9783527602117. DOI: 10.1002/3527602119.ch3.

[61] E. Wintermantel, B. Shah-Derler, A. Bruinink, M. Petitmermet, J. Blum, and S.-W. Ha. „Biokompatibilität“. In: *Medizintechnik*. Ed. by E. Wintermantel and S.-W. Ha. Berlin, Heidelberg: Springer Berlin Heidelberg, 2009, pp. 67–104. ISBN: 978-3-540-93935-1. DOI: 10.1007/978-3-540-93936-8{\textunderscore}3.

[62] D. F. Williams. „On the mechanisms of biocompatibility“. In: *Biomaterials* 29.20 (2008), pp. 2941–2953. ISSN: 01429612. DOI: 10.1016/j.biomaterials.2008.04.023.

[63] D. F. Williams and X. Zhang, eds. *Definitions of biomaterials for the Twenty-First Century: Proceedings of a Consensus Conference held in Chengdu, People's Republic of China, June 11th and 12th 2018, organized under the auspices of the International Union of Societies for Biomaterials Science & Engineering : hosted and supported by Sichuan University, Chengdu and the Chinese Society for Biomaterials, China*. Materials Today. Amsterdam, Netherlands: Elsevier, 2019. ISBN: 9780128182925. URL: https://www.sciencedirect.com/science/book/9780128182918.

[64] L. Ghasemi-Mobarakeh, D. Kolahreez, S. Ramakrishna, and D. Williams. „Key terminology in biomaterials and biocompatibility“. In: *Current Opinion in Biomedical Engineering* 10 (2019), pp. 45–50. ISSN: 24684511. DOI: 10.1016/j.cobme.2019.02.004.

[65] R. Schenk. „Bone response to grafts and implants“. In: *Perspectives on biomaterials: Proceedings of the International Symposium on Biomaterials*. Ed. by O. C. C. Lin and E. Y. S. Chao. Amsterdam: Elsevier, 1986, pp. 121–136. ISBN: 0444426728.

[66] S. Bose, S. Vahabzadeh, and A. Bandyopadhyay. „Bone tissue engineering using 3D printing“. In: *Materials Today* 16.12 (2013), pp. 496–504. ISSN: 13697021. DOI: 10.1016/j.mattod.2013.11.017.

[67] M. Geetha, A. K. Singh, R. Asokamani, and A. K. Gogia. „Ti based biomaterials, the ultimate choice for orthopaedic implants – A review“. In: *Progress in Materials Science* 54.3 (2009), pp. 397–425. ISSN: 00796425. DOI: 10.1016/j.pmatsci.2008.06.004.

[68] M. Geetha, D. Durgalakshmi, and R. Asokamani. „Biomedical Implants: Corrosion and its Prevention - A Review“. In: *Recent Patents on Corrosion Science* 2.1 (2010), pp. 40–54. ISSN: 1877-6108. DOI: 10.2174/1877610801002010040.

[69] N. A. Hodges, E. M. Sussman, and J. P. Stegemann. „Aseptic and septic prosthetic joint loosening: Impact of biomaterial wear on immune cell function, inflammation, and infection“. In: *Biomaterials* 278 (2021), p. 121127. ISSN: 01429612. DOI: 10.1016/j.biomaterials.2021.121127.

[70] S. B. Goodman, E. Gibon, and Z. Yao. „The basic science of periprosthetic osteolysis“. In: *Instructional course lectures* 62 (2013), pp. 201–206. ISSN: 0065-6895.

[71] J. Vishnu and G. Manivasagam. „Surface Modification and Biological Approaches for Tackling Titanium Wear-Induced Aseptic Loosening“. In: *Journal of Bio- and Tribo-Corrosion* 7.1 (2021). ISSN: 2198-4220. DOI: 10.1007/s40735-021-00474-y.

[72] M. A. McGee, D. W. Howie, K. Costi, D. R. Haynes, C. I. Wildenauer, M. J. Pearcy, and J. D. McLean. „Implant retrieval studies of the wear and loosening of prosthetic joints: a review“. In: *Wear* 241.2 (2000), pp. 158–165. ISSN: 00431648. DOI: 10.1016/S0043-1648(00)00370-7.

[73] W. He and R. Benson. „Polymeric Biomaterials“. In: *Handbook of Polymer Applications in Medicine and Medical Devices*. Elsevier, 2014, pp. 55–76. ISBN: 978-0323228053. DOI: 10.1016/B978-0-323-22805-3.00004-9.

[74] V. Hasirci and N. Hasirci. *Fundamentals of Biomaterials*. New York, NY: Springer New York, 2018. ISBN: 978-1-4939-8854-9. DOI: 10.1007/978-1-4939-8856-3.

[75] A. S. K. Kiran and S. Ramakrishna. *An Introduction to Biomaterials Science and Engineering*. WORLD SCIENTIFIC, 2021. ISBN: 978-981-12-2817-9. DOI: 10.1142/12038.

[76] A. J. T. Teo, A. Mishra, I. Park, Y.-J. Kim, W.-T. Park, and Y.-J. Yoon. „Polymeric Biomaterials for Medical Implants and Devices“. In: *ACS biomaterials science & engineering* 2.4 (2016), pp. 454–472. DOI: 10.1021/acsbiomaterials.5b00429.

[77] S. Punj, J. Singh, and K. Singh. „Ceramic biomaterials: Properties, state of the art and future prospectives“. In: *Ceramics International* 47.20 (2021), pp. 28059–28074. ISSN: 02728842. DOI: 10.1016/j.ceramint.2021.06.238.

[78] J. Huang and S. M. Best. „Ceramic biomaterials“. In: *Tissue Engineering Using Ceramics and Polymers*. Elsevier, 2007, pp. 3–31. ISBN: 9781845691769. DOI: 10.1533/9781845693817.1.3.

[79] Y. Liu. „Processing, microstructure and mechanical properties of beta-type titanium porous structures made by additive manufacturing“. Ph.D. Thesis. Edith Cowan University, 2017. URL: https://ro.ecu.edu.au/theses/2039.

[80] B. D. Ratner. „A Perspective on Titanium Biocompatibility“. In: *Titanium in Medicine*. Ed. by D. M. Brunette, P. Tengvall, M. Textor, and P. Thomsen. Engineering Materials. Berlin, Heidelberg: Springer Berlin Heidelberg, 2001, pp. 1–12. ISBN: 978-3-642-63119-1. DOI: 10.1007/978-3-642-56486-4{\textunderscore}1.

[81] M. A. Meyers and E. A. Olevsky. „Sintering Theory and Practice“. In: *Journal of Materials Engineering and Performance* 6.3 (1997), p. 278.

[82] M. Andersson, B. Bergman, C. Bessing, G. Ericson, P. Lundquist, and H. Nilson. „Clinical results with titanium crowns fabricated with machine duplication and spark erosion“. In: *Acta odontologica Scandinavica* 47.5 (1989), pp. 279–286. ISSN: 0001-6357. DOI: 10.3109/00016358909007713.

[83] M. Taira, J. B. Moser, and E. H. Greener. „Studies of Ti alloys for dental castings“. In: *Dental Materials* 5.1 (1989), pp. 45–50. ISSN: 01095641. DOI: 10.1016/0109-5641(89)90093-6.

[84] K. Otsuka and C. M. Wayman. *Shape memory materials*. 1. paperback ed. (with corr.) Cambridge: Cambridge Univ. Press, 1999. ISBN: 9780521663847.

[85] E. P. Lautenschlager and P. Monaghan. „Titanium and titanium alloys as dental materials“. In: *International dental journal* 43.3 (1993), pp. 245–253. ISSN: 0020-6539.

[86] J. P. Kruth, L. Froyen, J. van Vaerenbergh, P. Mercelis, M. Rombouts, and B. Lauwers. „Selective laser melting of iron-based powder“. In: *Journal of Materials Processing Technology* 149.1-3 (2004), pp. 616–622. ISSN: 09240136. DOI: 10.1016/j.jmatprotec.2003.11.051.

[87] T. P. Wirtz. „Herstellung von Knochenimplantaten aus Titanwerkstoffen durch Laserformen“. PhD thesis. Aachen, 2005, 145 S. : Ill., graph. Darst. URL: https://publications.rwth-aachen.de/record/60637.

[88] Q. Chen and G. A. Thouas. „Metallic implant biomaterials“. In: *Materials Science and Engineering: R: Reports* 87 (2015), pp. 1–57. ISSN: 0927796X. DOI: 10.1016/j.mser.2014.10.001.

[89] N. Eliaz. „Corrosion of Metallic Biomaterials: A Review“. In: *Materials (Basel, Switzerland)* 12.3 (2019). ISSN: 1996-1944. DOI: 10.3390/ma12030407.

[90] S. Ali, A. M. Abdul Rani, Z. Baig, S. W. Ahmed, G. Hussain, K. Subramaniam, S. Hastuty, and T. V. Rao. „Biocompatibility and corrosion resistance of metallic biomaterials“. In: *Corrosion Reviews* 38.5 (2020), pp. 381–402. ISSN: 0334-6005. DOI: 10.1515/corrrev-2020-0001.

[91] M. Niinomi. „Recent titanium R&D for biomedical applications in japan“. In: *JOM* 51.6 (1999), pp. 32–34. ISSN: 1047-4838. DOI: 10.1007/s11837-999-0091-x.

[92] M. I. Froimson, J. Garino, A. Machenaud, and J. P. Vidalain. „Minimum 10-year results of a tapered, titanium, hydroxyapatite-coated hip stem: an independent review“. In: *The Journal of arthroplasty* 22.1 (2007), pp. 1–7. ISSN: 0883-5403. DOI: 10.1016/j.arth.2006.03.003.

[93] K. L. Wapner. „Implications of metallic corrosion in total knee arthroplasty“. In: *Clinical orthopaedics and related research* 271 (1991), pp. 12–20. ISSN: 0009-921X.

[94] M. Semlitsch, F. Staub, and H. Weber. „Titanium-aluminium-niobium alloy, development for biocompatible, high strength surgical implants“. In: *Biomedizinische Technik. Biomedical engineering* 30.12 (1985), pp. 334–339. ISSN: 0013-5585. DOI: 10.1515/bmte.1985.30.12.334.

[95] A. Gutiérrez, C. Munuera, M. F. López, J. A. Jiménez, C. Morant, T. Matzelle, N. Kruse, and C. Ocal. „Surface microstructure of the oxide protective layers grown on vanadium-free Ti alloys for use in biomedical applications“. In: *Surface Science* 600.18 (2006), pp. 3780–3784. ISSN: 00396028. DOI: 10.1016/j.susc.2006.01.082.

[96] S. Nag, R. Banerjee, and H. L. Fraser. „Microstructural evolution and strengthening mechanisms in Ti–Nb–Zr–Ta, Ti–Mo–Zr–Fe and Ti–15Mo biocompatible alloys“. In: *Materials Science and Engineering: C* 25.3 (2005), pp. 357–362. ISSN: 09284931. DOI: 10.1016/j.msec.2004.12.013.

[97] M. Niinomi. „Mechanical properties of biomedical titanium alloys“. In: *Materials Science and Engineering: A* 243.1-2 (1998), pp. 231–236. ISSN: 09215093. DOI: 10.1016/S0921-5093(97)00806-X.

[98] R. Huiskes, H. Weinans, and B. van Rietbergen. „The relationship between stress shielding and bone resorption around total hip stems and the effects of flexible materials“. In: *Clinical orthopaedics and related research* 274 (1992), pp. 124–134. ISSN: 0009-921X.

[99] M. Ridzwan, S. Shuib, A. Y. Hassan, A. A. Shokri, and M. N. Mohamad Ib. „Problem of Stress Shielding and Improvement to the Hip Implant Designs: A Review“. In: *Journal of Medical Sciences* 7.3 (2007), pp. 460–467. ISSN: 16824474. DOI: 10.3923/jms.2007.460.467.

[100] K. K. Wang, L. J. Gustavson, and J. H. Dumbleton. „Microstructure and Properties of a New Beta Titanium Alloy, Ti-12Mo-6Zr-2Fe, Developed for Surgical Implants“. In: *Medical Applications of Titanium and Its Alloys: The Material and Biological Issues*. Ed. by S. A. Brown and J. E. Lemons. 100 Barr Harbor Drive, PO Box C700, West Conshohocken, PA 19428-2959: ASTM International, 1996, pp. 76-76–12. ISBN: 978-0-8031-2010-5. DOI: 10.1520/STP16071S.

[101] Y. Okazaki, Y. Ito, A. Ito, and T. Tateishi. „New Titanium Alloys to be Considered for Medical Implants“. In: *Medical Applications of Titanium and Its Alloys: The Material and Biological Issues*. Ed. by S. A. Brown and J. E. Lemons. 100 Barr Harbor Drive, PO Box C700, West Conshohocken, PA 19428-2959: ASTM International, 1996, pp. 45-45–15. ISBN: 978-0-8031-2010-5. DOI: 10.1520/STP16069S.

[102] Y. L. Hao, S. J. Li, S. Y. Sun, C. Y. Zheng, Q. M. Hu, and R. Yang. „Super-elastic titanium alloy with unstable plastic deformation“. In: *Applied Physics Letters* 87.9 (2005), p. 091906. ISSN: 0003-6951. DOI: 10.1063/1.2037192.

[103] J. N. Katz. „Total joint replacement in osteoarthritis“. In: *Best practice & research. Clinical rheumatology* 20.1 (2006), pp. 145–153. ISSN: 1521-6942. DOI: 10.1016/j.berh.2005.09.003.

[104] S. Griza, G. Zanon, E. P. Silva, F. Bertoni, A. Reguly, and T. R. Strohaecker. „Design aspects involved in a cemented THA stem failure case“. In: *Engineering Failure Analysis* 16.1 (2009), pp. 512–520. ISSN: 13506307. DOI: 10.1016/j.engfailanal.2008.06.016.

[105] A. Sargeant and T. Goswami. „Hip implants: Paper V. Physiological effects“. In: *Materials & Design* 27.4 (2006), pp. 287–307. ISSN: 02641275. DOI: 10.1016/j.matdes.2004.10.028.

[106] G. Bergmann, G. Deuretzbacher, M. Heller, F. Graichen, A. Rohlmann, J. Strauss, and G. Duda. „Hip contact forces and gait patterns from routine activities“. In: *Journal of Biomechanics* 34.7 (2001), pp. 859–871. ISSN: 00219290. DOI: 10.1016/S0021-9290(01)00040-9.

[107] F04 Committee. *ASTM F1295-16 - Specification for Wrought Titanium-6Aluminum-7Niobium Alloy for Surgical Implant Applications (UNS R56700)*. West Conshohocken, PA, 2016. DOI: 10.1520/F1295-16.

[108] Deutsche Institut für Normung e.V. *DIN ISO 5832-11:2015-12, Chirurgische Implantate - Metallische Werkstoffe - Teil 11: Titan Aluminium-6 Niob-7 Knetlegierung (ISO 5832-11:2014)*. Berlin, 2015. DOI: 10.31030/2364474.

[109] International Organization for Standardization. *ISO 7206-4:2010-06 - Implants for surgery - Partial and total hip joint prostheses - Part 4: Determination of endurance properties and performance of stemmed femoral components*. Geneva, CH, 2010. DOI: 10.3403/BSISO7206.

[110] J. R. Davis, ed. *Handbook of materials for medical devices*. Materials Park, Ohio: ASM International, 2003. ISBN: 978-0871707901.

[111] P. C. McLeod, D. B. Kettelkamp, V. Srinivasan, and O. L. Henderson. „Measurements of repetitive activities of the knee“. In: *Journal of Biomechanics* 8.6 (1975), pp. 369–373. ISSN: 00219290. DOI: 10.1016/0021-9290(75)90072-X.

[112] E. H. Chen and J. Black. „Materials design analysis of the prosthetic anterior cruciate ligament“. In: *Journal of biomedical materials research* 14.5 (1980), pp. 567–586. ISSN: 0021-9304. DOI: 10.1002/jbm.820140504.

[113] G. Bergmann, F. Graichen, and A. Rohlmann. „Hip joint loading during walking and running, measured in two patients“. In: *Journal of Biomechanics* 26.8 (1993), pp. 969–990. ISSN: 00219290. DOI: 10.1016/0021-9290(93)90058-m.

[114] G. Bergmann, F. Graichen, and A. Rohlmann. „Is staircase walking a risk for the fixation of hip implants?“ In: *Journal of Biomechanics* 28.5 (1995), pp. 535–553. ISSN: 00219290. DOI: 10.1016/0021-9290(94)00105-d.

[115] G. M. Kotzar, D. T. Davy, V. M. Goldberg, K. G. Heiple, J. Berilla, R. H. Brown, and A. H. Burstein. „Telemeterized in vivo hip joint force data: a report on two patients after total hip surgery“. In: *Journal of orthopaedic research : official publication of the Orthopaedic Research Society* 9.5 (1991), pp. 621–633. DOI: 10.1002/jor.1100090502.

[116] M. Baleani, L. Cristofolini, and M. Viceconti. „Endurance testing of hip prostheses: a comparison between the load fixed in ISO 7206 standard and the physiological loads“. In: *Clinical Biomechanics* 14.5 (1999), pp. 339–345. ISSN: 02680033. DOI: 10.1016/s0268-0033(98)00085-0.

[117] N. G. Turner and W. T. Roberts. „Fatigue behavior of titanium (Ti fatigue properties, noting minor importance of strain aging, annealing effects and dislocation locking)“. In: *Trans. Met. Soc. AIME* 242.7 (1968), pp. 1223–1230.

[118] C. Sauer and G. Lütjering. „Influence of α layers at β grain boundaries on mechanical properties of Ti-alloys“. In: *Materials Science and Engineering: A* 319-321 (2001), pp. 393–397. ISSN: 09215093. DOI: 10.1016/S0921-5093(01)01018-8.

[119] Y. Okazaki and E. Gotoh. „Comparison of fatigue strengths of biocompatible Ti-15Zr-4Nb-4Ta alloy and other titanium materials“. In: *Materials Science and Engineering: C* 31.2 (2011), pp. 325–333. ISSN: 09284931. DOI: 10.1016/j.msec.2010.09.015.

[120] J. Everaerts, B. Verlinden, and M. Wevers. „The influence of the alpha grain size on internal fatigue crack initiation in drawn Ti-6Al-4V wires“. In: *Procedia Structural Integrity* 2 (2016), pp. 1055–1062. ISSN: 24523216. DOI: 10.1016/j.prostr.2016.06.135.

[121] G. Q. Wu, C. L. Shi, W. Sha, A. X. Sha, and H. R. Jiang. „Effect of microstructure on the fatigue properties of Ti–6Al–4V titanium alloys“. In: *Materials & Design* 46 (2013), pp. 668–674. ISSN: 02641275. DOI: 10.1016/j.matdes.2012.10.059.

[122] L. Wagner, ed. *Shot Peening*. Weinheim, FRG: Wiley-VCH Verlag GmbH & Co. KGaA, 2003. ISBN: 9783527606580. DOI: 10.1002/3527606580.

[123] G. Schroeder, J. Albrecht, and G. Luetjering. „Fatigue crack propagation in titanium alloys with lamellar and bi-lamellar microstructures“. In: *Materials Science and Engineering: A* 319-321 (2001), pp. 602–606. ISSN: 09215093. DOI: 10.1016/S0921-5093(01)00984-4.

[124] G. Terlinde, H.-J. Rathjen, and K.-H. Schwalbe. „Microstructure and fracture toughness of the aged ‚β-Ti Alloy Ti-10V-2Fe-M“. In: *Metallurgical Transactions A* 19.4 (1988), pp. 1037–1049. ISSN: 0360-2133. DOI: 10.1007/BF02628388.

[125] M. Long, R. Crooks, and H. Rack. „High-cycle fatigue performance of solution-treated metastable-β titanium alloys“. In: *Acta Materialia* 47.2 (1999), pp. 661–669. ISSN: 13596454. DOI: 10.1016/S1359-6454(98)00343-7.

[126] A. Gysler, G. Lütjering, and V. Gerold. „Deformation behavior of age-hardened Ti-Mo alloys“. In: *Scripta Metallurgica* 8.3 (1974), p. xiv. ISSN: 00369748. DOI: 10.1016/0036-9748(74)90265-8.

[127] J. C. Williams, B. S. Hickman, and H. L. Marcus. „The effect of omega phase on the mechanical properties of titanium alloys“. In: *Metallurgical Transactions* 2.7 (1971), pp. 1913–1919. ISSN: 0026-086X. DOI: 10.1007/BF02913423.

[128] T. W. Duerig, J. E. Allison, and J. C. Williams. „Microstructural influences on fatigue crack propagation in Ti-10V-2Fe-3Al“. In: *Metallurgical Transactions A* 16.5 (1985), pp. 739–751. ISSN: 0360-2133. DOI: 10.1007/BF02814825.

[129] Y. Hu, W. Floer, U. Krupp, and H.-J. Christ. „Microstructurally short fatigue crack initiation and growth in Ti-6.8Mo-4.5Fe-1.5Al“. In: *Materials Science and Engineering: A* 278.1-2 (2000), pp. 170–180. ISSN: 09215093. DOI: 10.1016/S0921-5093(99)00575-4.

[130] U. Krupp, W. Floer, J. Lei, Y. Hu, H.-J. Christ, A. Schick, and C.-P. Fritzen. „Mechanisms of short-fatigue-crack initiation and propagation in a β-Ti alloy“. In: *Philosophical Magazine A* 82.17-18 (2002), pp. 3321–3332. ISSN: 0141-8610. DOI: 10.1080/01418610208240444.

[131] M. R. Bache, W. J. Evans, B. Suddell, and F. Herrouin. „The effects of texture in titanium alloys for engineering components under fatigue“. In: *International Journal of Fatigue* 23 (2001), pp. 153–159. ISSN: 01421123. DOI: 10.1016/S0142-1123(01)00124-4.

[132] D. B. Lanning, T. Nicholas, and G. K. Haritos. „Effect of plastic prestrain on high cycle fatigue of Ti–6Al–4V“. In: *Mechanics of Materials* 34.2 (2002), pp. 127–134. ISSN: 01676636. DOI: 10.1016/S0167-6636(01)00105-3.

[133] W. Evans, J. Jones, and M. Whittaker. „Texture effects under tension and torsion loading conditions in titanium alloys“. In: *International Journal of Fatigue* 27.10-12 (2005), pp. 1244–1250. ISSN: 01421123. DOI: 10.1016/j.ijfatigue.2005.06.045.

[134] S. K. Jha and K. S. Ravichandran. „Effect of mean stress (stress ratio) and aging on fatigue-crack growth in a metastable beta titanium alloy, Ti-10V-2Fe-3Al“. In: *Metallurgical Transactions A* 31.3 (2000), pp. 703–714. ISSN: 0360-2133. DOI: 10.1007/s11661-000-0012-7.

[135] L. Wagner and G. Lütjering. „Influence of Surface Treatment on Fatigue Resistance of Aircraft Alloys“. In: *Advances in Fatigue Science and Technology*. Ed. by C. M. Branco and L. G. Rosa. Dordrecht: Springer Netherlands, 1989, pp. 933–946. ISBN: 978-94-010-7521-3. DOI: 10.1007/978-94-009-2277-8{\textunderscore}49.

[136] H. Gray, L. Wagner, and G. Lütjering. „Influence of Surface Treatment on the Fatigue Behavior of Ti-Alloys at Room and Elevated Temperatures“. In: *Sixth World Conference on Titanium, P. Lacombe, R. Tricot, and G. Béranger, Ed., Les Éditions de Physique, Paris, France*. 1998, pp. 1895–1900.

[137] A. Berg, J. Kiese, and L. Wagner. „Microstructural gradients in Ti–3Al–8V–6Cr–4Zr–4Mo for excellent HCF strength and toughness“. In: *Materials Science and Engineering: A* 243.1-2 (1998), pp. 146–149. ISSN: 09215093. DOI: 10.1016/S0921-5093(97)00792-2.

[138] M. Kocan, A. Ostertag, and L. Wagner. „Shot Peening and Roller-Burnishing to Improve Fatigue Resistance of the (α+β) Titanium Alloy Ti-6Al-4V“. In: *Shot Peening*. Ed. by L. Wagner. Weinheim, FRG: Wiley-VCH Verlag GmbH & Co. KGaA, 2003, pp. 461–467. ISBN: 9783527606580. DOI: 10.1002/3527606580.ch59.

[139] J.-P. Kruth, M. C. Leu, and T. Nakagawa. „Progress in Additive Manufacturing and Rapid Prototyping“. In: *CIRP Annals* 47.2 (1998), pp. 525–540. ISSN: 00078506. DOI: 10.1016/S0007-8506(07)63240-5.

[140] D. Herzog, V. Seyda, E. Wycisk, and C. Emmelmann. „Additive manufacturing of metals“. In: *Acta Materialia* 117 (2016), pp. 371–392. ISSN: 13596454. DOI: 10.1016/j.actamat.2016.07.019.

[141] D. D. Gu, W. Meiners, K. Wissenbach, and R. Poprawe. „Laser additive manufacturing of metallic components: materials, processes and mechanisms“. In: *International Materials Reviews* 57.3 (2012), pp. 133–164. ISSN: 0950-6608. DOI: 10.1179/1743280411Y.0000000014.

[142] C. Y. Yap, C. K. Chua, Z. L. Dong, Z. H. Liu, D. Q. Zhang, L. E. Loh, and S. L. Sing. „Review of selective laser melting: Materials and applications“. In: *Applied Physics Reviews* 2.4 (2015), p. 041101. DOI: 10.1063/1.4935926.

[143] T. Wohlers and T. Caffrey. „Wohlers Report 2015 : 3D Printing and Additive Manufacturing State of the Industry Annual Worldwide Progress Report“. In: *Wohlers Associates* (2015).

[144] K. V. Wong and A. Hernandez. „A Review of Additive Manufacturing“. In: *ISRN Mechanical Engineering* 2012 (2012), pp. 1–10. DOI: 10.5402/2012/208760.

[145] S. L. Sing, J. An, W. Y. Yeong, and F. E. Wiria. „Laser and electron-beam powder-bed additive manufacturing of metallic implants: A review on processes, materials and designs“. In: *Journal of orthopaedic research : official publication of the Orthopaedic Research Society* 34.3 (2016), pp. 369–385. DOI: 10.1002/jor.23075.

[146] L. E. Murr, S. M. Gaytan, F. Medina, H. Lopez, E. Martinez, B. I. Machado, D. H. Hernandez, L. Martinez, M. I. Lopez, R. B. Wicker, and J. Bracke. „Next-generation biomedical implants using additive manufacturing of complex, cellular and functional mesh arrays“. In: *Philosophical transactions. Series A, Mathematical, physical, and engineering sciences* 368.1917 (2010), pp. 1999–2032. ISSN: 1364-503X. DOI: 10.1098/rsta.2010.0010.

[147] S. F. S. Shirazi, S. Gharehkhani, M. Mehrali, H. Yarmand, H. S. C. Metselaar, N. Adib Kadri, and N. A. A. Osman. „A review on powder-based additive manufacturing for tissue engineering: selective laser sintering and inkjet 3D printing“. In: *Science and technology of advanced materials* 16.3 (2015), p. 033502. ISSN: 1468-6996. DOI: 10.1088/1468-6996/16/3/033502.

[148] B. Vandenbroucke and J.-.-P. Kruth. „Selective laser melting of biocompatible metals for rapid manufacturing of medical parts“. In: *Rapid Prototyping Journal* 13.4 (2007), pp. 196–203. ISSN: 1355-2546. DOI: 10.1108/13552540710776142.

[149] DMG MORI AKTIENGESELLSCHAFT. *LASERTEC 12 SLM – Additive Manufacturing by selective laser melting (SLM) in powder bed*. URL: https://us.dmgmori.com/products/machines/additive-manufacturing/powder-bed/lasertec-12-slm. (accessed: 03.11.2022).

[150] L. Thijs, F. Verhaeghe, T. Craeghs, J. van Humbeeck, and J.-P. Kruth. „A study of the microstructural evolution during selective laser melting of Ti–6Al–4V“. In: *Acta Materialia* 58.9 (2010), pp. 3303–3312. ISSN: 13596454. DOI: 10.1016/j.actamat.2010.02.004.

[151] I. Yadroitsev, P. Krakhmalev, and I. Yadroitsava. „Selective laser melting of Ti6Al4V alloy for biomedical applications: Temperature monitoring and microstructural evolution“. In: *Journal of Alloys and Compounds* 583 (2014), pp. 404–409. ISSN: 09258388. DOI: 10.1016/j.jallcom.2013.08.183.

[152] P. Mercelis and J.-.-P. Kruth. „Residual stresses in selective laser sintering and selective laser melting“. In: *Rapid Prototyping Journal* 12.5 (2006), pp. 254–265. ISSN: 1355-2546. DOI: 10.1108/13552540610707013.

[153] F. Brenne. „Selektives Laserschmelzen metallischer Materialien“. PhD thesis. Kassel, Germany: Kassel University, 2018. DOI: 10.19211/KUP9783737605977.

[154] Y. Liu, Y. Yang, and Di Wang. „A study on the residual stress during selective laser melting (SLM) of metallic powder“. In: *The International Journal of Advanced Manufacturing Technology* 87.1-4 (2016), pp. 647–656. ISSN: 0268-3768. DOI: 10.1007/s00170-016-8466-y.

[155] L. Thijs, K. Kempen, J.-P. Kruth, and J. van Humbeeck. „Fine-structured aluminium products with controllable texture by selective laser melting of pre-alloyed AlSi10Mg powder“. In: *Acta Materialia* 61.5 (2013), pp. 1809–1819. ISSN: 13596454. DOI: 10.1016/j.actamat.2012.11.052.

[156] Q. Jia and D. Gu. „Selective laser melting additive manufacturing of Inconel 718 superalloy parts: Densification, microstructure and properties“. In: *Journal of Alloys and Compounds* 585 (2014), pp. 713–721. ISSN: 09258388. DOI: 10.1016/j.jallcom.2013.09.171.

[157] B. Cheng and K. Chou. „Melt pool evolution study in selective laser melting“. In: *2015 International Solid Freeform Fabrication Symposium*. University of Texas at Austin. 2015.

[158] H. Gong, H. Gu, K. Zeng, J. Dilip, D. Pal, and B. Stucker. „Melt pool characterization for selective laser melting of Ti-6Al-4V pre-alloyed powder“. In: *2014 International Solid Freeform Fabrication Symposium*. University of Texas at Austin. 2014.

[159] M. V. Pantawane, Y.-H. Ho, S. S. Joshi, and N. B. Dahotre. „Computational Assessment of Thermokinetics and Associated Microstructural Evolution in Laser Powder Bed Fusion Manufacturing of Ti6Al4V Alloy“. In: *Scientific reports* 10.1 (2020), p. 7579. DOI: 10.1038/s41598-020-63281-4.

[160] L. Thijs, M. L. Montero Sistiaga, R. Wauthle, Q. Xie, J.-P. Kruth, and J. van Humbeeck. „Strong morphological and crystallographic texture and resulting yield strength anisotropy in selective laser melted tantalum“. In: *Acta Materialia* 61.12 (2013), pp. 4657–4668. ISSN: 13596454. DOI: 10.1016/j.actamat.2013.04.036.

[161] P. Kanagarajah, F. Brenne, T. Niendorf, and H. J. Maier. „Inconel 939 processed by selective laser melting: Effect of microstructure and temperature on the mechanical properties under static and cyclic loading“. In: *Materials Science and Engineering: A* 588 (2013), pp. 188–195. ISSN: 09215093. DOI: 10.1016/j.msea.2013.09.025.

[162] C. J. Smith, S. Tammas-Williams, E. Hernandez-Nava, and I. Todd. „Tailoring the thermal conductivity of the powder bed in Electron Beam Melting (EBM) Additive Manufacturing“. In: *Scientific reports* 7.1 (2017), p. 10514. DOI: 10.1038/s41598-017-11243-8.

[163] W. E. Frazier. „Metal Additive Manufacturing: A Review“. In: *Journal of Materials Engineering and Performance* 23.6 (2014), pp. 1917–1928. ISSN: 1059-9495. DOI: 10.1007/s11665-014-0958-z.

[164] X. Zhang, C. J. Yocom, B. Mao, and Y. Liao. „Microstructure evolution during selective laser melting of metallic materials: A review“. In: *Journal of Laser Applications* 31.3 (2019), p. 031201. ISSN: 1042-346X. DOI: 10.2351/1.5085206.

[165] E. O. Olakanmi, R. F. Cochrane, and K. W. Dalgarno. „A review on selective laser sintering/melting (SLS/SLM) of aluminium alloy powders: Processing, microstructure, and properties“. In: *Progress in Materials Science* 74 (2015), pp. 401–477. ISSN: 00796425. DOI: 10.1016/j.pmatsci.2015.03.002.

[166] K. P. Monroy, J. Delgado, L. Sereno, J. Ciurana, and N. J. Hendrichs. „Effects of the Selective Laser Melting manufacturing process on the properties of CoCrMo single tracks“. In: *Metals and Materials International* 20.5 (2014), pp. 873–884. ISSN: 1598-9623. DOI: 10.1007/s12540-014-5011-0.

[167] D. Sun, X. Li, and W. Tan. „A parametric study on grain structure in selective laser melting process for stainless steel 316L“. In: *2017 International Solid Freeform Fabrication Symposium*. University of Texas at Austin. 2017.

[168] I. Yadroitsev, P. Krakhmalev, I. Yadroitsava, S. Johansson, and I. Smurov. „Energy input effect on morphology and microstructure of selective laser melting single track from metallic powder“. In: *Journal of Materials Processing Technology* 213.4 (2013), pp. 606–613. ISSN: 09240136. DOI: 10.1016/j.jmatprotec.2012.11.014.

[169] A. R. A. Dezfoli, W.-S. Hwang, W.-C. Huang, and T.-W. Tsai. „Determination and controlling of grain structure of metals after laser incidence: Theoretical approach“. In: *Scientific reports* 7 (2017), p. 41527. DOI: 10.1038/srep41527.

[170] J. Olsen, X. Zhou, Y. Zhong, L. Liu, D. Wang, C. Yu, Y. Wang, K. Li, L. Xing, J. Ma, D. Cui, W. Liu, and Z. Shen. „Tailoring hierarchical structures in selective laser melted materials“. In: *IOP Conference Series: Materials Science and Engineering* 219 (July 2017). DOI: 10.1088/1757-899x/219/1/012036. URL: https://doi.org/10.1088/1757-899x/219/1/012036.

[171] Y. M. Arısoy, L. E. Criales, T. Özel, B. Lane, S. Moylan, and A. Donmez. „Influence of scan strategy and process parameters on microstructure and its optimization in additively manufactured nickel alloy 625 via laser powder bed fusion“. In: *The International Journal of Advanced Manufacturing Technology* 90.5-8 (2017), pp. 1393–1417. ISSN: 0268-3768. DOI: 10.1007/s00170-016-9429-z.

[172] M. Easton and D. StJohn. „Grain refinement of aluminum alloys: Part I. the nucleant and solute paradigms—a review of the literature“. In: *Metallurgical Transactions A* 30.6 (1999), pp. 1613–1623. ISSN: 0360-2133. DOI: 10.1007/s11661-999-0098-5.

[173] S. Heiland, B. Milkereit, K.-P. Hoyer, E. Zhuravlev, O. Kessler, and M. Schaper. „Requirements for Processing High-Strength AlZnMgCu Alloys with PBF-LB/M to Achieve Crack-Free and Dense Parts“. In: *Materials (Basel, Switzerland)* 14.23 (2021), p. 7190. ISSN: 1996-1944. DOI: 10.3390/ma14237190.

[174] W.-C. Huang, C.-S. Chuang, C.-C. Lin, C.-H. Wu, D.-Y. Lin, S.-H. Liu, W.-P. Tseng, and J.-B. Horng. „Microstructure-controllable Laser Additive Manufacturing Process for Metal Products“. In: *Physics Procedia* 56 (2014), pp. 58–63. ISSN: 18753892. DOI: 10.1016/j.phpro.2014.08.096.

[175] J. Xu, J. Zhou, W. Tan, S. Huang, S. Wang, and W. He. „Study on laser surface melting of AZ31B magnesium alloy with different ultrasonic vibration amplitude“. In: *Corrosion Engineering, Science and Technology* 53.1 (2018), pp. 73–79. ISSN: 1478-422X. DOI: 10.1080/1478422X.2017.1398540.

[176] L. E. Murr, S. A. Quinones, S. M. Gaytan, M. I. Lopez, A. Rodela, E. Y. Martinez, D. H. Hernandez, E. Martinez, F. Medina, and R. B. Wicker. „Microstructure and mechanical behavior of Ti-6Al-4V produced by rapid-layer manufacturing, for biomedical applications“. In: *Journal of the mechanical behavior of biomedical materials* 2.1 (2009), pp. 20–32. DOI: 10.1016/j.jmbbm.2008.05.004.

[177] R. P. Mulay, J. A. Moore, J. N. Florando, N. R. Barton, and M. Kumar. „Microstructure and mechanical properties of Ti–6Al–4V: Mill-annealed versus direct metal laser melted alloys“. In: *Materials Science and Engineering: A* 666 (2016), pp. 43–47. ISSN: 09215093. DOI: 10.1016/j.msea.2016.04.012.

[178] D. Gu, Y.-C. Hagedorn, W. Meiners, G. Meng, R. J. S. Batista, K. Wissenbach, and R. Poprawe. „Densification behavior, microstructure evolution, and wear performance of selective laser melting processed commercially pure titanium“. In: *Acta Materialia* 60.9 (2012), pp. 3849–3860. ISSN: 13596454. DOI: 10.1016/j.actamat.2012.04.006.

[179] W. Xu, M. Brandt, S. Sun, J. Elambasseril, Q. Liu, K. Latham, K. Xia, and M. Qian. „Additive manufacturing of strong and ductile Ti–6Al–4V by selective laser melting via in situ martensite decomposition“. In: *Acta Materialia* 85 (2015), pp. 74–84. ISSN: 13596454. DOI: 10.1016/j.actamat.2014.11.028.

[180] Q. Wang, C. Han, T. Choma, Q. Wei, C. Yan, B. Song, and Y. Shi. „Effect of Nb content on microstructure, property and in vitro apatite-forming capability of Ti-Nb alloys fabricated via selective laser melting“. In: *Materials & Design* 126 (2017), pp. 268–277. ISSN: 02641275. DOI: 10.1016/j.matdes.2017.04.026.

[181] E. Chlebus, B. Kuźnicka, T. Kurzynowski, and B. Dybała. „Microstructure and mechanical behaviour of Ti—6Al—7Nb alloy produced by selective laser melting“. In: *Materials Characterization* 62.5 (2011), pp. 488–495. ISSN: 10445803. DOI: 10.1016/j.matchar.2011.03.006.

[182] W. Li, J. Liu, Y. Zhou, S. Li, S. Wen, Q. Wei, C. Yan, and Y. Shi. „Effect of laser scanning speed on a Ti-45Al-2Cr-5Nb alloy processed by selective laser melting: Microstructure, phase and mechanical properties“. In: *Journal of Alloys and Compounds* 688 (2016), pp. 626–636. ISSN: 09258388. DOI: 10.1016/j.jallcom.2016.07.206.

[183] Q. Liu and C. Qiu. „Variant selection of α precipitation in a β titanium alloy during selective laser melting and its influence on mechanical properties“. In: *Materials Science and Engineering: A* 784 (2020), p. 139336. ISSN: 09215093. DOI: 10.1016/j.msea.2020.139336.

[184] H. Fan and S. Yang. „Effects of direct aging on near-alpha Ti–6Al–2Sn–4Zr–2Mo (Ti-6242) titanium alloy fabricated by selective laser melting (SLM)“. In: *Materials Science and Engineering: A* 788 (2020), p. 139533. ISSN: 09215093. DOI: 10.1016/j.msea.2020.139533.

[185] J. Zhang, Y. Liu, M. Bayat, Q. Tan, Y. Yin, Z. Fan, S. Liu, J. H. Hattel, M. Dargusch, and M.-X. Zhang. „Achieving high ductility in a selectively laser melted commercial pure-titanium via in-situ grain refinement“. In: *Scripta Materialia* 191 (2021), pp. 155–160. ISSN: 13596462. DOI: 10.1016/j.scriptamat.2020.09.023.

[186] W. Xu, E. W. Lui, A. Pateras, M. Qian, and M. Brandt. „In situ tailoring microstructure in additively manufactured Ti-6Al-4V for superior mechanical performance“. In: *Acta Materialia* 125 (2017), pp. 390–400. ISSN: 13596454. DOI: 10.1016/j.actamat.2016.12.027.

[187] W. J. Sames, F. A. List, S. Pannala, R. R. Dehoff, and S. S. Babu. „The metallurgy and processing science of metal additive manufacturing“. In: *International Materials Reviews* 61.5 (2016), pp. 315–360. ISSN: 0950-6608. DOI: 10.1080/09506608.2015.1116649.

[188] Y. Wang, P. R. Jadhav, M. Lala, and J. V. Gobburu. „Clarification on precision criteria to derive sample size when designing pediatric pharmacokinetic studies“. In: *Journal of clinical pharmacology* 52.10 (2012), pp. 1601–1606. DOI: 10.1177/0091270011422812.

[189] H. Nasiri-Abarbekoh, A. Ekrami, and A. A. Ziaei-Moayyed. „Impact of phase transformation on mechanical properties anisotropy of commercially pure titanium“. In: *Materials & Design* 37 (2012), pp. 223–227. ISSN: 02641275. DOI: 10.1016/j.matdes.2011.12.040.

[190] H. Attar, M. Calin, L. C. Zhang, S. Scudino, and J. Eckert. „Manufacture by selective laser melting and mechanical behavior of commercially pure titanium“. In: *Materials Science and Engineering: A* 593 (2014), pp. 170–177. ISSN: 09215093. DOI: 10.1016/j.msea.2013.11.038.

[191] A. Sergueeva, V. Stolyarov, R. Valiev, and A. Mukherjee. „Advanced mechanical properties of pure titanium with ultrafine grained structure“. In: *Scripta Materialia* 45.7 (2001), pp. 747–752. ISSN: 13596462. DOI: 10.1016/S1359-6462(01)01089-2.

[192] P. Luo, D. T. McDonald, W. Xu, S. Palanisamy, M. S. Dargusch, and K. Xia. „A modified Hall–Petch relationship in ultrafine-grained titanium recycled from chips by equal channel angular pressing“. In: *Scripta Materialia* 66.10 (2012), pp. 785–788. ISSN: 13596462. DOI: 10.1016/j.scriptamat.2012.02.008.

[193] S. Nemat-Nasser, W. G. Guo, and J. Y. Cheng. „Mechanical properties and deformation mechanisms of a commercially pure titanium“. In: *Acta Materialia* 47.13 (1999), pp. 3705–3720. ISSN: 13596454. DOI: 10.1016/S1359-6454(99)00203-7.

[194] E. Yu, I. Kim, D. H. Shin, and J. Kim. „Deformation Mechanism of Severely Deformed CP-Titanium by Uniaxial Compression Test“. In: *MATERIALS TRANSACTIONS* 49.1 (2008), pp. 38–40. ISSN: 1345-9678. DOI: 10.2320/matertrans.ME200723.

[195] J. L. Sun, P. W. Trimby, F. K. Yan, X. Z. Liao, N. R. Tao, and J. T. Wang. „Grain size effect on deformation twinning propensity in ultrafine-grained hexagonal close-packed titanium“. In: *Scripta Materialia* 69.5 (2013), pp. 428–431. ISSN: 13596462. DOI: 10.1016/j.scriptamat.2013.06.001.

[196] S. Banerjee and P. Mukhopadhyay. *Phase transformations: examples from titanium and zirconium alloys*. Elsevier, 2010.

[197] M. Simonelli, Y. Y. Tse, and C. Tuck. „On the Texture Formation of Selective Laser Melted Ti-6Al-4V“. In: *Metallurgical Transactions A* 45.6 (2014), pp. 2863–2872. ISSN: 0360-2133. DOI: 10.1007/s11661-014-2218-0.

[198] B. E. Carroll, T. A. Palmer, and A. M. Beese. „Anisotropic tensile behavior of Ti–6Al–4V components fabricated with directed energy deposition additive manufacturing“. In: *Acta Materialia* 87 (2015), pp. 309–320. ISSN: 13596454. DOI: 10.1016/j.actamat.2014.12.054.

[199] N. Hrabe and T. Quinn. „Effects of processing on microstructure and mechanical properties of a titanium alloy (Ti–6Al–4V) fabricated using electron beam melting (EBM), Part 2: Energy input, orientation, and location“. In: *Materials Science and Engineering: A* 573 (2013), pp. 271–277. ISSN: 09215093. DOI: 10.1016/j.msea.2013.02.065.

[200] X. Wu, J. Liang, J. Mei, C. Mitchell, P. S. Goodwin, and W. Voice. „Microstructures of laser-deposited Ti–6Al–4V“. In: *Materials & Design* 25.2 (2004), pp. 137–144. ISSN: 02641275. DOI: 10.1016/j.matdes.2003.09.009.

[201] B. Vrancken, L. Thijs, J.-P. Kruth, and J. van Humbeeck. „Heat treatment of Ti6Al4V produced by Selective Laser Melting: Microstructure and mechanical properties“. In: *Journal of Alloys and Compounds* 541 (2012), pp. 177–185. ISSN: 09258388. DOI: 10.1016/j.jallcom.2012.07.022.

[202] N. Sridharan, A. Chaudhary, P. Nandwana, and S. S. Babu. „Texture Evolution During Laser Direct Metal Deposition of Ti-6Al-4V“. In: *JOM* 68.3 (2016), pp. 772–777. ISSN: 1047-4838. DOI: 10.1007/s11837-015-1797-6.

[203] Z. Wang, Z. Xiao, Y. Tse, C. Huang, and W. Zhang. „Optimization of processing parameters and establishment of a relationship between microstructure and mechanical properties of SLM titanium alloy“. In: *Optics & Laser Technology* 112 (2019), pp. 159–167. ISSN: 00303992. DOI: 10.1016/j.optlastec.2018.11.014.

[204] M. Wang, Y. Wu, S. Lu, T. Chen, Y. Zhao, H. Chen, and Z. Tang. „Fabrication and characterization of selective laser melting printed Ti–6Al–4V alloys subjected to heat treatment for customized implants design“. In: *Progress in Natural Science: Materials International* 26.6 (2016), pp. 671–677. ISSN: 10020071. DOI: 10.1016/j.pnsc.2016.12.006.

[205] L. Facchini, E. Magalini, P. Robotti, A. Molinari, S. Höges, and K. Wissenbach. „Ductility of a Ti–6Al–4V alloy produced by selective laser melting of prealloyed powders“. In: *Rapid Prototyping Journal* 16.6 (2010), pp. 450–459. ISSN: 1355-2546. DOI: 10.1108/13552541011083371.

[206] T. Vilaro, C. Colin, and J. D. Bartout. „As-Fabricated and Heat-Treated Microstructures of the Ti-6Al-4V Alloy Processed by Selective Laser Melting“. In: *Metallurgical Transactions A* 42.10 (2011), pp. 3190–3199. ISSN: 0360-2133. DOI: 10.1007/s11661-011-0731-y.

[207] M. T. Mohammed, Z. A. Khan, and A. N. Siddiquee. „Beta titanium alloys: the lowest elastic modulus for biomedical applications: a review“. In: *International Journal of Chemical, Nuclear, Metallurgical and Materials Engineering* 8.8 (2014), p. 726.

[208] L. C. Zhang, D. Klemm, J. Eckert, Y. L. Hao, and T. B. Sercombe. „Manufacture by selective laser melting and mechanical behavior of a biomedical Ti–24Nb–4Zr–8Sn alloy“. In: *Scripta Materialia* 65.1 (2011), pp. 21–24. ISSN: 13596462. DOI: 10.1016/j.scriptamat.2011.03.024.

[209] K. Zhuravleva, M. Bönisch, K. G. Prashanth, U. Hempel, A. Helth, T. Gemming, M. Calin, S. Scudino, L. Schultz, J. Eckert, and A. Gebert. „Production of Porous β-Type Ti-40Nb Alloy for Biomedical Applications: Comparison of Selective Laser Melting and Hot Pressing“. In: *Materials (Basel, Switzerland)* 6.12 (2013), pp. 5700–5712. ISSN: 1996-1944. DOI: 10.3390/ma6125700.

[210] M. A. Macias-Sifuentes, C. Xu, O. Sanchez-Mata, S. Y. Kwon, S. E. Atabay, J. A. Muñiz-Lerma, and M. Brochu. „Microstructure and mechanical properties of β-21S Ti alloy fabricated through laser powder bed fusion“. In: *Progress in Additive Manufacturing* 6.3 (2021), pp. 417–430. ISSN: 2363-9512. DOI: 10.1007/s40964-021-00181-7.

[211] S. L. Sing, W. Y. Yeong, and F. E. Wiria. „Selective laser melting of titanium alloy with 50 wt% tantalum: Microstructure and mechanical properties“. In: *Journal of Alloys and Compounds* 660 (2016), pp. 461–470. ISSN: 09258388. DOI: 10.1016/j.jallcom.2015.11.141.

[212] W. Chen, C. Chen, X. Zi, X. Cheng, X. Zhang, Y. C. Lin, and K. Zhou. „Controlling the microstructure and mechanical properties of a metastable β titanium alloy by selective laser melting“. In: *Materials Science and Engineering: A* 726 (2018), pp. 240–250. ISSN: 09215093. DOI: 10.1016/j.msea.2018.04.087.

[213] S. Guo, Q. Meng, X. Zhao, Q. Wei, and H. Xu. „Design and fabrication of a metastable β-type titanium alloy with ultralow elastic modulus and high strength“. In: *Scientific reports* 5 (2015), p. 14688. DOI: 10.1038/srep14688.

[214] Y. C. Lin, X.-Y. Jiang, C.-j. Shuai, C.-Y. Zhao, D.-G. He, M.-S. Chen, and C. Chen. „Effects of initial microstructures on hot tensile deformation behaviors and fracture characteristics of Ti-6Al-4V alloy“. In: *Materials Science and Engineering: A* 711 (2018), pp. 293–302. ISSN: 09215093. DOI: 10.1016/j.msea.2017.11.044.

[215] S. Hanada, H. Matsumoto, and S. Watanabe. „Mechanical compatibility of titanium implants in hard tissues“. In: *International Congress Series* 1284 (2005), pp. 239–247. ISSN: 05315131. DOI: 10.1016/j.ics.2005.06.084.

[216] H. Y. Kim, Y. Ikehara, J. I. Kim, H. Hosoda, and S. Miyazaki. „Martensitic transformation, shape memory effect and superelasticity of Ti–Nb binary alloys“. In: *Acta Materialia* 54.9 (2006), pp. 2419–2429. ISSN: 13596454. DOI: 10.1016/j.actamat.2006.01.019.

[217] X. Tang, T. Ahmed, and H. J. Rack. „Phase transformations in Ti-Nb-Ta and Ti-Nb-Ta-Zr alloys“. In: *Journal of Materials Science* 35.7 (2000), pp. 1805–1811. ISSN: 0022-2461. DOI: 10.1023/A:1004792922155.

[218] A. Barbas, A.-S. Bonnet, P. Lipinski, R. Pesci, and G. Dubois. „Development and mechanical characterization of porous titanium bone substitutes“. In: *Journal of the mechanical behavior of biomedical materials* 9 (2012), pp. 34–44. DOI: 10.1016/j.jmbbm.2012.01.008.

[219] J. D. Beal, R. Boyer, and D. Sanders. „Forming of titanium and titanium alloys.“ In: *Metalworking: Sheet Forming(ASM Handbook)* 14 (2006), pp. 656–669.

[220] U. Bathini, T. S. Srivatsan, A. Patnaik, and T. Quick. „A Study of the Tensile Deformation and Fracture Behavior of Commercially Pure Titanium and Titanium Alloy: Influence of Orientation and Microstructure“. In: *Journal of Materials Engineering and Performance* 19.8 (2010), pp. 1172–1182. ISSN: 1059-9495. DOI: 10.1007/s11665-010-9613-5.

[221] D. Iijima, T. Yoneyamab, H. Doib, H. Hamanakab, and N. Kurosakia. „Wear properties of Ti and Ti–6Al–7Nb castings for dental prostheses“. In: *Biomaterials* 24.8 (2003), pp. 1519–1524. ISSN: 01429612. DOI: 10.1016/S0142-9612(02)00533-1.

[222] W.-F. Ho. „A comparison of tensile properties and corrosion behavior of cast Ti–7.5Mo with c.p. Ti, Ti–15Mo and Ti–6Al–4V alloys“. In: *Journal of Alloys and Compounds* 464.1-2 (2008), pp. 580–583. ISSN: 09258388. DOI: 10.1016/j.jallcom.2007.10.054.

[223] B. Wysocki, P. Maj, R. Sitek, J. Buhagiar, K. Kurzydłowski, and W. Święszkowski. „Laser and Electron Beam Additive Manufacturing Methods of Fabricating Titanium Bone Implants“. In: *Applied Sciences* 7.7 (2017), p. 657. DOI: 10.3390/app7070657.

[224] M. Mihailović and A. Patarić. „On the properties of hot forged Ti-6Al-4V alloy aimed for surgical implants“. In: *Metallurgical and Materials Engineering* 25.1 (2019), pp. 23–29. ISSN: 2217-8961. DOI: 10.30544/412.

[225] M. Hein, K.-P. Hoyer, and M. Schaper. „Additively processed TiAl6Nb7 alloy for biomedical applications“. In: *Materialwissenschaft und Werkstofftechnik* 52.7 (2021), pp. 703–716. ISSN: 0933-5137. DOI: 10.1002/mawe.202000288.

[226] M. Hein, N. F. Lopes Dias, D. Kokalj, D. Stangier, K.-P. Hoyer, W. Tillmann, and M. Schaper. „On the influence of physical vapor deposited thin coatings on the low-cycle fatigue behavior of additively processed Ti-6Al-7Nb alloy“. In: *International Journal of Fatigue* 166 (2023), p. 107235. ISSN: 01421123. DOI: 10.1016/j.ijfatigue.2022.107235.

[227] *Material Data Sheet – Ti-Alloy TiAl6Nb7 / F1295*. TLE 4473 GV55-2. SLM Solutions Group AG. Lübeck, 2008. URL: https://docplayer.org/138896681-Materialdatenblatt-material-data-sheet-ti-alloy-tial6nb7-f1295-1-allgemeines-materialaufbau-general-material-structure.html. (accessed: 02.11.2022).

[228] M. Semlitsch. „Titanium alloys for hip joint replacements“. In: *Clinical Materials* 2.1 (1987), pp. 1–13.

[229] M. Hein, N. F. Lopes Dias, S. Pramanik, D. Stangier, K.-P. Hoyer, W. Tillmann, and M. Schaper. „Heat Treatments of Metastable β Titanium Alloy Ti-24Nb-4Zr-8Sn Processed by Laser Powder Bed Fusion“. In: *Materials (Basel, Switzerland)* 15.11 (2022). ISSN: 1996-1944. DOI: 10.3390/ma15113774.

[230] S. Q. Zhang, S. J. Li, M. T. Jia, Y. L. Hao, and R. Yang. „Fatigue properties of a multifunctional titanium alloy exhibiting nonlinear elastic deformation behavior“. In: *Scripta Materialia* 60.8 (2009), pp. 733–736. ISSN: 13596462. DOI: 10.1016/j.scriptamat.2009.01.007.

[231] S. J. Li, T. C. Cui, Y. L. Hao, and R. Yang. „Fatigue properties of a metastable beta-type titanium alloy with reversible phase transformation“. In: *Acta biomaterialia* 4.2 (2008), pp. 305–317. DOI: 10.1016/j.actbio.2007.09.009.

[232] Y. L. Hao, Z. B. Zhang, S. J. Li, and R. Yang. „Microstructure and mechanical behavior of a Ti–24Nb–4Zr–8Sn alloy processed by warm swaging and warm rolling“. In: *Acta Materialia* 60.5 (2012), pp. 2169–2177. ISSN: 13596454. DOI: 10.1016/j.actamat.2012.01.003.

[233] K. Bobzin. *Oberflächentechnik für den Maschinenbau*. 1. Aufl. Weinheim: Wiley-VCH, 2013. ISBN: 978-3-527-33018-8.

[234] P. M. Martin. *Handbook of deposition technologies for films and coatings: Science, applications and technology*. 3. ed. Norwich, N.Y. and Oxford: William Andrew and Elsevier Science, 2009. ISBN: 978-0-8155-2031-3. URL: http://www.sciencedirect.com/science/book/9780815520313.

[235] A. Goswami. *Thin Film Fundamentals*. New Age International Publishers, 1996. ISBN: 9788122408584. URL: https://books.google.de/books?id=K0e-8Nh9zSYC.

[236] Deutsche Institut für Normung e.V. *DIN 8580:2003-09, Manufacturing processes - Terms and definitions, division*. Berlin, 2003. DOI: 10.31030/9500683.

[237] M. Ohring. *Materials Science of Thin Films*. Elsevier, 2002. ISBN: 9780125249751. DOI: 10.1016/B978-0-12-524975-1.X5000-9.

[238] R. F. Bunshah, ed. *Handbook of hard coatings: Deposition technologies, properties and applications*. Vol. 3. Materials science and processing technology series. Park Ridge, NJ: Noyes Publications, 2001. ISBN: 9780815514381.

[239] R. Smallman and R. Bishop. *Modern Physical Metallurgy and Materials Engineering*. Elsevier Science, 1999. ISBN: 9780080511993. URL: https://books.google.de/books?id=xN0EN0d6h98C.

[240] S. Mahieu, P. Ghekiere, D. Depla, and R. de Gryse. „Biaxial alignment in sputter deposited thin films“. In: *Thin Solid Films* 515.4 (2006), pp. 1229–1249. ISSN: 00406090. DOI: 10.1016/j.tsf.2006.06.027.

[241] J. W. Bradley, S. Thompson, and Y. A. Gonzalvo. „Measurement of the plasma potential in a magnetron discharge and the prediction of the electron drift speeds“. In: *Plasma Sources Science and Technology* 10.3 (2001), pp. 490–501. ISSN: 0963-0252. DOI: 10.1088/0963-0252/10/3/314.

[242] J. A. Thornton. „Magnetron sputtering: basic physics and application to cylindrical magnetrons“. In: *Journal of Vacuum Science and Technology* 15.2 (1978), pp. 171–177. ISSN: 0022-5355. DOI: 10.1116/1.569448.

[243] E. Kay. „Magnetic Field Effects on an Abnormal Truncated Glow Discharge and Their Relation to Sputtered Thin–Film Growth“. In: *Journal of Applied Physics* 34.4 (1963), pp. 760–768. ISSN: 0021-8979. DOI: 10.1063/1.1729530.

[244] W. D. Gill and E. Kay. „Efficient Low Pressure Sputtering in a Large Inverted Magnetron Suitable for Film Synthesis“. In: *Review of Scientific Instruments* 36.3 (1965), pp. 277–282. ISSN: 0034-6748. DOI: 10.1063/1.1719553.

[245] K. Burcalova, A. Hecimovic, and A. P. Ehiasarian. „Ion energy distributions and efficiency of sputtering process in HIPIMS system“. In: *Journal of Physics D: Applied Physics* 41.11 (2008), p. 115306. ISSN: 0022-3727. DOI: 10.1088/0022-3727/41/11/115306.

[246] J. Singh and D. E. Wolfe. „Review Nano and macro-structured component fabrication by electron beam-physical vapor deposition (EB-PVD)“. In: *Journal of Materials Science* 40.1 (2005), pp. 1–26. ISSN: 0022-2461. DOI: 10.1007/s10853-005-5682-5.

[247] H. O. Pierson. *Handbook of chemical vapor deposition (CVD): Principles, technology, and applications*. 2. ed. Materials science and process technology series. Norwich, NY: Noyes Publ, 1999. ISBN: 9780815514329. URL: http://www.sciencedirect.com/science/book/9780815514329.

[248] D. M. Mattox. *Handbook of Physical Vapor Deposition (PVD) Processing: Film Formation, Adhesion, Surface Preparation and Contamination Control*. Burlington: Elsevier, 2007. ISBN: 9780815517634.

[249] J. Jagielski, A. S. Khanna, J. Kucinski, D. S. Mishra, P. Racolta, P. Sioshansi, E. Tobin, J. Thereska, V. Uglov, T. Vilaithong, J. Viviente, S.-Z. Yang, and A. Zalar. „Effect of chromium nitride coating on the corrosion and wear resistance of stainless steel“. In: *Applied Surface Science* 156.1-4 (2000), pp. 47–64. ISSN: 01694332. DOI: 10.1016/S0169-4332(99)00350-5.

[250] H.-P. Feng, C.-H. Hsu, J.-K. Lu, and Y.-H. Shy. „Effects of PVD sputtered coatings on the corrosion resistance of AISI 304 stainless steel“. In: *Materials Science and Engineering: A* 347.1-2 (2003), pp. 123–129. ISSN: 09215093. DOI: 10.1016/S0921-5093(02)00578-6.

[251] H. Altun and S. Sen. „The effect of PVD coatings on the wear behaviour of magnesium alloys“. In: *Materials Characterization* 58.10 (2007), pp. 917–921. ISSN: 10445803. DOI: 10.1016/j.matchar.2006.09.007.

[252] J. Daniel, R. Žemlička, J. Grossman, A. Lümkemann, P. Tapp, C. Galamand, and T. Fořt. „Comparison of Lifetime of the PVD Coatings in Laboratory Dynamic Impact Test and Industrial Fine Blanking Process“. In: *Materials (Basel, Switzerland)* 13.9 (2020). ISSN: 1996-1944. DOI: 10.3390/ma13092154.

[253] E. Lugscheider, K. Bobzin, C. Piñero, F. Klocke, and T. Massmann. „Development of a superlattice (Ti,Hf,Cr)N coating for cold metal forming applications“. In: *Surface and Coatings Technology* 177-178 (2004), pp. 616–622. ISSN: 02578972. DOI: 10.1016/S0257-8972(03)00935-6.

[254] L. Lind, P. Peetsalu, and F. Sergejev. „Wear of different PVD coatings at industrial fine-blanking field tests“. In: *Materials Science* 21.3 (2015). ISSN: 1392-1320. DOI: 10.5755/j01.ms.21.3.7249.

[255] W. Tillmann, N. F. Lopes Dias, D. Stangier, L. Hagen, M. Schaper, F. Hengsbach, and K.-P. Hoyer. „Tribo-mechanical properties and adhesion behavior of DLC coatings sputtered onto 36NiCrMo16 produced by selective laser melting“. In: *Surface and Coatings Technology* 394 (2020), p. 125748. ISSN: 02578972. DOI: 10.1016/j.surfcoat.2020.125748.

[256] W. Tillmann, N. F. Lopes Dias, D. Kokalj, D. Stangier, M. Hein, K.-P. Hoyer, M. Schaper, D. Gödecke, H. Oltmanns, and J. Meißner. „Tribo-functional PVD thin films deposited onto additively manufactured Ti6Al7Nb for biomedical applications“. In: *Materials Letters* 321 (2022), p. 132384. ISSN: 0167577X. DOI: 10.1016/j.matlet.2022.132384.

[257] X. Liu, P. Chu, and C. Ding. „Surface modification of titanium, titanium alloys, and related materials for biomedical applications“. In: *Materials Science and Engineering: R: Reports* 47.3-4 (2004), pp. 49–121. ISSN: 0927796X. DOI: 10.1016/j.mser.2004.11.001.

[258] A. P. Gopkalo, N. R. Muzyka, A. V. Rutkovskii, and V. P. Shvets. „Effect of PVD coatings on the strain and low-cycle fatigue resistance of stainless steel and titanium alloys“. In: *Strength of Materials* 43.6 (2011), pp. 604–614. ISSN: 0039-2316. DOI: 10.1007/s11223-011-9333-6.

[259] A. P. Gopkalo and A. V. Rutkovsky. „The effect of PVD coatings on the tensile strength and low-cycle fatigue resistance of stainless steel and titanium alloys“. In: *Fatigue & Fracture of Engineering Materials & Structures* 34.12 (2011), pp. 1012–1020. ISSN: 8756758X. DOI: 10.1111/j.1460-2695.2011.01590.x.

[260] E. Puchi-Cabrera, F. Matínez, I. Herrera, J. Berríos, S. Dixit, and D. Bhat. „On the fatigue behavior of an AISI 316L stainless steel coated with a PVD TiN deposit“. In: *Surface and Coatings Technology* 182.2-3 (2004), pp. 276–286. ISSN: 02578972. DOI: 10.1016/j.surfcoat.2003.07.003.

[261] K. R. Kim, C. M. Suh, R. I. Murakami, and C. W. Chung. „Effect of intrinsic properties of ceramic coatings on fatigue behavior of Cr–Mo–V steels“. In: *Surface and Coatings Technology* 171.1-3 (2003), pp. 15–23. ISSN: 02578972. DOI: 10.1016/S0257-8972(03)00229-9.

[262] J. A. Berríos, D. G. Teer, and E. S. Puchi-Cabrera. „Fatigue properties of a 316L stainless steel coated with different TiNx deposits“. In: *Surface and Coatings Technology* 148.2-3 (2001), pp. 179–190. ISSN: 02578972. DOI: 10.1016/S0257-8972(01)01346-9.

[263] D. S. Rickerby. „Internal stress and adherence of titanium nitride coatings“. In: *Journal of Vacuum Science & Technology A: Vacuum, Surfaces, and Films* 4.6 (1986), pp. 2809–2814. ISSN: 0734-2101. DOI: 10.1116/1.573683.

[264] A. J. Perry and M. Jagner. „Residual stress in physically vapor deposited films: A study of deviations from elastic behavior“. In: *Thin Solid Films* 171.1 (1989), pp. 197–216. ISSN: 00406090. DOI: 10.1016/0040-6090(89)90044-8.

[265] K. Bewilogua, G. Bräuer, A. Dietz, J. Gäbler, G. Goch, B. Karpuschewski, and B. Szyszka. „Surface technology for automotive engineering“. In: *CIRP Annals* 58.2 (2009), pp. 608–627. ISSN: 00078506. DOI: 10.1016/j.cirp.2009.09.001.

[266] P. Kelly and R. Arnell. „Magnetron sputtering: a review of recent developments and applications“. In: *Vacuum* 56.3 (2000), pp. 159–172. ISSN: 0042207X. DOI: 10.1016/S0042-207X(99)00189-X.

[267] E. Fuentes, S. Alves, A. López-Ortega, L. Mendizabal, and V. Sáenz de Viteri. „Advanced Surface Treatments on Titanium and Titanium Alloys Focused on Electrochemical and Physical Technologies for Biomedical Applications“. In: *Biomaterial-supported Tissue Reconstruction or Regeneration*. Ed. by M. Barbeck, O. Jung, R. Smeets, and T. Koržinskas. IntechOpen, 2019. ISBN: 978-1-83880-377-3. DOI: 10.5772/intechopen.85095.

[268] W. Tillmann, N. F. Lopes Dias, C. Franke, D. Kokalj, D. Stangier, V. Filor, R. H. Mateus-Vargas, H. Oltmanns, M. Kietzmann, J. Meißner, M. Hein, S. Pramanik, K.-P. Hoyer, M. Schaper, A. Nienhaus, C. A. Thomann, and J. Debus. „Tribomechanical properties and biocompatibility of Ag-containing amorphous carbon films deposited onto Ti6Al4V“. In: *Surface and Coatings Technology* 421 (2021), p. 127384. ISSN: 02578972. DOI: 10.1016/j.surfcoat.2021.127384.

[269] R. Rodríguez, J. García, A. Medrano, M. Rico, R. Sánchez, R. Martínez, C. Labrugère, M. Lahaye, and A. Guette. „Tribological behaviour of hard coatings deposited by arc-evaporation PVD“. In: *Vacuum* 67.3-4 (2002), pp. 559–566. ISSN: 0042207X. DOI: 10.1016/S0042-207X(02)00248-8.

[270] E. Román, J. L. de Segovia, A. Alberdi, J. Calvo, and J. Laucirica. „Comparative study of the interface composition of TiN and TiCN hard coatings on high speed steel substrates obtained by arc discharge“. In: *Materials Science and Engineering: A* 163.2 (1993), pp. 197–200. ISSN: 09215093. DOI: 10.1016/0921-5093(93)90789-H.

[271] J. de Damborenea, C. Navas, J. A. García, M. A. Arenas, and A. Conde. „Corrosion–erosion of TiN-PVD coatings in collagen and cellulose meat casing“. In: *Surface and Coatings Technology* 201.12 (2007), pp. 5751–5757. ISSN: 02578972. DOI: 10.1016/j.surfcoat.2006.10.009.

[272] J. A. García, P. J. Rivero, R. Ortiz, I. Quintana, and R. J. Rodríguez. „Advanced Surface Treatments for Improving the Biocompatibility of Prosthesis and Medical Implants“. In: *Advanced Surface Engineering Research*. Ed. by M. A. Chowdhury. InTech, 2018. ISBN: 978-1-78984-339-2. DOI: 10.5772/intechopen.79532.

[273] A. P. Serro, C. Completo, R. Colaço, F. dos Santos, C. L. Da Silva, J. Cabral, H. Araújo, E. Pires, and B. Saramago. „A comparative study of titanium nitrides, TiN, TiNbN and TiCN, as coatings for biomedical applications“. In: *Surface and Coatings Technology* 203.24 (2009), pp. 3701–3707. ISSN: 02578972. DOI: 10.1016/j.surfcoat.2009.06.010.

[274] H. Behrndt and A. Lunk. „Biocompatibility of TiN preclinical and clinical investigations“. In: *Materials Science and Engineering: A* 139 (1991), pp. 58–60. ISSN: 09215093. DOI: 10.1016/0921-5093(91)90596-F.

[275] J. Zhao, L. Li, D. Li, and H. Gu. „A study on biocompatibility of TiN thin films deposited by dual-energy ion beam assisted deposition“. In: *Journal of Adhesion Science and Technology* 18.9 (2004), pp. 1003–1010. ISSN: 0169-4243. DOI: 10.1163/1568561041257522.

[276] R. P. van Hove, I. N. Sierevelt, B. J. van Royen, and P. A. Nolte. „Titanium-Nitride Coating of Orthopaedic Implants: A Review of the Literature“. In: *BioMed research international* 2015 (2015), p. 485975. DOI: 10.1155/2015/485975.

[277] A. Wisbey, P. J. Gregson, and M. Tuke. „Application of PVD TiN coating to Co-Cr-Mo based surgical implants“. In: *Biomaterials* 8.6 (1987), pp. 477–480. ISSN: 01429612. DOI: 10.1016/0142-9612(87)90085-8.

[278] O. Knotek, F. Löffler, and K. Weitkamp. „Physical vapour deposition coatings for dental prostheses“. In: *Surface and Coatings Technology* 54-55 (1992), pp. 536–540. ISSN: 02578972. DOI: 10.1016/S0257-8972(07)80078-8.

[279] P. V. Kola, S. Daniels, D. C. Cameron, and M. Hashmi. „Magnetron sputtering of tin protective coatings for medical applications“. In: *Journal of Materials Processing Technology* 56.1-4 (1996), pp. 422–430. ISSN: 09240136. DOI: 10.1016/0924-0136(95)01856-5.

[280] A. Kamali, R. Farrar, P. Hatto, M. H. Stone, and J. Fisher. „Wear of ultrahigh-molecular-weight polyethylene against titanium-nitride-coated counterfaces“. In: *Proceedings of the Institution of Mechanical Engineers, Part J: Journal of Engineering Tribology* 219.1 (2005), pp. 41–47. ISSN: 1350-6501. DOI: 10.1243/135065005X9736.

[281] M. Hoseini, A. Jedenmalm, and A. Boldizar. „Tribological investigation of coatings for artificial joints“. In: *Wear* 264.11-12 (2008), pp. 958–966. ISSN: 00431648. DOI: 10.1016/j.wear.2007.07.003.

[282] R. A. Antunes, A. Rodas, N. B. Lima, O. Z. Higa, and I. Costa. „Study of the corrosion resistance and in vitro biocompatibility of PVD TiCN-coated AISI 316 L austenitic stainless steel for orthopedic applications“. In: *Surface and Coatings Technology* 205.7 (2010), pp. 2074–2081. ISSN: 02578972. DOI: 10.1016/j.surfcoat.2010.08.101.

[283] S. Surviliene, S. Bellozor, M. Kurtinaitiene, and V. Safonov. „Protective properties of the chromium–titanium carbonitride composite coatings“. In: *Surface and Coatings Technology* 176.2 (2004), pp. 193–201. ISSN: 02578972. DOI: 10.1016/S0257-8972(03)00716-3.

[284] M. P. Gispert, A. P. Serro, R. Colaço, E. Pires, and B. Saramago. „Wear of ceramic coated metal-on-metal bearings used for hip replacement“. In: *Wear* 263.7-12 (2007), pp. 1060–1065. ISSN: 00431648. DOI: 10.1016/j.wear.2006.11.036.

[285] F. Hollstein and P. Louda. „Bio-compatible low reflective coatings for surgical tools using reactive d.c.-magnetron sputtering and arc evaporation — a comparison regarding steam sterilization resistance and nickel diffusion“. In: *Surface and Coatings Technology* 120-121 (1999), pp. 672–681. ISSN: 02578972. DOI: 10.1016/S0257-8972(99)00357-6.

[286] F. Cui and D. Li. „A review of investigations on biocompatibility of diamond-like carbon and carbon nitride films“. In: *Surface and Coatings Technology* 131.1-3 (2000), pp. 481–487. ISSN: 02578972. DOI: 10.1016/S0257-8972(00)00809-4.

[287] R. Hauert. „A review of modified DLC coatings for biological applications“. In: *Diamond and Related Materials* 12.3-7 (2003), pp. 583–589. ISSN: 09259635. DOI: 10.1016/S0925-9635(03)00081-5.

[288] G. Dearnaley and J. H. Arps. „Biomedical applications of diamond-like carbon (DLC) coatings: A review“. In: *Surface and Coatings Technology* 200.7 (2005), pp. 2518–2524. ISSN: 02578972. DOI: 10.1016/j.surfcoat.2005.07.077.

[289] R. K. Roy and K.-R. Lee. „Biomedical applications of diamond-like carbon coatings: a review“. In: *Journal of biomedical materials research. Part B, Applied biomaterials* 83.1 (2007), pp. 72–84. DOI: 10.1002/jbm.b.30768.

[290] G. Francz, A. Schroeder, and R. Hauert. „Surface analysis and bioreactions of Ti- and V-containing a-C : H“. In: *Surface and Interface Analysis* 28.1 (1999), pp. 3–7. ISSN: 0142-2421. DOI: 10.1002/(SICI)1096-9918(199908)28:1{\textless}3::AID-SIA609{\textgreater}3.0.CO;2-U.

[291] N. K. Manninen, R. E. Galindo, S. Carvalho, and A. Cavaleiro. „Silver surface segregation in Ag-DLC nanocomposite coatings“. In: *Surface and Coatings Technology* 267 (2015), pp. 90–97. ISSN: 02578972. DOI: 10.1016/j.surfcoat.2014.12.029.

[292] L. J. Wang, F. Zhang, A. Fong, K. M. Lai, P. W. Shum, Z. F. Zhou, Z. F. Gao, and T. Fu. „Effects of silver segregation on sputter deposited antibacterial silver-containing diamond-like carbon films“. In: *Thin Solid Films* 650 (2018), pp. 58–64. ISSN: 00406090. DOI: 10.1016/j.tsf.2018.02.015.

[293] M. Braic, M. Balaceanu, V. Braic, A. Vladescu, G. Pavelescu, and M. Albulescu. „Synthesis and characterization of TiN, TiAlN and TiN/TiAlN biocompatible coatings“. In: *Surface and Coatings Technology* 200.1-4 (2005), pp. 1014–1017. ISSN: 02578972. DOI: 10.1016/j.surfcoat.2005.02.140.

[294] R. Hübler, A. Cozza, T. L. Marcondes, R. B. Souza, and F. F. Fiori. „Wear and corrosion protection of 316-L femoral implants by deposition of thin films“. In: *Surface and Coatings Technology* 142-144 (2001), pp. 1078–1083. ISSN: 02578972. DOI: 10.1016/S0257-8972(01)01321-4.

[295] Y. Leng, H. Sun, P. Yang, J. Chen, J. Wang, G. Wan, N. Huang, X. Tian, L. Wang, and P. Chu. „Biomedical properties of tantalum nitride films synthesized by reactive magnetron sputtering“. In: *Thin Solid Films* 398-399 (2001), pp. 471–475. ISSN: 00406090. DOI: 10.1016/S0040-6090(01)01448-1.

[296] M. Hein, D. Kokalj, N. F. Lopes Dias, D. Stangier, H. Oltmanns, S. Pramanik, M. Kietzmann, K.-.-P. Hoyer, J. Meißner, W. Tillmann, and M. Schaper. „Low Cycle Fatigue Performance of Additively Processed and Heat-Treated Ti-6Al-7Nb Alloy for Biomedical Applications“. In: *Metals* 12.1 (2022). ISSN: 2075-4701. DOI: 10.3390/met12010122. URL: https://www.mdpi.com/2075-4701/12/1/122.

[297] M. Hein. „Influence of Physical Vapor Deposition on High-Cycle Fatigue Performance of Additively Manufactured Ti-6Al-7Nb Alloy“. In: *Crystals* 12.9 (2022), p. 1190. DOI: 10.3390/cryst12091190.

Student Theses

The following list of theses were carried out at the Chair of Materials Science at Paderborn University as part of this dissertation. The definition of the objectives, the processing as well as the evaluation, interpretation, and visualization of results have been carried out under the scientific guidance of the supervisors Prof. Dr.-Ing. habil. Mirko Schaper, Dr.-Ing. Kay-Peter Hoyer, and Maxwell Hein. The results obtained have been partly incorporated into the publications included in this dissertation.

[AM20] A. G. Müller, (supervisor: M. Schaper, K.-P. Hoyer): "Pulverbasiertes, selektives Laserstrahlschmelzen einer Titanlegierung für die medizinische Anwendung". Paderborn University, Chair of Materials Science, unpublished master thesis, 2020.

[MS20] M. C. Schlichter, (supervisor: M. Schaper, K.-P. Hoyer): "Potenzialanalyse zur Verwendung von TiNb24Zr4Sn8 als Implantatwerkstoff in der Humanmedizin". Paderborn University, Chair of Materials Science, unpublished bachelor thesis, 2020.

[MH20] M. Hötger, (supervisor: M. Schaper, K.-P. Hoyer): "Charakterisierung wärmebehandelter, biomedizinisch relevanter Titanlegierungen". Paderborn University, Chair of Materials Science, unpublished bachelor thesis, 2020.

[YZ21] Y. Zhao, (supervisor: M. Schaper, K.-P. Hoyer): "Korrosionsverhalten von additiv verarbeitetem TiAl6Nb7". Paderborn University, Chair of Materials Science, unpublished bachelor thesis, 2021.

[AG21] A. Griskewitz, (supervisor: M. Schaper, K.-P. Hoyer): "Kurzzeitermüdungsverhalten von additiv gefertigtem TiAl6Nb7 für biomedizinische Anwendungen". Paderborn University, Chair of Materials Science, unpublished bachelor thesis, 2021.

[JB21] J. Braun, (supervisor: M. Schaper, K.-P. Hoyer): "Einfluss der physikalischen Gasphasenabscheidung auf das Kurzzeitermüdungsverhalten von additiv gefertigtem TiAl6Nb7". Paderborn University, Chair of Materials Science, unpublished bachelor thesis, 2021.

[PE21] P. Erckmann, (supervisor: M. Schaper, K.-P. Hoyer): "Mikrostruktureller Einfluss auf die mechanischen Eigenschaften von additiv gefertigtem TiAl6Nb7". Paderborn University, Chair of Materials Science, unpublished bachelor thesis, 2021.

[TS21] T. Schulz, (supervisor: M. Schaper, K.-P. Hoyer): "Einfluss der physikalischen Gasphasenabscheidung auf das Langzeitermüdungsverhalten von additiv verarbeitetem Ti-6Al-7Nb". Paderborn University, Chair of Materials Science, unpublished student thesis, 2021.

[PA22] P. Alter, (supervisor: M. Schaper, K.-P. Hoyer): “Charakterisierung der additiv verarbeiteten Titanlegierung Ti-24Nb-4Zr-8Sn für die Anwendung als Permanentimplantat“. Paderborn University, Chair of Materials Science, unpublished master thesis, 2022.

[CB22] C. Borchers, (supervisor: M. Schaper, K.-P. Hoyer): “Einfluss der physikalischen Gasphasenabscheidung auf das Korrosionsverhalten von additiv verarbeitetem Ti-6Al-7Nb in körperähnlichen Medien“. Paderborn University, Chair of Materials Science, unpublished student thesis, 2022.

Erklärung zur Zitation von Inhalten aus studentischen Arbeiten

In Ergänzung zu meinem Antrag auf Zulassung zur Promotion in der Fakultät für Maschinenbau der Universität Paderborn erkläre ich gemäß §11 der Promotionsordnung und unter Beachtung der Regelung zur Zitation studentischer Arbeiten:

Die von mit vorgelegte Dissertation habe ich selbstständig verfasst, und ich habe keine anderen als die angegebenen Quellen und Hilfsmittel benutzt. Es sind Inhalte studentischen Ursprungs (studentische Arbeiten) in dieser Dissertation enthalten.

Ich habe die verwendeten Arbeiten entsprechend der Regelung „Zitation aus studentischen Arbeiten in Dissertationen“ zitiert.

Paderborn, im November 2023

Maxwell Hein